Vanadium and Zinc Isotope Ratios in Lunar Basalts

Sean S. Hopkins

St. Cross College

Department of Earth Sciences



Thesis submitted to the University of Oxford for the degree of Doctor of Philosophy

Trinity Term 2019

Abstract

(290 words)

Measurements of isotopic ratios have been useful in understanding the formation and evolution of planetary bodies in our Solar System. However, studies have typically been limited in sample overlap, thereby limiting possible interpretation. This study presents the first high-precision vanadium isotope data, zinc isotope data (via double-spiking), and trace-element data for a suite of lunar basalts. Companion analyses of chlorine and sulphur isotope ratios were obtained at University of New Mexico and University of Maryland.

Vanadium isotope ratios span a larger range (~2.5‰) within this suite of lunar basalts than found in all igneous terrestrial rocks (~2.3‰). Lunar isotopic ratios are almost uniformly lighter than those from the bulk silicate Earth (BSE). Unlike on Earth, variation in vanadium isotope ratios is mainly due to cosmogenic effects, where bombardment of lunar samples by energetic particles (from solar and galactic cosmic rays) alters primary isotopic compositions. Modelling of cross-sections shows that iron is likely the most important target element in lunar samples. Correcting for cosmogenic effects shows lunar basalts to have uniform vanadium isotope ratios within error of recent estimates for the BSE. Where published meteorite data is available, accounting for cosmogenic exposure shows no resolvable difference between the BSE, Mars, Moon, and chondrites, in contrast to earlier studies.

Zinc displays a large isotopic range (~10‰) even amongst samples of the same lithological subtype, likely reflecting the volatile behaviour of zinc. Chlorine isotope ratios for the water-soluble fractions of the basalts in this suite (and for published data) correlate negatively with zinc isotope ratios, indicating a mixing trend between a heavy-Zn, light-Cl endmember, and a light-Zn, heavy-Cl endmember. Mobilisation of volatiles enriched in the lunar crust during magmatic ascent or eruption is the most plausible explanation for this trend.

Extended Abstract

The Moon is widely-accepted to have formed after a giant impact event, whereby a large planetary body struck the proto-Earth throwing off mainly silicate material from which the Moon formed. However, a growing body of isotopic data has shown the bulk silicate Earth (BSE) and the Moon to be remarkably similar compared to meteorites, particularly for the more refractory elements. This conflicts with simulations of the “canonical” view of lunar origin, which can only reconcile the dynamics of Moon-formation when it forms mainly from impactor material.

Isotopic measurements of lunar rocks have not only shed light upon the formation of the Moon, but also shown that significant variability exists within the lunar suite. This can be due to a variety of processes: partial melting, crystal fractionation, source heterogeneity, volatile behaviour, and cosmogenic effects. Previous studies, however, have typically been limited in overlap for the specific samples analysed, and this has correspondingly restricted the strength of interpretation. This study presents data for combined zinc (Zn) and vanadium (V) isotope and trace element analyses for a suite of 19 lunar basalts (10 high-Ti, 9 low-Ti). These samples were obtained in collaboration with partnering teams at the University of New Mexico and the University of Maryland who obtained chlorine (Cl) and sulphur (S) isotopic measurements on the same samples.

Vanadium is a refractory, moderately siderophile transition metal. Its multiple naturally-occurring oxidation states (0, +2, +3, +4, +5) have made it the subject of interest for natural systems where changes in oxidation state are significant. Vanadium has two isotopes, ^{50}V and ^{51}V. The extreme natural $^{51}V/^{50}V$ ratio (~400) and the proposed irradiative origin of ^{50}V has meant that obtaining high-precision V isotope data has been a long-term goal of the cosmochemistry field. However, only with recent advances in multiple-collector inductively-coupled-plasma mass-spectrometry has high-precision (< 0.2‰) measurement of V isotope

ratios been made possible. Terrestrial magmatic rocks display a ~2.3‰ range in V isotopic ratios, mostly reflecting crystallisation of (Fe,Ti)-bearing oxides. Original low-resolution ($M/\Delta M \sim 300$) measurements of meteorites showed a ~ -1‰ offset compared to the BSE. More recent higher-resolution ($M/\Delta M \sim 4000$) work has shown that – although chondrites are still isotopically-lighter than the Earth – the magnitude of this difference is reduced (~ -0.1‰ to -0.3‰).

This thesis presents a comparison of MC-ICPMS techniques for obtaining precise and accurate measurements of geological samples, in preparation for measurements of lunar rocks. The first high-precision V isotope data for the Moon is then presented. Lunar basalts span a range in V isotope ratios (~2.5‰) larger than for all terrestrial igneous samples measured to date (~2.3‰). Lunar basalts are typically isotopically-lighter than the terrestrial suite. Vanadium isotope ratios do not appear to vary with magmatic processes despite the large range in ilmenite contents observed in the lunar basalt suite. Instead, V isotope ratios appear strongly related to exposure age (t_e) and (where data exists) neutron-sensitive gadolinium isotope anomalies. Thus, it appears that cosmogenic effects largely control the V isotopic effects seen in the basalt suite. Cross-sections for the production and burnout of V isotopes through interactions between samples and high-energy particles (protons, alpha-particles and neutrons) indicate that Fe is likely the most important target element for production of cosmogenic V isotope anomalies in lunar samples. Correcting for cosmogenic effects by plotting V isotope ratios against $t_e \cdot [Fe]/[V]$ yields a strong linear correlation ($R^2 = 0.95$). There appear to be no differences between high-Ti and low-Ti lunar basalts prior to exposure. In contrast to previous work, there is no resolvable difference between the pre-exposure compositions of Earth, Moon, and chondrites.

Zinc is a moderately-volatile element with five stable isotopes (^{64}Zn, ^{66}Zn, ^{67}Zn, ^{68}Zn, ^{70}Zn) which has been widely studied in samples from across the solar system. Terrestrial mafic

and ultra-mafic Zn isotope variations ($^{66}Zn/^{64}Zn$) are limited in magnitude (~0.3‰). In contrast, lunar samples show the widest range of Zn isotope ratios (~20‰) observed throughout the Solar System. Previous studies of lunar mare basalts have shown that both heavy (+1-2‰ vs BSE) and light (~ -1‰ to -6‰) basalts exist and the heavy isotopic compositions have been used to estimate the bulk lunar composition (~ +1‰ to +2‰ vs BSE). The isotopically-light basalts have been discounted as exhibiting enrichments in light Zn of a volatile origin, although the nature of this phase has not been explored in detail.

This study presents combined Zn, Cl and S isotope measurements to try to identify the source of Zn isotope variability in the Moon and better estimate the bulk silicate Moon composition. In agreement with earlier work, this study finds that Zn isotope ratios are highly variable in lunar basalts (~12‰), even from within the same sub-type group. Zinc and water-soluble Cl isotope ratios correlate negatively and indicate a mixing trend between a light Zn, heavy Cl endmember, and a heavy Zn, light Cl endmember.

The results of this study show that by using multiple analytical techniques on the same samples, much stronger interpretations can be leveraged as a result.

Acknowledgements

Thank you to my wonderful DPhil supervisors (Jane Barling, Alex Halliday, Fiona Larner, Julie Prytulak, and Sara Russell) for their tireless support and hard work throughout the course of my DPhil. Despite the logistics of being spread across four institutions, they have always found a way to keep in touch, offer guidance and feedback, and help keep things moving forward. Thank you for being patient and encouraging during the more challenging aspects of this research project, and for your enthusiasm during its successes.

Thank you to all the sponsors for this project. Funding for this project came from the Science and Technology Facilities Council (STFC Planetary Origins and Developments: ST/M001318/1 to A.N.H.), Natural Environment Research Council (NERC: NE/N009568/1 to J.P.), with additional funding came from Department of Earth Sciences, Burdett-Coutts Fund, and Columbia University.

I would like to extend my sincere gratitude to all the colleagues who have spent countless hours supporting the mass-spectrometry in this project: Phil Holdship, Nick Belshaw, Alan Hsieh (Oxford) and Barry Coles (Imperial College London). Thanks also to Naomi, Matthew, Tim, Jo, Mel, and Pierre for being generous with your time and support. Thank you to our research partners Anthony Gargano, Zachary Sharp (University of New Mexico), James Dottin III, and James Farquhar (University of Maryland). Thank you to the NASA CAPTEM and NASA-JSC team (especially Ryan Zeigler and Jeremy Kent) for providing the lunar samples in this study and for quickly responding to multiple requests for information on the provenance and preparation of samples. Thanks also to the friends and colleagues within the department who have not only spent countless hours discussing ideas and providing advice in an academic context but have also been great friends along the way: Jo, Tim, Marta, Jon, Duane, Peter, Mel, Dave, Arola, Naomi, Matt, and so many others who have made this degree a pleasure.

On a more personal note, I'm grateful to my friends outside of academia for always being there and providing a refreshing perspective on things (by the way, I told you it's not made of cheese). Thank to my wonderful partner, Megan, who has kept me (almost) sane over the last few years and who has provided patience and support throughout all aspects of my life. Thank you to my family for their unwavering love over the years, especially my Mum to whom I owe everything.

SH

Table of Contents

Abstract.....ii
Extended Abstract iii
Acknowledgements vi
Table of Contents.....vii
List of Commonly Used Abbreviations/Acronyms viii
Chapter 1 Introduction.....1
Chapter 2 Methods 12
Chapter 3 Development of Analytical Protocols for the Measurement of Vanadium Isotope Ratios in Lunar Rocks.....26
Chapter 4 The Vanadium Isotopic Composition of Lunar Basalts 50
Chapter 5 Combined Zinc, Chlorine, and Sulphur Isotopes and Volatile Element Mass Transfer on the Moon.....83
Chapter 6 Conclusions and Outlook.....120
References.....126
Appendix 1: Results of Quad ICPMS Analysis for Lunar Basalts and BHVO2.....S1
Appendix 2: Literature Data S4
Appendix 3: Results of Zn Isotope Analysis S29
Appendix 4: Supplementary Figures S33
Appendix 5: Manuscript of Hopkins et al. 2019.....S52

List of Commonly Used Abbreviations/Acronyms

Abbreviation/Acronym	**Meaning**
AA	primary *Alfa Aesar* standard defined as zero for most V isotope analyses
BDH	secondary *BDH Chemicals* solution standard for V isotope analysis
BSE	Bulk Silicate Earth
Cl	chlorine
Ga	billion years before the present
Ma	million years before the present
MORB	Mid-Ocean Ridge Basalt composition
ppb	parts per billion (by weight)
ppm	parts per million (by weight)
S	sulphur
V	vanadium
Zn	zinc
$\delta^{51}V$	$[(^{51}V/^{50}V)_{measured}/(^{51}V/^{50}V)_{standard} - 1\ ] \times 1000$
$\delta^{66}Zn$	$[(^{66}Zn/^{64}Zn)_{measured}/(^{66}Zn/^{64}Zn)_{standard} - 1\ ] \times 1000$
[*X*]	concentration of element, *X* (in ppm unless otherwise stated)
‰	per mil (parts per thousand)
wt %	percentage (by weight)

1

Introduction

1.1 The Origin and Evolution of the Moon

1.1.1 The canonical Giant Impact

The Moon is generally accepted to have formed in a giant-impact whereby a planetary object collided with the proto-Earth, ejecting mainly silicate material from which the Moon later coalesced. The canonical giant impact model (Cameron and Ward, 1976; Hartmann and Davis, 1975) and subsequent numerical simulations of this model (e.g. Benz et al., 1986; Canup and Asphaug, 2001; Canup, 2004) proposes that a Mars-sized impactor struck the proto-Earth when it was ~90% accreted. Such an event can explain the different uncompressed densities of the Moon (~3.3g cm^{-3}) and the Earth (~4.4g cm^{-3}), the high angular momentum of the Earth-Moon system, and the broad geochemical similarities of the Earth and Moon (e.g. Barr et al., 2016). The Moon is proposed to have coalesced from mainly silicate material in the aftermath of the giant impact, leading to a Moon depleted in iron (~8%) compared to the Earth (Ringwood, 1986). Likewise, the Moon is considered depleted in volatiles and moderately volatile elements (MVEs) compared to the Earth, although the degree of this depletion is somewhat contested (Day and Moynier, 2014; Wolf and Anders, 1980).

1.1.2 Geochemistry of the Moon

Estimates of bulk lunar chemical composition derive mainly from analyses of rocks and soils obtained from the lunar surface during the Apollo and Luna sample return missions. In addition, a number of meteorites have been more recently identified as having a lunar provenance. Rocks from the lunar inventory mainly comprise either brecciated highlands anorthosites or more pristine (i.e. unbrecciated) basaltic rocks. The large-scale dichotomy exhibited by the presence of these highlands and basaltic regions provides evidence of a global lunar magma ocean (LMO) early in the Moon's history during which crystallising anorthositic

plagioclase was buoyantly lifted to the top of the LMO, forming the early lunar crust (Warren, 1985). Crystallisation of other phases in the LMO caused density instabilities and regional overturn of mantle material towards the end of LMO crystallisation, giving rise to the spatially-heterogeneous basalt sources in the lunar mantle (observed from the major and trace element characteristics of lunar basalts; Elkins-Tanton et al., 2011; Neal and Taylor, 1992). Because lunar mare basalts are typically less brecciated (and therefore less likely to have been contaminated by meteoritic materials) most chemical estimates of bulk lunar composition have been made from analysis of lunar basalts. However, lunar basalts have been exposed to the lunar atmosphere, have undergone differential amounts of partial melting and crystal fractionation, and derive from compositionally-distinct regions of the lunar mantle (e.g. Hallis et al., 2014). Therefore, care must be taken to account for processes that may obscure primitive lunar compositions.

Lunar basalts are primarily subdivided by their TiO_2 contents [very-low-Ti/VLT: TiO_2 < 1.5 wt%; low-Ti: 1.5 wt% < TiO_2 < 6 wt%, high-Ti, TiO_2 > 6%]. Analyses of their mineralogy and major and trace element compositions indicates that high-Ti and low-Ti basalts derive from lunar mantle regions with the presence and absence, respectively, of Ti-rich oxide minerals (e.g. ilmenite, armalcolite, Shearer et al., 2006). The crystallisation sequences of the parent magmas for these samples is different, with Ti-oxide minerals crystallising throughout magmatic evolution in the high-Ti basalts, but only at the end of differentiation for low-Ti basalts. This, in turn, causes significant differences in the trace elements of low-Ti and high-Ti basalts.

1.1.3 Isotopic uniformity and variability in the Moon

Isotopic abundances can vary both in a non-mass-dependent fashion, for example, as a result of radioactive decay, or cosmogenic, radiogenic and nucleosynthetic effects, or where the variations in isotopic ratios reflect mass-dependent fractionation.

1.1.3.1 Radiogenic and other non-mass-dependent isotopic effects

The Moon and the silicate Earth are remarkably similar in their atomic abundances of ^{17}O (Wiechert et al., 2001; Young et al., 2016; Greenwood et al., 2018), ^{54}Cr (Lugmair & Shukolyukov, 1998; Mougel et al., 2018), ^{50}Ti (Zhang et al., 2012), ^{182}W (Kruijer et al., 2015), and ^{92}Zr (Akram and Schonbachler, 2016). This has challenged understanding of the canonical giant impact which pre-supposes that an impactor and the proto-Earth should be isotopically-distinct (e.g. $\Delta^{17}O$ is widely variable in all meteorite classes, Clayton, 1993). The Moon formed mainly from impactor material according to dynamic models, (e.g. Canup, 2004) and so should also be isotopically-distinct (**Section 1.1.4**). Very small differences that have been statistically-resolved in $\Delta^{17}O$ and ^{182}W have been proposed to result merely from differential amounts of late-accretion to the Earth and Moon subsequent to lunar formation (Young et al., 2016; Kruijer et al., 2015).

On a local scale, analyses of lunar samples have shown that non-mass-dependent isotopic variability exists in some lunar samples which been exposed to cosmic rays. Samples exposed at or near to the lunar surface are subject to bombardment by high-energy particles (mainly protons, alpha particles, and secondary neutrons). Interaction of target elements with the energetic particles in solar (SCR) or galactic cosmic rays (GCR) can produce non-mass-dependent excesses in ^{158}Gd, ^{53}Cr, ^{54}Cr, ^{50}Ti and the noble gases (Marti 1967; Mougel et al., 2012; Zhang et al., 2012).

1.1.3.2 Mass-dependent isotopic variation

Mass-dependent isotopic fractionation has been found in lunar samples and interpreted to represent a number of different processes, depending upon the element. In general, more refractory elements ($T_{50\%-c}$ < 1400K) show mass-dependent isotopic fractionations within lunar samples on the order of ~ ± 0.2‰ resulting from equilibrium fractionation processes. For example, high-Ti basalts and low-Ti basalts show differences in $\delta^{56}Fe$ and $\delta^{57}Fe$ and this has been interpreted as source heterogeneity resulting from ilmenite fractionation in the LMO, or the effects of partial melting during parental magma generation (Liu et al., 2010; Poitrasson et al., 2004; Sossi and Moynier, 2017; Wiesli et al., 2003). Results of Cr isotope analysis in lunar basalts (Bonnand et al., 2016) show correlations with indices of magmatic differentiation (Mg#), but high-Ti and low-Ti basalts spanning a similar range in $\delta^{53}Cr$, indicating a source region more homogenous in Cr isotopes than for Fe or Ti (Millet et al., 2016). For the lunar mantle, mass dependent isotopic ratios are proposed to be similar to the BSE.

Moderately volatile elements (e.g. Zn, Ga, Rb, K) can display much large isotopic variability (> 0.5‰ – Kato et al., 2015; Kato and Moynier, 2017; Pringle and Moynier, 2017; Wang and Jacobsen, 2016) that has been interpreted as kinetic fractionation occurring during igneous degassing at the lunar surface, degassing from a lunar magma ocean, loss during the giant impact events, or evaporation/sputtering during meteoroid impact processes (Day and Moynier, 2014).

1.1.4 Implications for the giant impact model

In the wake of the discovery that the Earth and the Moon are isotopically-similar (for refractory elements), new theories and proposals have emerged which could explain the isotopic similarities in tandem with the dynamical properties of the Earth-Moon system.

A post-impact equilibration of isotopic signatures has been proposed (Pahlevan & Stevenson, 2007), although such a mechanism does not favour the equilibration of isotopic signatures of more refractory elements (e.g. W, Zr, Ti, Cr). In addition predicted isotopic offsets in Si isotopes (Pahlevan et al., 2011) were not observed (Armytage et al., 2012). Alternative impact scenarios have been proposed (Canup, 2012; Cuk and Stewart, 2012; Reufer et al., 2012; Rufu et al., 2017) where alternative relative masses and velocities of impactors are explored but these scenarios require a narrow range of pre-conditions in order to match the observed angular momentum within the Earth-Moon system today. The extent of inner solar system homogeneity at the time of Moon-forming impact has also been explored (Dauphas et al., 2014; Mastrobuono-Battisti et al., 2015) and impactors with an Earth-like composition may not be as unusual as previously-assumed. More recently, Lock et al., (2018) proposed that a terrestrial synestia following a very high-energy, high-angular momentum impact could form a Moon well-mixed with the Earth and with the characteristic MVE depletions observed. Importantly this model allows variety of impactor sizes and does not require the Earth to be in a high-angular momentum state prior to impact. Although conditions result in a well-mixed system, isotopic fractionation (especially of MVEs) during condensation from a high-T, high-angular momentum impact is possible, in line with results for K isotopes (Wang and Jacobsen, 2016).

1.2 This study

This study sets out to analyse a suite of lunar basalts for their isotopic compositions within two elements of differing geochemical behaviour: vanadium and zinc. A detailed introduction to the isotopic systems of each element and their application to planetary and magmatic systems can be found in **Chapters 3** and **4** (for V) and **Chapter 5** (for Zn), but an overview is given here.

Vanadium

Vanadium is a refractory transition metal, characterised by its multiple naturally-occurring oxidation states (V^{2+}, V^{3+}, V^{4+}, V^{5+}). As such, it has been of significant interest in igneous petrology and planetary geochemistry in understanding changing oxidation states of mantles and melts (Canil, 1997; Karner et al., 2006; Lee et al., 2005, 2003; Li and Lee, 2004; Mallmann and O'Neill, 2009; Papike et al., 2005; Sutton et al., 2005; Wood et al., 2008).

Vanadium has two stable isotopes: ^{50}V (0.25%) and ^{51}V (99.75%). Isotopic ratios of V have been of interest to cosmochemists for decades due to the low abundance and irradiative origin of ^{50}V. Early studies of V isotopes were hindered by a lack of precision (> ± 5‰) and reported relative isotopic homogeneity between the Earth, Moon and meteorites (Balsiger et al., 1976, 1969, Lipschutz et al., 1973, 1971). Early measurements of iron meteorites (Stauffer and Honda, 1962, 1961) yielded extreme $^{51}V/^{50}V$ ratios (between 2-100, compared to the natural $^{51}V/^{50}V$ ratio ~400). Since the advent of MC-ICPMS (Halliday et al., 1995), there has been renewed interest in V isotopes for application to terrestrial magmatic systems and planetary bodies. High-precision techniques (precision < 0.2‰) for measuring V isotopes by MC-ICPMS were first described by Nielsen et al., (2011), who also set the current precedent for reporting V isotope ratios in per mil relative to a *Alfa Aesar Specpure* V standard solution (defined as 0):

$$\delta^{51}V_{AA} = \left(\frac{\left({}^{51}V/_{50}{}_V \right)_{measured}}{\left({}^{51}V/_{50}{}_V \right)_{AA}} - 1 \right) \times 1000.$$

Difficulties in measuring V isotopes arise from the extreme natural $^{51}V/^{50}V$ ratio (~400), and the presence of significant amounts of chemically-similar Cr and Ti in natural samples (both with interfering isotopes on m/z = 50) which must be quantitatively-removed, whilst retaining

100% of the V. Vanadium shows isotopic fractionation in terrestrial magmas during the crystallisation of (Fe,Ti)-bearing oxide minerals, with lighter isotopies preferentially incorporated into the oxide structure (due to the change in coordination between mineral and melt, Prytulak et al., 2017; Sossi et al., 2018; Wu et al., 2018). This oxide crystallisation is responsible for most isotopic variability observed in terrestrial igneous rocks (~2.3‰, Prytulak et al., 2017). Initial measurements of a suite of meteorites (chondrites, achondrites and martian samples, Nielsen et al., 2014) showed a uniform offset (~-1‰) compared to the BSE which has an estimated composition of $\delta^{51}V = -0.7 \pm 0.2$‰ (Prytulak et al., 2013). Although now accepted that these initial meteorite measurements were affected by incomplete resolution of polyatomic interferences during analysis, the BSE still appears heavier than chondrites in more recent medium-resolution ($M/\Delta M$) analyses (Nielsen et al., 2019) by ~ 0.3-0.5‰ (which has been proposed as a result of nucleosynthetic heterogeneity in meteorite classes).

To date, no high-precision V isotopic measurements of lunar samples have been obtained (except those in this study, which have now been published in Hopkins et al., (2019) (**Appendix 5**). For Si isotopes, the BSE and Moon were found to be identical within error (Armytage et al., 2012), but meteorites were found to be lighter than the BSE, like V isotopes (Armytage et al., 2011). This was explained as a fractionation resulting from core-formation. The Moon is expected to be similar in V isotope ratios to the BSE (as a refractory element). However, previous studies have ruled out metal-silicate fractionation as a mechanism to fractionate V isotopes, in contrast to Si (Nielsen et al., 2014). This study aims to obtain the first V isotope data for the Moon in order to explore the difference presented between the BSE and meteorites (Nielsen et al., 2019, 2014; Prytulak et al., 2013).

Zinc

Zinc is a moderately-volatile element with 5 naturally-occurring isotopes: ^{64}Zn (49.2%), ^{66}Zn (27.8%), ^{67}Zn (4.0%), ^{68}Zn (18.4%), ^{70}Zn (0.6%). Zinc isotope ratios are reported in per mil relative to a *JMC-Lyon* Zn isotope standard, defined as zero in Marechal et al., (1999):

$$\delta^{66}Zn_{JMC-Lyon} = \left(\frac{\left({}^{66}Zn/{}_{64}Zn \right)_{measured}}{\left({}^{66}Zn/{}_{64}Zn \right)_{JMC-Lyon}} - 1 \right) \times 1000.$$

Zinc isotopes have been widely measured in terrestrial, lunar, and meteorite samples (Moynier et al., 2017, **Chapter 5**). Terrestrial mafic and ultramafic samples show a restricted range in δ^{66}Zn between ~ 0.1-0.3‰, and the BSE has most recently been estimated to have δ^{66}Zn = +0.16 ± 0.06‰ (Sossi et al., 2018). In contrast multiple studies of lunar samples (Day et al., 2017; Herzog et al., 2009; Kato et al., 2015; Moynier et al., 2006; Paniello et al., 2012) have shown there to be a range in δ^{66}Zn larger than all other solar system materials combined (total δ^{66}Zn variability ~ 20‰). Lunar soils are isotopically-heavy (≤ ~6‰) and this is thought to reflect sputtering and loss of light Zn during regolith processing (Herzog et al., 2009; Kato et al., 2015). In contrast, lunar pyroclastic glass beads (PGBs) are isotopically-light, and show a correlation between δ^{66}Zn and bead diameter (and an inverse correlation between [Zn] & bead diameter), indicating that a surface-precipitation of isotopically-light Zn during the explosive formation of lunar PGBs is a plausible origin (in line with the discovery of Zn-rich minerals on the surfaces of PGBs, Ma and Liu, 2019). Lunar basalts have typically been used to estimate lunar Zn isotope composition. Mare basalts typically show a range in δ^{66}Zn between +1‰ to +2‰ regardless of lithological subtype (e.g. high-Ti vs low-Ti). However, a handful of lunar basalts shows δ^{66}Zn values < 0‰ (Herzog et al., 2009; Kato et al., 2015; Paniello et al., 2012). Although the origin of this variability is likely due to volatile behaviour (due to the extreme

isotopic fractionations observed), the origin of this isotopically-light phase has not been constrained in previous studies, being rather generally ascribed to light Zn (as $ZnCl_2$) vapour precipitating on the surfaces of samples or being trapped in samples during exhalative eruption (Kato et al., 2015; Paniello et al., 2012). Estimates of lunar $\delta^{66}Zn$ composition have been made using the remaining isotopically-heavy basalts to give a bulk lunar composition ~ +1 ± 0.5‰ heavier than the BSE. The Moon is thought to have achieved this composition as a result of the giant impact, or global lunar degassing during the LMO, or at a more regional scale during later eruptive and/or impact processes (Day and Moynier, 2014).

Multi-fold isotopic and chemical analyses

Direct cross-comparison between data from different isotopic systems (e.g. between $\delta^{66}Zn$ and $\delta^{37}Cl$) is often hindered by a lack of sample overlap. In this study, a suite of lunar basalts (chosen for their unbrecciated nature and range in chemical compositions) was requested from NASA to perform a combined Zn, V, Cl, and S isotope and trace element study of lunar basalts. This combination of analyses should allow greater insight into a) the behaviour of volatiles on the lunar surface (Zn, Cl, S, trace elements), and b) better interpretation any variation in $\delta^{51}V$ that should arise (trace elements). Analyses of Zn and V isotopes and trace element concentrations were performed at the University of Oxford, with partnering aliquots of samples (for Cl and S isotope analyses) sent directly to collaborators at the University of New Mexico and the University of Maryland.

Structure of the thesis

Chapter 2 details the sample selection criteria, sample preparation and digestion procedures for the samples in this study. Details of the column chromatography and MC-ICPMS

techniques for lunar samples are provided. Analyses of trace-element concentrations were performed alongside isotopic measurements.

Chapter 3 records the attempts to identify a suitable improved mass-spectrometry and column chromatography procedure for measuring V isotope ratios in lunar basalts. The first MC-ICPMS studies of V isotope ratios in geological materials (Nielsen et al., 2011; Prytulak et al., 2011) were limited to analysis at low mass resolution. This resulted in inaccurate V isotope ratios being found for meteorites (Nielsen et al., 2014; Nielsen et al., 2019) due to the incomplete resolution of S-bearing compound interferences. A protocol for MC-ICPMS isotopic measurements at medium-resolution ($M/\Delta M > 4000$) is therefore highly desirable before analysis of lunar basalts.

Chapter 4 uses the outcomes of the preceding chapter and presents the results of the first V isotope data for the Moon. The origin of lunar V isotopic variability is explored and explained.

Chapter 5 presents the first combined Zn, Cl, and S isotope measurements of the same lunar samples in order to investigate the origin of Zn isotope variability on the Moon and its relation to volatile processes. Previous Zn isotope and Cl isotope work has proposed that metal chlorides (including $ZnCl_2$) may be a significant volatile phase during igneous degassing at the lunar surface (Paniello et al., 2012; Sharp et al., 2010). Sulphur isotopes also show variability in lunar samples (e.g. McCubbin et al., 2015) and may provide additional constraints on the nature of volatile/moderately volatile element behaviour on the Moon. Chlorine and sulphur isotopic measurements were carried out in partnership with teams at the University of New Mexico and the University of Maryland respectively, following a joint proposal to NASA for analysis of these isotopic systems in the same lunar basalts.

Finally, Chapter 6 presents the main conclusions from this study and the outlook for future work.

2

Methods

The following is adapted from the supplementary text of Hopkins et al. (2019) for sections regarding sample preparation for trace-element analysis via Quad ICPMS, and V isotope analysis via MC-ICPMS. All sample preparation, column chemistry, trace-element analyses, and Zn isotope analyses were performed in the Department of Earth Sciences, University of Oxford. Vanadium isotope analyses were performed at Imperial College, London.

2.1 Lunar Sample Selection

Previous isotopic studies of lunar materials have often been performed on different rock samples returned from the Moon, making direct comparison of isotopic variation in different systems more difficult. For example, there has been little overlap in samples analysed for both Zn and Cl isotopes, despite $ZnCl_2$ being proposed as a carrier for isotopically-light degassed Zn at the lunar surface (Paniello et al., 2012; Sharp et al., 2010). When there has been overlap in the samples analysed, these measurements were almost always performed on separate small aliquots of the larger parent samples. Intra-sample heterogeneity (e.g. due to the large grain size compared to sample size) may therefore present an obstacle to correctly interpreting the geochemistry of the parent samples.

Nineteen Apollo lunar basalts (**Table 2.1**) were requested from NASA as part of a joint proposal (with the University of New Mexico and the University of Maryland) to measure Zn, V, Cl, and S isotope ratios and trace-element concentrations on the same sub-samples. Lunar basalts were chosen as they represent the most primitive (i.e. unbrecciated) lunar rocks, and so therefore are less likely to be contaminated by meteorite processes at the lunar surface (Shearer, 2006). Ten high-Ti (TiO_2 > 6 wt%) and nine low-Ti (1.5 < TiO_2 < 6 wt%) basalts were chosen from five missions (Apollo 11, 12, 14, 15 & 17). Published TiO_2 contents for this suite spans a range from 2.2 wt% (15535) to 12.9% (70215, **Appendix 2a**). Interiors of all parent samples were requested as previous work has invoked surficial precipitation of isotopically-light Zn as

a mechanism for producing light $\delta^{66}Zn$ observed in a handful of lunar basalts (Day and Moynier, 2014; Herzog et al., 2009; Kato et al., 2015; Moynier et al., 2006; Paniello et al., 2012). Exteriors of two samples (10017 and 12054) were also chosen as a comparison to test this hypothesis. A sample of the glass splash coating from 12054 was obtained in Oxford (for Zn and V isotopic measurements) to test whether this emplaced material has been fractionated relative to its host (of similar composition, Hartung et al., 1978). A sample of high-Al/low-Ti Apollo 14 basalt, 14053, was chosen for its high-Al contents compared to other low-Ti basalts. Interior and exterior chips of high-K/high-Ti Apollo 11 basalt, 10017 were selected as these samples are enriched in K, REEs and other ITEs. Samples 15016 and 15556 are Apollo 15 olivine basalts with highly vesicular (~50% by volume) textures (Meyer, 2008).

Table 2.1 Lunar basalts requested from NASA in this study (for Zn and V isotope analysis and trace-element measurements).

Mission	Sample	Type	Sub-type	Location
A11	10017-400	High-Ti/High-K	11A	*exterior*
	10017-405	High-Ti/High-K	11A	*interior*
	10020-255	High-Ti/Low-K	11B3	*interior*
	10044-655	High-Ti/Low-K	11B1	*interior*
A12	12018-598	Low-Ti Olivine		*interior*
	12054-13	Glass Splash		
	12054-146	Low-Ti Ilmenite Basalt		*interior*
	12054-150	Low-Ti Ilmenite Basalt		*exterior*
	12063-343	Low-Ti Ilmenite Basalt		*interior*
A14	14053-305	Low-Ti/High-Al/Low-K	HA	*interior*
A15	15016-240	Low-Ti Olivine-normative		*interior*
	15535-165	Low-Ti Olivine-normative		*interior*
	15556-258	Low-Ti Olivine-normative		*interior*
A17	70215-389	High Ti	17B2	*interior*
	70255-56	High Ti	17A	*interior*
	71135-34	High Ti	17B2	*interior*
	71546-22	High Ti	17A	*interior*
	74275-355	High Ti	17C	*interior*
	75035-249	High Ti	*Unclassified*	*interior*

Measurements of S and Cl isotope ratios were performed at the University of Maryland (by James Dottin III and James Farquhar) and the University of New Mexico (by Anthony Gargano and Zachary Sharp). Ideally, Cl, S, and Zn isotope ratios would be measured within the same homogenised aliquots of sample. However, due to the conflicting sample preparation requirements for each analytical technique this was found to be unwise (due to the risk of contamination or loss of material). Instead for the S and Cl fractions, chips of rock were obtained from neighbouring locations within parent samples and sent to each institution. This should negate intra-sample heterogeneity at scales > ~ 1cm but may preserve heterogeneities at a smaller scale. The total mass for each separate sample was ~ 250mg (for V and Zn isotopes and trace-elements at Oxford), ~1000mg (for Cl isotope analysis at UNM) and 500mg (for S isotope analysis at UMD).

2.2 Sample Preparation

2.2.1 Washing, drying, powdering

Lunar basalt samples (initial mass ~ 250 mg) were received from NASA as chips in sealed containers, extracted from pre-determined (i.e. interior vs exterior) locations within the parent samples. After initial weighing, samples were sonicated in ultra-pure water (resistivity ~ 18.2 MΩ cm, hereon "MQ H_2O") to remove any surficial dust contaminants or water-soluble Zn from the chip-extraction process, centrifuged in pre-cleaned VWR® metal-free centrifuge tubes and dried on a hotplate set at 50 °C in 7 mL Savillex *[Savillex Corporation, MN, USA]* PFA vials for one week. The washing and drying procedures were carried out in a laminar flow hood. After drying, each sample was finely crushed using a pre-cleaned agate pestle and mortar. The washing and crushing procedure was tested and found to negligibly contribute to overall elemental concentrations. The resulting powder from each sample deviated from the initial chip mass by ≤2%.

2.2.2 Digestion

All acids used for sample digestion and in subsequent column chromatography and dilution procedures were sub-boiling distilled in quartz (HCl, HNO_3) and PTFE (HF) stills and have been previously tested and found clean for background elemental concentrations of Ti, Cr, Fe, V, and Zn. Zinc blank contributions from the washing, drying, powdering, and weighing procedures were ≤ 0.3ng. All water used in sample preparation was MQ H_2O.

Separate fractions were weighed into 7 mL Savillex PFA vials for elemental determinations by quadrupole inductively coupled-plasma mass spectrometry (ICPMS; *Perkin Elmer NexION 350D*) (~10 mg), for V isotope analysis (an aliquot containing 5-7.5 μg total V, 20-120 mg), and for Zn isotope analysis (20-140mg). Samples were dissolved using a multi-stage acid hotplate dissolution procedure. Specifically, 28 M HF:15.4M HNO_3 (ratio 1:3) was added to each sample vial, and the sample was refluxed on a hotplate set at 100 °C for two days. The volumes of HF required were calculated based upon the estimated SiO_2 contents of each sample and samples were dried gently to avoid the generation of insoluble fluorides, which can incorporate significant amounts of trace elements and yield inaccurate measurements (Yokoyama et al., 1999). Subsequently, 1 mL of 8M HNO_3 was added to each sample before further drying on a hotplate set at 100 °C. Samples were then refluxed in 6M HCl on a hotplate set at 100 °C for two days and gently dried. Samples were subject to repeated stages of refluxing in 6M HCl and drying until each sample was completely visually dissolved. For elemental determinations by ICPMS, dried samples were taken up in 2% HNO_3 and quantitatively transferred to pre-cleaned *VWR* metal-free centrifuge tubes. For purifications of V for isotopic analysis the dried samples were taken up in 1 mL 1M HNO_3 for loading onto the first chromatographic column (**Section 2.4**). For Zn isotope analysis, samples were dissolved in 5 mL 1M HCl prior to double-spike addition and equilibration (**Section 2.5**). Samples for ICPMS analysis were taken up in 2% HNO_3 (**Section 2.3**).

2.3 Trace Element Concentrations using ICPMS

Trace and some major element concentrations were obtained using a *Perkin Elmer NexION 350D* quadrupole ICPMS at the Department of Earth Sciences, Oxford University. Samples were diluted by a factor of 10000 by weight. Further dilution and addition of a Rh-Re-In internal standard was carried out in-line using an *ESI (Elemental Scientific) prepFAST* autodilution system. This reduces both the risk of human error and the possibility of additional contamination during manual dilution and standard addition to samples. The prepFAST introduced the blank, standard, and diluted sample solutions into a holding loop, with a peri-pump used to introduce samples into the plasma.

The *NexION 350D* has a reaction cell and this was utilised to minimise polyatomic interferences. All but two elements (K and Sc) were measured using the "kinetic-energy distribution" (KED) mode, which employs He gas to destroy the most problematic polyatomic compounds. Determinations of K and Sc abundances were carried out in "dynamic reaction cell" (DRC) mode using NH_3 gas. The instrument parameters were tuned to avoid the generation of doubly-charged species and oxide interferences, and analyses were only performed when Ce^{2+}/Ce^{+} <3%, and CeO^{+}/Ce^{+} <2.5%.

An internal standard (Re-Rh-In) was added to samples in-line to correct for short term variations in the efficiency of elemental ionisation and to monitor the drift of the instrument throughout the analytical session. Calibrated synthetic chemical standards were also measured throughout the session to assess the accuracy and precision of instrument performance. A separate quality-control standard comprised of analytical chemical standards (for the elements of interest in this analysis) was used to ensure the calibration of the monitor standards. The relative standard deviation (RSD) of all elemental determinations was <5%, except for Li

(7.9%). Blanks were run throughout the sequence to monitor the background levels of elements and calculate internal detection limits for each element.

2.4 Vanadium Isotopes: Column Chromatography and Multiple-Collector Inductively Coupled-Plasma Mass Spectrometry Analysis

Full details of the development of the V isotope protocol and comparison between different instrumental and column chromatography set-ups can be found in **Chapter 3**. The following section contains a summary of the analytical techniques used with USGS reference materials and lunar basalts after development of the most suitable lab protocol (adapted from Hopkins et al., 2019, Supplementary Information).

2.4.1 Column chromatography

Before V isotope analysis via multiple-collector inductively coupled-plasma mass spectrometer (MC-ICPMS), samples must be purified to ensure that the final solution is free from interfering elements. Chromium (Cr) and Titanium (Ti) have significant isobaric interferences on the minor ^{50}V isotope, and thus must be near quantitatively removed (see Nielsen et al. 2011). This is particularly key for lunar basalts, which generally have much higher Ti and Cr contents than terrestrial silicates. For lunar samples, the column chromatography procedures of Wu et al. (2016) were employed.

Wu et al. (2016) modifies procedures developed by Nielsen et al. (2011) (see **Table 3.2, 3.3** in **Chapter 3**) by first using two cation-exchange columns in sequence to remove the majority of matrix elements (Fe, Ti, Al, Ca, Mn and some Cr) from the samples. For this 2 mL of pre-cleaned *Bio-Rad* AG50W-X12 (200-400 mesh) cation-exchange resin was packed in *Bio-Rad Poly-Prep* columns. The resin was then cleaned further with a 20 mL wash of 6M HCl and 10 mL MQ H_2O, and conditioned twice with 3 mL 1M HNO_3. Dissolved samples were loaded in 1 mL 1M HNO_3 and matrix elements were eluted in 4 mL 1M HNO_3 + 0.1M HF. Vanadium

was then eluted in 1.2M HNO_3. The first 1 mL of this elution is generally V-free and was collected separately. A further 19 mL 1.2M HNO_3 was added to collect the V, before a final 1 mL cut was taken. The 1 mL cuts before and after V collection were checked to ensure that no V was lost at this stage.

After the two cation-exchange columns, any remaining matrix elements and residual Cr was removed in two anion-exchange column steps. For the first anion-exchange stage, *Bio-Rad* Poly-Prep columns were loaded with 1.4 mL of pre-cleaned *Bio-Rad* AG1-X8 (200-400 mesh) chloride form anion-exchange resin. This resin was then further cleaned with 10 mL 6M HCl, 10 mL MQ H_2O, 10 mL 1M HNO_3 and 10 mL MQ H_2O. The column was conditioned twice with 3 mL 0.01M HCl + 1% v/v H_2O_2. Samples, dissolved in 1 mL 0.01M HCl, had 33 μL H_2O_2 added prior to loading to oxidise the vanadium to its pentoxide form, speciating as $(VO(O_2)_2)^-$, and ensure partitioning of V onto the resin (Nielsen et al., 2011). Matrix elements were eluted in 15 mL 0.01M HCl + 1% v/v H_2O_2. Vanadium was converted to the cationic species $(VO(O)_2)^+$ and eluted in 17 mL 1M HCl followed by 3 mL 6M HCl. A smaller, similar clean-up anion-exchange column was used to remove any remaining Cr after Nielsen et al. (2011). For this, 0.1 mL of *Bio-Rad* AG1-X8 (200-400 mesh) was loaded in columns (column length ~ 15mm, internal diameter ~3mm) made in-house from heat shrinkable PTFE tubing. The resin was cleaned with 2 mL 6M HCl, 2 mL MQ H_2O, 2 mL 1M HNO_3, and 2 mL MQ H_2O. The resin was then conditioned with 0.5 mL 0.01M HCl + 1% v/v H_2O_2. Samples were loaded in 1 mL 0.01M HCl with addition of 33 μL H_2O_2 prior to loading. Matrix elements were eluted in 2 mL 0.01M + 1% v/v H_2O_2. Vanadium was eluted in 1.7 mL 1M HCl, followed by 0.3 mL 6M HCl. For the two anion-exchange stages, fresh solutions containing H_2O_2 were made within hours of use to ensure the oxidative properties of H_2O_2 by reducing the potential for decomposition of H_2O_2 into H_2O and O_2. Procedural blanks for dissolution and chemistry were <0.3 ng V.

2.4.2 Vanadium Isotope Mass Spectrometry

Vanadium isotope analyses were performed on a *Nu Instruments Nu II* multiple-collector inductively-coupled-plasma mass spectrometer (MC-ICPMS) in the MAGIC laboratories at Imperial College London. The Faraday cups on the *Nu II* offer a greater dynamic range (≤55 V) than those on the *Nu HR* (≤10 V). This increased dynamic range allows the use of high ohmic resistors to amplify low-abundance isotopes, whilst retaining a good signal-to-noise ratio. This increased dynamic range is very useful for the V isotope system, where the abundance of isotopes is significantly different (in nature ^{50}V ~0.25%, ^{51}V ~99.75%). In the analytical set-up of Nielsen et al. (2011), using *Nu HR* MC-ICPMS, the current of the 51 mass:charge (*m/z*) ion beam was compensated with the use of a 10^9 Ω resistor to generate a voltage 100 times lower (relative to the other *m/z* ratios monitored using Faraday cups equipped with the standard 10^{11} Ω resistor). For acceptable signal-to-noise ratios on the minor ^{50}V isotope on the *Nu HR*, samples had to be run at a V concentration of 5 μg g^{-1}.

On the *Nu II*, low abundance isotope signals (*m/z*: 49, 50, 53) were measured on Faraday cups equipped with 10^{12} Ω resistors, generating voltages 10x greater relative to the other isotopes measured using standard 10^{11} Ω resistors (**Table 3.4**). Acceptable signal-to-noise ratios were generated at V concentrations up to a factor of 10 lower than in Nielsen et al. (2011). The lower amounts of total processed V required with this setup allows the measurement of samples with lower V concentrations, and the dissolution and chemical processing of less sample material. Standard and sample solutions were run with V concentrations of 600-800 ng g^{-1}. These solution concentrations are similar to those used in MC-ICPMS techniques developed more recently using Thermo Neptune *Plus* technologies (Nielsen et al., 2016; Sossi et al., 2017; Wu et al., 2016).

Given that V has only two isotopes, double-spiking is not possible and measurements were therefore conducted by sample-standard bracketing. Samples were diluted in 0.1M HNO_3 so that their V concentrations matched the bracketing standards to better than 10%. Standard and sample solutions were introduced using a *Glass Expansion* ICP Nebuliser (uptake rate: ~100 μL min^{-1}) before passing through a *Nu Instruments* desolvating nebuliser (DSN) for the removal of solvent. Radio-frequency (RF) power was set at 1300W. Isotope analyses were carried out in pseudo-high-resolution mode ($M/\Delta M$ ~ 4800 - 6000) to allow resolution of the single-nucleus ions from the significant number of polyatomic mass interferences generated at the plasma interface (see Nielsen et al., 2016 for a summary of the principal mass interferences). Peaks were tuned for left-hand alignment, since interferences for these isotopes are heavier than the ions of interest (**Figure 3.1**). Mass-offset was performed every measurement using an automated function to ensure a consistent offset of ~+0.01 mass units from half-peak height of the low mass peak edge. The 52:53 beam ratio was monitored to ensure consistent resolution of the interferences, in particular $^{40}Ar^{12}C$. Incidentally, resolution of argon carbide from ^{52}Cr yields 52:53 values close to the natural ^{52}Cr:^{53}Cr ratio of ~8.8 (de Laeter John et al., 2003) and higher values indicate measurement of at least part of the interference beam. Sensitivities at pseudo-high-resolution were 40-50 V/ppm at 100μL·min^{-1}.

Samples were analysed for 70 5s integrations after an ESA-deflection background measurement of 60 s. Idle time between measurement ESA-deflection and measurement was 15 s, to allow for 10^{12} Ω resistor response time. Contributions from ^{50}Cr and ^{50}Ti to the 50 *m/z* beam were calculated by monitoring the signals on *m/z* = 49 (^{49}Ti), 52 (^{52}Cr), and 53 (^{53}Cr), using a mass-bias calculation.

Sample analyses were bracketed with four determinations of the Alfa Aesar (AA) V solution and a secondary V standard from BDH chemicals (BDH) Nielsen et al. (2011) [i.e. AA-AA-

BDH-AA-AA-*sample*]. The Oxford AA standard defines zero for most V isotope data reported thus far, and BDH yields a long-term reproducibility determined in six labs (Oxford University, Imperial College London, Australia National University, Leibniz Universitat Hannover, University of Science and Technology of China, Hefei, and Woods Hole Oceanographic Institute, USA) over 7 years of $\delta^{51}V_{AA}$ = -1.17 ± 0.17 ‰ (n = 1329, Prytulak et al., 2017). Intermediate precision for this study taking place over 10 months on the MC-ICPMS housed at Imperial was $\delta^{51}V_{AA}$ = -1.21 ± 0.22 ‰ (n = 65). USGS reference materials BCR-2, BIR1a, and BHVO-2 were measured alongside lunar samples and $\delta^{51}V$ values were found to be in agreement with the literature (See **Table 3.5**).

2.5 Zinc Isotopes: Column Chromatography and MC-ICPMS Analysis

2.5.1 Zinc double-spiking

Lunar basalts have previously been measured for Zn isotope ratios using sample-standard bracketing (Herzog et al., 2009; Kato et al., 2015; Moynier et al., 2006; Paniello et al., 2012) and isotopic variations have been shown to be mass-dependent. Samples may alternatively be analysed using double-spiking techniques (Arnold et al., 2010; Bridgestock et al., 2014; Siebert et al., 2001). This enables a more precise correction for instrumental mass bias (and potential fractionation during sample processing). In addition, double-spiking allows more precise determination of Zn concentrations within measured samples (previous sample-standard bracketing Zn concentrations had been determined by beam voltage matching with a standard of known concentration) and allows for correction of isotopic fractionation occurring during chromatography and isotope analysis. In this study, a ^{64}Zn-^{67}Zn double spike (with $^{64}Zn/^{67}Zn$ ~ 2.5, Arnold et al., 2010) was employed.

2.5.2 Zinc concentrations

For sample digestion, published values for Zn concentrations were used to approximate the mass of sample powder required (target total Zn ~ 250 μg, mass of sample powder 20-140 mg, **Appendix 2a**). However, for accurate and precise measurement of Zn isotopes via double-spiking, precise determination of Zn concentrations is required. Zinc is a widespread contaminant in laboratory-wear (including gloves, plastic bottles, centrifuge tubes, pipette tips, Garçon et al., 2017) and it is difficult to achieve sufficiently-low blanks using ICPMS techniques. There is significant variation in the lunar literature for Zn concentrations (Appendix 2F), therefore Zn concentrations for each dissolved aliquot were determined using isotope dilution.

A small aliquot (~250 μL) of the samples (in 5 mL 1M HCl) was weighed into a separate 7 mL Savillex PFA vial. Approximately 60 μL of double-spike (concentration: 5.10025 $\mu g \cdot g^{-1}$ Zn) was added to the sample, and samples were equilibrated at 60 °C for 48 hours. Samples were then dried and taken up in 1 mL 1M HCl prior to loading onto chromatographic columns (follow the technique in **Section 2.5.3**). Following one pass of column chemistry, samples were dried and dissolved in 1 mL 0.1M HNO_3. Concentrations were determined via MC-ICPMS (following the techniques outlined in **Section 2.5.4**). Samples were diluted to 50 ng g^{-1} Zn and were measured for 20 × 10 second integrations.

2.5.3 Zinc purification using anion-exchange chromatography

Using Zn concentrations obtained by isotope dilution, the remaining lunar sample solutions were weighed and mixed with an appropriate amount of ^{64}Zn-^{67}Zn double spike to give Zn_{spike}/Zn_{sample} ratios ~1.15. Previous work has shown that standard solutions with $Zn_{spike}/Zn_{standard}$ ratios between 0.4 and 1.7 yield $\delta^{66}Zn$ values within error (±0.05 to ±0.10‰) of samples measured using optimal mixing ratios Zn_{spike}/Zn_{sample} ~ 1-1.2 (Arnold et al., 2010; Bridgestock et al., 2014). After weighing appropriate masses of sample and double-spike,

samples were equilibrated at 60 °C for 48 hours before drying and being redissolved in 1 mL 1M HCl.

Column chromatography followed an amended method of that presented in Arnold et al. (2010). Custom PTFE columns (resin volume ~ 200 μL) were loaded with *BioRad* AG MP-1 (100-200 mesh) anion-exchange resin. The columns were cleaned in 0.1M HNO_3 (6 mL), rinsed in MQ H_2O (1.5 mL), conditioned with 6M HCl (3 mL), and equilibrated using 4 × 0.5 mL 1M HCl. Samples were then loaded in 1 m 1M HCl. Sample matrix was removed using 8 mL 1M HCl, and Zn was collected using 6 mL 0.01M HCl. Samples for concentration checks were passed once through the column chemistry. Samples for isotopic analysis were passed through the procedure twice: samples were dried after Zn elution and dissolved in 1 mL 1M HCl before loading onto columns using fresh AG-MP1 resin.

Following column chromatography, samples were dried and ~50 μL of 15.4M HNO_3 was applied to each sample and dried at 135°C (twice) to oxidise any residual organic material from the resin before samples were dissolved in 1 mL 0.1M HNO_3 in preparation for MC-ICPMS analysis.

2.5.4 Zinc isotope analysis by MC-ICPMS

Isotopic analysis was performed using a *Nu Instruments* Plasma HR MC-ICPMS. Samples were taken up using an *ESI* PFA nebuliser (flow rate ~100 μL min^{-1}) and introduced to the plasma after passing through a *Nu Instruments* DSN-100.

Samples were bracketed with a standard solution using the "London-Zn" zinc standard (Arnold et al., 2010). The "London Zn" standard has a well-characterised offset from the widely-used "JMC-Lyon" Zn standard (Marechal et al., 1999) of $\delta^{66}Zn_{London\text{-}Lyon}$ = +0.12 ± 0.04‰ (Arnold et al., 2010; Bridgestock et al., 2014; Larner and Rehkämper, 2012; Moeller et al., 2012) Standards were matched to sample Zn_{spike}/Zn_{sample} ratios ± 1%. Standards and samples were

diluted to ~50 ppb (sensitivity ~ 100 V/ppm) and within 10% of one another using the same batch of 0.1M HNO_3 to ensure no difference in acid molarity, and therefore minimising matrix effects.

Masses 62, 64, 66, 67, 67.5 and 68 were simultaneously monitored using Faraday cups equipped with 10^{11} Ω resistors. Masses 62 and 67.5 were monitored for interferences from $^{62}Ni^{+}$ and $^{135}Ba^{2+}$ respectively. Samples were measured for 60 × 10 second integrations (with a 15 second baseline measurement prior to each analysis).

Double-spike deconvolution and interference correction was performed offline using a data-reduction protocol developed by Siebert et al. (2001). Double-spike equations are solved in three-dimensional space using a geometric approach. This iterative method accounts for non-linear mass bias during MC-ICPMS measurement. Typical interferences for Ni ($^{64}Ni^{+}/^{64}Zn^{+} < 1 \times 10^{-5}$) and Ba ($^{134}Ba^{2+}/^{67}Zn^{+} < 1 \times 10^{-5}$) were low and insignificant. Total procedural blanks (for column chemistry and MC-ICPMS analyses) were ≤ 5 ng (total Zn processed through column chemistry for samples ~100 ng or greater). Typical errors (2SE internal) on a single analysis was 0.03-0.04‰. Typical reproducibility (2SD) for London-Zn was ~ 0.10‰. Sample reproducibility between sessions (2SD for samples with n ≥ 3) was between 0 and 0.23‰. USGS measurements are within error of widely-accepted values using sample-standard bracketing, and values from Bridgestock et al., (2014) who used the same double-spike (**Appendix 3a**).

3

Development of Analytical Protocols for the Measurement of Vanadium Isotope Ratios in Lunar Rocks

Chapter Abstract

The first high-precision techniques for the measurements of V isotopes by MC-ICPMS (Nielsen et al., 2011) allowed natural isotopic variations in geological samples to be accurately resolved for the first time. However, due to the sensitivity (~30-40 V/ppm) and limited dynamic range of the Nu HR (~10 V), the minimum amount of V required for a single analysis was > 2 μg, thus placing limitations on the feasibility of determining the isotopic composition of low V samples. Measurements were carried out in low resolution mode to maximise ion beam transmission, and direct resolution of molecular interferences was not possible. Lunar basalts are limited in availability and have high Ti/V and Cr/V ratios when compared to terrestrial silicates. Thus, the initial laboratory techniques were tested against those of more recent publications to identify the most suitable protocol to achieve optimal separation of V from Cr an Ti and minimise the amount of V required for high precision measurements. Three MC-ICPMS instruments (*Nu HR*, *Nu 1700*, *Nu Plasma II*) were tested. The use of the *Nu Plasma II*, in medium resolution mode, equipped with three 10^{12} Ω resistors on minor ion beams allowed the direct resolution of compound interferences from the ions of interest, and the reduction of required sample sizes by a factor of 6-10 over initial work by Nielsen et al. (2011). Isotope ratios for chemical solution standards and USGS reference materials agree with initial work using a Nu HR and subsequent studies by other research groups using a Neptune MC-ICPMS. Although the *Nu 1700* and *Nu Plasma II* have similar sample-instrument interfaces, collector arrays, and dynamic ranges, the *Nu 1700* was found to be unsuitable for sample measurement, due to unpredictable (and therefore un-correctable) secular variations in beam intensity and mass-bias. In addition to instrumental tests, two column chromatography procedures were compared to identify the most suitable method for purification of V from Cr and Ti interferences in lunar basalts. Terrestrial high-Ti basaltic samples from Heard Island (Kerguelen Plateau) were processed through chromatographic protocols to ascertain which

techniques will be more reliable for lunar samples. A protocol for lunar basalt preparation and analysis was identified.

3.1 Background

3.1.1 Properties of V isotopes and historical attempts at measurement

Although the motivations behind measuring V isotope ratios in geological and extra-terrestrial samples has been outlined in Chapter 1, it is worth revisiting the properties of V isotopes to explain why high-precision V isotope measurement has only relatively recently been made possible (Nielsen et al., 2011). Vanadium has two "stable" isotopes: ^{50}V and ^{51}V. Although ^{50}V is technically radioactive, its half-life is longer than the age of the universe by several orders of magnitude ($t_{1/2} \sim 1.4 \times 10^{17}$ years, Simpson et al., 1989) and so is regarded as "stable" for geochemical purposes. The ratio of naturally-occurring ^{51}V to ^{50}V ($^{51}V/^{50}V$) is ~ 400 (Berglund and Wieser, 2011). There are significant isobaric interferences from Ti and Cr at mass 50, so V must be isolated quantitatively (yield ~ 100%) from these elements prior to analysis. Incomplete recovery of V during sample preparation may lead to artificial chromatography-induced mass-fractionations and inaccurate measurements.

Typically, the most precise isotopic measurements of transition metals are performed using either thermal-ionisation mass-spectrometry (TIMS) or multiple-collector inductively-coupled-plasma mass-spectrometry (MC-ICPMS). Both techniques impart an instrumental mass-fractionation. Correction of mass-fractionation via internal normalisation or double-spiking (Dodson, 1963) is not possible for V due to it possessing only two isotopes. External normalisation (the addition of another element in the mass-range of V with very similar ionisation potential) is problematic for V since it lies in a mass-range containing a significant number of isobaric and compound interferences. In addition, divergent elemental fractionation can occur during the introduction of sample solutions to MC-ICPMS, hindering accurate

correction (Albarede et al., 2004). Sample-standard bracketing using MC-ICPMS is therefore the chosen method for accurate measurements of V isotopes at sufficiently high precision for geological use ($2\sigma < 0.2‰$).

3.1.2 Historical attempts to measure V isotopes

Prior to the development of MC-ICPMS, several early studies into the V isotope ratios of meteorites and terrestrial samples (e.g. Balsiger et al., 1969; Balsiger et al., 1976; Pelly et al., 1970; Stauffer & Honda, 1961, 1962) were performed using TIMS, but poor analytical precision (>1‰) resulted from the aforementioned lack of ability to correct for instrumental mass-fractionation. In addition, most studies lack detailed description of measurement protocols, and thus the unaddressed risk of incomplete recovery of V during sample preparation leaves doubts over the accuracy of the measurements.

3.1.3 First high-precision V isotope measurements

Successes in the measurement of other transition metal isotope ratios in geological samples by MC-ICPMS (e.g. Cu & Zn isotopes: Marechal et al., 1999; Fe isotopes: Belshaw et al., 2000) renewed interest in developing techniques for measuring V isotope ratios in natural samples. The breakthrough was achieved in 2011, with the publication of two papers detailing the analytical techniques for measuring V isotope ratios (Nielsen et al., 2011) and the first analyses of geological reference materials (Prytulak et al., 2011). Nielsen et al. (2011) presents a five-stage ion-exchange chromatography protocol for the quantitative separation of V from interfering Cr and Ti (and other matrix elements). Two manufactured chemical solutions of V were routinely analysed: a primary bracketing “Specpure” V solution from *Alfa Aesar* (AA), and a secondary V solution from *BDH Chemicals* (BDH). The AA solution (as of 2019) represents the standard most studies use for reporting V isotope ratios in the isotope geochemistry field and is reported in per mil notation:

$$\delta^{51}V_{AA} = \left\{ \frac{(^{51}V/^{50}V)_{sample}}{(^{51}V/^{50}V)_{AA}} - 1 \right\} * 1000$$

Initial MC-ICPMS measurements of the V isotope ratios of chemical standards and USGS reference materials (Nielsen et al., 2011; Prytulak et al., 2011) and subsequent studies of geological samples (Prytulak et al., 2013, 2017) and meteorites (Nielsen et al., 2014; Nielsen et al., 2019) were carried out using two *Nu Instruments Plasma HR* MC-ICPMSs (Nu *HR*) at Imperial College London, and at University of Oxford. Due to the extreme natural ratio of V ($^{51}V/^{50}V \sim 400$), compensation for the disparate resultant ion beam currents must be applied to ensure that all voltages generated from the Faraday detectors have good signal-to-noise ratio and lie within the dynamic range of the Faraday detectors (< 10V for the Nu *HR*). This was carried out with the use of a 10^9 Ω resistor on the Faraday cup receiving the ^{51}V ion beam. This has the effect of multiplying the resulting "voltage" generated on the Faraday collector by a factor of 0.01 ($V = IR$) when compared to the voltages generated on the other Faraday cups, which are equipped with standard 10^{11} Ω resistors. An alternative approach to compensating for the disparate ion beam currents would be to use resistors of a higher resistance (e.g. 10^{12} Ω) on the low-abundance isotope beams to amplify the voltage generated. However, to ensure good signal-to-noise ratios on the small ion beams the resultant voltage on ^{51}V would be far higher than the dynamic range of the Faraday cups equipped on the Nu *HR*. To accommodate this instrumental limitation, at least 2 μg V was consumed during a sample run (20 × 10 second integrations, Oxford or 40 × 5 second integrations, Nielsen et al., 2011) and measurements were carried out in low-resolution mode ($M/\Delta M \sim 400$) to maximise beam transmission. This requires a significant amount of raw sample to be processed and restricts the range of samples to be analysed to those with [V] > 20 $\mu g \cdot g^{-1}$ before sample dissolutions risk overloading the capacity of the chromatographic columns. At this point, samples must be split into multiple

aliquots before loading into separate chromatographic columns and recombined before analysis (which entails further risk of incomplete V recovery and human error).

Corrections to the ^{50}V voltages from any remaining ^{50}Cr and ^{50}Ti were applied using the intensities of ^{49}Ti, ^{52}Cr and ^{53}Cr. However, at low resolution, compound interferences generated at the plasma-vacuum interface (see Nielsen et al., 2016, **Table 3.1**) cannot be directly resolved. This is important for all the ion beams but is particularly important for the beams at mass 52 (where the major interfering species are $^{40}Ar^{12}C^+$, $^{36}Ar^{16}O^+$ and $^{38}Ar^{14}N^+$) and mass 53 (where the major interfering species are $^{40}Ar^{13}C^+$, **Table 3.1**). Unable to directly resolve these species, Nielsen et al. (2011) applied corrections for these molecular interferences under the assumption that the only significant compound interferences were from $^{40}Ar^{12}C^+$ and $^{40}Ar^{13}C^+$ at masses 52 and 53 respectively – however, this may not be the case. To avoid error propagation from the correction of Cr and Ti contributions to the ^{50}V signal, chemical purification of samples must result in $^{53}Cr/^{51}V$ and $^{49}Ti/^{51}V$ beam intensity ratios of < 0.00001 (Nielsen et al., 2011).

3.1.1 Recent Developments in Analytical Techniques

Since the 2011 publication of the first high-precision studies, updated techniques for the analysis of V isotope ratios by MC-ICPMS have been published (Nielsen et al., 2016; Wu et al., 2016). These studies apply higher-resolution ($M/\Delta M > 4000$) MC-ICPMS techniques to allow the direct resolution of mass interferences and find an identical offset for BDH relative to AA of $\delta^{51}V = -1.17$ ($2\sigma < 0.10‰$). Higher-resolution data for USGS reference materials is identical to initial MC-ICPMS studies (Prytulak et al., 2011, Wu et al., 2016; Prytulak et al., 2017; Sossi et al., 2018; Nielsen et al., 2019, **Table 3.5**). Discrepancies between early meteorite studies performed at low resolution (Nielsen et al., 2014) and recent higher-resolution studies (Xue et al., 2018; Nielsen et al., 2019) likely result from the higher abundance of S-bearing

compounds during analysis, which are not present in significant abundance in terrestrial magmatic rocks analysed to date (Prytulak et al., 2011; 2013; 2017; Wu et al., 2016; 2018). At higher-resolution MC-ICPMS artificially-generated compound interferences (**Table 3.1**) are resolvable from ion beams of interest. Thus higher-resolution MC-ICPMS work is desirable for accurate results, especially in extra-terrestrial samples.

In addition to higher-resolution MC-ICPMS protocols, Wu et al., (2016) presented an alternative ion-exchange chromatography procedure for the isolation of V from interfering matrix elements (and Cr and Ti). This employed the use of cation-exchange resins to remove the majority of sample Ti (instead of more expensive and temperamental *TRU* resin). The resulting eluants after initial Ti-removal are "cleaner" (i.e. less sticky organic material) and are easier to prepare for loading onto the subsequent columns than in the original techniques of Nielsen et al. (2011).

Comparison of data for meteorites and USGS standards prepared through both the column chromatography methods of Nielsen et al., (2011) and Wu et al., (2016) and measured via medium-resolution ($M/\Delta M > 4000$) MC-ICPMS at different laboratories shows there to be no difference in the $\delta^{51}V$ observed for individual samples once compound interferences can be resolved (Nielsen et al., 2019, **Table 3.5**).

Schuth et al., (2017) measured $\delta^{51}V$ by femtosecond laser ablation (LA-)MC-ICPMS and solution MC-ICPMS in a number of V-rich minerals and commercially-available V metal and solution standards. Comparison of the original Specpure "Alfa Aesar" solution (purchased in the UK, Nielsen et al., 2011) to two different solutions of "Alfa Aesar" V solution from Germany (one from 2015, one from ~2007) shows there to be a ~1‰ variation in $\delta^{51}V$ and ~ 10× variation in the $^{51}V/^{52}Cr$ of these solutions. Likewise, the $\delta^{51}V$ of "Alfa Aesar" V metal (99.5%) displays $\delta^{51}V \sim +1.4$‰ relative to the original AA standard (Schuth et al., 2017). From

Alfa Aesar standards alone, it should be noted that $\delta^{51}V$ spans ~2.3‰, almost equal to the total range in $\delta^{51}V$ observed for magmatic terrestrial rock samples. In summary, it should be noted that reporting of $\delta^{51}V$ relative to AA refers to the original batch of standard first prepared and presented in Nielsen et al., (2011), and not to any other standard from the same manufacturer, except where clearly specified. Two litres of 1000 $\mu g \cdot g^{-1}$ of the initial AA solution has been characterised and distributed to the community on request. It is still readily available from either J. Prytulak or S. Nielsen.

3.1.2 Aims of this study

At the beginning of this study (2014), only low-resolution analytical techniques had been developed. These required significant amounts of sample to be dissolved (up to 5$\mu g.g^{-1}$ V per single analysis) and prepared through ion-exchange chromatography. Samples with low V concentrations had to be "split" into separate columns to avoid over-loading the resin capacities and recombined before isotopic analysis by MC-ICPMS. Lunar basalts have not been measured for V isotopic compositions. However, they are rare and sample-limited, thus it is desirable to develop higher-resolution and more sensitive (i.e. requiring less sample) MC-ICPMS protocols before application to lunar samples.

<u>The aims of this chapter are as follows:</u>

1) Identify an MC-ICPMS instrumental set-up for the measurement of V isotope ratios at higher-resolution ($M/\Delta M > 4000$).
2) Compare $\delta^{51}V$ of solution standards and USGS reference materials measured using higher-resolution MC-ICPMS to literature values to ensure suitable accuracy and similar precision.
3) Reduce sample size requirements from those in Nielsen et al., (2011), so that samples with lower V concentrations may be analysed.

4) Identify whether chemical techniques from Nielsen et al. (2011), or Wu et al., (2016) are more appropriate for application to lunar basalts (which typically have high Ti/V and Cr/V compared to terrestrial igneous rocks).

Table 3.1 – *Compound interferences in mass range 48-53. Adapted from Nielsen et al., 2016. Only molecular species with abundances of more than 0.001% of the total species are listed. M/ΔM is the mass resolution required to resolve the interference from its nearest ion of interest.*

Molecular species	Species abundance	Reference isotope	M/ΔM
$^{32}S^{16}O^{+}$	0.94793	^{48}Ti	2518
$^{36}Ar^{12}C^{+}$	0.00333	^{48}Ti	2446
$^{36}S^{12}C^{+}$	0.00019	^{48}Ti	2506
$^{34}S^{14}N^{+}$	0.04194	^{48}Ti	2085
$^{33}S^{15}N^{+}$	0.00002	^{48}Ti	2030
$^{35}Cl^{13}C^{+}$	0.00833	^{48}Ti	1976
$^{37}Cl^{12}C^{+}$	0.23954	^{49}Ti	2715
$^{33}S^{16}O^{+}$	0.00748	^{49}Ti	2646
$^{34}S^{15}N^{+}$	0.00015	^{49}Ti	2435
$^{36}Ar^{13}C^{+}$	0.00004	^{49}Ti	2125
$^{32}S^{17}O^{+}$	0.00036	^{49}Ti	2098
$^{35}Cl^{14}N^{+}$	0.75503	^{49}Ti	2035
$^{38}Ar^{12}C^{+}$	0.00062	^{50}V	3208
$^{34}S^{16}O^{+}$	0.042	^{50}V	3198
$^{35}Cl^{15}N^{+}$	0.00278	^{50}V	2291
$^{37}Cl^{13}C^{+}$	0.00266	^{50}V	2261
$^{36}S^{14}N^{+}$	0.0002	^{50}V	2172
$^{36}Ar^{14}N^{+}$	0.00336	^{50}V	2129
$^{32}S^{18}O^{+}$	0.0019	^{50}V	2075
$^{35}Cl^{16}O^{+}$	0.756	^{51}V	2572
$^{34}S^{17}O^{+}$	0.00002	^{51}V	2212
$^{36}Ar^{15}N^{+}$	0.00001	^{51}V	2150
$^{37}Cl^{14}N^{+}$	0.24131	^{51}V	2037
$^{33}S^{18}O^{+}$	0.00002	^{51}V	1911
$^{36}S^{16}O^{+}$	0.0002	^{52}Cr	2418
$^{40}Ar^{12}C^{+}$	0.98504	^{52}Cr	2375
$^{36}Ar^{16}O^{+}$	0.00336	^{52}Cr	2366
$^{38}Ar^{14}N^{+}$	0.00063	^{52}Cr	2053
$^{37}Cl^{15}N^{+}$	0.00089	^{52}Cr	2037
$^{34}S^{18}O^{+}$	0.00008	^{52}Cr	1959
$^{35}Cl^{17}O^{+}$	0.00029	^{52}Cr	1891
$^{37}Cl^{16}O^{+}$	0.24162	^{53}Cr	2626
$^{40}Ar^{13}C^{+}$	0.01096	^{53}Cr	2111
$^{35}Cl^{18}O^{+}$	0.00152	^{53}Cr	1935

3.2 Methods

3.2.1 Standards and Samples

3.2.1.1 Chemical standards

The primary and secondary bracketing standards for this work are the AA and BDH solutions first presented in Nielsen et al., (2011). These solutions are prepared from a stock solution (~1 part per thousand V by mass) and taken up in 2% (n/n) HNO_3 solution of appropriate concentration prior to analysis. Samples of AA are also run through column chromatography procedures as a check on artificial fractionation during column chromatography (**Section 3.2.3**).

3.2.1.2 USGS Standards

USGS reference materials BCR2, BHVO2, and BIR1a were chosen as rock standards. These samples have been studied widely for their $\delta^{51}V$ in the literature (**Table 3.5**).

3.2.1.3 Heard Island Basalts

Heard Island is a subaerial expression of the Kerguelen plateau located in the southern Indian Ocean. The island is dominated by the Big Ben volcano massif, which is thought derive to its activity from the Kerguelen hotspot (Storey et al., 1989). Heard Island has lavas with the highest sampled TiO_2 content (6.02 wt%) of any basaltic rocks currently found on Earth (Barling et al., 1994). Eight samples characterised by their elevated TiO_2 contents (3.2 – 6.0 wt%) were selected and processed alongside the USGS and chemical standards. These samples have V concentrations between ~ 200 to 400 $\mu g \cdot g^{-1}$ and used here as terrestrial analogues for lunar samples which have elevated Ti/V levels compared to rocks previously analysed using the column chromatographic procedures of Nielsen et al. (2011) and Wu et al. (2016).

3.2.2 Sample preparation

Heard Island basalts were chipped and finely crushed in an agate pestle-and-mortar. Aliquots of the resulting powders were weighed (to give V ~ 5 to 7.5µg total based upon previous trace element analysis, Barling et al., 1994) into 7ml Savillex PTFE vials. Samples were digested using a hotplate dissolution procedure (described in detail in **Chapter 2**). After dissolution, samples were prepared for column chromatography. Samples processed through the chromatographic protocol described in Nielsen et al., (2011) were taken up in 6 M HCl prior to loading onto the first column. Samples processed via the protocol of Wu et al., (2016) were taken up in 1ml 1M HNO_3 prior to loading on to the first column.

3.2.3 Column chromatography

Full details of the steps involved in chromatographically-separating V from interfering matrix elements can be found in Nielsen et al. (2011) and Wu et al. (2016). The protocol of Nielsen et al., (2011) involves 5 column steps (**Table 3.2**). Titanium is mostly removed in the second column stage, which requires the use of *Eichrom* TRU Resin. In contrast, the column chromatographic procedures in Wu et al. (2016) make use of two identical cation exchange columns, using *BioRad* AG50W-X12 to remove most of the matrix elements before separation of V from Cr in two anion-exchange columns, similar to Nielsen et al. (2011) (**Table 3.3**). USGS reference materials (BCR2, BHVO2, BIR1a), chemical standards AA and BDH, and the Heard Island basalts were run through both protocols. Processed samples were taken up in 2% (n/n) HNO_3 prior to analysis via MC-ICPMS.

Table 3.2 – *Column chromatography procedure for separation of V from other matrix elements presented in Nielsen et al. (2011).*

Column Number	1	2	3	4	5
Resin	1ml BioRad AG1X8 200-400 mesh	0.75ml TRU SPEC RESIN	1ml BioRad AG1X8 200-400 mesh	0.1ml BioRad AG1X8 200-400 mesh	0.1ml BioRad AG1X8 200-400 mesh
Cleaning	5ml 1M HCl	7.5ml 1M HCl	5ml 1M HCl	1ml 1M HCl	
Equilibrating	2 × 3ml 6M HCl	2 × 4ml 7M HNO_3	2 × 3ml 0.01M HCl + 1% v/v H_2O_2	2 × 0.5 ml 2M HF	2 × 0.3ml 6M HCl + 1% v/v H_2O_2
Loading	**in 6M HCl**	**in 7M HNO_3**	in 0.01M HCl + 1% v/v H_2O_2	**in 2M HF**	in 0.01M HCl + 1% v/v H_2O_2
Elution	**6ml 6M HCl**	**12ml 7M HNO_3**	2 + 10 ml 0.01M HCl + 1% v/v H_2O_2	**0.5ml 2M HF**	0.2 + 1 ml 0.01M HCl + 1% v/v H_2O_2
Elution 2			**1 + 5ml 1M HCl**	**0.1 + 0.8ml 0.5M Hcl + 0.5M HF**	**0.1 + 0.5ml 1M HCl**

Steps in **bold** indicate V collection

Table 3.3 – *Column chromatography procedure for V purification presented in Wu et al. (2016).*

Column Number	1	2	3	4
Resin	2ml AG50W-X12 200-400mesh	2ml AG50W-X12 200-400mesh	1.4ml BioRad AG1X8 200-400 mesh	0.1ml BioRad AG1X8 200-400 mesh
Cleaning	20ml 6M HCl, 10 ml MQ H_2O	20ml 6M HCl, 10 ml MQ H_2O	10ml 6M HCl, 10ml 1M HNO_3, 10ml MQ H_2O	2ml 6M HCl, 2ml 1M HNO_3, 2ml MQ H_2O
Equilibrating	2 × 3ml 1M HNO_3	2 × 3ml 1M HNO_3	2 × 3ml 0.01M HCl + 1% v/v H_2O_2	2 × 0.5 ml 0.01M HCl + 1% v/v H2O2
Loading	in 1M HNO3	in 1M HNO_3	in 0.01M HCl + 1% v/v H_2O_2	in 0.01M HCl + 1% v/v H_2O_2
Elution	4ml 1M HNO3 + 0.1M HF	4ml 1M HNO3 + 0.1M HF	15ml 0.01M HCl + 1% v/v H_2O_2	2ml 0.01M HCl + 1% v/v H_2O_2
Elution 2	1ml 1.2M HNO_3, **19ml** 1.2M **HNO_3,** 1ml 1.2M HNO_3	1ml 1.2M HNO_3, **19ml** 1.2M **HNO_3,** 1ml 1.2M HNO_3	**17ml 1M HCl, 3ml 6M HCl**	**1.7ml 1M HCl, 0.3ml 6M HCl**

Steps in **bold** indicate collection of V

3.2.4 Instrumental Comparison

Three instruments were chosen for comparison: a Nu Instruments Plasma *HR* (Nu *HR*) and a Nu Instruments *Plasma 1700* (Nu *1700*) based at the University of Oxford, and a Nu Instruments Plasma *II* (Nu *II*) at Imperial College London. The Nu *HR* provides the baseline in MC-ICPMS performance (this instrument was one of those used in Nielsen et al., 2011) for comparison with the higher-resolution Nu *1700* and the Nu *II*. The Nu *1700* a large geometry magnetic sector MC-ICPMS equipped with a similar plasma/vacuum interface and primary tuning optics to the Nu *HR*. The large geometry of the instrument allows significant mass-resolution of ion beams, even at "low" mass-resolution (i.e. with analyser slits fully open) where typical $M/\Delta M \sim 8000$ on the mass 51 ion beam after tuning. The Nu *II* is a smaller-geometry instrument, similar in schematic to the Nu *HR*, but has an improved plasma-vacuum interface (sample throughput/sensitivity is higher).

The Nu *HR* is equipped with a 10^9 Ω resistor on the 51 mass detector. This allows resulting voltages to be ~ 100× smaller proportionally than those on other detectors, equipped with standard 10^{11} Ω resistors, ensuring that all ion beams detected have good signal/noise ratio. The larger dynamic range on Nu *1700* and Nu *II* (~50V vs ~10 V on Nu *HR*) allows the employment of 10^{12} Ω resistors on the smaller ion beams. Smaller sample sizes can thus be run with good signal noise ratio on (at least) both V isotopes. The Nu *1700* is equipped with a 10^{12} Ω resistor on the Faraday cup receiving the 50 mass ion beam (i.e. $^{50}V^+$), and the Nu *II* is equipped with 10^{12} Ω resistors on the 49, 50, and 53 masses (i.e. $^{49}Ti^+$, $^{50}V^+$, and $^{53}Cr^+$).

Details of the instrumental set-ups after finding the optimal configurations are presented in **Table 3.4**.

3.2.1 Limitations in directly-comparing between instruments

Where possible, as many external factors were controlled as possible. For example, when beginning investigation of Nu *1700* performance, the introduction system (a Nu Instruments desolvating nebuliser, *DSN*), nebuliser (*ESI* PTFE 100μL·min^{-1}), and cones (A-Type) which gave best performance on the Nu *HR* were used. However, there are significant differences between each instrument. For example, cones suitable for the Nu *HR* and Nu *1700* are not compatible with the interface of the Nu *II*. The use of 10^{12} **Ω** resistors on the Nu *HR* and Nu *1700* requires consideration of the extended response time of signals from these Faraday cups. Where these resistors were employed, baseline deflection times and wait times before beginning measurement were increased. Likewise, since the Nu *II* instrument was located at Imperial College London, it was impossible to perform cross-instrument tests using the same desolvaters as in Oxford.

The optimal configurations of each instrument (introduction system, sample measurement time, solution concentration and uptake speed) was investigated and chemical and USGS standards were run to ascertain the performance of each instrument (**Tables 3.4, 3.5**). Samples were run as part of a sequence (AA-AA-BDH-AA-AA-*sample*) where they are bracketed by four AA standard runs and run in sequence with the secondary BDH standard. The 2sd on the BDH measurements throughout a run sequence provides the reported error for one sample measurement.

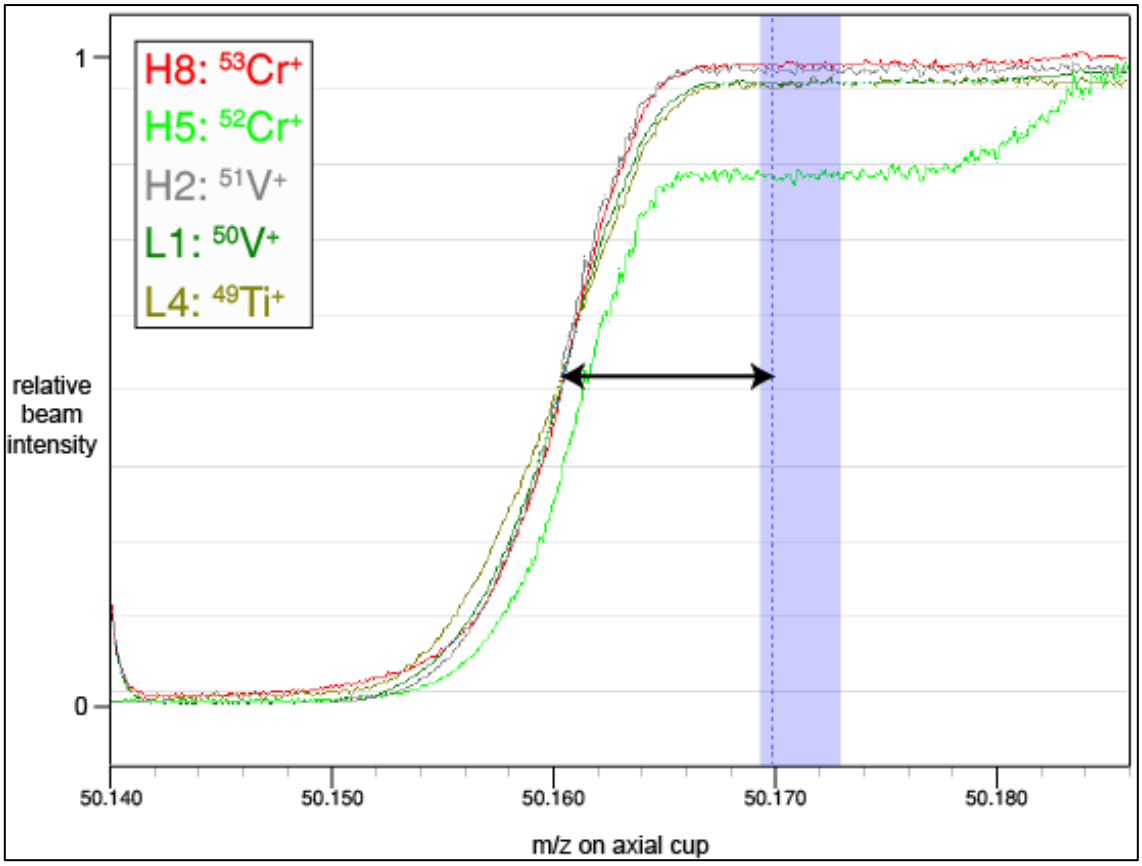


Figure 3.1 – *Peak alignment and illustration of plateau width with mass ^{52}Cr resolved* from *Nu II MC-ICPMS (Imperial College London)*

Figure 3.1 depicts the traces from a tuning standard of 50 ng g^{-1} V:10 ng g^{-1} Cr:10ng g^{-1} Ti. All peaks have contributions from molecular species, although H5 shows this most clearly, with $^{40}Ar^{12}C^{+}$ interference resolved from $^{52}Cr^{+}$. The blue bar denotes the optimal range for axial mass settings. The black arrow shows the ΔM offset from left peak slope half height, here ~ 0.098. Resolution of >5000 is needed to sufficiently resolve the LHS of peaks from isobaric interferences, which have higher atomic masses than the monatomic ions of interest. Figure from Supplementary Material of Hopkins et al., (2019).

3.3 Results

3.3.1 Instrumental performance

3.3.1.1 Resolution

The Nu *HR* has resolution ~ 300, Nu *1700* ~ 8000, Nu *II* ~ 4800-6000 (depending upon the wear on the analyser slit in pseudo-high-resolution mode, **Figure 3.1**). Both the Nu *1700* and the Nu *II* are able to resolve the compound interferences present at the heavy edge of the mass-peaks (especially on 52 and 53) and return 52:53 values ~ 9 (**Table 3.4**). This is in line with the natural $^{52}Cr/^{53}Cr$ ratio (~8.8, de Laeter John et al., 2003). This indicates that, now resolved, only trace residual Cr remaining in the measured samples is contributing to the 52 and 53 signals, enabling more accurate mass correction for Cr on the 50 mass unit (^{50}V).

3.3.1.2 Sensitivity

In low-resolution, the Nu *HR* yields about 20-40 V/ppm using a Nu *DSN* introduction system (depending upon the age of the sampler cone), whereas the Nu *1700* yields about 40-50 V/ppm using a *Cetac Aridus II*. The Nu *II* yields ~ 400-500 V/ppm in low resolution mode (probably due to the enhanced sample transmission at the vacuum-plasma interface on this generation of instruments). However, to achieve sufficient mass resolution, a narrower analyser slit setting is used, in combination with alpha-slits, reducing sample transmission by ~ 90%. Under these running conditions, the Nu *II* has a sensitivity ~ 40-50 V/ppm (**Table 3.4**). Note that all sensitivities are normalised to a solution uptake rate of $100\mu l \cdot min^{-1}$ (which was the uptake rate of the nebulisers used in this study).

3.3.1.3 Internal precision (RSE)

The relative standard error (RSE, in ppm) of the $^{51}V/^{50}V$ ratio represents the internal precision for one analysis of V isotope ratios:

$$RSE = \frac{\sigma}{\sqrt{n}} \cdot \frac{1\,000\,000}{\bar{x}}$$

Where $\bar{x}$ is the average (here the $^{51}V/^{50}V$ ratio), σ is the standard deviation, and n is the number of cycles in an analysis. The RSE is a measure of the variability inside one measurement. The Nu *II* has the best RSE (~15 ppm) but it also had the longest total measurement time (350 seconds, versus 200 seconds for Nu *HR* and Nu *1700*). Measurements of 50x5 second ratios (total 250 seconds) yielded RSE ~ 19 ppm, indicating that the internal precision on each measurement is likely still better for the Nu *II* than for the Nu *HR*. Increasing the total measurement time on Nu *1700* to 400 seconds reduced RSE to ~ 50ppm. However, this also significantly worsened bracketing standard RSD. In general, RSE was relatively stable for Nu *HR* and Nu *II* across runs and between measurement sessions but became extremely large (> 200 ppm) for Nu *1700* after a short period of time (typically < 2 hours).

3.3.1.4 Bracketing Standard Reproducibility

The relative standard deviation (RSD) of the four bracketing AA standard solutions is defined as:

$$RSD_{4AA} = \frac{\sigma_{4AA}}{\bar{x}_{4AA}} \cdot 1\,000\,000$$

where $\sigma_{4AA}$is the standard deviation and $\bar{x}_{4AA}$is the mean of the four AA bracketing solutions, reported in ppm. When running well, all instruments have RSD < 100ppm, but the Nu *1700* (as for RSE) loses its precision after a short period of time, recording values > 300ppm.

Table 3.4 – *Optimal running setups for the Nu HR, Nu 1700, and Nu II instruments in this study.*

		Nu HR	Nu 1700	Nu II
RF Power		1300 W	1300 W	1300 W
Amplifiers	*m/z* 49	$10^{11}\,\Omega$	$10^{11}\,\Omega$	$10^{12}\,\Omega$
	m/z 50	$10^{11}\,\Omega$	$10^{12}\,\Omega$	$10^{12}\,\Omega$
	m/z 51	$10^{9}\,\Omega$	$10^{11}\,\Omega$	$10^{11}\,\Omega$
	m/z 52	$10^{11}\,\Omega$	$10^{11}\,\Omega$	$10^{11}\,\Omega$
	m/z 53	$10^{11}\,\Omega$	$10^{11}\,\Omega$	$10^{12}\,\Omega$
Faraday Cup Dynamic Range		~10 V	~50 V	~50 V
Resolution	*M/ΔM*	~300	~8000	4800-6000
Introduction System		Nu DSN	Nu DSN/Aridus II	Nu DSN
Nebuliser		ESI PTFE	Glass Expansion	Glass Expansion
Sensitivity	*norm. to 100 μL min^{-1}*	20-40 V.ppm^{-1}	40-50 V.ppm^{-1}	40-50 V.ppm^{-1}
Solution Concentration		5000 μg g^{-1}	800 μg g^{-1}	600-800 μg g^{-1}
Uptake Rate		100 μL min^{-1}	100 μL min^{-1}	100 μL min^{-1}
Integrations		20 X 10 s	20 X 10 s	70 X 5 s
Typical RSE		~40ppm	~70ppm	~15ppm
RSD for 4AA standards in standard run		20-80ppm	50-500ppm	20-120ppm
52 beam : 53 beam		≤ 20	9 ± 3	9 ± 2

Table 3.5 – *Comparison between chemical standards (BDH) and USGS reference materials (BCR2, BHVO2, BIR1a) measured in this and other studies.*

			BDH			**BCR2**			**BHVO2**			**BIR1a**		
Reference	**Instrument**	**Location**	$\delta^{51}V_{AA}$ (‰)	±	n	$\delta^{51}V_{AA}$ (‰)	±	n	$\delta^{51}V_{AA}$ (‰)	±	n	$\delta^{51}V_{AA}$ (‰)	±	n
This Study														
	Nu HR	Oxford	-1.18	0.12	179	-1.07	0.15	8	-1.18	0.15	1	-1.02	0.37	10
	Nu 1700	Oxford	-1.23	0.30	25[a]	-1.10	0.13	2				-1.12	0.2	2
	Nu II	Imperial	-1.19	0.21	123	-0.85	0.26	5	-0.86	0.12	2	-0.89	0.23	3
Literature														
Prytulak et al, 2017*	Nu HR	Oxford & Imperial	-1.17	0.17	1329	-0.95	0.16	27	-0.89	0.08	9	-0.94	0.15	52
Wu et al., 2016	Neptune Plus	USTC, China	-1.23	0.08	197	-0.78	0.08	36	-0.83	0.09	22	-0.92	0.09	52
Schuth et al., 2017	Neptune	Leibniz University	-1.22	0.08	10	-1.03	0.09	9						
Sossi et al., 2017	Neptune Plus	IPGP	-1.10	0.16	10									
Sossi et al., 2018	Neptune Plus	RSES, ANU	-1.13	0.12	28	-1.11	0.08	2				-1.05	0.22	7
Nielsen et al., 2019	Neptune	WHOI	-1.18	0.11	31	-0.79	0.15	24						
	Nu II	Imperial	-1.11	0.20	4	-0.8	0.14	3						

*Represents a compilation of all BDH and USGS values published in Nielsen et al., 2011; Prytulak et al., 2011; Prytulak et al., 2013; Prytulak et al., 2017

[a]Comiled from across 6 measurement sessions where tuning was stable enough.

3.3.2 Standards and USGS reference materials

As explained in **3.3.1.3-3.3.1.4**, the Nu *1700* typically only stayed tuned for a short period of time before RSE and RSDs of bracketing standards increased dramatically. During the periods of good tuning, some measurements of BDH and USGS reference materials were able to be performed. The secondary BDH standard shows average $\delta^{51}V$ within the range of expected values (**Table 3.5**) for all instruments tested. However, the Nu *1700* shows a larger 2SD (±0.3 ‰) compared to the Nu *II* and the Nu *HR*. USGS reference materials display $\delta^{51}V$ within error of published values (**Table 3.5**).

3.3.3 Heard Island Samples

Data from Heard Island shows a range in $\delta^{51}V$ between -0.93‰ and -0.56‰ (**Table 3.6**), within the range of measured terrestrial basalts from other locations (e.g. Prytulak et al. 2013; 2017).

Table 3.6 – *Results from analysis of Heard Island samples. TiO_2 data from Barling et al., (1994).*

Sample Name	Location	Rock Name	TiO_2 (wt%)	$\delta^{51}V$	2sd
65001	Satellite Cone	Basanite	6.02	-0.78	0.17
65082	Big Ben - South Flank	Trachyandesite	3.43	-0.67	0.17
65085	Big Ben - South Flank	Basalt	3.15	-0.78	0.17
65104	Big Ben - South Flank	Trachybasalt	3.16	-0.70	0.17
65148	Big Ben - South Flank	Trachyandesite	3.67	-0.73	0.17
65171	Summit	Trachybasalt	3.66	-0.56	0.17
65183	Big Ben - South Flank	Basalt	4.42	-0.93	0.17
69244		Basanite	5.3	-0.75	0.17

3.4 Discussion

3.4.1 Comparison of standards and USGS reference materials to literature

Results from the Nu HR and Nu II used in this study can be seen in **Table 3.5**. Values for BDH are well in accordance with literature values (Prytulak et al., 2017; Wu et al., 2016; Schuth et al., 2017; Sossi et al., 2017; Sossi et al., 2018; Nielsen et al., 2019). As with earlier medium-resolution MC-ICPMS work, there is no discernible difference between $\delta^{51}V$ in USGS reference materials measured using Nu *II* versus initial low-resolution work (Prytulak et al., 2011) indicating that the incomplete resolution of mass-interferences in these first studies is less critical for terrestrial igneous samples.

3.4.2 Poor internal and external precision on Nu 1700

Although some limited data were obtained from the Nu *1700,* the typical instrumental stability was poor (becoming de-tuned in < 2 hours typically, often shorter). This detuning was characterised by instability in the ^{51}V voltage, and the resulting $^{51}V/^{50}V$ ratio (**Figure 3.2**). Numerous attempts were made to identify the source of this instability in the instrument. No changes to the introduction system (e.g. Nu *DSN* vs Aridus II vs an alternative Aridus II), nebuliser type (glass vs PTFE) or uptake rate (50, 75, 100, 150µl·min^{-1}), cones, or gas flows improved instrumental performance. It was noted that the detuning of the instrument was especially noticeable in instances where data was obtained over midnight (**Figure 3.2**). At midnight, the air-pressure within the laboratory (and the whole mass-spectrometry wing of the Dept of Earth Sciences) changed. This was observable as an absence of any overpressure from the lab out into the corridors, and was later found to be due to a bug in the software for the Dept of Earth Sciences building management software. Data obtained just before midnight would display smoothly-varying changes in 51/50 ratio, but at midnight (and thereafter) would detune to a non-smoothly varying pattern. Although this effect was particularly noticeable at midnight, changes in room pressure throughout the day (largely governed by the spin-up and

spin-down of the department's air handling systems) may contribute to the reasonably poor RSE and RSD observed for the Nu *1700*.

It is not clear why this would affect the Nu *1700* more than Nu *HR* (which is based in a different laboratory in the same corridor), but it could be due to a) an effect specific to the Nu *1700* lab, or b) particularly noticeable on the Nu *1700* where small fluctuations in front-end characteristics can effect big changes at the detectors due to the large geometry of the instrument.

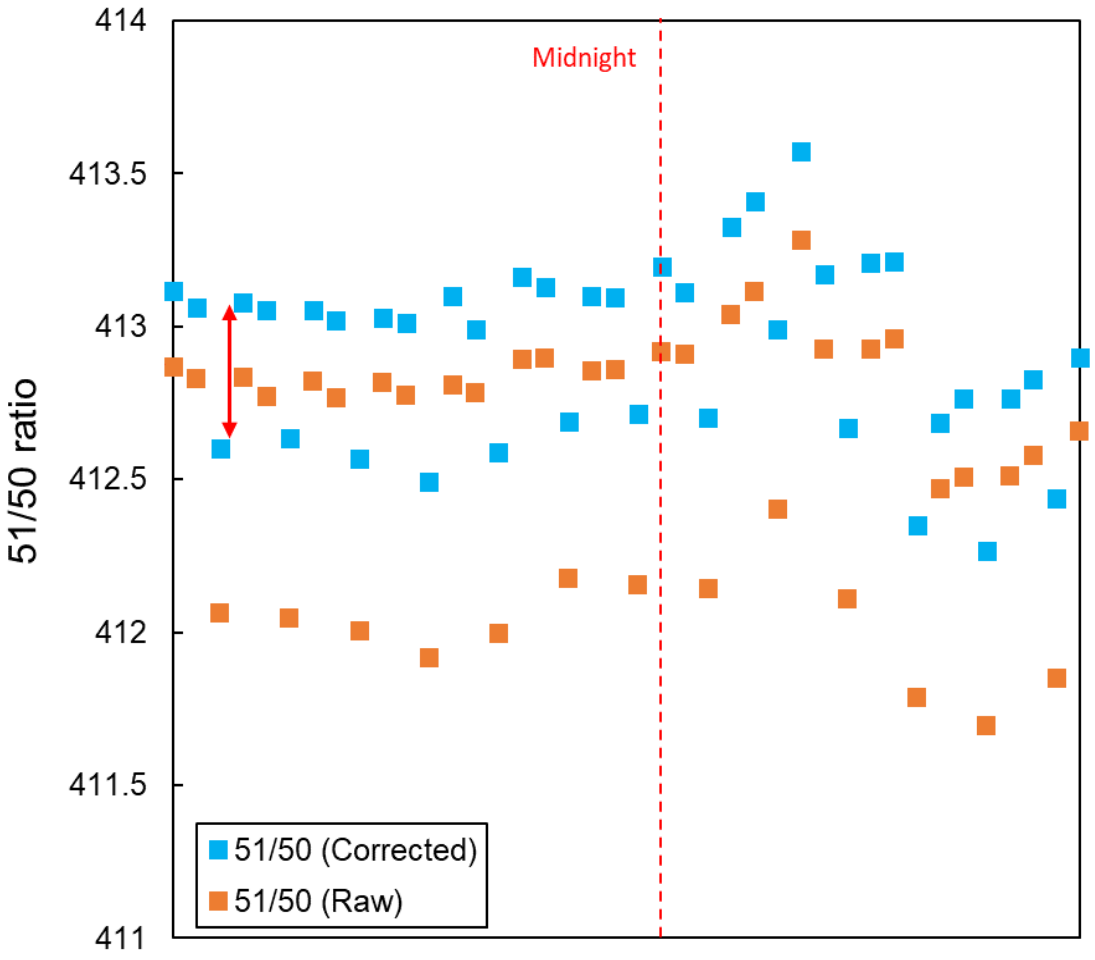


Figure 3.2 – *Overnight run from 27th July 2016. Raw 51/50 and corrected 51/50 ratios for an AA-AA-BDH standard sequence running over midnight. Runs are stable and instrumental drift is more smoothly changing until midnight, where the air-pressure in the laboratory drops as the Dept of Earth Sciences building management system resets (~ 7 minutes total). After normal functioning is restored, the magnitude of the instrumental drift is more rapidly changing and*

irregular. For context, note that the magnitude off the instrumental drift over 2-3 runs after midnight is almost as large as the offset between AA and BDH corrected ratios.

3.4.3 Chemical separation protocols

The chemical techniques of Nielsen et al. (2011) and Wu et al. (2016) (**Table 3.2, 3.3**) were tested using USGS reference materials and Heard Island basalts. In general, it was found that the procedures of Wu et al. (2016) handled the high-Ti matrix samples more effectively than the Nielsen et al. (2011) techniques. This is likely due to the limited capacity of the *Eichrom TRU* resin (**Table 3.2**). Processing sample 65001 (TiO_2 ~ 6%) through Nielsen et al. (2011) was not possible without splitting the sample into separate aliquots and recombining after this second column stage. In instances where this wasn't performed, samples would precipitate a milky-white solid during application of H_2O_2 prior to loading onto column 3 of Nielsen et al. (2011) (**Figure 3.3**), which made continuing with the procedure impractical. The techniques of Wu et al. (2016) typically handled samples more effectively (including the high-Ti Heard Island basalts, **Table 3.6**), displaying $^{49}Ti/^{51}V$ (and $^{53}Cr/^{51}V$) ratios < 0.00001. Pre- and post-V collection cuts (of 1ml 1.2M HNO_3, **Table 3.3**) during columns 1 and 2 typically yielded ≤ 50ng V, indicating that column calibration curves had not shifted from Wu et al. (2016)

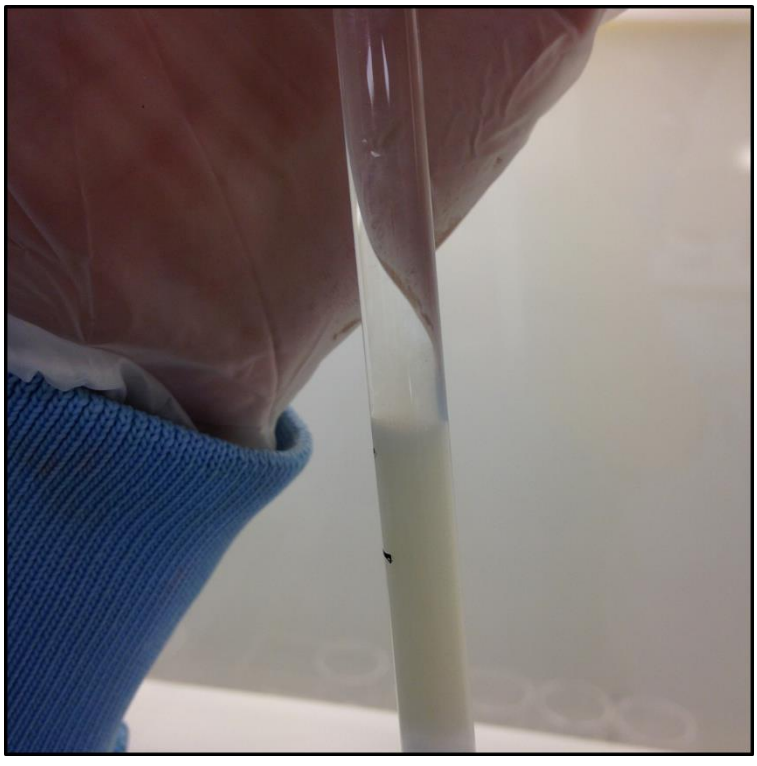


Figure 3.3 – *Sample 65001 upon loading to column stage 3 of Nielsen et al. (2011). Milky-white precipitates can be observed just above the resin bed.*

3.5 Conclusion

Three MC-ICPMS instruments (Nu *HR*, Nu *1700*, Nu *II*) were tested and compared in preparation for measurement of vanadium isotope ratios in lunar basalts (**Chapter 4**). Although Nu *HR* was used in earlier studies, the low dynamic range of this instrument meant that a large amount of sample (total V $\geq$ 2 $\mu g \cdot g^{-1}$) was used for every analysis. The low resolution of these techniques meant that incomplete resolution of mass-interferences on *m/z 52* and *m/z 53* was impossible and estimations of the contribution of compound interferences had to be used. Data for both Nu *1700* and Nu *II* are of sufficiently high-resolution to resolve mass interferences, yielding 52:53 ratios similar to the natural $^{52}Cr/^{53}Cr$ ratio. However, data from the Nu *1700* is hindered by poor voltage stability (and thus isotopic ratio stability) probably caused by secular changes in room pressure from the air-handling system. Small variations in beam stability at the plasma-instrument interface cause large changes in beam stability at the back-end of the instrument. Over the course of testing, only a handful of chemical standards and USGS reference materials were able to be run at reasonable precision. The Nu *II* provided the best results and the analytical set-up in **Table 3.4** will be used to measure lunar samples (**Chapter 4**). The chemical techniques of Wu et al. (2016) appear more robust for high-TiO_2 samples, due to the use of two large cation exchange columns instead of the Eichrom TRU resin column used in Nielsen et al. (2011). These techniques will therefore be employed for lunar samples.

4

The Vanadium Isotopic Composition of Lunar Basalts

Note to readers

This chapter has been adapted from a paper recently published in *Earth and Planetary Science Letters*:

"Hopkins, S.S.[a], Prytulak, J.[b,c], Barling, J.[a], Russell, S.S.[d], Coles., B.J.[b], Halliday, A.N.[a,e], 2019. The Vanadium Isotopic Composition of Lunar Basalts. *Earth and Planetary Science Letters*, **511**, 12-24. doi:10.1016/j.epsl.2019.01.008"

[a] Department of Earth Sciences, University of Oxford, OX1 3AN, United Kingdom

[b] Department of Earth Sciences and Engineering, Imperial College, London, SW7 2AZ, United Kingdom

[c] Department of Earth Sciences, Durham University, DH1 3LE, United Kingdom

[d] Natural History Museum, London, SW7 5BD, United Kingdom

[e] The Earth Institute, Columbia University, Hogan Hall, 2910 Broadway, New York, NY 10025, USA

High-quality copies of figures can be found in **Appendix 4**.

4.1 Introduction

4.1.1 Lunar Origin

The most widely-accepted theory of lunar origin is the so-called "giant impact" model whereby a smaller planetary object struck the proto-Earth in its final stages of accretion leading to an impact-generated disk from which the Moon formed (Cameron and Ward, 1976; Hartmann and Davis, 1975). The model satisfies constraints on the geodynamical properties, planetary densities, and broad chemical features of the Earth-Moon system. In early numerical simulations of the giant impact most of the Moon-forming material derives from the impactor, with only a small contribution from Earth (e.g. Canup, 2004). Extra-terrestrial bodies typically have distinct isotopic compositions (Goderis et al., 2016), thus it was assumed that the Moon should also be isotopically distinct. The Earth and the Moon are remarkably similar in mass-independent isotope variations such as ^{54}Cr (Lugmair and Shukolyukov, 1998; Mougel et al., 2018), ^{50}Ti (Zhang et al., 2012), ^{17}O (Young et al., 2016) and ^{96}Zr (Akram and Schonbachler, 2016), mass-dependent isotope variations of moderately refractory element such as Si (Armytage et al., 2012), Cr (Bonnand et al., 2016), Ti (Millet et al., 2016), Fe (Sossi and Moynier, 2017; Weyer et al., 2005; Liu et al., 2010; Wiesli et al., 2003), and in radiogenic ^{182}W (Kruijer et al., 2015).

Several explanations have been advanced for the unexpected isotopic similarity between the Earth and the Moon. In the aftermath of a giant impact, a re-equilibration of isotopes between the Earth and newly-forming Moon might have taken place (Pahlevan & Stevenson, 2007). However, the timescales and temperatures of re-equilibration do not favour isotopic homogenisation of refractory elements – e.g. Cr and Ti. Predicted isotopic offsets in silicon based upon this model (Pahlevan et al., 2011) were not found (Armytage et al., 2012). Alternative impact scenarios have been proposed to reconcile the isotopic similarity of the

Earth and the Moon. These include high-energy impacts (Canup, 2012; Cuk and Stewart, 2012), a hit-and-run model (Reufer et al., 2012), and a multiple-impact scenario (Rufu et al., 2017). Compared to the canonical model, each of these scenarios invokes restricted dynamic conditions prior, or subsequent, to impact.

Models of an impactor with Earth-like isotopic composition (Dauphas et al., 2014), and models of inner Solar System homogeneity have also been proposed (Mastrobuono-Battisti et al., 2015). These studies argue against the assumption of an isotopically-distinct impactor. However, a consensus on the best model of lunar formation has yet to be reached.

4.1.2 Chemical and isotopic variations in lunar basalts

Lunar basalts are primarily divided by TiO_2 contents into very-low-Ti basalts (VLT) (<1.5 wt% TiO_2), low-Ti basalts (1.5-6 wt% TiO_2) and high-Ti basalts (> 6 wt% TiO_2). Chemically-distinct regions of the lunar mantle must exist to explain the compositional diversity of mare basalts (Papike et al., 1976), with high-Ti basalts requiring significant amounts of ilmenite in their sources. Lunar mantle heterogeneities arise from the differentiation of the lunar magma ocean (LMO), a global melting of the lunar mantle as a result of accretion, during which differentially-dense regions of the mantle inefficiently mixed as crystallisation proceeded (Elkins-Tanton et al., 2011). Stable isotope studies of lunar basalts have not only provided evidence of the isotopic kinship between the Moon and the Earth, but also the extent of lunar mantle heterogeneity, the provenance of lunar sample subsets and the nature of lunar differentiation processes. For example, high-Ti basalts show light Mg (Sedaghatpour et al., 2013), and heavy Fe and Ti isotope ratios (Liu et al., 2010; Sossi & Moynier, 2017; Wiesli et al., 2003). These isotopic differences are thought to relate to crystallisation of ilmenite during LMO differentiation, or partial melting during formation of high-Ti and low-Ti parental melts. In contrast, Cr isotope ratios show mass-dependent fractionations correlating with indices of

magmatic differentiation, but no difference between high-Ti and low-Ti basalts (Bonnand et al., 2016). Fractionations in Cr isotopes result from crystallisation of Cr-spinel and Cr-bearing ülvospinel. Post-crystallisation processes can modify isotopic compositions further (in a mass-independent fashion), and lead to difficulty in identifying the original isotopic signatures of the samples. For example, small excesses in ^{53}Cr and ^{54}Cr (Mougel et al., 2018) and depletions in $\varepsilon^{50}Ti$ (Zhang et al., 2012) have been found in mare basalts, reflecting cosmogenic processes at the lunar surface.

4.1.3 Vanadium

Vanadium occurs in multiple oxidation states (V^{2+}, V^{3+}, V^{4+}, V^{5+}) and behaves as a moderately incompatible element in terrestrial igneous systems. Previous studies have taken advantage of the strongly redox-dependent behaviour of V to investigate oxidation states of mantle and melts throughout Earth's history (e.g. Canil, 1997; Lee et al., 2003; Lee et al., 2005; Li and Lee, 2004; Mallmann and O'Neill, 2009; Wood et al., 2008). Vanadium is depleted in the Earth's mantle compared to CI chondrites (McDonough and Sun, 1995), and its abundance relative to siderophile elements has been used to argue for changes in mantle oxidation during Earth's accretion and core formation (Wood et al., 2008). The lunar and terrestrial upper mantles are estimated to have similar V contents (79 ppm and 81 ppm, respectively; Seifert and Ringwood, 1988). Vanadium is incompatible in plagioclase, and so is unaffected by anorthite crystallisation during LMO differentiation. Differing oxygen fugacity (fO_2) of planetary mantles can affect the partitioning behaviour of V. For example, at low lunar fO_2, 1 to 2 log units below the Iron-Wüstite buffer (IW-1 to IW-2) most V is present in lunar magmas as V^{3+}. Vanadium is more compatible in lunar olivine, pyroxene, and spinel than for terrestrial analogues, where V^{4+} is the major species (Papike et al., 2005). The multiple valence states of

V over a wide range of fO_2 makes it attractive as a potential tracer of planetary magmatic processes.

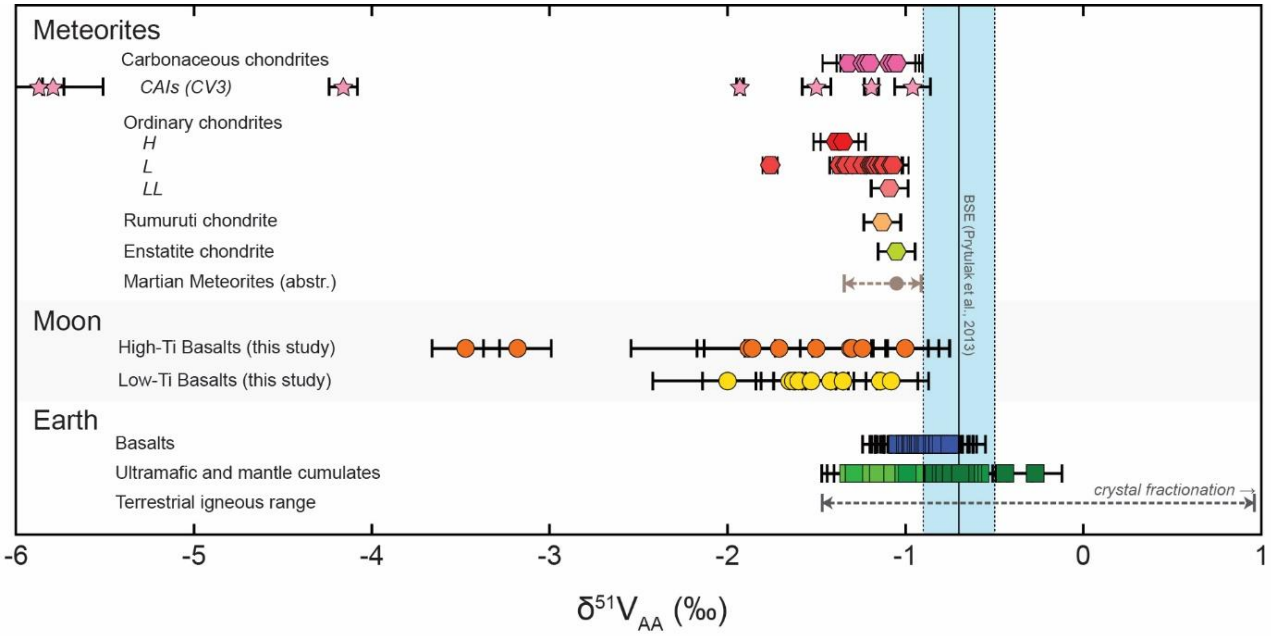


Figure 4.1: *Compilation of published V isotope data for Solar System materials including the lunar basalts measured in this study. Lunar basalts vary more widely in composition than all other samples, except CAIs (Sossi et al., 2017). Some CAIs show the isotopically-lightest values measured in the Solar System. Published data for chondrites is from Xue et al., (2018) and Nielsen et al. (2019) Recent data for Martian meteorites (presented only in abstract form) is included (Davis et al. 2018). The BSE estimate is indicated by the blue bar (Prytulak et al., 2013). Terrestrial basalts from multiple settings shows a much more restricted range than lunar basalts (Prytulak et al., 2011; 2013; 2017; Wu et al., 2018). The measured V isotope range (~2.3‰) of terrestrial magmatic rocks is displayed by the grey dashed line, with the heaviest V isotope samples thought to result from oxide fractionation (Prytulak et al., 2017).*

4.1.4 Vanadium isotopes

Vanadium has two stable isotopes: ^{50}V (0.25%) and ^{51}V (99.75%) and has been of cosmochemical interest for decades, due to the hypothesis that ^{50}V could be generated by cosmic ray irradiation processes (Stauffer and Honda, 1961). Advances in high precision multiple collector inductively-coupled-plasma mass spectrometry (MC-ICPMS) and the development of more effective separation procedures (e.g. Nielsen et al., 2011; Wu et al., 2016) now allow V isotope determination to precisions useful for geological applications (~0.2‰).

Vanadium isotopes are reported in per mil (‰) deviation relative to an Alfa Aesar (AA) V solution standard introduced by Nielsen et al. (2011):

$$\delta^{51}V_{AA} = \left\{ \frac{(^{51}V/^{50}V)_{sample}}{(^{51}V/^{50}V)_{AA}} - 1 \right\} * 1000$$

Terrestrial magmatic samples show a range of ~2.3‰ in $\delta^{51}V$. This variability has been interpreted in terms of equilibrium fractionation (Prytulak et al., 2011; Prytulak et al., 2013; Prytulak et al., 2017; Wu et al., 2018, **Figure 4.1**). The bulk silicate Earth (BSE) is estimated at $\delta^{51}V_{AA}$ = -0.7 ± 0.2‰ based on analyses of bulk peridotites (Prytulak et al., 2013), although more recent work suggests a lighter BSE ($\delta^{51}V$ = -0.91 ± 0.05, 2SD; Qi et al., 2018). Metal-silicate experiments suggest terrestrial core formation does not significantly fractionate V isotopes (Nielsen et al., 2014). Much of the variation in magmatic samples has been proposed to result from crystallisation of (Fe,Ti)oxides during magmatic differentiation (Prytulak et al., 2017; Sossi et al., 2018; Wu et al., 2018). The similarity in whole rock $\delta^{51}V$ variation with respect to indicators of magmatic evolution in two cogenetic lava suites with disparate redox conditions (Hekla, Iceland and Anatahan, Mariana arc) suggests crystallisation of (Fe,Ti)oxides and the coordination difference between melt and mineral are dominant in driving isotope fractionation rather than $\delta^{51}V$ variation directly reflecting changes in oxidation state (Prytulak et al., 2017). Recent experimental work directly determining V magnetite-melt isotope fractionation factors ($\Delta^{51}V_{magnetite\text{-}melt}$) at variable, controlled redox conditions yields $\Delta^{51}V_{magnetite\text{-}melt}$ consistent with those needed to explain the variation seen in ~closed system crystallisation and resulting Rayleigh isotope fractionation (Sossi et al., 2018). Interestingly, Sossi et al. (2018) also observed a strong positive relationship between the magnitude of $\Delta^{51}V_{magnetite\text{-}melt}$ and fO_2.

Initial analyses of chondrites, achondrites and martian meteorites returned a restricted range of $\delta^{51}V$ compositions ($\delta^{51}V_{AA}$ = -1.7 ± 0.2) uniformly-lighter than BSE (Nielsen et al., 2014). This was suggested to be due to incorporation of irradiated components in meteorites. However, more recent analyses of chondrites with medium-resolution mass spectrometry ($M/\Delta M > 4000$) suggests a revised isotopically-heavier composition for chondrites ($\delta^{51}V_{AA}$ between -1.35 to -1.05‰ for all chondrites except Xinglongquan, $\delta^{51}V$ = -1.76 ± 0.05‰; Xue et al., 2018; Nielsen et al., 2019) and martian meteorites ($\delta^{51}V_{AA}$ = -1.3 to -0.7‰; Davis et al., 2018) (**Figure 4.1**). Nielsen et al. (2019) suggest that incomplete resolution of mass interferences (e.g. polyatomic S interferences) during analyses of extra-terrestrial samples resulted in inaccurate and light $\delta^{51}V$ values for initial studies of meteorites, which were performed at lower-resolution (Nielsen et al., 2014; Prytulak et al., 2011). At medium-resolution (e.g. Wu et al., 2016; Nielsen et al., 2016) these interferences are resolved. Inter-laboratory comparison shows no resolvable differences in $\delta^{51}V$ for silicate rock reference materials (which generally have low S contents) at low- or medium-resolution MC-ICPMS (Nielsen et al., 2019). Despite the heavier, revised $\delta^{51}V$, chondrites are isotopically-lighter than BSE (Nielsen et al., 2019; Xue et al., 2018, **Figure 4.1**). Nielsen et al., (2019) attributed this to nucleosynthetic-heterogeneity in the Solar System (demonstrated by correlations between chondrite class average $\delta^{51}V$ and $\varepsilon^{54}Cr$). Measurements of calcium-aluminium inclusions (CAIs) in CV chondrites show one subset (fine-grained CV3 CAIs) to have the lightest $\delta^{51}V$ measured thus far in the solar system ($\delta^{51}V_{AA}$ < -5.87‰, Sossi et al., 2017, **Figure 4.1**). These light $\delta^{51}V$ values have been attributed to ^{50}V production during intense early solar cosmic ray (SCR) irradiation, in agreement with mathematical predications for CAI formation close to an early, active Sun (Gounelle et al., 2001; Lee et al., 1998). This suggests cosmogenic reactions are viable mechanisms for production of light $\delta^{51}V$.

One body for which $\delta^{51}V$ data is lacking is the Moon. As a refractory element, V is expected to be isotopically-similar in the Moon and the Earth. Data from the Moon may also provide constraints on the origin of the difference in $\delta^{51}V$ observed between chondrites and the Earth.

4.2 Sampling Approach

Nineteen unbrecciated lunar basalts from Apollo missions 11, 12, 14, 15, and 17 were selected based on geochemical and mineralogical variability (**Table 4.1**). Samples were processed in sufficient quantities for both V isotope and trace element measurements. The samples include both low-Ti and high-Ti basalts, with reported TiO_2 contents ranging from 2.2 wt% (15535) to 12.9 wt% (70215) (**Appendix 2a**) and have reported modal ilmenite contents from 0.5% (12018) to 17% (70215, **Appendix 2b**). An Apollo 11 Type A (high-K) basalt (10017), enriched in K, REEs and other incompatible trace elements (**Appendix 2a, Appendix 2g**, Neal and Taylor, 1992), and a high-Al/low-K Apollo 14 basalt (14053) were included. Samples were extracted from the interior of their parents, with three exceptions. The exteriors of the parent samples 10017 and 12054 were sampled and a fragment of a glass-splash coating from sample 12054 was also analysed. The glass was emplaced after a nearby impact or an eruptive event and has an Apollo 12 ilmenite basalt composition (similar to its host rock, Hartung et al., 1978). Interior aliquots of samples were obtained from a maximum depth of 2.5cm within their parent samples (except 12063–343 which was located between 0.5-5cm).

4.3 Methods

4.3.1 Sample preparation

Details of procedures for sample preparation, dissolution, ion-exchange chromatography and elemental and isotopic analyses can be found in **Chapter 2**. Briefly, sample chips were washed in ~18.2 MΩ•cm ultra-pure water (MQ H_2O), centrifuged and dried at low temperature.

Samples were crushed to homogenise any intra-sample geochemical variation using an agate pestle and mortar. Separate fractions of these powders were weighed for trace element determinations (~10mg) and vanadium isotope analyses (20-100mg). Samples were digested in a multi-stage hotplate dissolution procedure.

4.3.2 Trace element analysis by ICPMS

Trace element analyses were performed using a *PerkinElmer® NexION® 350D* quadrupole ICPMS (at the Department of Earth Sciences, University of Oxford) on ×10000 dilutions of digested sample solutions. A Re-Rh-In internal standard addition (for monitoring instrumental drift) was performed using an in-line *ESI* prep*FAST* auto-dilution system. The relative standard deviation was <5%, except for Li (7.9%). United States Geological Survey (USGS) reference material, BHVO-2, was measured alongside the lunar sample suite to assess accuracy.

4.3.3 Vanadium isotope analysis by MC-ICPMS

Chemical isolation of V was performed using methods outlined in Wu et al. (2016). Sample aliquots containing 5-10 μg of V were passed twice through cation-exchange columns (using *Bio-Rad®* AG50W-X12 200-400 mesh resin) to remove the majority of matrix elements (Fe, Ti, Al, Ca). An anion-exchange column (using *Bio-Rad®* AG1-X8 200-400 mesh resin) was then used to separate V from Cr, and repeated in scaled-down form to remove any remaining Cr.

Quantitative yield of V must be obtained to exclude possible isotopic fractionation during incomplete elution in ion-exchange chromatography. The yield was found to be 100 ± 15% at the end of the procedure (by comparing MC-ICPMS beam intensities to Quad ICP-MS measurements). Cuts were collected before and after the vanadium elution steps in the cation-exchange columns to ensure the calibration of V elution (Wu et al., 2016). Total V blanks were

< 0.3ng, which is insignificant compared to the amount of V processed. Samples returned $^{49}Ti/^{51}V$ and $^{53}Cr/^{51}V$ ratios < 0.00001 (Nielsen et al., 2011), confirming negligible contributions of ^{50}Cr and ^{50}Ti to the ^{50}V signal.

Vanadium isotopes were analysed on a *Plasma II* (*Nu Instruments*) MC-ICPMS in the MAGIC laboratories at the Department of Earth Sciences and Engineering, Imperial College London. Measurements were performed at solution concentrations of 600-800 ng g^{-1}. Samples were aspirated into a *Nu Instruments* DSN-100 to desolvate before injection into the plasma. Masses 49, 50, 51, 52 and 53 were monitored to measure V isotopes and to correct for Ti and Cr interferences on mass 50 (**Table 3.4**). Pseudo-high-resolution mode ($M/\Delta M > 5000$) was used to resolve polyatomic interferences (particularly $^{40}Ar^{12}C^+$ from $^{52}Cr^+$) from the isotopes of interest. Faraday cups were equipped with 10^{11} Ω resistors, except for cups with low-intensity signals (m/z: 49, 50, 53), which were equipped with 10^{12} Ω resistors. This amplifies the resultant signal by a factor of 10 and improves signal/noise ratios. Each sample analysis was bracketed by two measurements of an Alfa Aesar (AA) V solution, and a well-characterised secondary standard from BDH chemicals (BDH, Nielsen et al., 2011). The AA standard defines zero (**Section 4.1.4**). BDH has been measured (n= 1329) to have a composition of $\delta^{51}V_{AA} = -1.17 \pm 0.17‰$ (Prytulak et al., 2017). Measurements of BDH in this study gave an average $\delta^{51}V_{AA} = -1.21 \pm 0.22‰$ (n = 121). United States Geological Survey (USGS) reference materials BCR-2, BHVO-2, and BIR-1a were processed through the same ion-exchange procedures and $\delta^{51}V$ values were found to be in agreement with literature values (**Table 3.5**).

Table 4.1: $\delta^{51}V_{AA}$, selected element concentrations from ICPMS data, literature values for $^{158}Gd/^{157}Gd$, and sample exposure age.

Mission	Sample	Type	Sub-type	Location	$\delta^{51}V_{AA}$ (‰)	2s.d. (‰)	n	[V] ($\mu g\ g^{-1}$)	TiO_2 (wt.%)	$^{158}Gd/^{157}Gd$[a]	+/-	Exposure Age (Ma)[b]
A11	10017-	High-Ti/High-K	11A	*exterior*	-3.47	0.19	1	55	11.2	1.59726	0.00046	479 ± 60
	10017-	High-Ti/High-K	11A	*interior*	-3.18	0.19	1	61	11.3			479 ± 60
	10020-	High-Ti/Low-K	11B3	*interior*	-1.88	0.29	2	113	10.7			127 ± 25
	10044-	High-Ti/Low-K	11B1	*interior*	-1.30	0.19	3	56	9.6	1.58681	0.00030	70 ± 17
A12	12018-	Low-Ti Olivine		*interior*	-1.42	0.20	3	185	2.1	1.58924	0.00040	195 ± 16
	12054-	Glass Splash			-1.63	0.21	4	168*	4.7*			–
	12054-	Low-Ti Ilmenite		*interior*	-1.65	0.49	3	152	5.3			260 ±
	12054-	Low-Ti Ilmenite		*exterior*	-1.60	0.21	4	126	4.1			260 ±
	12063-	Low-Ti Ilmenite		*interior*	-1.35	0.21	3	188	4.9	1.58768	0.00016	95 ± 5
A14	14053-	Low-Ti/High-	HA	*interior*	-1.08	0.21	3	106	2.7			21 ± 5
A15	15016-	Low-Ti Olivine-		*interior*	-1.53	0.21	2	224	2.1			322 ± 83
	15535-	Low-Ti Olivine-		*interior*	-1.14	0.21	2	197	2.1			110 ± 20
	15556-	Low-Ti Olivine-		*interior*	-2.00	0.42	2	227	2.4			546 ±
A17	70215-	High Ti	17B2	*interior*	-1.31	0.21	2	167*	12.9*			126 ± 3
	70255-	High Ti	17A	*interior*	-1.86	0.68	3	83	10.8			280 ± 85
	71135-	High Ti	*17B2*	*interior*	-1.50	0.63	3	90	10.3			103 ± 3
	71546-	High Ti	17A	*interior*	-1.24	0.49	2	120*	12.2*			110 ±
	74275-	High Ti	17C	*interior*	-1.00	0.19	3	131	12.4	1.58524	0.00001	32 ± 1
	75035-	High Ti	*Unclassified*	*interior*	-1.71	0.19	2	31	10.5			77 ± 19
	Average High-Ti				*-1.85*	*1.66*						
	– excluding 10017				*-1.48*	*0.64*						
	Average Low-Ti				*-1.49*	*0.56*						

* Samples 12054-13, 70215-389, 71546-22 were not analysed for element concentrations by ICPMS in this study. An average of previously-reported elemental concentrations is used hereon (see **Appendix 2e**). [a,b] Gd isotopes and exposure ages compiled from published values (**Appendix 2d, 2c**). Exposure ages for 12054 (independently-calculated) and 71546 (estimated from other samples in the same rake) are less reliable than for the other samples in the suite (**Section 4.4.5**, **Appendix 2b**).

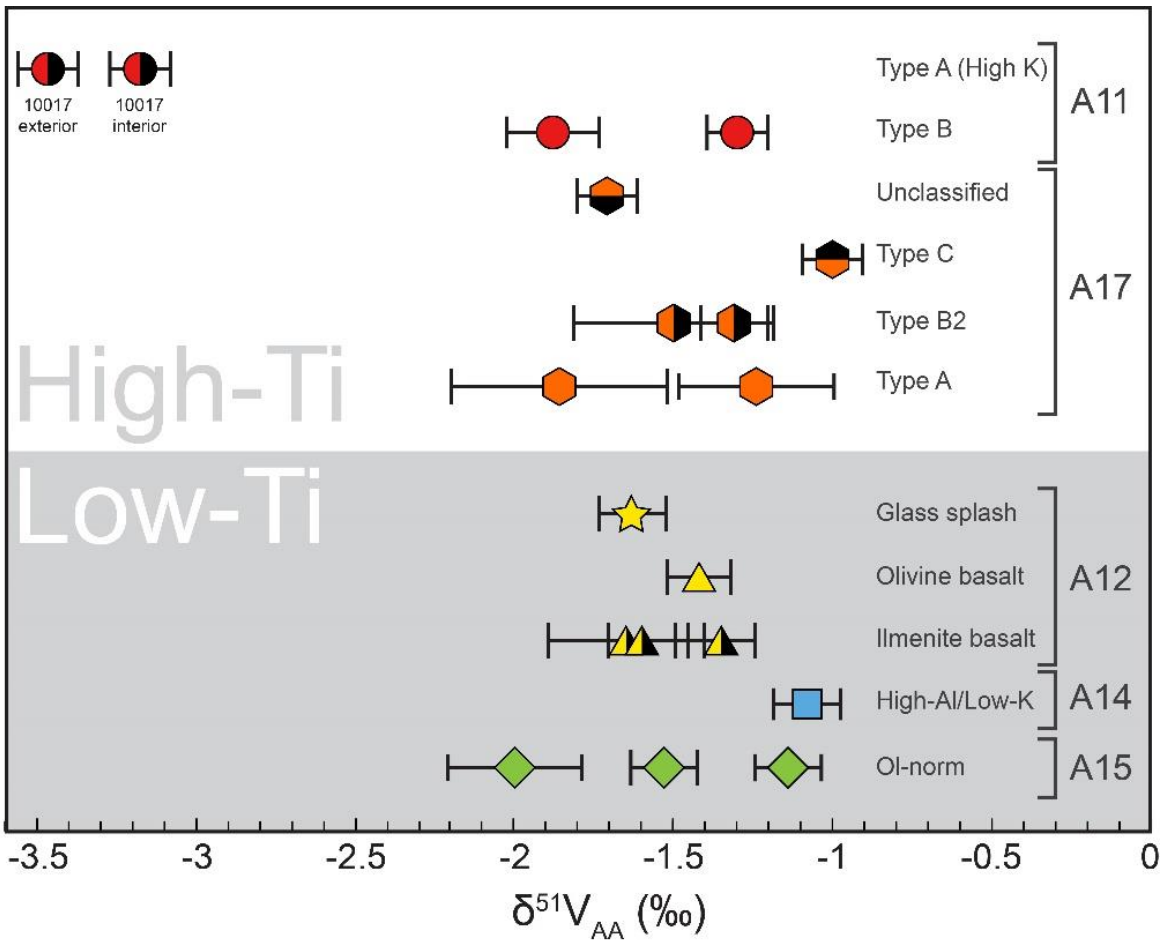


Figure 4.2: *$\delta^{51}V$ of the samples measured in this study. Samples are divided by high-Ti vs low-Ti type, mission, and sub-classification (Neal and Taylor, 1992). Aside from the two samples of 10017 (Apollo 11 Type A basalt), all chemical groups show an overlap in $\delta^{51}V$ between ~-2‰ to ~-1‰. Note in particular the range displayed by Apollo 15 olivine-normative basalts, despite their similarity in major and trace element compositions.*

4.4 Results & Discussion

4.4.1 Major and trace elements

Comparison of ICPMS elemental concentrations to previous analyses of lunar basalts shows that samples lie within expected ranges for their mare basalt subtype (**Table 4.1**, **Figure 4.3c, Figures S1, S2**). Sample sizes in this study are small (up to 125 mg) compared to the majority of literature chemical analyses (**Appendix 2a**), which were typically performed on much larger aliquots (>1g) and would be expected to be more representative of the geochemistry of parent samples (e.g. Ryder and Schuraytz, 2001). However, obtaining major and trace element

concentrations and V isotope ratios on the same aliquots allows internally-consistent interpretation of isotopic variations. Major element concentrations of samples lie within 5% of published values, with minor exceptions. Samples 12018 (-9%), 12054-150 (+6.3%), and 70255 (-9.8%) show TiO_2 contents that differ by more than 5% from published values. Sample 12054-146 differs in K_2O by +8%, and sample 70255 differs in MnO by -6.3%. Chondrite-normalised REE patterns of the lunar samples match those of previous analyses and show the characteristic patterns expected for their sub-groups (**Figure S1**). A detailed discussion of the trace element behaviour of the sample suite is beyond the scope of this study, however, elemental concentrations from this study and previously-reported values can be found in **Appendix 1, Appendix 2a & Appendix 2g** and **Figures S1 & S2**.

4.4.2 Vanadium isotopes

Lunar basalts span a $\delta^{51}V$ range of ~2.5‰, varying from $\delta^{51}V_{AA}$ = -3.47‰ (10017-400) to -1.00‰ (74275-355) (**Table 4.1, Figure 4.2**). There is no systematic difference between $\delta^{51}V$ in high-Ti and low-Ti basalts (High-Ti: $\delta^{51}V_{AA}$ = -1.85 ± 1.66‰; Low-Ti: $\delta^{51}V_{AA}$ = -1.49 ± 0.56‰, 2SD, **Table 4.1, Figures 4.2, 4.3a,b**). Interior and exterior aliquots of Apollo 11 Type-A (high-K) basalt 10017 have the lightest isotopic compositions ($\delta^{51}V_{AA}$ = -3.18 ± 0.19‰ and -3.47 ± 0.19‰, **Figure 4.2**). Excluding these two samples reduces the lunar $\delta^{51}V$ range to ~1‰ and populations of high-Ti and low-Ti basalts are essentially indistinguishable (high-Ti basalt excl. 10017: $\delta^{51}V_{AA}$ = -1.48 ± 0.64‰). The total lunar $\delta^{51}V$ range is larger than the total range of magmatic samples yet measured on the Earth (~2.3‰, **Figure 4.1**). Thirteen of the nineteen lunar basalts show $\delta^{51}V$ lighter than any terrestrial samples ($\delta^{51}V_{AA}$ < -1.32‰). Only three samples, 74275-355, 14053-305, and 15535-165 have isotopic compositions within the published range for terrestrial basalts ($\delta^{51}V_{AA}$ = -0.95 ± 0.25‰ 2SD, Prytulak et al., 2013; Wu et al., 2018, **Figure 4.1**).

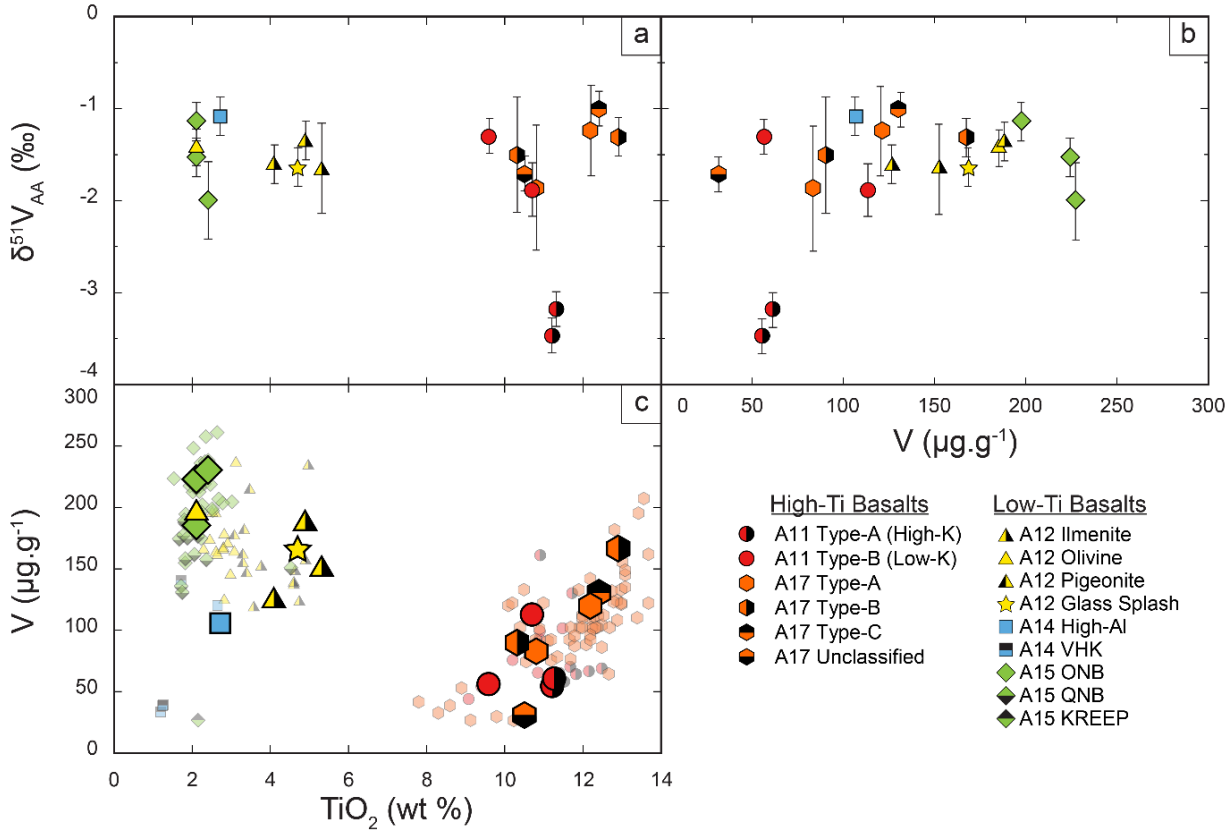


Figure 4.3: *Comparison of $\delta^{51}V$, V and TiO_2 concentrations: a) $\delta^{51}V$ versus TiO_2 (wt%) contents; b) $\delta^{51}V$ versus V concentration; c) V concentration against TiO_2 concentration. Samples analysed in this study lie in the regions expected for their mare basalt subtype (**4.3c**). A strong correlation exists between V and TiO_2 in the high-Ti basalts. Larger, solid symbols represent data from the samples in this study. Semi-transparent symbols are a compilation of literature-reported values for V and TiO_2 in lunar basalts (**Appendix 2e**). There is no similar correlation between TiO_2 and $\delta^{51}V$ (**4.3a**) or between V and $\delta^{51}V$ (**4.3b**). Sample 10017 (two Apollo 11 high-K basalts) has $\delta^{51}V$ values which lie outside of the range of the other mare basalts.*

4.4.3 Magmatic effects on V and $\delta^{51}V$

Under terrestrial magmatic conditions V behaves relatively incompatibly through magmatic evolution except during crystallisation of (Fe,Ti)oxides into which V^{3+} partitions readily (O'Neill and Navrotsky, 1984). On Earth, the most extreme $\delta^{51}V$ arises from ~closed system crystallisation of isotopically light (Fe, Ti)oxides, which drives residual melts to heavier compositions (up to $\delta^{51}V_{AA}$ ~ +1‰; Prytulak et al., 2017). Given the high modal proportions of (Fe,Ti)oxides (particularly ilmenite) in lunar basalts, it is tempting to assume that the large variability recorded in the lunar sample suite is a result of ilmenite-melt fractionation.

However, oxygen fugacity is much lower on the Moon (IW-1 to IW-2) than in terrestrial melts, which not only affects the speciation and partitioning behaviour of V (V^{3+}>V^{4+}, on Earth V^{4+}>V^{3+}), but also the crystallising mineral phases (e.g. from lack of available Fe^{3+}). Analyses of minerals in lunar basalts show V present in spinel (<8000ppm, Papike et al., 2005), armalcolite (<3000ppm) and ilmenite (<2500ppm, El Goresy et al., 1974), pyroxene (<500ppm), and olivine (<80ppm – Papike et al., 2005). Likewise, partition coefficients for V at low fO_2, show V to be compatible in spinel, armalcolite, ilmenite and pyroxene (in decreasing order of compatibility, Karner et al., 2006; Klemme et al., 2006; Papike et al., 2005). Under lunar conditions, V appears more compatible than in terrestrial settings. The abundances of minerals in samples is highly-variable (**Appendix 2b**) and crystal fractionation may control the observed range of $\delta^{51}V$.

Although V varies within the suite with varying major element compositions (**Figure 4.3c, Figure S2**) and mineralogy (e.g. ilmenite, pyroxene **Figure S3**) there is no systematic relationship between $\delta^{51}V$ and TiO_2 or V (**Figure 4.3a, b**) or between $\delta^{51}V$ and modal proportions of the major hosts for V (spinel, ilmenite, pyroxene, **Figure S3**). Likewise, samples previously studied for mass-dependent isotopes (e.g. Cr, Fe, **Figure S4**) do not show correlations with $\delta^{51}V$ (Bonnand et al., 2016; Liu et al., 2010; Millet et al., 2016; Sossi and Moynier, 2017; Wiesli et al., 2003). Apollo 11 Type-A basalt 10017 is >1‰ lighter than the other basalts (**Table 4.1**, **Figure 4.2**). Although the origin of the Apollo 11 Type-A basalts remains contested, the high-abundances of K, REEs, and other incompatible trace elements suggest involvement of a KREEP-like component (Neal and Taylor, 1992). The light $\delta^{51}V$ in this sample may reflect the extreme composition of this KREEP-y reservoir. However, KREEP is thought to represent the last vestiges of LMO prior to crystallisation. Prior removal of oxides from the LMO should leave this reservoir enriched in heavy $\delta^{51}V$ (i.e. opposite to the direction of $\delta^{51}V$ offset observed, assuming similar mineral-melt fractionations to terrestrial settings).

The lack of evidence for systematic magmatic-driven $\delta^{51}V$ variability in this suite is further highlighted by the 0.84‰ isotopic difference between samples 15535 and 15556 (**Figure 4.2**). These samples are genetically-related by olivine fractionation (Mason et al., 1972), which is unlikely to account for the large $\delta^{51}V$ difference observed.

4.4.4 Reduced magmatic δ51V fractionation at lower fO_2

Considering the magnitude of isotopic fractionation associated with (Fe,Ti)oxide crystallisation on Earth (e.g. $\Delta^{51}V_{magnetite\text{-}melt}$ = -0.4 to -0.5‰ in Hekla and Anatahan lavas, Prytulak et al., 2017), the lack of correlation of $\delta^{51}V$ with TiO_2 or ilmenite or oxide content is notable, particularly since the range in abundances of (Fe,Ti)oxides in lunar basalts is much larger than in terrestrial samples. Wu et al. (2018) recently proposed a smaller terrestrial $\Delta^{51}V_{mineral\text{-}melt}$ of -0.15‰. However, this factor was derived from a MORB-suite that is not cogenetic and has documented evidence of magma-mixing (indeed, their isotope-mixing calculations fit the $\delta^{51}V$ variation observed just as well as their reduced mineral-melt V isotope fractionation factor). A recent experimental study of V isotope fractionation between magnetite and hydrous granitic melt at 800 °C and controlled fO_2 conditions (from FMQ-1 to FMQ+5) suggests $\Delta^{51}V_{magnetite\text{-}melt}$ reduces with decreasing fO_2 (Sossi et al., 2018). Extrapolating these results to lunar fO_2 and temperatures ($1/T^2$ dependence; Schauble, 2004; Urey, 1947) yields a $\Delta^{51}V_{oxide\text{-}melt} \sim$ -0.2‰ (assuming lunar oxides fractionate $\delta^{51}V$ similarly to magnetite, which is not present at lunar fO_2). For lunar basalts, a reduced fractionation factor at lower fO_2 may explain a lack of variation between $\delta^{51}V$ and other geochemical parameters but cannot explain the wide range and light $\delta^{51}V$ of the suite.

4.4.5 Cosmogenic irradiation

Exposure ages have been previously-determined for most of the samples in this suite (**Table 4.1**, **Appendix 2d**). To allow the most consistent cross-sample comparisons, exposure ages

calculated using ^{81}Kr-Kr and ^{38}Ar (where ^{81}Kr-Kr data are absent) were chosen over other techniques due to their widespread adoption and inter-calibration (e.g. Hohenberg et al., 1978; see **Appendix 2d**). The range of sample δ^{51}V is lighter and more variable at longer exposure ages (t_e, **Figure 4.4**), implicating modification of primitive isotopic compositions by exposure-related processes.

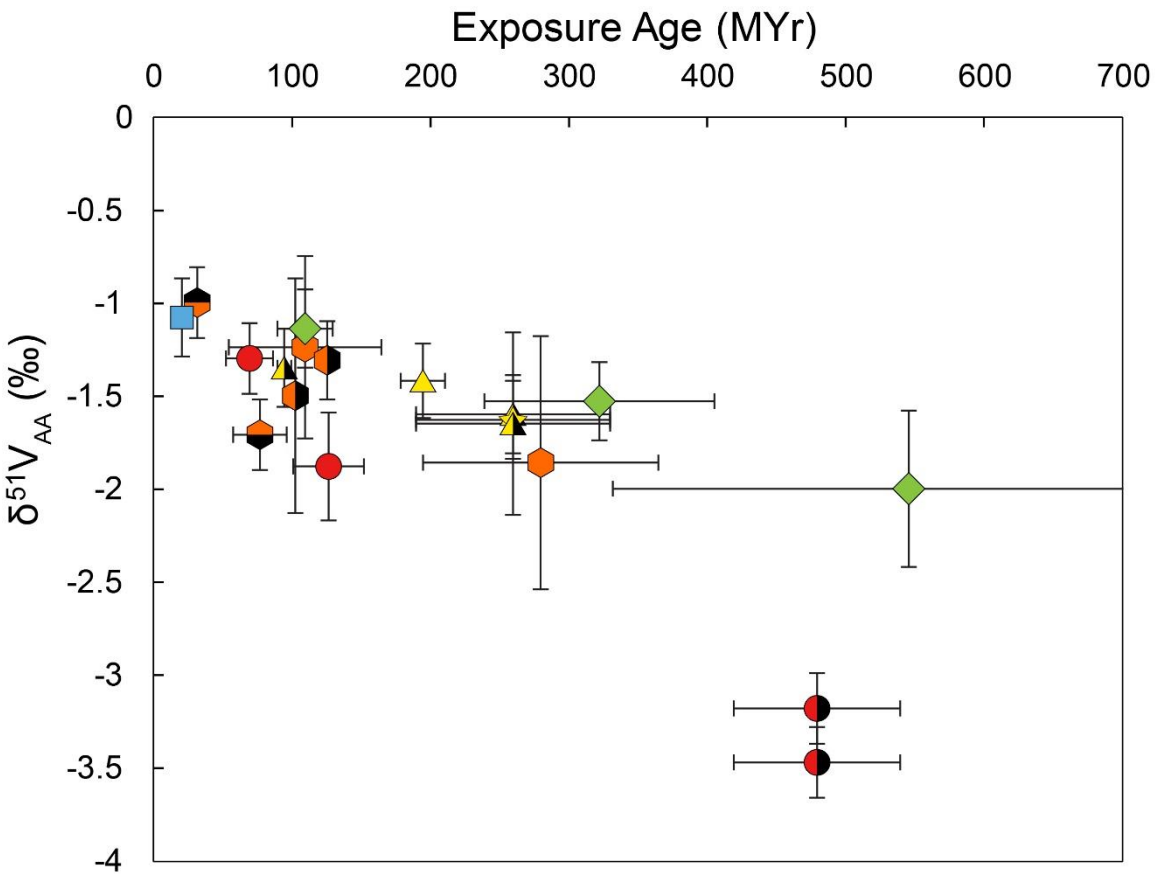


Figure 4.4: *Exposure age versus δ^{51}V. Samples with longer exposure ages have lighter V isotopic compositions. Details of sample exposure ages are outlined in the* ***Appendix 2d****. Symbols as in* ***Figure 4.2****.*

Samples exposed at the lunar surface may be affected by meteorite sputtering, surficial contamination, solar wind implantation, or irradiation from high-energy particles derived from solar and galactic cosmic rays (SCRs and GCRs). If exposure-related isotopic variability is achieved after crystallisation (as indicated by **Figure 4.4**), sputtering, surficial contamination and solar wind implantation processes are unlikely to explain the observed δ^{51}V variability. All

but three samples are picked from the interiors of their parents and would be shielded from these weakly-penetrating processes. Thus, cosmogenic irradiation from SCRs and GCRs is most likely. Cosmogenic effects have been observed in lunar samples for neighbouring Ti and Cr isotope systems, with negative anomalies in ε^{50}Ti (Zhang et al., 2012) and positive anomalies in ε^{54}Cr and ε^{53}Cr (Mougel et al., 2018) attributed to neutron-capture processes. It is possible that similar processes operate on V isotopes.

The flux of energetic particles in SCRs and GCRs consists mainly of protons and alpha-particles (with minor fluxes of heavier nuclei). These primary particles can react with sample material to produce a cascade of secondary energetic particles (e.g. protons, neutrons, alpha-particles, ^{3}He, deuterium, muons, kaons, and pions) which can then further interact with sample material. Secondary neutrons are of particular interest for a number of elements, particularly those having isotopes with large neutron-capture cross-sections (e.g. gadolinium, Gd, where neutron-capture cross-sections for ^{157}Gd>>^{156}Gd; Eugster et al., 1970). The ^{158}Gd/^{157}Gd ratio is sensitive to the flux of thermal neutrons generated during cosmic-ray reactions. Sample δ^{51}V shows a negative correlation with ^{158}Gd/^{157}Gd for five samples with published Gd isotope data (**Figure 4.5, Appendix 2c**), although the strength of this relationship may be enhanced by the position of sample 10017, which lies far outside the range of δ^{51}V and ^{158}Gd/^{157}Gd for the other samples. This correlation operates in a similar sense to that between δ^{51}V and exposure age (i.e. the most-exposed samples have the lightest δ^{51}V). However, three different samples (15016, 15556, 70215) have been measured for ε^{50}Ti (another neutron-capture-sensitive proxy, Zhang et al., 2012) and show similar trends (**Figure S5**).

4.4.6 Cross-sections

Earlier modelling of cosmogenic V isotope effects focused on production of ^{50}V from solar proton and He-nuclei interactions with CAI-precursor target materials (Gounelle et al., 2001;

Lee et al., 1998). However, only a select handful of reaction pathways and target elements (Ti, Cr, and ^{51}V) were considered. Under lunar conditions, other target elements (e.g. Fe, Mn) may be important. Secondary particle fluxes (e.g. neutrons, **Figure 4.5, Figure S5**) are clearly present in these samples and should be considered. Cosmogenic reactions affecting ^{51}V must also be considered to ascertain the resultant effects on $\delta^{51}V$.

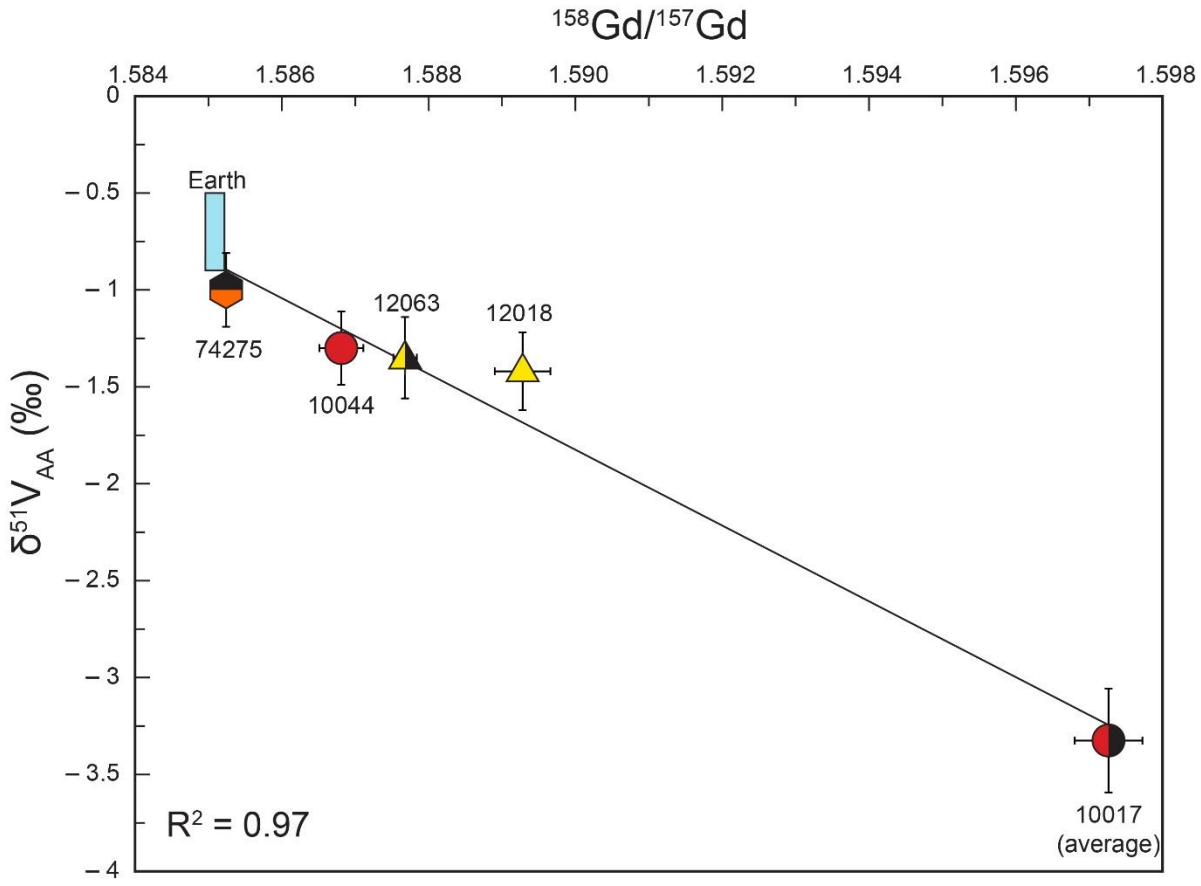


Figure 4.5: *Neutron-sensitive gadolinium isotope ratios versus $\delta^{51}V$. The ratio of $^{158}Gd/^{157}Gd$ is a sensitive monitor of secondary neutrons produced during cosmic-ray bombardment of lunar material. Published $^{158}Gd/^{157}Gd$ for samples in this study linearly correlate with $\delta^{51}V$. The internal and external aliquots of 10017 are averaged (for both $\delta^{51}V$ and $^{158}Gd/^{157}Gd$) and plotted here as analyses were performed on different aliquots of this sample. The blue box represents the BSE estimate for $\delta^{51}V$ (Prytulak et al., 2013) and the terrestrial Gd isotope value from Dubois et al. (1992). A linear regression is calculated on the lunar samples. References for the Gd isotope data can be found in* ***Appendix 2c****. Symbols as in* ***Figure 4.2****.*

Cross-sections for reactions involving the production or burnout of both ^{50}V and ^{51}V via proton-, alpha particle- and neutron-interactions with lunar sample compositions were calculated using

TALYS-1.9 (Koning et al., 2008). This is the most recent iteration of the TALYS nuclear-modelling code and one of the most accurate codes for energies < 200MeV, being regularly evaluated and updated against experimental data. Although the energies of incident SCR and GCR particles regularly exceed this upper energy limit, this energy range should provide insights into both spallation- and capture-processes, and the relative importance of different target elements.

Cross-sections were calculated for nuclear reactions between target elements Ti, V, Cr, Mn and Fe (assumed to be present in natural isotope proportions) and incident neutrons (at energies 10^{-11}MeV-200MeV), protons, and alpha-particles (energies 0.1MeV-200MeV). To allow comparison between the reactions (n>1000), cross-section data was sub-divided into three categories: *burnout* of V isotopes (where target V isotope, *j*, forms another resulting element, *R*), *internal production* (target V isotope, *i*, produces the other V isotope, *j* – i.e. $^{50}V \rightarrow {}^{51}V$ or vice versa), and *external production* (where ^{nat}Ti, ^{nat}Cr, ^{nat}Mn, or ^{nat}Fe produces V isotope, *j*). All other factors being constant, *burnout* and *internal* production are controlled by the abundance of target V, and *external* production is controlled by the abundance of the non-V target element. The sums of the cross-sections, $\sum {}^{j}\sigma_{X,k}$, for *burnout*, *internal* and *external* production were calculated for each target, *X*, at different energies of incident particle, *k*, (where *k* = proton, neutron, or alpha-particle; **Fig S7**).

Reactions producing radioactive isotopes ^{51}Sc, ^{51}Ti, ^{51}Cr, ^{51}Mn, ^{51}Fe included in the sum of cross-sections for ^{51}V production (these isotopes are assumed to decay to before further interaction with energetic particles). Cross-sections for reaction pathways where the product nucleus is the same as the target nucleus (e.g. $^{50}V(n,n)^{50}V$, or $^{51}V(p,n)^{51}Cr$ which decays to ^{51}V) were excluded.

The compiled cross-sections for each target ($\sum {}^{j}\sigma_{X,k}$) were adjusted to reflect atomic abundances of target elements relative to V in samples via:

$$\sum {}^{j}\sigma_{X,k,adjusted} = \sum {}^{j}\sigma_{X,k} * [X]/[V] \qquad \textbf{(1)}$$

where [X]/[V] is the ratio of target isotope or element relative to V. Total concentration-adjusted cross-sections ($\sum {}^{j}\sigma_{X,k,adjusted}$) of different particle pathways are compared for their effects on ^{50}V and ^{51}V (**Figure 4.6**, where the "average" lunar sample composition is used).

Internal production displays lower cross-sections than external production in all scenarios, indicating that non-V target elements likely dominate cosmogenic production. Above ~50MeV, Fe displays the largest cross-sections for production of both V isotopes in proton and alpha-particle reactions (**Figure 4.6b,c,e,f**). Between 5-50 MeV, cross-sections for production of ^{50}V from protons with ^{nat}Ti (**Figure 4.6b**) is higher than for production of ^{51}V (**Figure 4.6e**). Burnout of either V isotope becomes increasingly-important at lower proton and alpha-particle energies (<5 MeV). At neutron energies >1 MeV, Cr and Fe appear to be most important for production of ^{51}V and ^{50}V (**Figure 4.6a,d**). At neutron energies > 50 MeV, Fe is the most important target element for production of either V isotope. Below 1 MeV, there are numerous pathways towards production of ^{51}V (via neutron interaction with Ti, Cr, ^{50}V), but no pathways for ^{50}V production. This has important implications: if thermal neutron capture is most significant amongst the array of possible reaction pathways, it is impossible to reconcile with the direction of cosmogenic isotope shift. Thus, charged-particle reactions or high-energy neutrons must contribute a significant amount to the total cosmogenic V production. In general, production cross-sections for ^{51}V appear larger than for ^{50}V (**Figure 4.7a,b,c**) – however, a direct comparison must be carried out to ascertain the resulting effect on sample δ^{51}V.

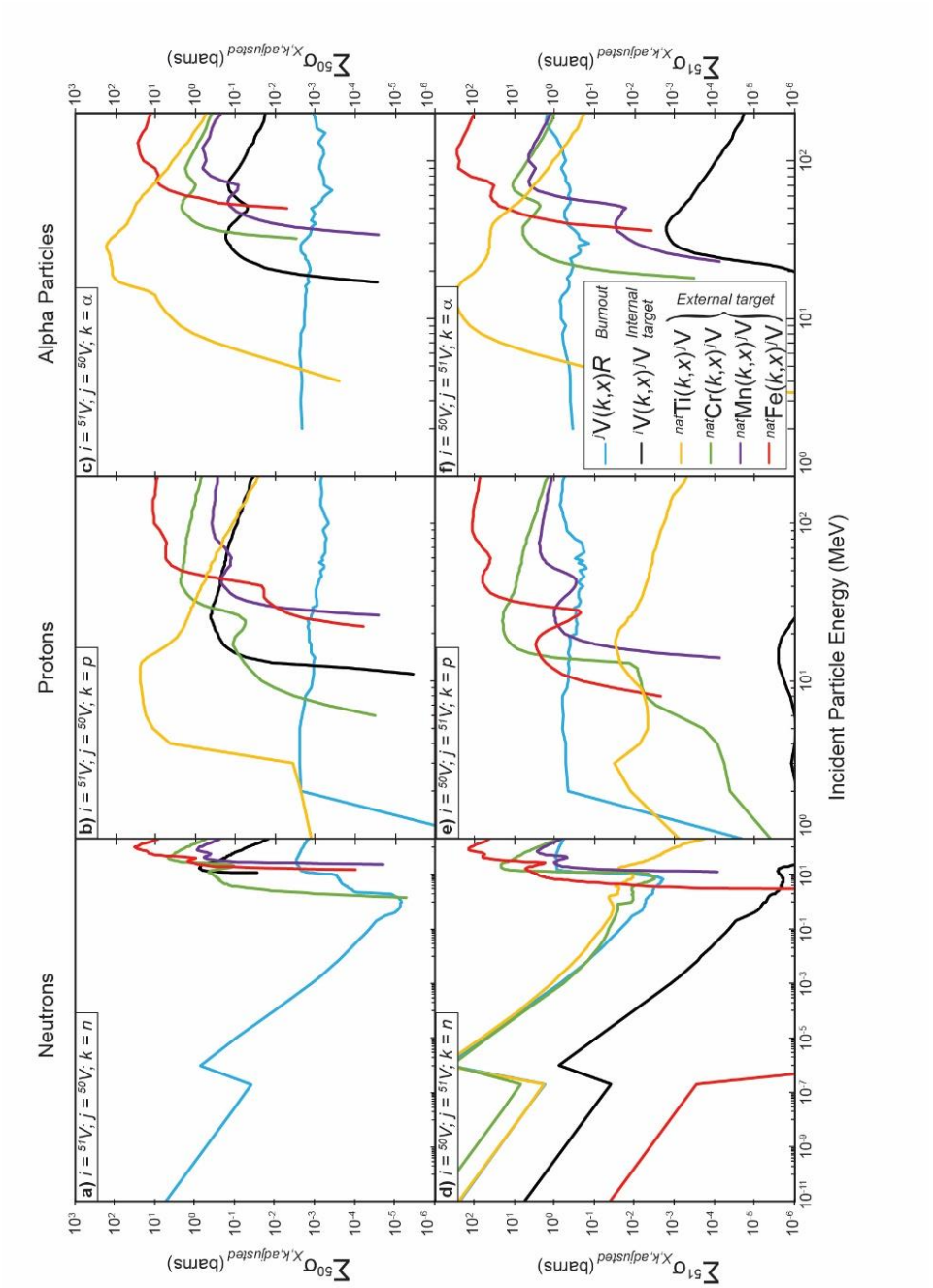


Figure 4.6: *The sum of adjusted cross-sections ($\Sigma^{j}\sigma_{X,k}$, y-axes) for reactions between an incident particle, k, (k = neutron, proton or alpha particle) and nuclei (X) to either produce or burn out ^{j}V (where j is the V-isotope of interest – i.e. ^{50}V, ^{51}V) at different particle energies (x-axis). Reactions are broken down into three categories: burnout (light blue) of ^{j}V to another isotope, R; internal production (black) of ^{j}V from ^{i}V (j = 50, 51; i = 51, 50); external production of ^{j}V from target elements ^{nat}Ti (gold); ^{nat}Cr (green); ^{nat}Mn (purple); ^{nat}Fe (red). Cross-sections are adjusted to the average composition of the suite via [X]/[V] (where [X] is the atomic abundance of the target element or isotope, [V] is the atomic abundance of V). Targets are assumed to have natural isotopic abundances. Cross-section curves are displayed for each incident particle (neutrons **4.6a, 4.6d**; protons **4.6b, 4.6e**; alpha-particles **4.6c, 4.6f**) and its effect on each isotope of V (^{50}V: **4.6a, 4.6b, 4.6c**; ^{51}V: **4.6d, 4.6e, 4.6f**). Within each panel, the curves represent reactions which add to the abundance of isotope ^{j}V, except the burnout curves (light blue) which will decrease the abundance of ^{j}V. Note the different energy scales for neutrons and protons/alpha-particles.*

4.4.7 Contribution to sample $\delta^{51}V$

The total $^{51}V/^{50}V$ in irradiated samples can be displayed as follows:

$$\left(\frac{n(^{51}V)}{n(^{50}V)}\right)_{final} = \frac{[n(^{51}V)_0 + n(^{51}V)_{cosm}]}{[n(^{50}V)_0 + n(^{50}V)_{cosm}]} \quad \textbf{(2)}$$

where $n(\,^{j}V)_0$ is the initial number of atoms of isotope, *j*, and $n(\,^{j}V)_{cosm}$ is the number of atoms of isotope, *j* (i.e. ^{51}V, ^{50}V), produced through cosmogenic reactions:

$$n(\,^{j}V)_{cosm} = n(\,^{j}V)_{external} + n(\,^{j}V)_{internal} - n(\,^{j}V)_{burnout} \quad \textbf{(3)}$$

The resulting isotopic effect is:

$$\Delta^{51}V_{cosm} = \left[\frac{\frac{n(^{51}V_{final})}{n(^{50}V_{final})}}{\frac{n(^{51}V_0)}{n(^{50}V_0)}} - 1\right] \times 1000 \qquad \textbf{(4)}$$

Assuming a natural isotopic ratio ($\frac{n(^{51}V_0)}{n(^{50}V_0)}$ = 400) substituting for the terms in **Equation 2** gives:

$$\Delta^{51}V_{cosm} = \left[\frac{n(^{51}V_{cosm}) - n(^{50}V_{cosm}) \times 400}{n(^{50}V_{cosm}) + n(^{51}V_0)}\right] \times 1000 \quad \textbf{(5)}$$

Thus, for a resulting cosmogenic isotopic shift ($\Delta^{51}V_{cosm}$) of 0‰:

$$n(^{51}V_{cosm}) = n(^{50}V_{cosm}) \times 400 \qquad \textbf{(6)}$$

The production of cosmogenic ^{51}V and ^{50}V is proportional to the sum (i.e. *internal + external – burnout*) of their concentration-adjusted cross-sections ($\sum {}^{j}\sigma_{total-adjusted}$). Assuming $[V]_0 >> [V]_{cosm}$, if $\sum {}^{51}\sigma_{total-adjusted} > (\sum {}^{50}\sigma_{total-adjusted} \times 400)$ the resulting isotope ratio will increase and if $\sum {}^{51}\sigma_{total-adjusted} < (\sum {}^{50}\sigma_{total-adjusted} \times 400)$ the resulting isotope ratio

will decrease. For ease of comparison between the total adjusted cross-sections a new variable, the "excess total ^{51}V cross-section" is defined:

$$\varepsilon^{51}\sigma_{total} = (\sum {}^{51}\sigma_{total-adjusted} - \sum {}^{50}\sigma_{total-adjusted} \times 400) / [^{51}\mathrm{V}] \quad \textbf{(7)}$$

This is more useful than a direct cross-section ratio ($\sum {}^{51}\sigma_{total-adjusted}/\sum {}^{50}\sigma_{total-adjusted}$) since it allows direct inspection of the isotopic effects of particular pathways at different energies and can account for instances where the sum of concentration-adjusted cross-sections for an isotope is ≤ 0 (e.g. where burnout is more significant than production).

For all the particle reactions considered, it appears that only neutron capture (<1×10^{-3} MeV) can produce excesses in $\varepsilon^{51}\sigma_{total}$ **(Figure 4.7d,g)**. There are negative excursions in $\varepsilon^{51}\sigma_X$ for proton and alpha-particle reactions with Ti between 20–100MeV (**Figure 4.7e,f**), and smaller negative excursions in $\varepsilon^{51}\sigma_{total}$ for Fe reactions with protons >50 MeV. Similarly, high-energy neutrons display negative $\varepsilon^{51}\sigma_X$ for Fe (>10MeV, **Figure 4.7d**). The magnitude of the cosmogenic isotope effect is expected to vary with sample compositions (i.e. changing [X]/[V] ratio, **Figure 4.7g,h,i**). High-Ti samples are expected to show a stronger $\varepsilon^{51}\sigma$ response to interactions with protons and alpha-particles when compared to average sample or low-Ti sample compositions. However, at lower neutron energies (<10^{-3} MeV), high-Ti samples would be expected to display isotopically-heavier cosmogenic signatures when compared to low-Ti samples (**Figure 4.7g**). It appears that for protons and alpha-particles, Fe and Ti are the primary contributors to V isotope anomalies for the energy ranges investigated. Burnout of V and internal production are relatively unimportant in affecting the final isotopic ratio.

4.4.8 Reconciling with chemical compositions

Plotting sample δ^{51}V against exposure age over V concentration (t_e/[V]) yields a strong linear correlation (**Figure 4.8a**). This correlation is stronger than the relationship between δ^{51}V and

t_e* [Ti]/[V] (and t_e* [Cr]/[V], **Figure S6***)*, and similar to the correlation between $\delta^{51}V$ and t_e* [Fe]/[V] (**Figure 4.8b**) and t_e* [Mn]/[V] (**Figure S6**). The strong correlation between $\delta^{51}V$ and t_e/[V] suggests the concentration of [V] (assuming $[V]_0 >> [V]_{cosm}$) in samples is more important in controlling the resultant $\delta^{51}V$ after cosmogenic exposure than the concentration of the target element – i.e. the target element concentration doesn't vary much compared to [V]. Both Mn and Fe are relatively restricted in variability compared to V, Cr, and Ti (**Appendix 1, Appendix 2a**)**.** However, the concentration-adjusted cross-sections for Mn are orders of magnitude lower than for Fe (**Figure 4.6**), and Fe is therefore more likely to be the primary target element. Iron is relatively invariable within this suite (RSD ~ 8%). A lone high-energy (600MeV and 21GeV) experimental-study of V-production from proton-induced Fe-spallation (Perron, 1976) indicates that production cross-sections are still significant at high-energies, and the ratio of $^{51}V/^{50}V$ produced is low (<1, and this ratio is lower at higher proton energies). Thus, Fe appears to remain an important target for production of light $\delta^{51}V$ for higher-energies particle fluxes (e.g. as seen in GCRs) than directly calculated here.

The weaker correlation with t_e×[Ti]/[V] (despite strong $\varepsilon^{51}\sigma$ depletion at certain energy intervals, **Figure 4.7e,f**) could be due to a number of reasons: 1) the real energetic particle flux is stronger for parts of the energy spectrum where cross-sections with Fe are strongest (typically energies > 50 MeV), or 2) thermal neutron capture on Ti at low energies is quantitatively-important – the production of ^{51}V here would counteract production of lower $^{51}V/^{50}V$ from Ti reactions and protons/alpha-particles.

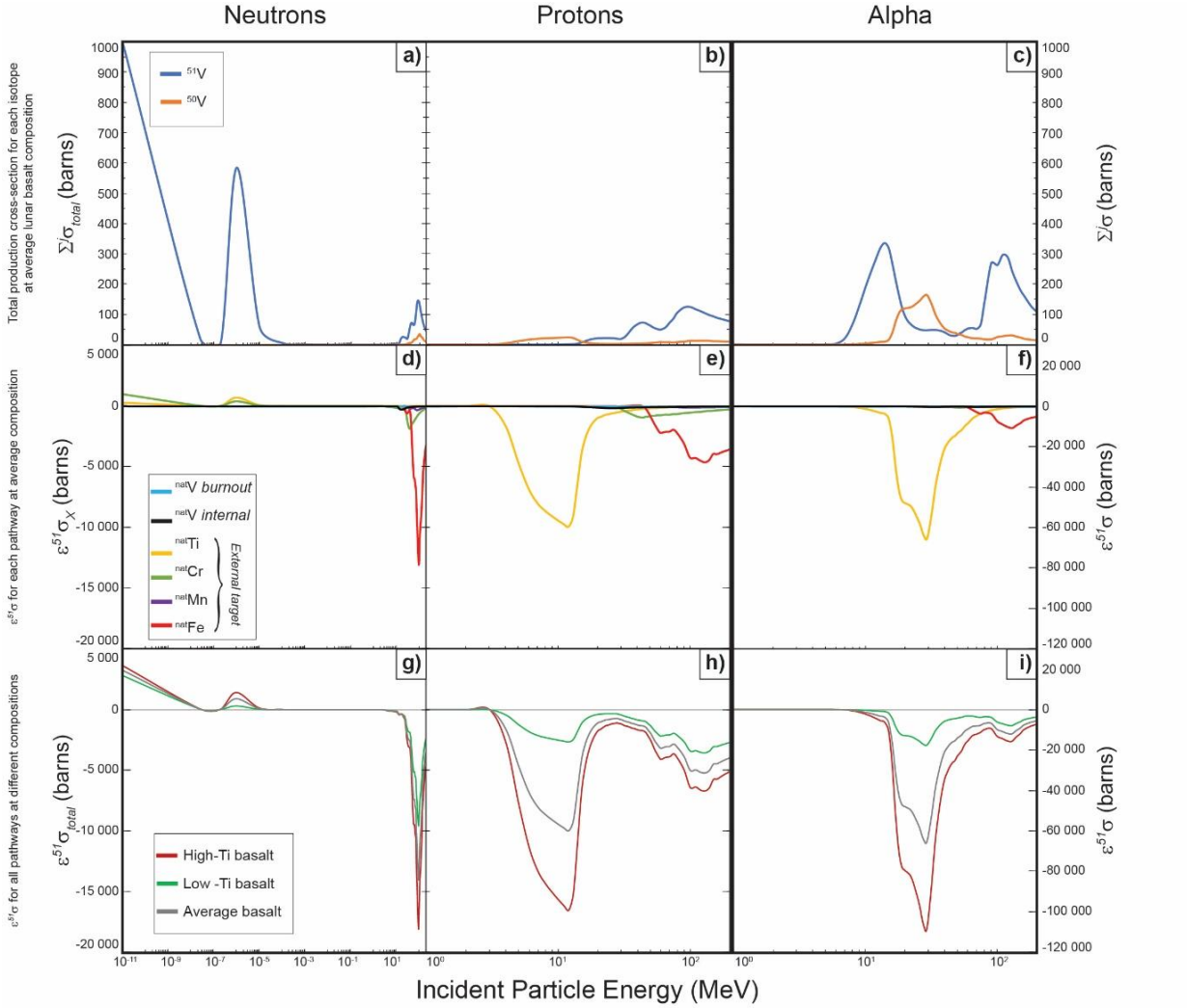


Figure 4.7: *The resulting isotopic effects of cosmogenic reactions between neutrons, protons, and alpha-particles and lunar basalt compositions at different energies. The total concentration-adjusted cross-sections affecting ^{50}V and ^{51}V from interactions between neutrons (**4.7a**), protons (**4.7b**), and alpha-particles (**4.7c**) and targets of average lunar basalt composition at different energies are displayed. Cross-sections for production of ^{51}V is higher than ^{50}V, except for alpha-particle reactions between 20-50 MeV. The excess ^{51}V production cross-section for different target elements ($\varepsilon^{51}\sigma_X$, see **Section 4.7**) varies across the range of incident particle energies and particle compositions (**4.7d, 4.7e, 4.7f**). The total excess ^{51}V production cross-section ($\varepsilon^{51}\sigma_{total}$) changes in intensity with changing target chemical compositions (**4.7g, 4.7h, 4.7i**). For all particles (except neutrons below 10^{-5} MeV) there are significant negative $\varepsilon^{51}\sigma$ deviations. Thermal neutrons ($\leq 2.5 \times 10^{-8}$ MeV) show positive $\varepsilon^{51}\sigma$ deviations (**g**), as only ^{51}V production is viable the target elements investigated (**Figure 4.6a, 4.6d**). Average and low-Ti basalts show reduced $\varepsilon^{51}\sigma_{total}$ deviations compared to high-Ti basalts reflecting variation in [X]/[V] between samples. At high-energies (> 50 MeV) negative deviations in $\varepsilon^{51}\sigma$ are seen from the effect of Fe as a target. Key displayed in **4.7a, 4.7d, 4.7g**.*

In summary, thermal neutrons – although clearly present in sufficient fluxes to impart significant $^{158}Gd/^{157}Gd$ excesses (**Figure 4.5**) and $\varepsilon^{50}Ti$ depletions (**Figure S5**) – cannot be the

sole cause of $\delta^{51}V$ alteration due the lack of viable pathways for neutron capture production of ^{50}V (**Figure 4.6**). Significant fluxes of higher-energy neutrons (>1MeV, **Figure 4.7d,f**), protons, or alpha-particles (>5MeV) must have been present in the samples during their periods of exposure at the lunar surface. The most plausible target element is Fe (**Figure 4.8a,**b). Although SCRs have significantly weaker penetrative-ability than GCRs, both processes may be important for these samples obtained from shallow depths (**Section 4.4.2**).

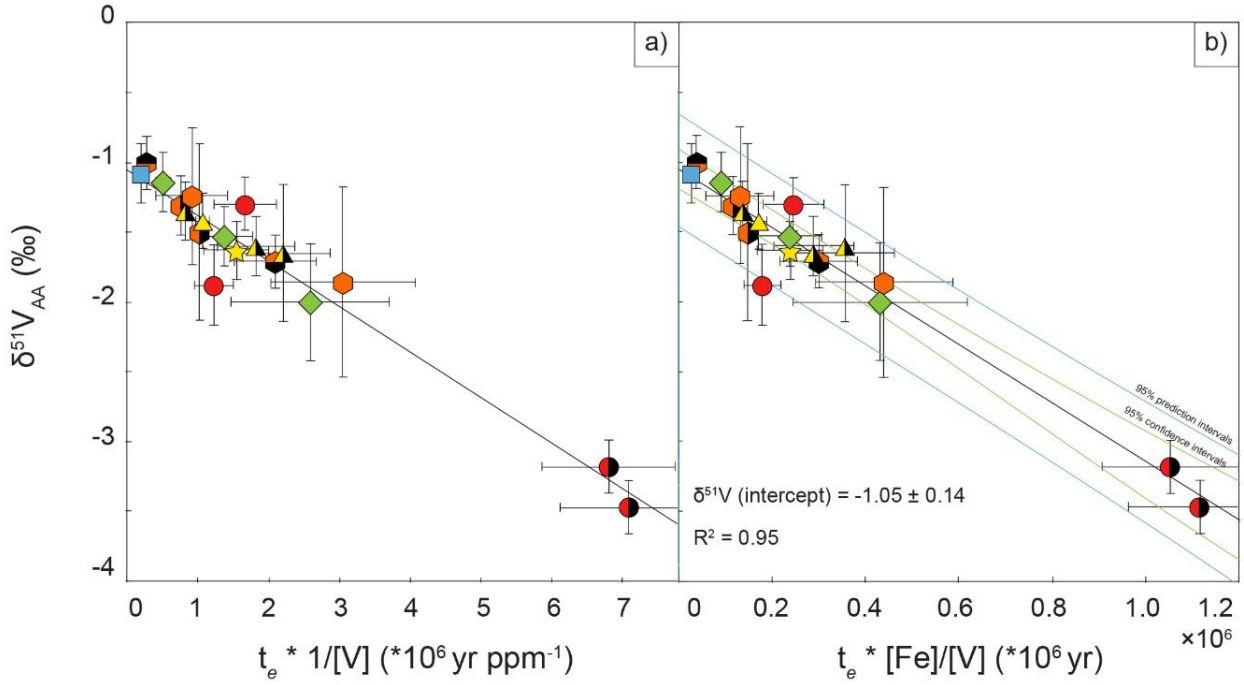


Figure 4.8: *Sample $\delta^{51}V$ versus $t_e \times 1/[V]$ and $t_e \times [Fe]/[V]$. Strong correlations between $\delta^{51}V$ and $t_e \times 1/[V]$ (**a**) indicate that the important targets for isotopic effects are relatively invariant in abundance in the samples. The most likely target element of importance is Fe (**b**) due to its high-concentration within the samples, relative invariance in concentration, high cross-sections (especially > 50 MeV) and negative $\varepsilon^{51}\sigma$ deviations (where cosmogenic reactions will shift $\delta^{51}V$ to lighter values). Correlations between $\delta^{51}V$ and $t_e \times 1/[V]$ and $t_e \times [Fe]/[V]$ are stronger than those for Ti, Cr and Mn (**Figure S6**). The fact that most samples fall on the same trendline indicates that pre-irradiation $\delta^{51}V$ variation is restricted, despite highly-variable magmatic histories. A linear regression ($R^2 = 0.95$) is calculated to intercept at $\delta^{51}V = -1.05 \pm 0.14$ (95% confidence intervals). Samples with only literature chemical compositions available (**Table 1**) or estimated exposure ages (12054-13, 12054-146, 12054-150, 70215-389, 71546-22) were excluded from regression calculations, but included in the calculation of R^2 (excluding literature samples: slope = -2.0911, intercept = -1.054, R^2 = 0.9500; including all samples: slope = -2.0915, intercept = -1.043, R^2 = 0.9477). Symbols same as **Figure 4.2, 4.3, 4.4, 4.5**.*

4.4.9 Pre-irradiation compositions and implications for the Solar System

A linear regression is calculated on the data in **Figure 4.8b** yielding a slope of -2.091×10^{-6}, and a y-intercept of -1.05 (R^2 = 0.95). Samples with less-reliable exposure ages (12054, 71546, **Appendix 2d**) or where only literature chemical data exists (12054-13, 70215, 71546) were excluded from this calculation, but their inclusion only slightly affects the resulting regression (slope = -2.092×10^{-6}, R^2 = 0.95). The coincidence of high-Ti and low-Ti basalts upon the same regression line indicates that, despite different mantle sources and magmatic histories, high-Ti and low-Ti basalts have similar pre-exposure $\delta^{51}V$. The two samples with the shortest exposure age (14053-305, 74275-355) have similar $\delta^{51}V$ values despite their significant geochemical differences. Exclusion of the unusually-light sample, 10017, (**Section 4.4.3**) results in a similar regression with slope -1.989×10^{-6} and intercept -1.06. Thus, the $\delta^{51}V$ range across all samples can largely be attributed to cosmogenic processes post-crystallisation. The intercept of **Figure 4.8b** defines the pre-irradiation average $\delta^{51}V$ for the suite. Pre-irradiation lunar basalt composition is estimated to be $\delta^{51}V_{AA}$ = -1.05 ± 0.14‰ (95% CI). Although fractionation during partial melting cannot be excluded, and so an estimate of the bulk lunar mantle $\delta^{51}V$ cannot be confidently made, the convergence of high-Ti and low-Ti suites suggests $\delta^{51}V$ may be relatively uniform in the basalt source regions.

Recent work by Nielsen et al., (2019) and Xue et al., (2018) using higher-resolution MC-ICPMS shows chondrites to have a restricted range in isotopic compositions (**Section 4.1.4**). For chondrites with published noble gas data, cosmogenic exposure ages (using Ne isotopes following Scherer et al., 1998, **Appendix 2f**) vary between 0.3 and 33.1 Ma. This is shorter than most of the lunar basalts in this study. Plotting meteorite sample $\delta^{51}V$ against t_e*[Fe]/[V] shows meteorites to lie on the same trend as lunar samples (within analytical error, **Figure 4.9**). Linear regression shows meteorites to intercept at $\delta^{51}V_{AA}$ = -1.06 ± 0.06‰ (95% CI). Thus, it

appears that recent cosmogenic exposure can explain $\delta^{51}V$ variations in chondrites in Nielsen et al., (2019). This is not related to differential incorporation of irradiated components (e.g. CAIs), but to irradiation processes operating after the breakup of meteorite parent bodies. The $\delta^{51}V$ variability seen in chondrites is unlikely to be related to nucleosynthetic heterogeneities: ordinary chondrites show $\varepsilon^{54}Cr$ deficits relative to carbonaceous chondrites (Qin et al., 2010), but variable $\delta^{51}V$ (Nielsen et al., 2019; Xue et al., 2018). In summary, not only do lunar samples and chondrites show small pre-irradiation $\delta^{51}V$ variability within their own suites, but the Moon and chondrites have similar pre-irradiation values.

Early studies of V isotope ratios in geological materials (prior to the development of MC-ICPMS) were hindered by relatively poor analytical precision, but studies of iron meteorites (e.g. Stauffer and Honda, 1961) reported samples with remarkable $^{51}V/^{50}V$ ratios (ranging from ~ 5 to 150). In light of the relationship between $\delta^{51}V$ and t_e*[Fe]/[V] seen in lunar samples and chondrites, and the apparent importance of Fe as a target element, these extreme ratios appear to be in accordance with the chemical compositions of iron meteorites where [V] typically is <1ppm.

The pre-irradiation $\delta^{51}V$ calculated for the Moon ($\delta^{51}V_{AA}$ = -1.05 ± 0.14‰, 95% CI) is in accordance with the value obtained for chondrites ($\delta^{51}V_{AA}$ = -1.06 ± 0.06‰, 95% CI) and Mars ($\delta^{51}V_{AA}$ = -1.05 ± 0.20‰, 2SD, Davis et al., 2018). These values are similar to the composition of BSE ($\delta^{51}V_{AA}$ = -0.7 ± 0.2‰) from Prytulak et al. (2013) and largely overlap with a more recent estimate from Qi et al. (2018) ($\delta^{51}V_{AA}$ = -0.91 ± 0.05, 2SD, **Figure 4.9**). In contrast to initial studies (Nielsen et al., 2014) it appears that the $\delta^{51}V$ of planetary bodies (Earth, Moon, Mars) and chondrites are remarkably similar.

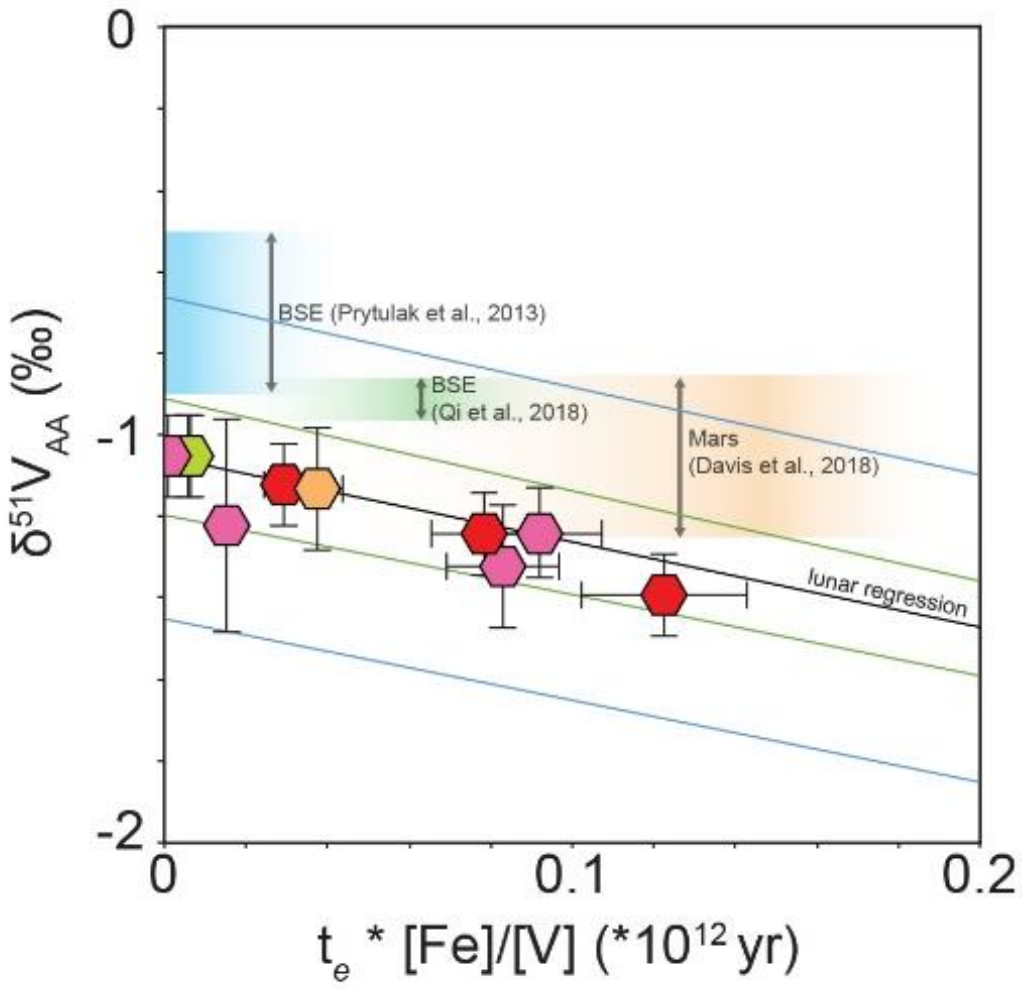


Figure 4.9: Chondrite $\delta^{51}V$ versus $t_e \times$ [Fe]/[V]. Samples with available exposure age, chemical and $\delta^{51}V$ data (from Nielsen et al., 2019) fall on the linear regression calculated for lunar samples (within analytical error, **Figure 4.8b**), strongly suggesting the variation observed in recent chondrite data (Nielsen et al., 2019; Xue et al., 2018) is also due to irradiation of samples. Pre-irradiation values overlap with estimates for the BSE (Prytulak et al., 2013; Qi et al., 2018) and Mars (Davis et al., 2018) suggesting that $\delta^{51}V$ is relatively uniform between planetary and chondrite parent bodies measured thus far. Symbols as in **Figure 4.1** (carbonaceous chondrites: pink; ordinary chondrites: red; enstatite chondrite: green; Rumuruti-chondrite: yellow). Data displayed in **Appendix 2f**.

4.5 Conclusions

1) Vanadium is more compatible during melting, and has higher partition coefficients in crystallising mineral phases, on the Moon compared to the Earth. Therefore, multiple phases can host V in significant quantities during lunar fractional crystallisation.
2) There is no correlation between sample $\delta^{51}V$ and mineralogy or chemical composition. High-Ti (excluding 10017) and low-Ti basalts span a similar range in $\delta^{51}V$. Lunar basalts are mostly isotopically lighter than terrestrial basalts, but also show a high degree of variability, spanning a range equal to the most extreme products of magmatic differentiation processes on Earth (Prytulak et al., 2017).
3) Terrestrial crystallisation of (Fe,Ti)oxides strongly fractionates V isotopes, but despite large variations in oxide content in the lunar suite, there is little evidence for oxide crystallisation controlling $\delta^{51}V$. Recent experiments demonstrate $\Delta^{51}V_{magnetite\text{-}melt}$ decreases with progressively reducing conditions (Sossi et al., 2018). Thus, it is possible that reduced lunar fO_2 could render $\Delta^{51}V_{oxide\text{-}melt}$ analytically-insignificant.
4) Vanadium isotopes correlate with exposure age and neutron-sensitive Gd isotopes, with longer-exposed samples having lighter $\delta^{51}V$ (**Figure 4.4**). Calculations of reaction cross-sections protons, alpha-particles and neutrons indicate that Ti and Fe are most important potential targets for cosmogenic alteration of $\delta^{51}V$. However, neutron-capture alone cannot drive the isotopic variability observed.
5) The correlation observed between $\delta^{51}V$ and t_e*[Fe]/[V] suggests Fe is the primary target element of importance for cosmogenic V isotope effects, and similar pre-exposure $\delta^{51}V$ for high-Ti and low-Ti basalts ($\delta^{51}V_{AA}$ = -1.05 ± 0.14‰, 95% CI, **Figure 4.8b**). The similarity in V isotope ratios between lunar basalts and the BSE adds further weight to the growing body of evidence that the Moon is the Earth's isotopic twin.

6) The co-linearity of the lunar and meteorite correlations for V isotopes versus t_e*[Fe]/[V] implicates cosmogenic effects as the dominant cause of solar system V isotope variability. There is no longer evidence for a significant difference between the BSE and other reservoirs.
7) The magnitude of cosmogenic isotope effects seen in vanadium isotope ratios is much larger than those seen in Cr and Ti isotopes. Vanadium isotopes therefore have the potential to be a useful proxy for recording exposure histories in extra-terrestrial materials.

5

Combined zinc, chlorine, and sulphur isotopes and volatile element mass transfer on the Moon

Preceding statement:

This chapter presents zinc, chlorine, and sulphur isotopic data that has not previously been published. Except where noted, all zinc isotope measurements were made by Sean Hopkins at the University of Oxford. New chlorine isotope data were obtained by Zachary Sharp and Anthony Gargano at the University of New Mexico (UNM). New sulphur isotope data were obtained by James Farquhar and James Dottin III at the University of Maryland (UMD).

5.1 Introduction

5.1.1 Volatile elements in the Moon

The Moon is depleted in volatile and moderately volatile elements (i.e. elements with $T_{c\text{-}50\%}$ < 1135K at $<10^{-4}$ atm; Lodders, 2003) relative to the Earth and chondrites (Ringwood, 1986). However, the magnitude and origin of this volatile element depletion remains highly contested. Estimates of lunar composition are complicated by the limitations to our understanding of the subsequent behaviour of volatile elements during lunar core formation, magma ocean (LMO) differentiation, basalt melting and differentiation, and interactions with the solar wind, cosmic rays, as well as meteorites impacting the lunar surface. Isotopes of volatile and moderately volatile elements (MVEs) offer the opportunity to explore the behaviour of these elements during Moon formation and subsequent magmatic processes.

Early studies of potassium (K) isotopes in lunar samples failed to identify the large (> 1‰) isotopic BSE-Moon offsets in MVEs predicted from giant impact models of lunar formation (Humayan and Clayton, 1995). However, more recent studies have resolved isotopic variations in lunar samples and these have been attributed in part to a difference between the BSE and bulk Moon composition. Such a difference has been proposed for Zn (Moynier et al., 2006; Herzog et al., 2009; Paniello et al., 2012; Kato et al., 2015), K (Wang and Jacobsen, 2016), Ga (Kato and Moynier, 2017), Rb (Pringle et al., 2017), and Cl (Barnes et al., 2019, 2016, Boyce et al., 2018, 2015; Potts et al., 2018). These isotopic fractionations have been ascribed to the giant impact, lunar magma ocean degassing, or more local degassing or sputtering processes – often with distinct explanations for different isotopic systems. Within the suite of lunar samples, there are significant variations in the isotopic compositions of Zn, K, Ga, Rb, and Cl, depending upon the lithologies of the samples analysed with mare basalt compositions generally being taken as the closest analogues for the bulk lunar composition. This study

presents the first combined Zn, Cl, and S isotope measurements on a suite of lunar mare basalts to pin down the origin of isotopic-variability within these systems and provide a better estimate of bulk lunar composition.

5.1.2 Zinc isotopes

Zinc is a moderately-volatile ($T_{c\text{-}50\%}$ = 726K at $<10^{-4}$ atm; Lodders, 2003) element which exhibits lithophile and slightly siderophile characteristics. Zinc has five naturally-occurring stable isotopes: ^{64}Zn (49.2%), ^{66}Zn (27.8%), ^{67}Zn (4.0%), ^{68}Zn (18.4%) and ^{70}Zn (0.6%). Techniques for the high-precision isotopic measurements of Zn isotope ratios were first published by Maréchal et al. (1999) and a multitude of studies have expanded these initial investigations to a number of fields: oceanography, igneous petrology, palaeoclimate research, medical sciences, and cosmochemistry (Moynier et al., 2017). Zinc isotope ratios are typically reported in per mil notation as the ratio of ^{66}Zn/^{64}Zn relative to the "*JMC-Lyon"* standard described by Maréchal et al. (1999):

$$\delta^{66}Zn_{JMC-Lyon} = \left(\frac{(^{66}Zn/^{64}Zn)_{sample}}{(^{66}Zn/^{64}Zn)_{JMC-Lyon}} - 1\right) * 1000$$

Zinc Isotopes on Earth

Only a handful of studies have been applied to the partitioning behaviour of Zn (and δ^{66}Zn) fractionation during igneous processes. Le Roux et al., (2011) identified that the similarity in ionic radii between Fe^{2+} and Zn^{2+} leads to MORB with Fe/Zn ratios identical to those of the parental magmas. Davis et al., (2013) experimentally determined partition coefficients for Zn during partial melting of peridotite at 3GPa ($D_{(olivine\text{-}melt)}$ ~ 0.96, $D_{(opx\text{-}melt)}$ ~ 0.45, $D_{(cpx\text{-}melt)}$ ~ 0.33, $D_{(grt\text{-}melt)}$ ~ 0.21, $D_{(spl\text{-}melt)}$ ~ 5.2). Compared to meteorites (**5.1.2.2**, **5.1.2.3**), terrestrial igneous rocks show remarkably little variation in δ^{66}Zn. Chen et al., (2013) identified ranges of ~ 0.1‰ in two lava suites (Kilauea Iki: +0.26‰ < δ^{66}Zn < +0.36‰, and Hekla: +0.22‰ < δ^{66}Zn < +0.32‰), although only Kilauea Iki samples display evidence of δ^{66}Zn correlation with

tracers of magmatic differentiation (e.g. SiO_2, MgO). The crystallisation of light-Zn olivine, or (Fe,Ti) oxides at the end of differentiation, is thought to drive the increase in $\delta^{66}Zn$. Measurements of ultramafic rocks (komatiites and peridotites) extend the relationship between $\delta^{66}Zn$ and MgO further and underpin the most recent estimate of BSE ($\delta^{66}Zn = +0.16 \pm 0.06$‰, Sossi et al., 2018). Telus et al. (2012) reported $\delta^{66}Zn$ in granitoid samples to lie within the range of mafic rocks. Pegmatitic and migmatitic samples show $\delta^{66}Zn$ up to ~ 0.88‰ and are thought to have undergone fluid exsolution, whereby light Zn isotopes are preferentially stripped and residual magmas are enriched in heavier isotopes. Subducted Alpine serpentinites display $\delta^{66}Zn$ values which correlate with S contents (Pons et al., 2016). During prograde metamorphism, oxidised, sulphate rich fluids are released from down-going slab serpentinites and heavy Zn isotopes are preferentially-incorporated into sulphate complexes. Core formation is thought unlikely to fractionate $\delta^{66}Zn$ significantly as Bridgestock et al., (2014) reported no isotopic effect associated with metal-silicate equilibration. Thus, the bulk Earth is similar to the BSE in $\delta^{66}Zn$ and is similar to that of carbonaceous chondrites, EH-chondrites and unequilibrated ordinary chondrites.

Zinc Isotopes in Chondrites

Carbonaceous chondrites (CCs) exhibit a range of $\delta^{66}Zn$ values from +0.16‰ to +0.52‰ (Luck et al., 2005; Barrat et al., 2012). Thus, CCs lie greater than or equal to the $\delta^{66}Zn$ of the BSE (+0.16 ± 0.06‰, Sossi et al., 2018). CI chondrites exhibit the heaviest $\delta^{66}Zn = +0.46 \pm 0.08$‰ (Barrat et al., 2012). There is a negative trend between $\delta^{66}Zn$ and Mg/Zn for CCs which indicates that the isotopic variability shown is nebular (rather than evaporative) in origin.

Ordinary chondrites (OCs) define a larger range in isotopic compositions (-1.30‰ < $\delta^{66}Zn$ < 0.76‰) than CCs. The range in isotopic values has been attributed to parent body metamorphism and/or secondary aqueous alteration on the Earth's surface. When only fall-

witnessed OCs are considered, the range is restricted to ~ -0.48‰ < δ^{66}Zn < +0.55‰ (Luck et al., 2005). Differences between groups (H, L, LL) are not clear.

Enstatite chondrites (ECs) of low metamorphic grade have similar Zn isotope compositions to the Earth (+0.15‰ < δ^{66}Zn < +0.31‰). However, EL6-type meteorites (i.e. those having undergone significant thermal metamorphism) display strong enrichments in heavy Zn isotopes (δ^{66}Zn < + 7.35‰, Moynier et al., 2011), along with accompanying depletions in [Zn] and other MVEs. These characteristics have been explained as evidence of volatilisation during thermal metamorphism.

Zinc Isotopes in Achondrites

Moynier et al., (2011) measured multiple aubrites and found them to be depleted in Zn (relative to ECs) and to display light Zn isotope compositions (-7.08‰ < δ^{66}Zn < -0.37). This is the opposite to what would be expected if Zn depletion in aubrites was due to volatilisation. An isotopically-light mobile phase may have contaminated aubrites (perhaps derived from vapour lost during thermal metamorphism of EL6-type ECs). One aubrite, Shallowater (the only "find" aubrite in this study), displays isotopically-heavy compositions (+1.48‰ < δ^{66}Zn < +2.36‰).

Ureilites with varying degrees of shock processes show Zn isotopic compositions which almost all lie between +0.17‰ and +1.26‰ (with one highly-shocked sample having a composition of δ^{66}Zn = +2.71‰, Moynier et al., 2010; Brugier et al., 2019). Moynier et al., 2010 found a striking positive correlation between δ^{66}Zn and 1/Zn and argued for an evaporative control of δ^{66}Zn in ureilites, although this strong relationship was not reproduced in Brugier et al., (2019). Nevertheless, evaporative fractionation of varying degrees is the best explanation for the range in δ^{66}Zn seen across all ureilite samples, and samples with higher shock-states have heavier δ^{66}Zn, potentially implicating an impact as the trigger for such an episode.

The Howardite, Eucrite and Diogenite (HED) meteorites display a large range in Zn isotope compositions, with a significant difference observed between non-Antarctic HEDs (range -2‰ < δ^{66}Zn < +1.67‰, *n = 20,* Paniello et al., 2012b) and Antarctic (and unbrecciated) HEDs (range +0.94‰ < δ^{66}Zn < +6.29‰, *n = 7*). A complex history for HED samples is presented by Paniello et al., (2012b) with unbrecciated samples achieving heavy Zn isotope enrichment during evaporation of volatile from the Vestan crust. Impact gardening of the Vestan surface, and associated admixture of chondritic Zn (with lighter Zn isotopic compositions) is invoked to explain the lighter δ^{66}Zn of brecciated HEDs.

Iron meteorites show a significant range in Zn isotope variation between groups (Luck et al., 2005; Chen et al., 2013; Bridgestock et al., 2014). Luck et al., (2005) reported δ^{66}Zn values for groups IA (+ 0.78‰ < δ^{66}Zn < +3.68‰), IIICD (+1.42‰ < δ^{66}Zn < 2.03‰), and IIIA (-0.59‰ < δ^{66}Zn < -0.50‰). Bridgestock et al., (2014) measured meteorites from the IAB, IIAB, and IIIAB groups and reported within-group correlations between δ^{66}Zn and 1/Zn. This was explained by chromite crystallisation (which would incorporate light δ^{66}Zn) and segregation from the metal. Chen et al., (2013) measured IAB, IIC, IID, IIE, IIF, IIIAB, IIIE, IIIF, IVA ungrouped meteorites (range -0.1‰ < δ^{66}Zn < +5.61‰) and proposed evaporation of light Zn as a mechanism to produce isotopically-heavy iron compositions.

Zinc Isotopes on the Moon

Zinc is more isotopically-variable in lunar samples than for all other planetary materials analysed to date, spanning a range in δ^{66}Zn ["Rusty Rock" 66095: δ^{66}Zn = -13.6‰, to lunar soil 15231: δ^{66}Zn = +6.39‰] greater than that seen across all samples in the solar system (Moynier et al., 2006; Herzog et al., 2009; Paniello et al., 2012; Day & Moynier, 2014; Kato et al., 2015; Day et al., 2017, **Figure 1, 2**). Most lunar mare basalts show δ^{66}Zn values between +1 to +2‰, and Zn concentrations between 1-2 ppm. However, some lunar basalts are

isotopically-lighter than the Earth ($\delta^{66}Zn < \sim 0.16 \pm 0.06‰$, **Figure 3**) and it has been proposed that these samples achieved their light-isotopic compositions following later eruptive or impact events, which vaporised and precipitated light Zn (as $ZnCl_2$) onto the exteriors of these samples (Day and Moynier, 2014; Kato et al., 2015; Paniello et al., 2012). As such, these light basalts have previously been excluded from consideration when reporting the Zn isotope composition of the bulk Moon (typically reported as $\delta^{66}Zn$ between +1 to +2‰). However, the origin of this light Zn vapour and the mechanism behind such isotopic alteration is poorly constrained. The Zn isotopic composition of heavy lunar basalts has been used to argue for a Moon depleted in isotopically-light Zn and volatile elements in general (Paniello et al., 2012). Light Zn has been proposed to have been lost from the proto-lunar disk following giant impact, from the lunar-magma ocean, or from regional or local degassing events (Day and Moynier, 2014; Herzog et al., 2009; Kato et al., 2015; Paniello et al., 2012).

Lunar soils are enriched in Zn (13 – 33 ppm, Moynier et al., 2006; Kato et al., 2015) and heavy Zn isotopes ($\delta^{66}Zn$ +2.18‰ to +6.39‰, Moynier et al., 2006). This is also observed in the isotopes of other elements (e.g. S, Ding et al., 1983; Kerridge et al., 1975a, 1975b, Thode and Rees, 1979, 1976) and is thought to reflect preferential loss to space of isotopically-light material through sputtering and/or meteorite impact processes (Haskin & Warren, 1991). Lunar pyroclastic glass beads show surface-correlated enrichments between 1/[Zn] and $\delta^{66}Zn$ (Moynier et al., 2006; Herzog et al., 2009; Kato et al., 2015), which has been used to argue for the presence of isotopically-light vapours at the lunar surface. Ferroan anorthosites show a correlation between $\delta^{66}Zn$ and 1/[Zn], with a range in $\delta^{66}Zn$ between -11.37‰ – 4.24‰. During cataclasis and brecciation, infiltration of isotopically-light vapour may have altered the primary, Zn-depleted compositions of these samples (Kato et al., 2015).

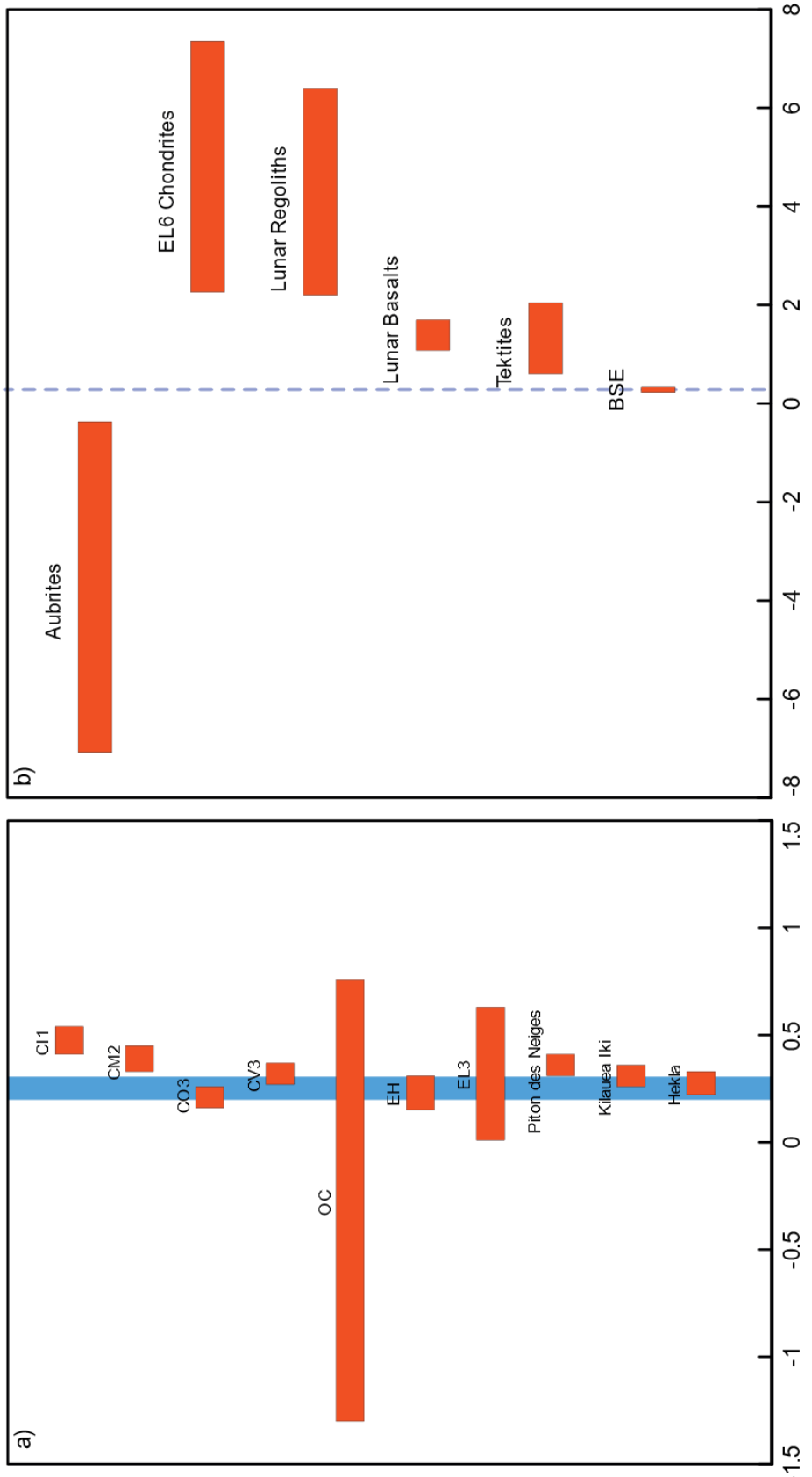


Figure 5.1 – *Summary of zinc isotope data for terrestrial and extraterrestrial objects as displayed in Chen et al. (2013).* ***1a)*** *displays the terrestrial range of basaltic materials from Hekla, Kilauea Iki, and Piton des Neiges, alongside δ^{66}Zn data for carbonaceous, ordinary, and EH enstatite chondrites.* ***1b)*** *displays the most extreme δ^{66}Zn fractionated solar system material. Note that the lunar basalt range here excludes isotopically-light basalts. To see all lunar δ^{66}Zn data, see* ***Figure 5.2****. The blue line denotes the BSE composition from Chen et al. (2013) (δ^{66}Zn = +0.28± 0.05‰). Data from Luck et al. (2005), Chen et al. (2013), Barrat et al. (2012), Moynier et al. (2006, 2009, 2011), Herzog et al. (2009), Paniello et al. (2012).*

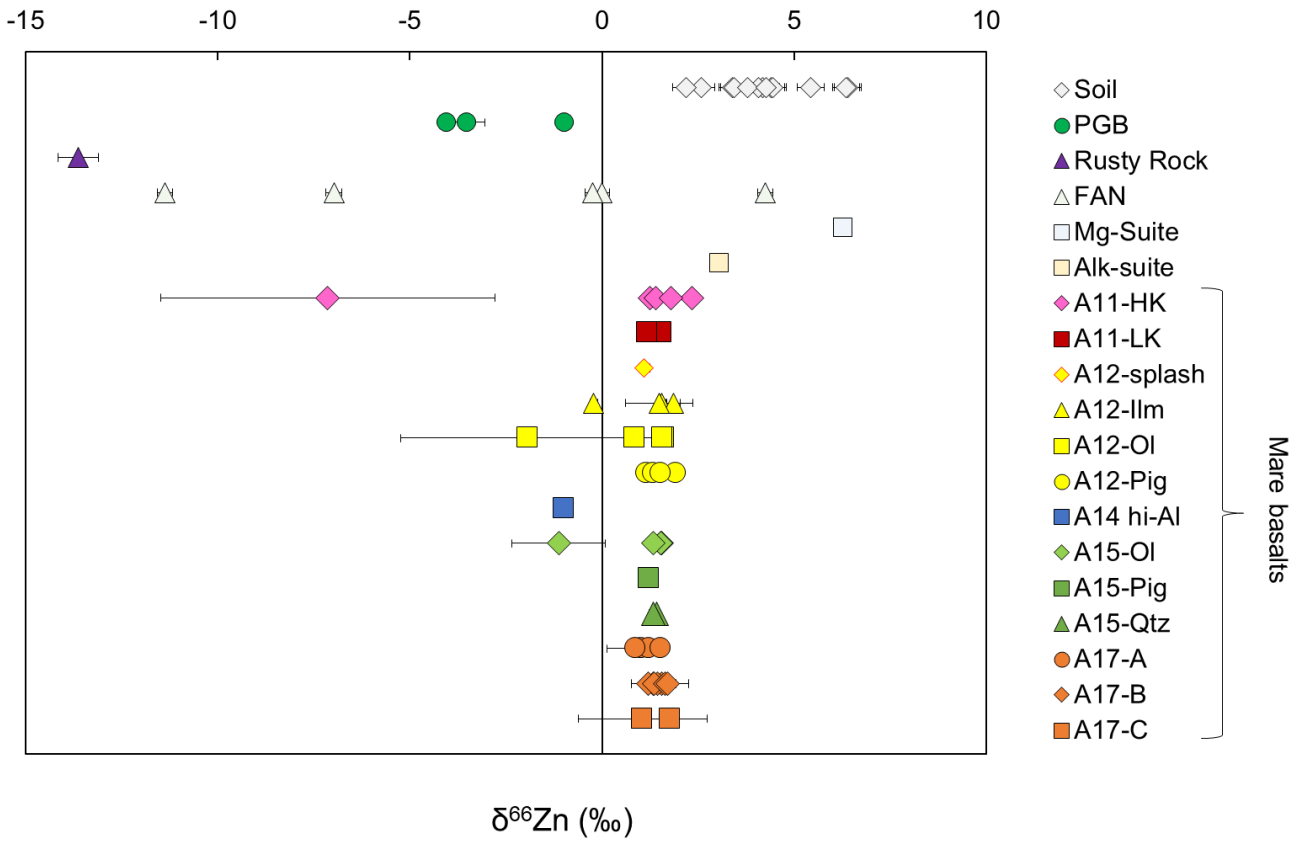


Figure 5.2 – *Compilation of all lunar sample δ^{66}Zn data to date. Error bars represent either the reported 2SD on measurements, or the 2SD of repeat measurements between studies (whichever is larger). Lunar basalts largely lie between +1 to +2‰, but there are a few samples which have isotopic values lighter than that of the Earth. The Moon records the widest range in δ^{66}Zn in the Solar System. Data is compiled from Day et al., 2017; Herzog et al., 2009; Kato et al., 2015; Moynier et al., 2006; Paniello et al., 2012, Hopkins et al. (Masters thesis) and this study.*

5.1.3 Chlorine Isotopes

Chlorine has two stable naturally-occurring isotopes: ^{35}Cl (75.76%) and ^{37}Cl (24.24%, Berglund and Wieser, 2011). Isotopes of Cl are reported in per mil relative to Standard Mean Ocean Chloride (SMOC).

$$\delta^{37}Cl_{SMOC} = \left(\frac{(^{37}Cl/^{35}Cl)_{sample}}{(^{37}Cl/^{35}Cl)_{SMOC}} - 1\right) * 1000$$

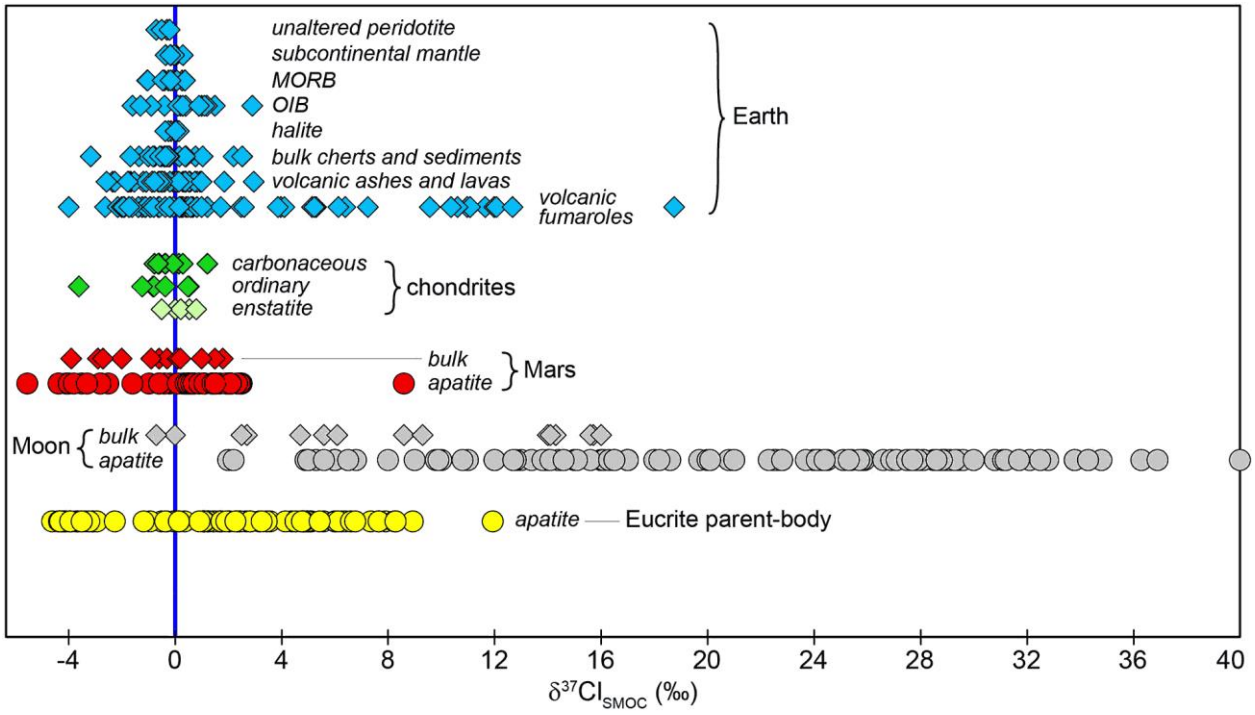


Figure 5.3 *Compilation of all $\delta^{37}Cl$ data for terrestrial and extra-terrestrial reservoirs from Tartese et al. (2019). Diamonds represent bulk analyses and circles represent apatite measurements. Original data from* (Barnes et al., 2009, 2016; Bellucci et al., 2017; Boyce et al., 2015; John et al., 2010; Potts et al., 2018; Sarafian et al., 2017; Selverstone and Sharp, 2011; Sharp et al., 2016, 2007; Z D Sharp et al., 2010; Z.D. Sharp et al., 2010a; Z. D. Sharp et al., 2013; Tartèse et al., 2014)

Terrestrial systems generally show a range in $\delta^{37}Cl$ from ~ -2‰ to +2‰, owing to relatively small equilibrium fractionation factors. However, in systems where kinetic fractionation mechanisms exist (e.g. volcanic fumeroles) $\delta^{37}Cl$ variation can be much larger (**Figure 5.3**). Mid-ocean ridge basalt (MORB) and sub-continental mantle samples average ~ -0.2-0.3‰ (Sharp et al., 2007), which is indistinguishable from the chondritic value ($\delta^{37}Cl$ ~ -0.3 ± 0.3‰, Sharp et al., 2013). However, some studies suggest that mantle heterogeneities exist, with in-situ $\delta^{37}Cl$ measurements of glasses spanning a range of compositions from -1.6 to +2.9‰ (John et al., 2010).

Chondrites show a range in $\delta^{37}Cl$ from -4 to +1‰, with most chondrites showing a negative correlation between $\delta^{37}Cl$ and degree of aqueous alternation (Sharp et al., 2013). Unaltered chondrite and BSE $\delta^{37}Cl$ likely represent an unmodified, nebular Cl composition. Martian

meteorites span a range between -3.9‰ and +1.8‰ with the lightest samples representing a martian mantle, and heaviest samples representing the martian crust (Sharp et al., 2016). For a thorough review of Cl isotopic variations in geological materials and meteorites, see Barnes and Sharp, (2017).

Chlorine isotope measurements have also been made in lunar rocks. Sharp et al., (2010) made bulk analyses of water-soluble chlorine (WSC), and structurally-bound chlorine (SBC) isotope ratios and in-situ apatite $\delta^{37}Cl$ measurements in a suite of lunar basalts, soils, and glasses. Enrichments in $\delta^{37}Cl$ and the large isotopic range recorded were explained by degassing of lunar rocks in an H-poor environment. Under such a regime, Cl in melts will degas primarily as metal-chloride species (e.g. $FeCl_2$, $GaCl_x$). However, bulk measurements of $\delta^{37}Cl$ in lunar rocks are limited to this study. Subsequent studies of $\delta^{37}Cl$ in lunar rocks focusing on the compositions of apatite grains within lunar rocks (Barnes et al., 2019, 2016, Boyce et al., 2018, 2015; Potts et al., 2018). Apatite (ideally, $Ca_5(PO_4)_3(F,Cl,OH)$) is the most common mineral in lunar rocks which bears large concentrations of volatile elements, including, Cl. Apatite is a trace mineral within lunar rocks, but occurs in most samples analysed, and incorporates varying amounts of F, OH, and Cl as essential structural components. Apatite is generally enriched in isotopically-heavy Cl ($\leq$ +80‰, Wang et al., 2012) and $\delta^{37}Cl$ correlated with concentrations of Th and La/Lu ratios. This has been used to argue for an isotopically-distinct lunar reservoir enriched in ITEs and REEs (urKREEP), which underwent Cl isotope fractionation during degassing and loss of isotopically-light Cl to space – perhaps during a large crust-breaching impact (Barnes et al., 2016). However, recent analyses of lunar meteorite samples (which originated on the far side of the Moon) show isotopically-heavy Cl isotope ratios but are geographically- and temporally-isolated from the urKREEP reservoir (Barnes et al., 2019). One meteorite sample shows high $\delta^{37}Cl$ in apatites, but low ITE concentrations, indicating that earlier models of a two-reservoir lunar system (one characterised by high [Cl], high ITE

concentrations and elevated $\delta^{37}Cl$; one characterised by low [Cl], mantle ITE concentrations, and $\delta^{37}Cl \sim 0‰$) may be overly-simplistic.

5.1.4 Sulphur isotopes:

Sulphur has four naturally-occurring stable isotopes: ^{32}S (95.02%), ^{33}S (0.75%), ^{34}S (4.21%), ^{36}S (0.02%). Sulphur isotope variations are reported relative to that of Canyon Diablo meteorite troilite inclusions (CDT):

$$\delta^{34}S_{CDT} = \left(\frac{(^{34}S/^{32}S)_{sample}}{(^{34}S/^{32}S)_{CDT}} - 1\right) * 1000$$

A figure summarising the published variation shown in lunar samples is presented in **Figure 5.4**. It can be seen that, unlike the wide variability exhibited by S in breccias, soils and sulphides, the composition in basalts is very limited. Recent work by Wing and Farquhar, (2015) confirms this with $\delta^{34}S$ = +0.58‰ ± 0.05. Soils are enriched in $\delta^{34}S$ and it has been proposed by Kerridge et al., (1975a, 1975b) that this reflects addition of meteoritic sulphur and fractionation during sputtering (and loss of isotopically-light S).

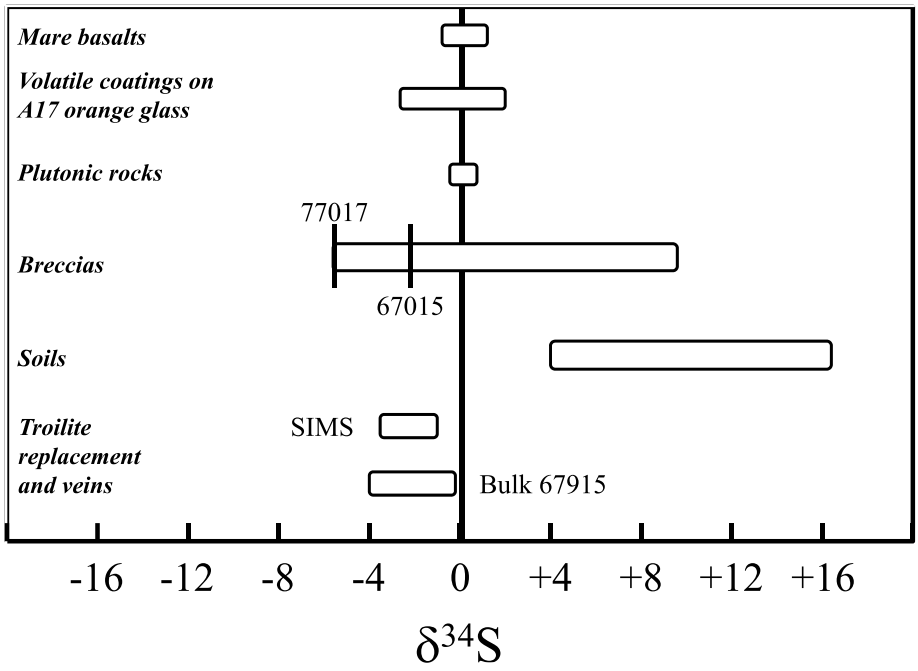


Figure 5.4 – *Variations in $\delta^{34}S_{CDT}$ in lunar lithologies (from Shearer et al. 2012). Data from* (Chanq et al., 1974; Ding et al., 1983; Haskin and Warren, 1991; Kerridge et al., 1975a, 1975b)

5.2 Methods

Full description of sample selection, preparation, digestion, and trace element analysis are provided in Chapter 2 "Methods", as these procedures are the same for both Zn (this chapter) and V isotope analysis (Chapters 3 & 4). The justification for the sample selection with respect to investigating Zn isotope fractionation on the Moon is laid out below. A summary of the techniques for Zn isotope, Cl isotope, and S isotope analyses follow this.

5.2.1 Sample selection and preparation

Nineteen lunar basalt aliquots were requested from NASA for combined Zn, V, and trace element analyses (**Chapter 2, Table 2.1**) to allow internally-consistent comparison of Zn isotopes and elemental concentrations. Partnering chips were requested for Cl and S isotope analyses to investigate the behaviour of isotopes of Zn, Cl, and S within the same samples. Due to the risk of contamination or loss of material during the sample preparation procedures in Oxford, it was considered unwise to perform the sample preparation for Zn, Cl, and S on the same rock chips. Thus, neighbouring chips from the same locations within parent samples were chosen and sent directly to teams at the University of New Mexico (UNM, for Cl isotope analyses) and the University of Maryland (UMD, for S isotope analyses).

Both high-Ti (TiO_2 > 6 wt%, Neal and Taylor, 1992) and low-Ti samples (1.5 wt% < TiO_2 < 6 wt%) were selected, spanning a range in TiO_2 contents from 2.2 wt% (15535,165) to 12.9 wt% (70215,389). Sample 10017 is a Type-A Apollo 11 (high-K, high-Ti) basalt and is enriched in K, REEs, and other incompatible trace elements (Neal and Taylor, 1992). Sample 14053 is a High-Al/low-K Apollo 14 basalt. Samples were obtained from the interiors (typical depth <5cm) of their host rocks and thus should be shielded from the lunar atmosphere. In addition, exterior aliquots (i.e. with a portion having been exposed to the lunar atmosphere) were taken of samples 10017 and 12054. A sampling of a glass splash emplaced on the surface of 12054

(originating either as ejecta from a nearby impact or vigorous eruption) was also sampled (which is of almost identical composition, Hartung et al., 1978). Samples 15016 and 15556 were chosen as highly vesicular (up to 50% by volume) Apollo 15 olivine-normative basalts. Sample 15016 has been previously analysed and reported to have light δ^{66}Zn (-1.47 ± 0.11‰, Kato et al., 2015). When this study was conceived (2014), five of the samples in the sample set had been previously studied for their Zn isotope compositions (using sample-standard bracketing): 10017, 12018, 12063, 70215, 74275 (Moynier et al., 2006; Herzog et al., 2009; Paniello et al., 2012). Since then, Zn isotope data for 15016 and 14053 have been presented by Kato et al., (2015). A comparison of the data obtained from these different sample aliquots may shed light on within-sample heterogeneity for [Zn] and δ^{66}Zn.

Basaltic USGS reference materials BCR2, BHVO2 and BIR1a were analysed alongside lunar samples to ensure the accuracy of the techniques, and the robustness of the column chromatography procedures.

Sample Preparation (Oxford)

Washing and Digestion

Sample chips were transferred to metal-free centrifuge tubes and rinsed in ultrapure water (MQ H_2O) with resistivity 18.2MΩ·cm for 2 hours. Samples were then centrifuged, extracted from vials, and left to dry at 50°C for 48 hours. The washes from this stage were stored for later analysis of Zn concentrations. Samples were powdered in an agate mortar and pestle and weighed to obtain approximately 0.25µg Zn (typical sample size ~20-140 mg). Hotplate dissolution was performed using HF-HNO3 and HCl over a number of days, and visually inspected to ensure no undissolved components remained.

5.2.2 Trace Element Analysis by ICPMS (Oxford)

Full details of trace-element analysis by Quad ICP-MS can be found in Hopkins et al. (2019). Approximately 10mg of sample powder was weighed in pre-cleaned PTFE vials. Samples were dissolved using a hotplate dissolution procedure (**Chapter 2**) and visually inspected to ensure no undissolved components remained.

5.2.3 Zinc isotope measurements (Oxford)

Zinc contamination

Although Zn concentrations are reported in a number of studies for lunar mare basalts (see Meyer et al., 2008) values typically vary by an order of magnitude or more between studies using different analytical techniques. The variation in [Zn] is most likely due to contamination from non-lunar Zn sources, as Zn found in ubiquitous everyday products including most major brands of laboratory gloves. A single contact between glove and labware releases an average of ~ 6 ng Zn (δ^{66}Zn +0.10 ± 0.32‰) and thus significant care must be taken to avoid any contamination from non-lunar sources if accurate data is to be obtained (Garçon et al., 2017).

Zinc concentrations by isotope-dilution

After digestion, a small aliquot (~5%) of each sample was weighed and mixed with a weighed amount of ^{64}Zn-^{67}Zn double-spike (5.10025 $\mu g \cdot g^{-1}$, Arnold et al., 2010) before equilibration at 60°C on a hotplate for 48 hours. These fractions were then passed through an anion-exchange chromatography procedure (**Section 2.5**) adapted from Arnold et al., (2010), before analysis using MC-ICPMS to determine the precise concentrations of Zn within the dissolved samples. These concentrations were used to calculate appropriate mass-ratios of spike-solution/sample-solution. The spike-sample mixtures were passed through the column-chromatography procedure twice to purify Zn from matrix and other interfering elements. Analysis was performed using a *Nu Instruments* Plasma HR mass spectrometer. Masses 62, 64, 66, 67, 67.5,

and 68 were simultaneously measured (with 62 used for $^{64}Ni^{+}$ correction, and 67.5 for Ba^{2+} corrections). Data reduction and deconvolution was performed offline using techniques described by Siebert et al., (2001). Real time $^{64}Ni^{+}/^{64}Zn^{+}$ and $^{134}Ba^{2+}/^{67}Zn^{+}$ ratios were typically $< 1 \times 10^{-5}$. Exterior washes of the samples were found to have zinc concentrations (by measuring total Zn beam intensities) <0.2ng, thus contributing insignificantly to the bulk sample Zn compositions. Total procedural blanks were <5ng (which is small compared to total Zn from each sample ~100ng). USGS reference materials BCR2, BHVO2, and BIR1a were twice processed through chemistry and ran alongside lunar samples. Relative to JMC-Lyon, these samples returned values in agreement with the literature (Bridgestock et al., 2014; Moynier et al., 2017**, Appendix 3a**).

5.2.4 Chlorine isotopes

Chlorine isotopes were measured by Anthony Gargano and Zach Sharp at the University of New Mexico following the protocol of Sharp et al. (2013).

Sample preparation and chlorine extraction

Sample chips were thoroughly cleaned in MQ H_2O to clean the surface of contamination and dried, before crushing to a fine powder in a dry mortar and pestle. The resulting powder was sonicated and leached with MQ H_2O overnight in order to obtain the water-soluble chlorine (WSC). Residual leachates were then washed again to remove any residual WSC. The structurally-bound chlorine (SBC) was extracted from the residual sample powders using pyrohydrolysis. Samples were loaded into quartz tubing and heated to melting in a water-vapour stream, which was then condensed (Magenheim et al., 1994). The aqueous WSC and SBC fractions were reacted overnight with 10ml 50% HNO_3 to remove dissolved sulphur (Barnes et al., 2009). The $Cl^{-}_{(aq)}$ was then converted to $AgCl_{(s)}$ via reaction with 0.4 M $AgNO_3$

overnight. The precipitate was filtered, dried, and vacuum-flame sealed in 8mm diameter pyrex tubes with 10µl CH_3I (Eggenkamp, 1994).

Production of CH_3Cl and mass-spectrometry.

Samples were heated at 80°C for 48 hours to produce CH_3Cl via:

$$CH_3I + AgCl \rightleftharpoons AgI + CH_3Cl$$

Excess CH_3I is removed from CH_3Cl via gas chromatography (Barnes & Sharp, 2006) in a He stream. The resulting CH_3Cl gas was analysed using a ThermoQuest Finnigan Delta Plus XL mass spectrometer in continuous flow mode (Sharp et al., 2007). Two Faraday detectors monitor *m/z= 50* and *52* ($CH_3{}^{35}Cl^+$ and $CH_3{}^{37}Cl^+$ respectively). Samples are measured relative to standard waters (SMOC) and long term $\delta^{37}Cl$ external reproducibility is ± 0.26‰ (1σ, Barnes & Sharp, 2006).

5.2.5 Sulphur isotopes

Sulphur isotopes were measured by James Dottin III and James Farquhar at the University of Maryland, following the protocol of Antonelli et al. (2014).

Sample preparation

Lunar samples were cleaned in an ultrasonic cleaner (*VWR*) and a methanol bath, before crushing using a steel impact mortar and pestle. Samples were further crushed with an agate pestle and mortar using ~5ml of ethanol to reduce escape of dust. This slurry was transferred to the reaction vessels quantitatively.

Sulphur extraction

To minimize the risk of oxidation and loss of sulphide, samples were immediately introduced to the reaction apparatus. The remaining ethanol was allowed to evaporate under N_2. The reaction apparatus is described by Forrest and Newman (1977). Samples were heated in two-necked 50 ml boiling flasks for 3 hours in 20ml 5M HCl (through which nitrogen is continually

bubbled). Released H_2S vapour is carried through a condenser and acid trap, where the S is captured as Ag_2S (via reaction $AgNO_3$ in an $AgNO_3$–HNO_3 solution). After 3 hours of boiling in 5M HCl, chromium-reducible sulphur (CRS) was obtained by injecting a reduced Cr (II) solution into the boiling flasks (following Canfield et al., 1986). The reduced Cr solution was reacted with the sample residues for a further 3 hours. Following this, the precipitated Ag_2S was stored under dark conditions for one week to remove impurities in the crystals, before being centrifuged and rinsed with MQ water three times. Further impurities were removed from the samples via overnight treatment with 1 M NH_4OH. Samples were then rinsed three times in MQ water and dried overnight in an oven at 50°C.

Sample fluorination and mass-spectrometry

The extracted Ag_2S (~3 mg) was wrapped in clean aluminium foil and reacted with ~ 10 times the stoichiometric excess of pure F_2 in Ni-fluorination bombs at 250°C overnight. This yields SF_6 (and other fluorinated by-products). Excess fluorine and other non-condensable gases were separated from HF and SF_6 by cryogenic freezing (using liquid N_2, ~ -196°C). Samples were thawed and refrozen using an N_2-ethanol slurry (T ~ -115°C), which cryogenically traps HF but not SF_6. The SF_6 is then purified via gas chromatography (using a 12' 5Å/Hasep Q column equipped with a thermal conductivity detector). Samples were then introduced cryogenically into the cold-finger of a *ThermoFinnigan* MAT 253 dual-inlet mass spectrometer. Purified sample or standard SF_6 molecules are ionised to SF_5^+ via electron impact. Ion beams of m/z 127 ($^{32}SF_5^+$), 128 ($^{33}SF_5^+$), 129 ($^{34}SF_5^+$) and 131 ($^{36}SF_5^+$) are simultaneously monitored using multiple Faraday detectors. Each sample measurement comprises a cycle of 8 individual sample runs, each bracketed by a measurement of an in-house standard (with known S isotope composition relative to CDT). Samples were run in conjunction with International Atomic Energy Agency (IAEA) S1 standard to monitor isobaric interferences on *m/z* = 131 (typically

from $C_3F_5^+$ contamination). Results were normalised to the long-term average value of a single sample of Canyon Diablo Troilite (CDT) measured in-house at UMD.

Sulphur Isotope Errors

Steps are taken to ensure that no kinetic isotopic fractionation occurs during the extraction and preparation S from samples. Fractionation could result from the incomplete reaction of sulphides of the loss of reaction products via oxidation or leakage. The apparatus is leak-checked before use and purged with N_2 for > 30 min before introducing HCl. The reaction solutions of HCl and Cr (II) are degassed with N_2 prior to introduction to the reaction flasks to minimise the amount of trace oxygen present. Typical repeat measurements of samples yield errors on the order of $\delta^{34}S \sim 0.09‰$, $\Delta^{33}S \sim 0.008‰$, $\Delta^{36}S \sim 0.09‰$, which indicates the total extraction, purification and analysis procedure are reliable.

Long-term instrumental drift and the naturally-occurring isotopic variability in CDT places a limit on the errors, however. Because of this, samples are reported with errors based upon the long-term (> 2 years) reproducibility of the IAEA S1 reference material: $\delta^{34}S \pm 0.3‰$, $\Delta^{33}S \pm 0.008‰$, $\Delta^{36}S \pm 0.3‰$ (2s.d.).

5.3 Results

Results for Zn, Cl, and S isotope analyses are presented in **Table 5.1**. Full results, including USGS reference materials can be seen in **Appendix 3b**. Trace element concentrations from ICPMS analyses can be seen in **Appendix 1.**

Table 5.1: *Results of zinc, chlorine, and sulphur isotopic analyses for the samples in this study. Zn isotopes are reported relative to "JMC-Lyon". The Zn error is two standard deviations of the repeat measurement of the same sample aliquots, plus the adjustment for converting from London Zn to JMC-Lyon (~0.04‰). Cl is reported relative to SMOC (Standard Mean Ocean Chloride), and S is reported relative to CDT.*

	Zinc				***Chlorine***			*Structurally-bound*		*Water-soluble*		***Sulphur***			
	[Zn]	$\delta^{66}Zn_{JMC\text{-}Lyon}$	2s	n	[Cl]	$\delta^{37}Cl_{SMOC}$	1s	[Cl]	$\delta^{37}Cl_{SMOC}$	[Cl]	$\delta^{37}Cl_{SMOC}$	[S]	$\delta^{34}S_{CDT}$	$\Delta^{33}S$	$\Delta^{36}S$
	ppm	*(‰)*			*ppm*	*(‰)*		*ppm*	*(‰)*	*ppm*	*(‰)*	*ppm*	*(‰)*		
10017–400	6.7	-6.42	0.15	3								1900	0.39	-0.010	0.028
10017–405	5.5	-9.59	0.23	4	42	11.20	0.26	18	9.23	24	12.63	2500	0.93	0.013	-0.147
10020–255	1.3	1.55	0.06	3	13	n/a	n/a	n/a	n/a	13	0.39	1300	0.71	0.016	-0.119
10044–566	2.1	1.19	0.18	3	34	2.22	0.26	21	2.62	14	1.60	1100	0.81	-0.009	-0.191
12018–277	1.5	-0.76	0.06	3	16	5.09	0.26	3	5.00	13	5.03	500	0.48	0.015	0.490
12054–13	1.5	1.10	0.14	3											
12054–146	0.8	1.92	0.13	3	66	-0.07	0.26	16	2.14	50	-0.78	900	0.58	0.005	-0.056
12054–150	0.8	1.80	0.18	3	35	2.29	0.26	17	4.29	18	0.43	1000	0.47	0.001	-0.027
12063–343	0.8	1.80	0.13	2	21	2.10	0.26	9	4.19	12	0.48	900	0.69	-0.009	0.076
14053–305	1.6	-1.00	0.08	2	50	8.87	0.26	27	11.24	23	6.11	700	0.60	-0.010	-0.106
15016–240	1.0	-1.49	0.12	3	14	1.45	0.26	7	2.14	8	0.84	400	0.88	-0.008	0.020
15535–165	1.0	1.53	0.21	3								400	0.00	0.016	0.030
15556–258	0.9	1.54	0.07	3								800	0.57	0.012	-0.017
70215–389	2.1	1.46	0.09	3								1700	0.55	0.007	0.260
70255–56	1.6	1.22	0.17	4								1600	0.89	-0.005	-0.086
71135–34	1.5	1.65	0.11	4								800	0.59	-0.011	-0.035
71546–22	1.8	1.54	0.27	3								1100	0.69	-0.008	-0.066
74275–355	1.2	1.64	0.17	3								1200	0.41	0.001	0.310
75035–249	1.0	0.87	0.75	2								1600	0.37	-0.006	0.230

5.3.1 Results of isotopic analyses

The samples in this study have zinc concentrations between 0.8 (12054,146) and 6.7 ppm (10017,400), and isotope ratios between δ^{66}Zn = -9.67 ± 0.23‰ (10017,405) and +1.92 ± 0.13‰ (12054,146) (**Table 5.1**). There are examples of isotopically light basalts from all of the missions except Apollo 17.

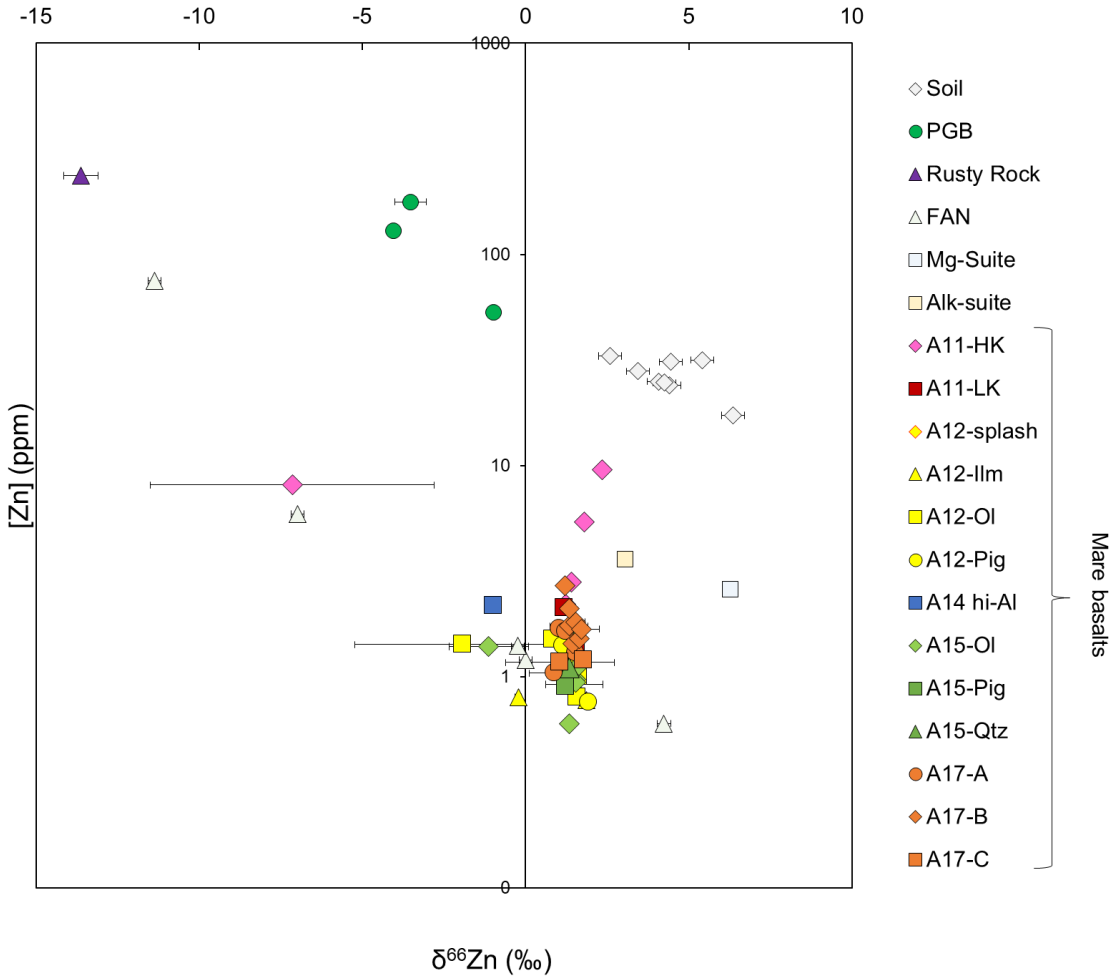


Figure 5.5 *The zinc isotope compositions of all lunar materials analysed to date vs. their zinc concentrations. Soils and glasses lie distinct from lunar rock samples. Isotopically-light lunar basalts are not characterised by significant [Zn] excesses (when compared to their heavy basalt counterparts from the same subtype). Isotopically-light basalts, FANs and Rusty Rock appear to lie on the same trend line, indicating that admixture of extremely isotopically-light (δ^{66}Zn ~ -14‰) material to these samples may have altered their pristine rock values. Note the log-scale for [Zn].*

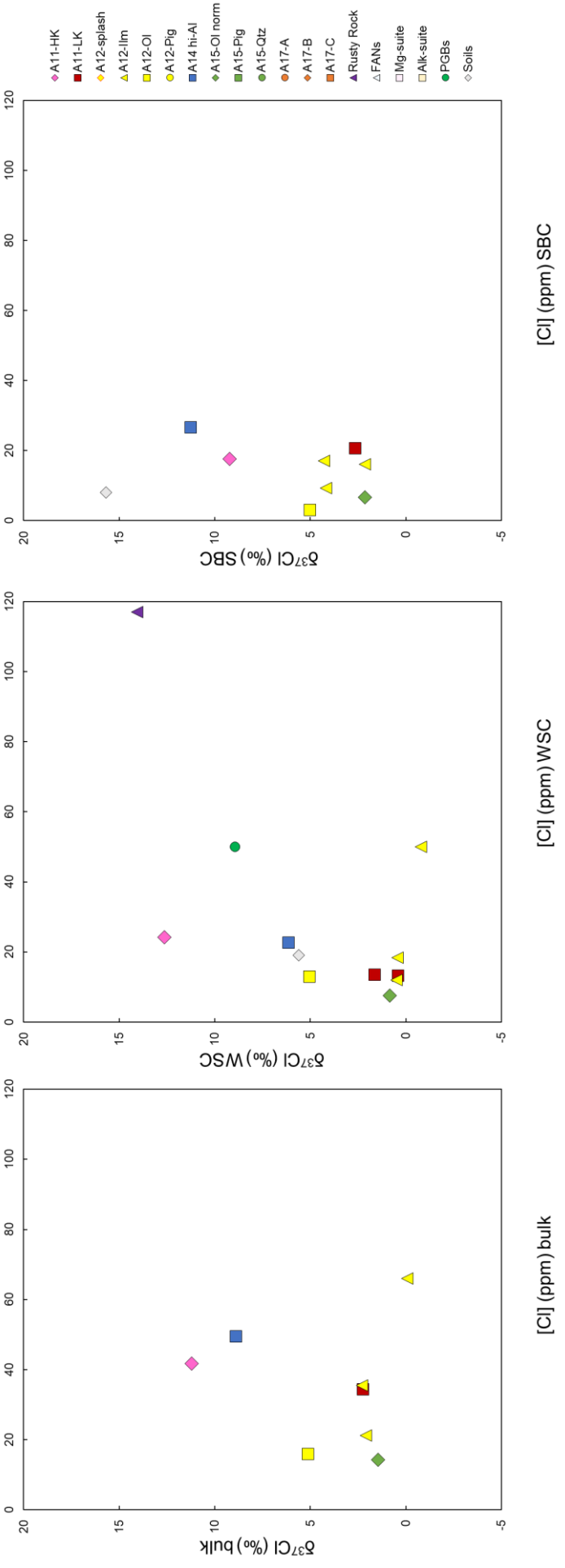


Figure 5.6 – *Chlorine isotope ratios versus chlorine concentrations in the bulk, water-soluble chlorine, and structurally-bound fractions of chlorine for the mare basalts in this suite. Additional data for soils and PGBs from Sharp et al. (2010). Data for Rusty Rock is from Shearer et al. (2014). Error bars are ~ ± 0.27‰ (smaller than the symbol size here).*

S

Chlorine concentrations and isotope ratios are reported for nine of the samples in the suite (**Table 5.1**). Bulk samples span a range in [Cl] between 13 – 46 ppm, and δ^{37}Cl between -0.07‰ and +11.20‰. Water-soluble chlorine (WSC) spans a range between [Cl]: 8 – 50 ppm, δ^{37}Cl: -0.78 – 12.63‰. Structurally-bound chlorine (SBC) spans a range between [Cl]: 3 – 21 ppm, δ^{37}Cl: 2.14 – 11.24‰. The long-term external error on measurements is 0.26‰ (1*s*). Samples typically have $\delta^{37}Cl_{WSC} < \delta^{37}Cl_{SBC}$ although 10017 is an exception (with $\Delta^{37}Cl_{WSC\text{-}SBC}$ = 3.4‰). Samples have significant proportions of both WSC and SBC with $[Cl]_{WSC}$:$[Cl]_{SBC}$ ratios between 0.65 – 4.14 (mean: 1.50). The S isotope compositions range between δ^{34}S = -0.07‰ and +0.93‰ with a mean of 0.61 ± 0.44‰. This is in line with previous studies (Fig 5.3). Concentrations (500ppm to 2500ppm) are also in line with previous studies.

5.3.2 Comparison with previous studies and intra-sample heterogeneity

Zinc

Zinc concentrations and isotope ratios in lunar basalts obtained by double-spiking in this study are comparable to those for previous work using sample-standard bracketing (Moynier et al., 2006; Herzog et al., 2009; Paniello et al, 2012; Kato et al., 2015), with the majority of lunar basalts having δ^{66}Zn between +1 and +2‰, and [Zn] between 1 and 2ppm. Four lunar basalts (10017, 12018, 14053, 15016) have light δ^{66}Zn (<0‰). These samples have been measured previously (Herzog et al., 2009; Paniello et al., 2012; Kato et al., 2015) and have also been reported to be isotopically light. There are no samples which have previously been measured to be light, which are now found to be heavy, and vice versa. However, samples that have been measured more than once show resolvable Zn concentration and isotopic variability between aliquots/studies. Sample 10017 was reported to have δ^{66}Zn = -5.42 ± 0.06‰ in Herzog et al., (2009). In this work, 10017-400 (from the exterior) has δ^{66}Zn = -6.42 ± 0.15 and 10017-405 (from the interior) has δ^{66}Zn = -9.59 ± 0.23. Sample 12018 was measured in this study to have δ^{66}Zn = -0.76 ± 0.06‰, which differs from the results of Paniello et al., (2012) (δ^{66}Zn = -3.10

± 0.08). The isotopic variability within 10017 alone spans a greater $\delta^{66}Zn$ than all terrestrial matter (Moynier et al., 2017). The measured $\delta^{66}Zn$ for samples 14053 and 15016 are very similar to that reported in Kato et al., (2015) differing by ≤ 0.03‰, however.

Chlorine

Chlorine isotopes for bulk lunar samples have previously been presented in Sharp et al., (2010). The only sample that has been re-analysed from this study is 10017. This sample shows significant differences between the Sharp et al., (2010) measurements ($[Cl]_{SBC}$ = 24.7ppm, $[Cl]_{WSC}$ = 12.3ppm, $\delta^{37}Cl_{SBC}$ = 4.7‰, $\delta^{37}Cl$ = 2.7‰) and this study (**Table 5.1**). Many more $\delta^{37}Cl$ measurements have been performed on apatite minerals found within lunar samples (e.g. Wang et al., 2012; Boyce et al., 2015; Barnes et al., 2016; Boyce et al., 2018; Potts et al., 2018; Barnes et al., 2019). For the first time, it is possible to compare the $\delta^{37}Cl$ obtained from apatite grains to that of the bulk sample (and the WSC, SBC fractions). In the three samples where overlap exists, apatites appear significantly heavier than for the bulk sample, WSC, and SBC fractions (**Table 5.2**).

Table 5.2 – *Comparison of published values for $\delta^{37}Cl$ in apatite and bulk samples.*

	Apatite (nanoSIMS)				***Bulk (Gas-source)***						
Sample	**$[Cl]_{ap}$**	**1s**	**$\delta^{37}Cl_{ap}$**	**1s**	**$[Cl]_{tot}$**	**$\delta^{37}Cl_{tot}$**	$[Cl]_{SBC}$	$\delta^{37}Cl_{SBC}$	$[Cl]_{WSC}$	$\delta^{37}Cl_{WSC}$	**Reference (for apatite)**
	(ppm)		**(‰)**		(ppm)	(‰)	µg	(‰)	µg	(‰)	
10044	710	550	9	2	34.4	2.22	5.6	2.62	3.7	1.6	Boyce et al., 2015
14053	6100	2800	26	3	49.6	8.87	6.7	11.24	5.7	6.11	Potts et al., 2018
15016	1100	580	12	1	14.2	1.45	1.7	2.14	1.9	0.84	Barnes et al., 2019

Sulphur

The $\delta^{34}S$ values are in line with the expected range for lunar basalts (~ 0.5‰, **Figure 5.3**). Sample 10017 again stands out as having highly variable $\delta^{34}S$ (with the exterior sub-sample displaying $\delta^{34}S$ = 0.34‰, and the interior sub-sample displaying $\delta^{34}S$ = 0.93‰). Sample 15535 (olivine-normative Apollo 15 basalt) is ~ 0.4‰ lighter than the rest of the basalt $\delta^{34}S$ population.

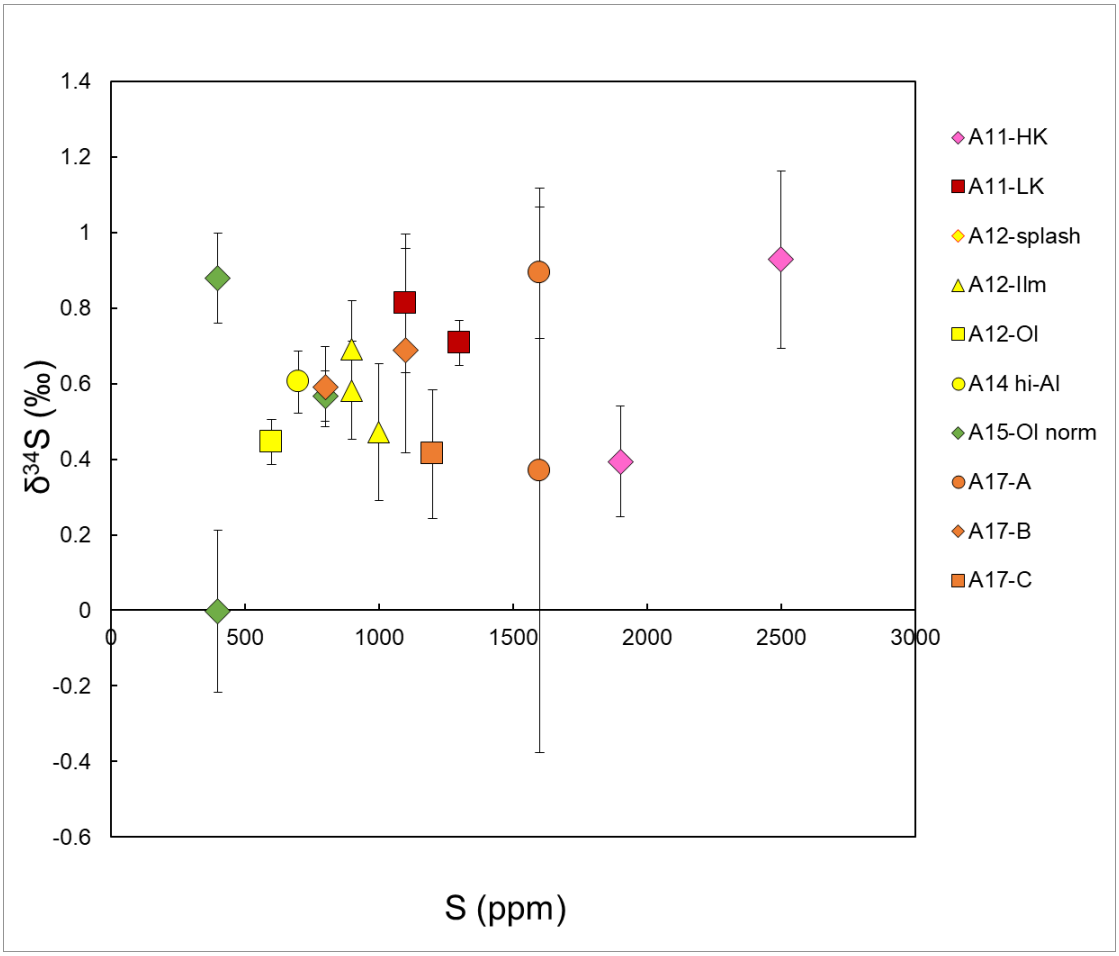


Figure 5.7 – *Results of sulphur isotopic analysis (performed at UMD). Sulphur concentration differs between mare basalt sub-type, but $\delta^{34}S$ spans a range in compositions for most missions (although Apollo 12 basalts appear more restricted in composition).*

5.4 Discussion

5.4.1 Is excluding light $\delta^{66}Zn$ basalts justified?

The results from this work and previous studies (Moynier et al., 2006; Herzog et al., 2009; Paniello et al, 2012; Kato et al., 2015) convincingly show that lunar basalts span a large range in $\delta^{66}Zn$ (from -9.52‰ to +2.34‰, Hopkins et al., 2014). Previous studies have excluded the lunar basalts with $\delta^{66}Zn < 0$‰ when reconstructing the composition of the bulk Moon, attributing basalts with light $\delta^{66}Zn$ to secondary condensation of light Zn vapour (carried as $ZnCl_2$) onto the surfaces (Paniello et al., 2012; Kato et al., 2015) and/or interiors (Day et al., 2017) of samples – in a similar mode to the enrichment of pyroclastic glass bead surfaces in Zn and other volatiles during eruption. Leaching experiments by Day et al., (2017) on a

powdered aliquot of 14053 suggest that Zn released during 3M HCl leaching is isotopically-light compared to the silicate-residues (which have $\delta^{66}Zn \sim +1.4 \pm 0.5‰$). It also has been argued that "light" basalts have higher Zn concentrations than "heavy" basalts (Day & Moynier, 2014; Kato et al., 2015) and that this is evidence of the addition of Zn (with isotopically-light $\delta^{66}Zn$). A number of these previous justifications for excluding light basalts can be shown to be incorrect.

Firstly, this study presents five samples extracted from the interiors of their parent samples with isotopically-light $\delta^{66}Zn$ (10017-405, 12018-277, 12054-146, 14053-305, 15016-240). This precludes the external condensation of light Zn vapour in a lunar atmosphere (originating from nearby volcanic activity, or meteorite impacts). Furthermore, the exterior fraction of 10017 has an isotopic composition which is heavier than its corresponding interior fraction (10017,400 $\delta^{66}Zn = -6.42 \pm 0.15‰$).

Secondly, the [Zn] enrichment in light $\delta^{66}Zn$ basalts proposed by Day & Moynier (2014) is only observed when the "light" basalts are averaged, with one Apollo 11 Type A (i.e. high-Ti, high-K; Neal & Taylor, 1992) basalt, 10017,52 (Herzog et al., 2009), skewing the [Zn] average for the rest of the population. Excluding the Apollo 11 Type A basalts, the "light" population shows a range in [Zn] from 0.8 to 2.7 $\mu g \cdot g^{-1}$ (average [Zn] = 1.7 $\mu g \cdot g^{-1}$, n=4). Indeed, all but one "heavy" basalt, which is also Zn rich (74275,318, [Zn] = 6 $\mu g \cdot g^{-1}$, Moynier et al., 2006) lies in a similar range of 0.6-2.7 $\mu g \cdot g^{-1}$ (average [Zn] = 1.3 $\mu g \cdot g^{-1}$, n=21). Apollo 11 Type A basalts are distinctly enriched in incompatible trace elements, and there are examples of "heavy" A11 Type A basalts with [Zn] higher than 2.7 $\mu g \cdot g^{-1}$ (e.g. 10057,283, [Zn] = 5.4 $\mu g \cdot g^{-1}$, Herzog et al., 2009). When lunar basalts from all studies are compared (**Figure 5.5)** samples with isotopically-light $\delta^{66}Zn$ do not have abnormal [Zn] when compared to heavy basalts from

the same lithology. Thus, a lunar basalt with high [Zn] does not necessarily preclude enrichment in light Zn isotopes by later processes.

It has been proposed that metal chlorides (including $ZnCl_2$) are the primary degassing species for chlorides in the absence of H- in the vapour (Sharp et al., 2010), and that $ZnCl_2$ is the isotopically-light phase secondarily-altering lunar basalt $\delta^{66}Zn$ (Paniello et al., 2012; Day & Moynier, 2014; Kato et al, 2015; Day et al., 2017). However, there is no direct evidence for the presence of $ZnCl_2$ amongst any lunar materials (either as precipitates on PGB surfaces, or deposits within veins of altered breccias – e.g. "Rusty Rock" 66095). Zinc is recorded in high concentrations in these vapour-exposed samples, but it is likely mainly ZnS (and is found associated with troilite). Other metal chlorides – for example, $FeCl_2$ – are found in PGB surface coatings and within altered breccia veins (Shearer et al., 2014). Renggli et al., (2017) modelled the speciation of volatiles during degassing of the parental magmas of the lunar pyroclastic glass beads (at 10^{-6} bar and 1 bar pressures, IW-2, and lunar compositions) and found that the overwhelming Zn-bearing vapour phase between 1500°C-500°C is $Zn_{(g)}$ – not $ZnCl_{2(g)}$ as previously proposed. This has important implications for isotopic fractionation during degassing: Rayleigh fractionation could theoretically produce a vapour with $1000\ln\alpha \sim -15‰$ when $Zn_{(g)}$ is the degassing species, but $ZnCl_2$ vapour would result in $1000\ln\alpha = -7.4‰$ under a similar regime. If $ZnCl_{2(g)}$ was the primary Zn-bearing volatile phase, the Zn in the lightest lunar samples would require more than one stage of isotopic-fractionation to achieve $\delta^{66}Zn$ similar to that measured ($\delta^{66}Zn \sim -13.6‰$ in Rusty Rock, 66095, Day et al., 2017). In contrast, ~20% Rayleigh evaporation of $Zn_{(g)}$ from a magma with initial composition $\delta^{66}Zn = 0‰$ can produce vapours with $\delta^{66}Zn \sim -13.5‰$ (**Figure 5.8**).

In summary, the prior justifications (Day and Moynier, 2014; Kato et al., 2015; Paniello et al., 2012) for excluding light Zn basalts from the lunar average composition appears tenuous without further investigation of the origin of this isotopic variability.

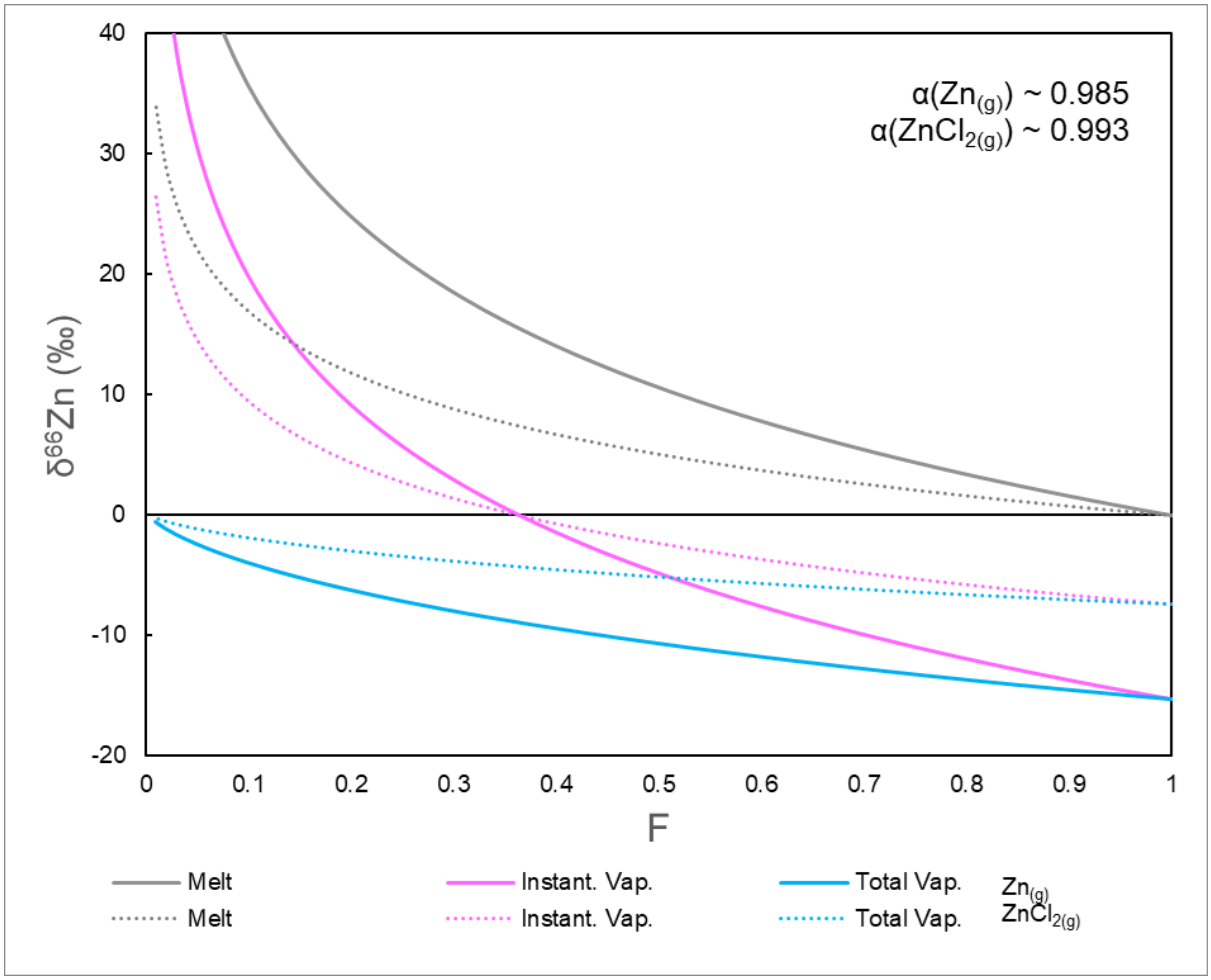


Figure 5.8 Calculated $\delta^{66}Zn$ of evolving melt, instantaneous vapour, and total vapour as evaporation of $Zn_{(g)}$ (solid lines) or $ZnCl_{2(g)}$ (dotted lines) proceeds from a melt ($\delta^{66}Zn$ = 0‰). The isotopic composition of the melt (grey) increases as the fraction of Zn in the melt (F) decreases. Evaporated $Zn_{(g)}$ is able to achieve much lighter $\delta^{66}Zn$ than $ZnCl_{2(g)}$, roughly equal to that of the lightest lunar samples (e.g. Rusty Rock, 66095).

5.4.2 Volatile-phase mass transfer and the variability in lunar basalt $\delta^{66}Zn$

Despite the above, it is likely that volatile behaviour of Zn has played a role in the isotopic variability observed. The wide range in $\delta^{66}Zn$ within the lunar basalts (~12‰ within the high-K Apollo 11 basalts alone, **Figure 5.2**) is much larger than any equilibrium fractionation observed during magmatic differentiation on Earth (~0.3‰, Chen et al., 2013; Sossi et al.,

2018). Powerful evidence in support of volatile fractionation caused by processes on the Moon is provided by the strong negative relationship between Zn and WSC Cl isotopic compositions (**Figure 5.9**). This trend appears to define a mixing relationship between an end-member with heavy δ^{66}Zn, light δ^{37}Cl, and high Zn/Cl, and an endmember with light δ^{66}Zn, heavy δ^{37}Cl and low Zn/Cl. It should be noted that the relationship between δ^{66}Zn and δ^{37}Cl is strongest for the water-soluble chlorine fraction (rather than structurally-bound Cl). Before discussing this in more detail, alternative explanations for the isotopic variability are discussed.

The range in Zn isotopic composition in lunar basalts has been shown to be mass dependent (Herzog et al., 2009; Moynier et al., 2006; Paniello et al., 2012). Therefore, cosmogenic effects are irrelevant, consistent with the fact that no correlation is found with cosmic ray exposure age (**Appendix 2d**). Solar wind is low in [Zn] and the samples in this study are mostly extracted from the shielded interiors of their parent samples. Therefore, it is unlikely that implantation of Solar wind or Solar energetic particles have contributed to the δ^{66}Zn variation observed.

Meteorite contamination at the lunar surface is also unlikely. The highly siderophile elements are not elevated in the basalts from this study, and samples are unbrecciated and mainly from the interiors of their parent samples. Furthermore, only aubrites have δ^{66}Zn ($\geq$ -7‰, Moynier et al., 2011) approaching that of the lightest lunar basalts. It would be difficult to produce a light Rusty Rock (δ^{66}Zn ~ -13.6‰) and FANs (lightest δ^{66}Zn ~ -11.4‰) via this mechanism. Even here, the addition of an aubrite impactor would likely leave evidence: the lightest aubrites are roughly equal to the δ^{66}Zn observed for 10017. Addition of material of this composition would need to raise [Zn] significantly relative to the other A11 Type A heavy δ^{66}Zn basalts – there is no clear evidence that 10017 is significantly enriched in [Zn] (**Figure 5.5**).

A key feature of the isotopic variability is that samples from the same lithologies have both light and heavy $\delta^{66}Zn$. There is no consistent correlation between $\delta^{66}Zn$ and major or trace elements, or bulk mineralogy for all lunar basalts (or even within the same subtypes). For example, Apollo 11 type-A (high-K) basalts are all thought to be related to the same episode of magmatism at the lunar surface (e.g. Neal and Taylor, 1992). However, the lightest and the heaviest lunar basalts ($\delta^{66}Zn$ = -9.59‰ and +2.34‰) are found within this suite. Likewise, Apollo 15 olivine-normative basalts show restricted major and trace element compositions, but 15016 stands out as having $\delta^{66}Zn$ = -1.48‰ – approximately 1.5-2.5‰ lighter than the other Apollo 15 olivine-normative samples. Thus, it is unlikely that partial melting or crystal fractionation provide mechanisms for the large (~12‰) isotope fractionations observed.

The strong negative relationship between Zn and Cl isotopic compositions (**Figure 5.9**) appears to define a mixing relationship between a heavy $\delta^{66}Zn$, light $\delta^{37}Cl$, high Zn/Cl end-member, and a light $\delta^{66}Zn$, heavy $\delta^{37}Cl$, low Zn/Cl end-member. The negative trend (**Fig 5.9**) found between $\delta^{66}Zn$ and $\delta^{37}Cl$ is the opposite to that expected for degassing of $ZnCl_2$ vapour from an H-poor melt (e.g. Sharp et al., 2010).

The light $\delta^{66}Zn$, heavy $\delta^{37}Cl$ endmember composition is typified by 66095 (Rusty Rock, **Figure 5.9**), which shows high enrichments in Zn, Cl, S, and other volatile elements (Day et al., 2017; Shearer et al., 2014). Likewise, light $\delta^{66}Zn$ lunar basalts, FANs and Rusty Rock all lie on a similar mixing trend between Zn and $\delta^{66}Zn$ (**Figure 5.5**). Rusty Rock and FANs have proposed to show a relationship between $\delta^{66}Zn$ and 1/[Zn] (Day et al., 2017; Kato et al., 2015) due to the incorporation of isotopically-light Zn vapour into their brecciated textures. Vapour-phase crystallisation products and replacement textures have been found in Apollo 14 breccias (McKay et al., 1972) and Apollo 16 breccias (Shearer et al., 2014, 2012), indicating that late-stage fluids enriched in volatile components likely represent one end-member of the mixing

relationship. It's apparent that volatile-enriched fluids (either S-bearing, or C-O-S-bearing) have been pervasive throughout the lunar crust (Shearer et al., 2012).

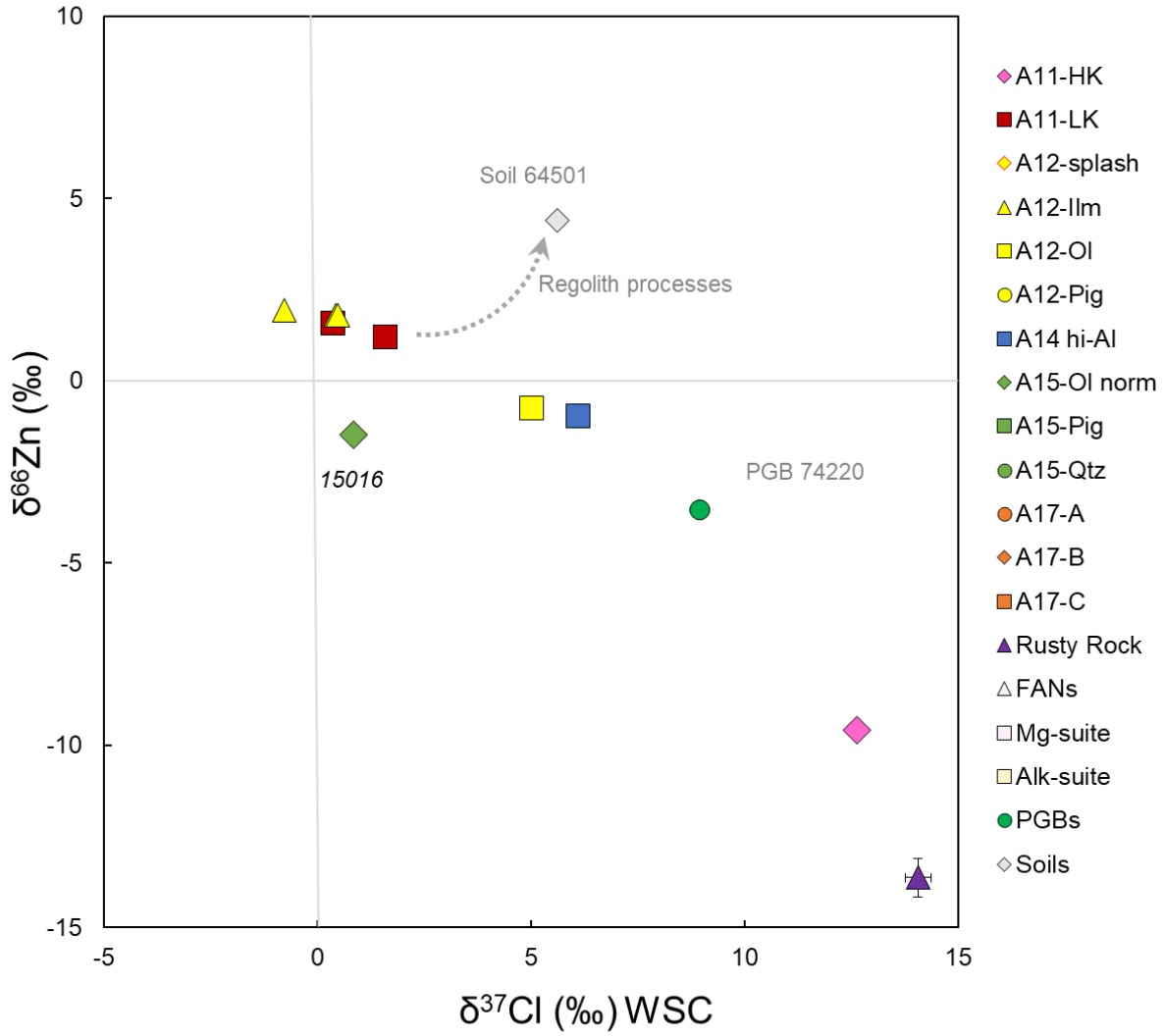


Figure 5.9 *Zinc isotopes versus the water-soluble Cl isotopes of the same samples. Lunar basalt data represents $\delta^{66}Zn$ and $\delta^{37}Cl$ from this study (i.e. from neighbouring locations within the same parent sample). Soils, glasses, and "Rusty Rock" may be from different internal locations. Soils lie heavier in both $\delta^{37}Cl$ and $\delta^{66}Zn$ – a feature that is repeated in other isotopic systems. Meteorite impact and sputtering is thought to fractionate soil isotope ratios to heavier values (Haskin & Warren, 1991). Data for $\delta^{37}Cl$ form this study, Sharp et al. (2010) (PGB and soil), and Shearer et al. (2014) (Rusty Rock).*

It is possible that late-stage flow of vapour-phases through vesicles and vugs in samples might have allowed the vapours to precipitate along the physical boundaries of these features. However, unlike the FANs and Rusty Rock, the light $\delta^{66}Zn$ lunar basalts have not been found

to display veining or replacement textures. Samples 10017 and 15016 display vesicularity (10017 ~ <5% by volume; 15016 ~ 50% by volume) and light δ^{66}Zn. However, samples 14053 and 12018 display light δ^{66}Zn but display no vesicularity or cracks along which vapours might flow. Likewise, sample 15016 displays similar geochemical and mineralogical compositions to 15016 and has similar vesicularity (~ 50% by volume) yet has δ^{66}Zn = + 1.54 ± 0.07‰.

Therefore, incorporation of a light δ^{66}Zn, heavy δ^{37}Cl phase likely occurred during the period prior to cooling and crystallisation. Cryptic metasomatism of samples by a fluid or vapour enriched in light δ^{66}Zn and heavy δ^{37}Cl or assimilation/remobilisation of volatiles in wallrocks during ascent or emplacement of magmas is the best explanation for the light δ^{66}Zn, heavy δ^{37}Cl observed in the interiors of the light lunar basalts. It may also explain the heterogeneity of δ^{66}Zn within samples of the same basalt sub-type (i.e. those samples geographically situated closer to the wall-rock are more likely to be subject to vapours).

Origin of heavy δ^{37}Cl

The coincidence of lunar basalts and Rusty Rock on the same mixing trend (**Figure 5.9**), and the coincidence of light lunar basalts, FANs, and Rusty Rock on the same trend in δ^{66}Zn-[Zn] space (**Figure 5.5**) suggests that the light δ^{66}Zn, heavy δ^{37}Cl, low Zn/Cl end-member composition is widespread and pervasive throughout (at least) the lunar nearside crust, rather than localised in origin. Small amounts of Rayleigh degassing can produce δ^{66}Zn ~ -14‰ (**Figure 5.8**). However, the mechanism for producing a reservoir enriched in heavy δ^{37}Cl (~+15‰) is unclear.

Evaporation of HCl under equilibrium conditions shows that small enrichments in δ^{37}Cl may occur in the vapour phase (Sharp et al., 2010b), but distillation experiments show that significant enrichment in heavy δ^{37}Cl is possible, in line with extreme δ^{37}Cl enrichments (~ +15‰) in fumarolic gases measured at some locations on Earth (Rizzo et al., 2013).

The urKREEP reservoir has been proposed as a Cl-enriched reservoir which may provide an endmember for the correlations observed between apatite $\delta^{37}Cl$ and [Th], La/Lu in low-Ti basalts and KREEP (Barnes et al., 2016; Boyce et al., 2015). It has been proposed that this reservoir achieved its heavier $\delta^{37}Cl$ via preferential degassing of light Cl during the LMO or via a crust-breaching impact (Barnes et al., 2016). However, such a mechanism would not work to explain the observed $\delta^{66}Zn$ signatures, due to its relative compatibility as a trace element in the major rock-forming minerals, and its highly negative $\delta^{66}Zn$. Experimental work has shown that late-stage cryptic metasomatism by a S-Cl-bearing, F-poor fluid phase can deliver Cl and other trace elements (including REEs) to apatite grains growing within magmas, reproducing the characteristic rim-enrichments in Cl (Konecke et al., 2017). If this fluid phase is also heavy in $\delta^{37}Cl$ (relative to bulk magmas), it may explain the correlations observed in lunar apatite between $\delta^{37}Cl$ and [Cl] and [Th], La/Lu.

Modelling of the S-bearing fluids (C-O-H-S) responsible for replacement textures in lunar breccia 67915 (Bell et al., 2015) suggests that typical mare basalt magma (90 ppm H_2O) at 2.5km depth can readily provide the source for these fluids. To initiate degassing at greater depths, H_2 contents to achieve fluid saturation must be increased higher than the known content of lunar magmas.

Combining the evidence, it is proposed that the light-Zn, heavy-Cl endmember is a metasomatic fluid derived from lunar magmas. This phase is pervasive throughout the lunar crust, and provides the source for light Zn (and heavy Cl, where measurements are available) observed in veins and replacement textures within brecciated lunar FANs (Kato et al., 2015) and Rusty Rock 66095 (Day et al., 2017; Shearer et al., 2014). Because this fluid can be released at depths ~2.5km (Bell et al., 2015), it is proposed that precipitation of the condensed phase may occurs throughout veins in overlying lunar crust. The vapour may be re-mobilised

by ascent and eruption of nearby magmas, and this can be observed in the isotopic signatures of Zn and water-soluble Cl in the light δ^{66}Zn lunar basalts. Samples which are physically closer to the wallrock are affected, but those further away are unaffected, explaining the large range of δ^{66}Zn observed within the same basalt sub-types (e.g. high-K Apollo 11 basalts, **Appendix 3b**). Cryptic metasomatism after cooling and crystallisation is possible, but not consistent with textures observed in 12018 and 14053 (or 10017).

5.4.3 The Zn isotope composition of the Moon

The Zn bulk isotopic composition of the Moon is of interest to models of the giant impact. Paniello et al., (2012) provided the first evidence of an isotopic system in which the Earth and the Moon were significantly different ($\Delta^{66}Zn_{Moon\text{-}Earth}$ = ~+1.4‰), arguing that this reflects loss of isotopically-light Zn due to the giant impact, or evaporation from a LMO. Similar proposals have been made for isotopes of K (Wang and Jacobsen, 2016; Tian et al., 2018) which appears ~0.4‰ heavier in the Moon, Rb (Pringle and Moynier, 2017), and Ga (Kato and Moynier, 2017), but the differences between the Earth and the Moon are not as large as for δ^{66}Zn, and (for Rb and Ga) show significant isotopic variability.

The "heavy" lunar basalts span a range in compositions between ~+1-+2‰, which is larger than all terrestrial magmatic rock samples on Earth. This range may reflect source heterogeneity in the lunar mantle, or a more complex history related to release of Zn during degassing or fluid exsolution. The heavy lunar basalts in this study (**Figure 5.10b**) show a negative correlation between δ^{66}Zn and [Zn] indicating that loss of isotopically-light Zn may fractionate residual melts to heavier values. Thus, although lunar basalts represent the best estimate for the lunar mantle to date, experimental determination of the fractionation between basalts and vapours/exsolved fluids help better estimate the primary compositions of basaltic magmas and the lunar mantle.

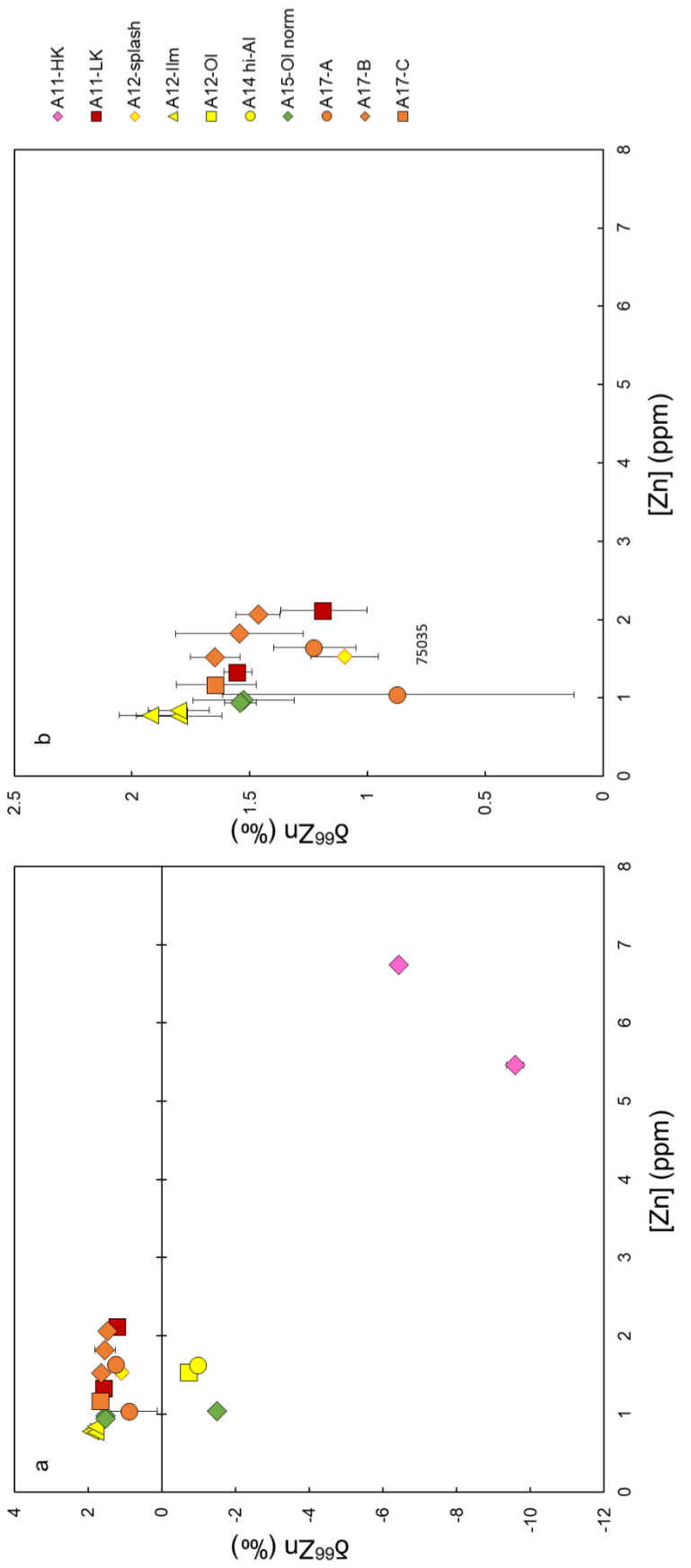


Figure 5.10 *δ^{66}Zn vs [Zn] for a) all samples in this study, b) for the "heavy" (i.e. δ^{66}Zn > 0‰) lunar basalts. Note that sample 75035 has large 2SD due to inaccurate spike-application during analysis.*

5.5 Conclusions

We have measured a suite of lunar basalts for their Zn, Cl and S isotopic compositions. We find that – in keeping with previous studies – there is a population of isotopically-heavy and light lunar basalts (for $\delta^{66}Zn$). The isotopically-light basalts do not vary with indices of magmatic differentiation, or other trace element concentrations. The [Zn] recorded in light lunar basalts is not significantly higher than in heavy basalts from the same lithologies – thus contribution of additional Zn must be of extremely light $\delta^{66}Zn$ to produce the bulk $\delta^{66}Zn$ observed.

Lunar basalts (except 15016) fall on a negative trend between $\delta^{66}Zn$ and $\delta^{37}Cl$. When other lunar lithologies are included, they also fall on this line (except soils, which are fractionated to heavier isotopic values. This is counter to previous explanations of a $ZnCl_2$ degassing vapour from an H-poor Moon. Rather, the Zn isotopic composition of lunar basalts appears to reflect assimilation of fluids from altered wallrocks with light $\delta^{66}Zn$ and heavy $\delta^{37}Cl$. These altered materials have led to a very wide range of compositions recorded in basalts. Published experimental work suggests that basaltic magmas can readily provide the source of these fluids. The production of high concentrations of isotopically-light Zn in altered rocks must leave a residue that is isotopically-heavy. It is unclear if the heavier Zn isotopic compositions recorded in most lunar basalts reflects a heavier bulk lunar composition, but the variability in $\delta^{66}Zn$ in the heavy lunar basalts (~1‰) would suggest either variable source compositions, or differential amounts of degassing or fluid exsolution during presence at near-surface depths (≤ 2.5km). Further experimental determination of fluid-production mechanisms, and the partitioning of Zn and Cl (and associated isotopic fractionation factors) would significantly aid reconstruction of the bulk lunar compositions.

6

Conclusion and Outlook

6.1 Conclusions

Geochemical and isotopic analysis of lunar rocks have provided stringent constraints on our understanding of lunar formation and evolution. Despite very significant Solar System heterogeneity (e.g. Goderis et al., 2016), previous studies have discovered that the isotopic compositions of a variety of elements in the Moon are identical (within error) to those found in the BSE (**Chapter 1**). These have provided powerful constraints on the most suitable models of lunar origin. Isotopic studies may also be useful for determining processes occurring on the Moon subsequent to its formation.

This study presents new V and Zn isotopic data, plus companion isotopic data for S and Cl, for a suite of lunar basalts. Vanadium and zinc were both chosen because it was thought these elements might shed light on lunar origins. Instead, in this thesis it is shown that isotopic variations are dominated by other effects (cosmogenic and volatile) produced on or in the Moon itself. The first step was to develop techniques for higher-resolution V isotope analysis (**Chapter 3**). These methods were then applied to generate the first high-precision V isotope data for the Moon (**Chapter 4**). Like silicon (Armytage et al., 2011), vanadium shows a isotopic dissimilarity between the BSE and meteorites (Nielsen et al., 2019, 2014). Armytage et al., (2012) showed that the Moon and BSE were isotopically similar, but this was unknown for vanadium. In **Chapter 5**, combined Zn, Cl and S isotope compositions were determined in the same suite of lunar basalts. These were specifically selected to test previous theories of volatile element loss associated with the Giant Impact.

Vanadium

Previous studies have presented V isotope data for the BSE and meteorites, with the BSE appearing ~ 1‰ heavier in $\delta^{51}V$ than in meteorites (Nielsen et al., 2014; Prytulak et al., 2013, 2011). Subsequent work (Nielsen et al., 2019) has shown that the $\delta^{51}V$ offset of chondrites is

smaller ($\Delta^{51}V_{BSE\text{-}chondrites}$: +0.3 to +0.5‰), because data from initial studies were affected by incomplete resolution of compound interferences.

In this study, a higher-resolution MC-ICPMS technique for measuring $\delta^{51}V$ in geological samples has been described and tested using USGS reference materials (**Chapter 3**). These techniques were used to obtain the first V isotope data for the Moon (**Chapter 4**). The suite of lunar basalts measured here spans a range in $\delta^{51}V \sim 2.5‰$, which is larger than the range of $\delta^{51}V$ measured in all terrestrial igneous rocks (~2.3‰, Prytulak et al., 2017, 2013, 2011, Wu et al., 2018, 2016). Lunar basalts are also isotopically-lighter than almost all terrestrial igneous rocks.

Unlike $\delta^{51}V$ fractionation on Earth, lunar basalts do not show $\delta^{51}V$ fractionation with sample geochemistry or mineralogy, despite the wide variation in ilmenite contents (and other minerals) in this suite. A reduced isotopic fractionation factor due to the low lunar fO_2 (and thus the absence of V^{4+} in melts) may explain the lack of difference between high-Ti and low-Ti lunar basalts, in line with analogous experiments into changing $\delta^{51}V$ fractionation factors at variable (but higher) fO_2 (Sossi et al., 2018).

Vanadium isotopes in lunar basalts correlate with indices of cosmogenic exposure: sample exposure ages (obtained via noble gas measurements), Gd isotope ratios, and excesses in $\varepsilon^{50}Ti$. Modelling the cross-sections for target elements in the mass-range for V isotopes shows that the primary pathways to producing the negative $\delta^{51}V$ excursions observed is via spallation of Fe. Corrected for each sample's composition (here, the Fe/V ratio), $\delta^{51}V$ and exposure age correlate well ($R^2 = 0.95$). Regressing the data yields an intercept of $\delta^{51}V = -1.05 \pm 0.14‰$. From existing meteorite $\delta^{51}V$, compositional, and exposure age data (**Appendix 2f**, Nielsen et al., 2019), it appears that the spread in chondritic $\delta^{51}V$ can be readily explained by similar cosmogenic processes. This study has shown that the range in $\delta^{51}V$ in the Solar System is likely

due to cosmogenic effects, and that the Moon, chondrites, Mars, and the Earth are similar in $\delta^{51}V$.

Zinc

This study presents combined Zn, Cl and S isotope ratios, and trace element measurements within the same lunar samples. This has allowed a more rigorous investigation of the behaviour of Zn (and $\delta^{66}Zn$) under lunar conditions. Isotopically-light Zn isotopes are not surface correlated (as proposed in Day and Moynier, 2014; Kato et al., 2015; Paniello et al., 2012). Both exteriors and interiors of samples can be heavy or light for $\delta^{66}Zn$ (12054 and 10017).

A negative correlation is found between $\delta^{66}Zn$ and $\delta^{37}Cl_{WSC}$ in lunar samples supporting a mixing-model where isotopically-light basalts, FANs, and Rusty Rock achieved their light $\delta^{66}Zn$ compositions from the same source. Under this model, light mare basalts are likely to have assimilated light $\delta^{66}Zn$ during heating and remobilisation of volatile-enriched fluid phases pervasive in the lunar crust. This $\delta^{66}Zn$ light, $\delta^{37}Cl$ heavy vapour is likely to be endogenous to the Moon and should be considered in estimates of bulk lunar composition.

6.2 Future Work

Vanadium isotopes in iron meteorites

This study has shown that V isotopes are extremely sensitive to cosmogenic effects in extra-terrestrial samples. Initial studies of V isotopes in iron meteorites proposed extreme $^{51}V/^{50}V$ ratios between 5 and 140 (Stauffer and Honda, 1962, 1961). These early studies had been largely dismissed due to the relatively poor precision (≥ 5‰) and the potential for significant artificial isotopic fractionation during incomplete extraction or collection of V during sample preparation. However, based upon the finding that Fe is a significant target for V isotope alteration under high-energy particle fluxes, these extreme $^{51}V/^{50}V$ ratios may be accurate.

Future measurements of V in iron meteorites will require a significant amount of sample material. The intensities of ion beams will mean that mass spectrometry protocols will need to be adaptable to measure both ^{50}V and ^{51}V at different intensities.

Vanadium isotopes as a cosmogenic proxy

More precise modelling of the nuclear pathways affecting V isotope abundances in bombarded samples should be carried out if V isotopes is to become a useful proxy for cosmogenic effects. From the simple cross-section modelling performed in this study, it seems as though (of the particles modelled) only high-energy neutrons, protons, and alpha particles can produce the depletions in ^{51}V observed. Thermal and epithermal neutrons would appear to produce $\delta^{51}V$ excesses (**Figure 5.7**). In contrast to noble gases, loss of V through sample reheating is highly unlikely. Thus, V isotopes may be a useful proxy for reconstructing charged particle fluxes or high-energy neutron fluxes, especially when thermal neutron fluxes can be corrected for with existing proxies (e.g. Gd isotopes).

Multi-fold analyses of the same aliquots

Lunar samples are typically small and may be affected by internal heterogeneity. Thus, relying on literature elemental concentrations or general comparisons between lithologies (e.g. because there aren't specific sample overlaps between studies) is sub-optimal. This study has shown the value of performing isotopic and elemental analyses on the same aliquots of lunar samples. Firstly, combined $\delta^{66}Zn$ and $\delta^{37}Cl$ analyses show that the range in Zn and Cl isotope compositions in lunar basalts is due to volatile mixing between two endmember compositions (one with $\delta^{66}Zn$ ~ 1-2‰, $\delta^{37}Cl$ ~ 0‰, and high Zn/Cl; one with $\delta^{66}Zn$ ~ -14‰, $\delta^{37}Cl$ ~ 15‰, and low Zn/Cl). Secondly, trace element analysis of lunar basalts has allowed the confidence to determine that $\delta^{51}V$ variations in lunar basalts are not due to magmatic processes. Finally,

aliquot-specific correction of cosmogenic effects in $\delta^{51}V$ (via [Fe]/[V]*t_e) can be made with the trace-element analyses performed in this study.

Future geochemical (and isotopic) studies should endeavour to collect as much useful information from the same sample aliquots as possible, particularly in lunar and meteorite studies where samples are limited in size and may show internal heterogeneity. Perhaps due to the costs of laboratory hardware, and the barriers to setting up high-precision analytical techniques (e.g. where bespoke equipment is required) geochemical studies often work in isolation from one another to the detriment of scientific understanding. This work demonstrates that it is possible to coordinate a cross-laboratory geochemical study, even when samples are restricted in availability.

References

Akram, W., Schonbachler, M., 2016. Zirconium isotope constraints on the composition of Theia and current Moon-forming theories. Earth Planet Sc Lett 449, 302-310.

Albarede, F., Telouk, P., Blichert-Toft, J., Boyet, M., Agranier, A., Nelson, B., 2004. Precise and accurate isotopic measurements using multiple-collector ICPMS. Geochim Cosmochim Ac 68, 2725-2744.

Anders, E., Grevesse, N., 1989. Abundances of the Elements - Meteoritic and Solar. Geochim Cosmochim Ac 53, 197-214.

Antonelli, M.A., Kim, S.-T., Peters, M., Labidi, J., Cartigny, P., Walker, R.J., Lyons, J.R., Hoek, J., Farquhar, J., 2014. Early inner solar system origin for anomalous sulfur isotopes in differentiated protoplanets. Proc. Natl. Acad. Sci. 111, 17749–17754. https://doi.org/10.1073/pnas.1418907111

Armytage, R.M.G., Georg, R.B., Savage, P.S., Williams, H.M., Halliday, A.N., 2011. Silicon isotopes in meteorites and planetary core formation. Geochim. Cosmochim. Acta 75, 3662–3676. https://doi.org/10.1016/j.gca.2011.03.044

Armytage, R.M.G., Georg, R.B., Williams, H.M., Halliday, A.N., 2012. Silicon isotopes in lunar rocks: Implications for the Moon's formation and the early history of the Earth. Geochim Cosmochim Ac 77, 504-514.

Arnold, T., Schonbachler, M., Rehkamper, M., Dong, S.F., Zhao, F.J., Kirk, G.J.D., Coles, B.J., Weiss, D.J., 2010. Measurement of zinc stable isotope ratios in biogeochemical matrices by double-spike MC-ICPMS and determination of the isotope ratio pool available for plants from soil. Anal. Bioanal. Chem. 398, 3115–3125. https://doi.org/10.1007/s00216-010-4231-5

Arvidson, R., Drozd, R., Guinness, E., Hohenberg, C., Morgan, C., Morrison, R., Oberbeck, V. 1976. Cosmic ray exposure ages of Apollo 17 samples and the age of Tycho. Proc. Lunar Sci. Conf. 7. 2817-2832.

Balsiger, H., Geiss, J., Lipschutz, M.E., 1969. Vanadium Isotopic Composition in Meteoritic and Terrestrial Matter. Earth Planet. Sci. Lett. 6, 117–+.

Balsiger, H., Mendia, M.D., Pelly, I.Z., Lipschutz, M.E., 1976. Vanadium Isotopic Composition and Contents in Gas-Rich Meteorites. Earth Planet. Sci. Lett. 28, 379–384.

Barling, J., Goldstein, S.L., Nicholls, I.A., 1994. Geochemistry of Heard-Island (Southern Indian-Ocean) - Characterization of an Enriched Mantle Component and Implications for Enrichment of the Sub-Indian Ocean Mantle. J. Petrol. 35, 1017–1053.

Barnes, J.D., Sharp, Z.D., 2006. A chlorine isotope study of DSDP/ODP serpentinized ultramafic rocks: Insights into the serpentinization process. Chem. Geol. 228, 246–265. https://doi.org/10.1016/J.CHEMGEO.2005.10.011

Barnes, J.D., Sharp, Z.D., 2017. Chlorine Isotope Geochemistry. Rev. Mineral. Geochemistry 82, 345–378. https://doi.org/10.2138/rmg.2017.82.9

Barnes, J.D., Sharp, Z.D., Fischer, T.P., Hilton, D.R., Carr, M.J., 2009. Chlorine isotope variations along the Central American volcanic front and back arc. Geochemistry, Geophys. Geosystems 10, n/a-n/a. https://doi.org/10.1029/2009GC002587

Barnes, J.J., Franchi, I.A., McCubbin, F.M., Anand, M., 2019. Multiple reservoirs of volatiles in the Moon revealed by the isotopic composition of chlorine in lunar basalts. Geochim. Cosmochim. Acta. https://doi.org/10.1016/j.gca.2018.12.032

Barnes, J.J., Tartèse, R., Anand, M., McCubbin, F.M., Neal, C.R., Franchi, I.A., 2016. Early degassing of lunar urKREEP by crust-breaching impact(s). Earth Planet. Sci. Lett. 447, 84–94. https://doi.org/10.1016/j.epsl.2016.04.036

Barr, A.C., 2016. On the origin of Earth's Moon. J. Geophys. Res. Planets 121, 1573–1601. https://doi.org/10.1002/2016JE005098

Barrat, J.A., Zanda, B., Moynier, F., Bollinger, C., Liorzou, C., Bayon, G., 2012. Geochemistry of CI chondrites: Major and trace elements, and Cu and Zn Isotopes. Geochim. Cosmochim. Acta 83, 79–92. https://doi.org/10.1016/j.gca.2011.12.011

Bell, A.S., Shearer, C., deMoor, J.M., Provencio, P., 2015. Using the sulfide replacement petrology in lunar breccia 67915 to construct a thermodynamic model of S-bearing fluid in the lunar crust. Geochim. Cosmochim. Acta 171, 50–60. https://doi.org/10.1016/j.gca.2015.08.002

Bellucci, J.J., Whitehouse, M.J., John, T., Nemchin, A.A., Snape, J.F., Bland, P.A., Benedix, G.K., 2017. Halogen and Cl isotopic systematics in Martian phosphates: Implications for the Cl cycle and surface halogen reservoirs on Mars. Earth Planet. Sci. Lett. 458, 192–202. https://doi.org/10.1016/J.EPSL.2016.10.028

Belshaw, N.S., Zhu, X.K., Guo, Y., O'Nions, R.K., 2000. High precision measurement of iron isotopes by plasma source mass spectrometry. Int J Mass Spectrom 197, 191-195.

Benz, W., Slattery, W.L., Cameron, A.G.W., 1986. The origin of the moon and the single-impact hypothesis I. Icarus 66, 515–535. https://doi.org/10.1016/0019-1035(86)90088-6

Berglund, M., Wieser, M.E., 2011. Isotopic compositions of the elements 2009 (IUPAC Technical Report). Pure Appl. Chem. 83, 397–410.

Bogard, D.D., Funkhouser, J.G., Schaeffer, O.A., Zahringer, J., 1971. Noble Gas Abundances In Lunar Material - Cosmic-Ray Spallation Products And Radiation Ages From Sea Of Tranquility And Ocean Of Storms. J Geophys Res 76, 2757-+.

Bonnand, P., Parkinson, I.J., Anand, M., 2016. Mass dependent fractionation of stable chromium isotopes in mare basalts: Implications for the formation and the differentiation of the Moon. Geochim. Cosmochim. Acta 175, 208–221. https://doi.org/10.1016/j.gca.2015.11.041

Boyce, J.W., Kanee, S.A., McCubbin, F.M., Barnes, J.J., Bricker, H., Treiman, A.H., 2018. Early loss, fractionation, and redistribution of chlorine in the Moon as revealed by the low-Ti lunar mare basalt suite. Earth Planet. Sci. Lett. 500, 205–214. https://doi.org/10.1016/j.epsl.2018.07.042

Boyce, J.W., Treiman, A.H., Guan, Y., Ma, C., Eiler, J.M., Gross, J., Greenwood, J.P., Stolper, E.M., 2015. The chlorine isotope fingerprint of the lunar magma ocean. Sci. Adv. 1, e1500380. https://doi.org/10.1126/sciadv.1500380

Bridgestock, L.J., Williams, H., Rehkämper, M., Larner, F., Giscard, M.D., Hammond, S., Coles, B., Andreasen, R., Wood, B.J., Theis, K.J., Smith, C.L., Benedix, G.K., Schönbächler, M., 2014. Unlocking the zinc isotope systematics of iron meteorites. Earth Planet. Sci. Lett. 400, 153–164. https://doi.org/10.1016/j.epsl.2014.05.029

Brugier, Y.-A., Barrat, J.-A., Gueguen, B., Agranier, A., Yamaguchi, A., Bischoff, A., 2019. Zinc isotopic variations in ureilites. Geochim. Cosmochim. Acta, Vol. 246, p. 450-460. 246, 450–460. https://doi.org/10.1016/J.GCA.2018.12.009

Cameron, A.G.W., Ward, W.R., 1976. The Origin of the Moon. Abstracts of the Lunar and Planetary Science Conference 7, p120.

Canfield, D.E., Raiswell, R., Westrich, J.T., Reaves, C.M., Berner, R.A., 1986. The use of chromium reduction in the analysis of reduced inorganic sulfur in sediments and shales. Chem. Geol. 54, 149–155. https://doi.org/10.1016/0009-2541(86)90078-1

Canil, D., 1997. Vanadium partitioning and the oxidation state of Archaean komatiite magmas. Nature 389, 842–845. https://doi.org/10.1038/39860

Canup, R.M., 2004. Simulations of a late lunar-forming impact. Icarus 168, 433–456. https://doi.org/10.1016/j.icarus.2003.09.028

Canup, R.M., 2012. Forming a Moon with an Earth-like Composition via a Giant Impact. Science (80-.). 338, 1052–1055. https://doi.org/10.1126/science.1226073

Canup, R.M., Asphaug, E., 2001. Origin of the Moon in a giant impact near the end of the Earth's formation. Nature 412, 708–712. https://doi.org/10.1038/35089010

Chen, H., Savage, P.S., Teng, F.-Z., Helz, R.T., Moynier, F., 2013. Zinc isotope fractionation during magmatic differentiation and the isotopic composition of the bulk Earth. Earth Planet. Sci. Lett. 369–370, 34–42. https://doi.org/10.1016/j.epsl.2013.02.037

Clayton, R.N., 1993. Oxygen Isotopes in Meteorites. Annu. Rev. Earth Planet. Sci. 21, 115–149. https://doi.org/DOI 10.1146/annurev.earth.21.1.115

Cuk, M., Stewart, S.T., 2012. Making the Moon from a Fast-Spinning Earth: A Giant Impact Followed by Resonant Despinning. Science (80-.). 338, 1047–1052. https://doi.org/10.1126/science.1225542

Dauphas, N., Burkhardt, C., Warren, P.H., Fang-Zhen, T., 2014. Geochemical arguments for an Earth-like Moon-forming impactor. Philosophical Transactions of the Royal Society A: Mathematical, Physical and Engineering Sciences 372.

Davis, D.M., Nielsen, S.G., Magna, T., Mezger, K., 2018. Constraints on the Vanadium Isotope Composition of Mars, LPSC 49th abstr., p. 1696.

Day, J.M.D., Moynier, F., 2014. Evaporative fractionation of volatile stable isotopes and their bearing on the origin of the Moon. Philos. Trans. R. Soc. A Math. Phys. Eng. Sci. 372, 20130259–20130259. https://doi.org/10.1098/rsta.2013.0259

Day, J.M.D., Moynier, F., Shearer, C.K., 2017. Late-stage magmatic outgassing from a volatile-depleted Moon 114, 9547–9551. https://doi.org/10.1073/pnas.1708236114

de Laeter John, R., Böhlke John, K., De Bièvre, P., Hidaka, H., Peiser, H.S., Rosman, K.J.R., Taylor, P.D.P., 2003. Atomic weights of the elements. Review 2000 (IUPAC Technical Report), Pure and Applied Chemistry, p. 683.

Ding, T.P., Thode, H.G., Rees, C.E., 1983. Sulphur content and sulphur isotope composition of orange and black glasses in Apollo 17 drive tube 74002/1. Geochim. Cosmochim. Acta 47, 491–496. https://doi.org/10.1016/0016-7037(83)90271-5

Dodson, M.H., 1963. A Theoretical Study of Use of Internal Standards for Precise Isotopic Analysis by Surface Ionization Technique .1. General First-Order Algebraic Solutions. J Sci Instrum 40, 289-&.

Drozd, R.J., Hohenber.Cm, Morgan, C.J., Ralston, C.E., 1974. Cosmic-Ray Exposure History at Apollo-16 and Other Lunar Sites - Lunar-Surface Dynamics. Geochim Cosmochim Ac 38, 1625-1642.

Dubois, J.C., Retali, G., Cesario, J. (1992) Isotopic analysis of rare earth elements by total vaporization of samples in thermal ionization mass spectrometry. Int. Journ. Mass Spec. Ion Processes, 120, 163-177.

Eggenkamp, H.G.M., 1994. [Delta]37Cl : the geochemistry of chlorine isotopes, Geologica Ultraiectina. [Faculteit Aardwetenschappen, Universiteit Utrecht].

El Goresy, A., Ramdohr, P., Medenbach, O., Bernhardt, H.J., 1974. Taurus-Littrow TiO2-rich basalts: opaque mineralogy and geochemistry. In: Lunar Science Conference, 5th, Houston, Tex., March 18-22, 1974, Proceedings. Volume 1. (A75-39540 19-91) New York, Pergamon Press, Inc., 1974, p. 627-652. 1, 627-652.

Elkins-Tanton, L.T., Burgess, S., Yin, Q.Z., 2011. The lunar magma ocean: Reconciling the solidification process with lunar petrology and geochronology. Earth Planet Sc Lett 304, 326-336.

Elkins-Tanton, L.T., Burgess, S., Yin, Q.Z., 2011. The lunar magma ocean: Reconciling the solidification process with lunar petrology and geochronology. Earth Planet. Sci. Lett. 304, 326–336. https://doi.org/10.1016/j.epsl.2011.02.004

Eugster, O. 2003. Cosmic-ray Exposure Ages of Meteorites and Lunar Rocks and Their Significance. Chem. Erde Geochemiistry 3-30.

Eugster, O., Tera, F., Burnett, D.S., Wasserburg, G.J., 1970. Isotopic Composition of Gd and Neutron Capture Effects in Samples from Apollo-11. Earth Planet Sc Lett 8, 20-+.

Forrest, J., Newman, L., 1977. Silver-110 microgram sulfate analysis for the short time resolution of ambient levels of sulfur aerosol. Anal. Chem. 49, 1579–84.

Garçon, M., Sauzéat, L., Carlson, R.W., Shirey, S.B., Simon, M., Balter, V., Boyet, M., 2017. Nitrile, Latex, Neoprene and Vinyl Gloves: A Primary Source of Contamination for Trace Element and Zn Isotopic Analyses in Geological and Biological Samples. Geostand. Geoanalytical Res. 41, 367–380. https://doi.org/10.1111/ggr.12161

Goderis, S., Chakrabarti, R., Debaille, V., Kodolanyi, J., 2016. Isotopes in cosmochemistry: recipe for a Solar System. J. Anal. At. Spectrom. 31, 841–862. https://doi.org/10.1039/c5ja00411j

Gounelle, M., Shu, F.H., Shang, H., Glassgold, A.E., Rehm, K.E., Lee, T., 2001. Extinct radioactivities and protosolar cosmic rays: Self-shielding and light elements. Astrophys J 548, 1051-1070.

Greenwood, R.C., Barrat, J.-A., Miller, M.F., Anand, M., Dauphas, N., Franchi, I.A., Sillard, P., Starkey, N.A., 2018. Oxygen isotopic evidence for accretion of Earth's water before a high-energy Moon-forming giant impact. Sci. Adv. 4, eaao5928. https://doi.org/10.1126/sciadv.aao5928

Halliday, A.N., Lee, D.C., Christensen, J.N., Walder, A.J., Freedman, P.A., Jones, C.E., Hall, C.M., Yi, W., Teagle, D., 1995. Recent Developments in Inductively-Coupled Plasma

Magnetic-Sector Multiple Collector Mass-Spectrometry. Int. J. Mass Spectrom. Ion Process. 146, 21–33.

Hallis, L.J., Anand, M., Strekopytov, S., 2014. Trace-element modelling of mare basalt parental melts: Implications for a heterogeneous lunar mantle. Geochim. Cosmochim. Acta 134, 289–316. https://doi.org/10.1016/J.GCA.2014.01.012

Hartmann, W.K., Davis, D.R., 1975. Satellite-Sized Planetesimals and Lunar Origin. Icarus 24, 504–515. https://doi.org/Doi 10.1016/0019-1035(75)90070-6

Hartung, J.B., Hauser, E.E., Horz, F., Morrison, D.A., Schonfeld, E., Zook, H.A., Mandeville, J.-C., McDonnell, J.A.M., Schaal, R.B., Zinner, E., 1978. Lunar surface processes - Report of the 12054 consortium, Lunar and Planetary Science Conference Proceedings, pp. 2507-2537.

Haskin, L., Warren, P., 1991. Lunar Chemistry, in: Heiken, G.H., Vaniman, D.T., French, B.M. (Eds.), Lunar Sourcebook. Cambridge University Press, pp. 357–474.

Herzog, G.F., Moynier, F., Albarède, F., Berezhnoy, A.A., 2009. Isotopic and elemental abundances of copper and zinc in lunar samples, Zagami, Pele's hairs, and a terrestrial basalt. Geochim. Cosmochim. Acta 73, 5884–5904. https://doi.org/10.1016/j.gca.2009.05.067

Hohenberg, C.M., Marti, K., Podosek, F.A., Reedy, R.A., Shirk, J.R. 1978. Comparisons between observed and predicted cosmogenic noble gases in lunar samples. Proc. Lunar Planet. Sci. Conf. 9. 2311-2344.

Hopkins, S.S., Prytulak, J., Barling, J., Russell, S.S., Coles, B.J., Halliday, A.N., 2019. The vanadium isotopic composition of lunar basalts. Earth Planet. Sci. Lett. 511, 12–24. https://doi.org/10.1016/j.epsl.2019.01.008

John, T., Layne, G.D., Haase, K.M., Barnes, J.D., 2010. Chlorine isotope evidence for crustal recycling into the Earth's mantle. Earth Planet. Sci. Lett. 298, 175–182. https://doi.org/10.1016/j.epsl.2010.07.039

Karner, J., Papike, J.J., Shearer, C.K., 2006. Comparative planetary mineralogy: Pyroxene major- and minor-element chemistry and partitioning of vanadium between pyroxene and melt in planetary basalts. Am Mineral 91, 1574-1582.S

Karner, J.M., Sutton, S.R., Papike, J.J., Shearer, C.K., Jones, J.H., Newville, M., 2006. Application of a new vanadium valence oxybarometer to basaltic glasses from the Earth, Moon, and Mars. Am. Mineral. 91, 270–277. https://doi.org/DOI 10.2138/am.2006.1830

Kato, C., Moynier, F., 2017. Gallium isotopic evidence for extensive volatile loss from the Moon during its formation. Sci. Adv. https://doi.org/10.1126/sciadv.1700571

Kato, C., Moynier, F., Valdes, M.C., Dhaliwal, J.K., Day, J.M.D.D., Kato, C., Moynier, F., 2015. Extensive volatile loss during formation and differentiation of the Moon. Nat. Commun. 6, 1–4. https://doi.org/ARTN 7617 10.1038/ncomms8617

Kerridge, J.., Kaplan, I.., Petrowski, C., Chang, S., 1975. Light element geochemistry of the Apollo 16 site. Geochim. Cosmochim. Acta 39, 137–162. https://doi.org/10.1016/0016-7037(75)90167-2 1939–1948.

Kerridge, J.F., Kaplan, I.R., Kung, C.C., Winter, D.A., Friedman, D.L., DesMarais, D.J., 1975a. Light element geochemistry of the Apollo 12 site. Geochim. Cosmochim. Acta 42, 391–402. https://doi.org/10.1016/0016-7037(78)90270-3

Kerridge, J.F., Kaplan, I.R., Petrowski, C., 1975b. Evidence for meteoritic sulfur in the lunar regolith. Lunar Sci. Conf. 6th, Houston, Tex., March 17-21, 1975, Proceedings. Vol. 2. (A78-46668 21-91) New York, Pergamon Press. Inc., 1975, p. 2151-2162. 6, 2151–2162.

Klemme, S., Gunther, D., Hametner, K., Prowatke, S., Zack, T., 2006. The partitioning of trace elements between ilmenite, ulvospinel, annalcolite and silicate melts with implications for the early differentiation of the moon. Chem Geol 234, 251-263.

Konecke, B.A., Fiege, A., Simon, A.C., Holtz, F., 2017. Cryptic metasomatism during late-stage lunar magmatism implicated by sulfur in apatite. Geology 45, 739–742. https://doi.org/10.1130/G39249.1

Koning, A.J., Hilaire, S. and Duijvestijn, M.C. 2008. “TALYS-1.0”, Proceedings of the International Conference on Nuclear Data for Science and Technology, April 22-27, 2007, Nice, France, editors O.Bersillon, F.Gunsing, E.Bauge, R.Jacqmin, and S.Leray, EDP Sciences, p. 211-214.

Kruijer, T.S., Kleine, T., Fischer-Gödde, M., Sprung, P., 2015. Lunar tungsten isotopic evidence for the late veneer. Nature 520, 534–537. https://doi.org/10.1038/nature14360

Larner, F., Rehkämper, M., 2012. Evaluation of Stable Isotope Tracing for ZnO Nanomaterials—New Constraints from High Precision Isotope Analyses and Modeling. Environ. Sci. Technol. 46, 4149–4158. https://doi.org/10.1021/es204440d

Lee, C.-T.A., Brandon, A.D., Norman, M., 2003. Vanadium in peridotites as a proxy for paleo-fO2 during partial melting: prospects, limitations, and implications. Geochim. Cosmochim. Acta 67, 3045–3064. https://doi.org/https://doi.org/10.1016/S0016-7037(03)00268-0

Lee, C.-T.A., Leeman, W.P., Canil, D., Li, Z.-X.A., 2005. Similar V/Sc Systematics in MORB and Arc Basalts: Implications for the Oxygen Fugacities of their Mantle Source Regions. J. Petrol. 46, 2313–2336. https://doi.org/10.1093/petrology/egi056

Lee, T., Shu, F.H., Shang, H., Glassgold, A.E., Rehm, K.E., 1998. Protostellar cosmic rays and extinct radioactivities in meteorites. Astrophys J 506, 898-912.

Li, Z.-X.A., Lee, C.-T.A., 2004. The constancy of upper mantle fO2 through time inferred from V/Sc ratios in basalts. Earth Planet. Sci. Lett. 228, 483–493. https://doi.org/https://doi.org/10.1016/j.epsl.2004.10.006

Lipschutz, M.E., Balsiger, H., Rey, P., Pelly, I.Z., Mendia, M.D., 1973. Vanadium isotopic composition and ferromagnesian element contents of three Apollo 15 samples. Proc. Lunar Sci. Conf. vol. 4, p.1369 4, 1369.

Liu, Y., Spicuzza, M.J., Craddock, P.R., Day, J.M.D., Valley, J.W., Dauphas, N., Taylor, L.A., 2010. Oxygen and iron isotope constraints on near-surface fractionation effects and the composition of lunar mare basalt source regions. Geochim. Cosmochim. Acta 74, 6249–6262. https://doi.org/10.1016/j.gca.2010.08.008

Lock, S.J., Stewart, S.T., Petaev, M.I., Leinhardt, Z., Mace, M.T., Jacobsen, S.B., Cuk, M., 2018. The Origin of the Moon Within a Terrestrial Synestia. J. Geophys. Res. Planets 123, 910–951. https://doi.org/10.1002/2017JE005333

Lodders, K., 2003. Solar System Abundances and Condensation Temperatures of the Elements. Astrophys. J. 591, 1220–1247. https://doi.org/10.1086/375492

Luck, J.M., Othman, D. Ben, Albarède, F., 2005. Zn and Cu isotopic variations in chondrites and iron meteorites: Early solar nebula reservoirs and parent-body processes. Geochim. Cosmochim. Acta 69, 5351–5363. https://doi.org/10.1016/j.gca.2005.06.018

Lugmair, G.W., Shukolyukov, A., 1998. Early solar system timescales according to Mn-53-Cr-53 systematics. Geochim Cosmochim Ac 62, 2863-2886.

Ma, C., Liu, Y., 2019. Discovery of a zinc-rich mineral on the surface of lunar orange pyroclastic beads. Am. Mineral. 104, 447–452. https://doi.org/10.2138/am-2019-6896

Magenheim, A.., Spivack, A.., Volpe, C., Ransom, B., 1994. Precise determination of stable chlorine isotopic ratios in low-concentration natural samples. Geochim. Cosmochim. Acta 58, 3117–3121. https://doi.org/10.1016/0016-7037(94)90183-X

Mallmann, G., O'Neill, H.S.C., 2009. The Crystal/Melt Partitioning of V during Mantle Melting as a Function of Oxygen Fugacity Compared with some other Elements (Al, P, Ca, Sc, Ti, Cr, Fe, Ga, Y, Zr and Nb). J. Petrol. 50, 1765–1794. https://doi.org/10.1093/petrology/egp053

Marechal, C.N., Telouk, P., Albarede, F., 1999. Precise analysis of copper and zinc isotopic compositions by plasma-source mass spectrometry. Chem. Geol. 156, 251–273.

Marti, K. 1967. Mass-Spectrometric Detection of Cosmic-Ray-Produced Kr81 in Meteorites and the Possibility of Kr-Kr Dating. Physical Review Letters, 18, 264-266.

Mason, B., Jarosewich, E., Melson, W.G., 1972. Mineralogy, petrology, and chemical composition of lunar samples 15085, 15256, 15271, 15471, 15475, 15476, 15535, 15555, and 15556. Proceedings of the Lunar Science Conference, vol. 3, p.785 3, 785.

Mastrobuono-Battisti, A., Perets, H.B., Raymond, S.N., 2015. A primordial origin for the compositional similarity between the Earth and the Moon. Nature 520, 212.

https://doi.org/10.1038/nature14333https://www.nature.com/articles/nature14333#supplementary-information

McCubbin, F.M., Kaaden, K.E.V., Tartèse, R., Klima, R.L., Liu, Y., Mortimer, J., Barnes, J.J., Shearer, C.K., Treiman, A.H., Lawrence, D.J., Elardo, S.M., Hurley, D.M., Boyce, J.W., Anand, M., 2015. Magmatic volatiles (H, C, N, F, S, Cl) in the lunar mantle, crust, and regolith: Abundances, distributions, processes, and reservoirs. Am. Mineral. https://doi.org/10.2138/am-2015-4934ccbyncnd

McDonough, W.F., Sun, S.s., 1995. The composition of the Earth. Chem Geol 120, 223-253.

McKay, D.S., Clanton, U.S., Morrison, D.A., 1972. Vapor phase crystallization in Apollo 14 breccia. Proc. Lunar Sci. Conf. vol. 3, p.739 3, 739.

Meyer, C., n.d. Lunar Sample Compendium [WWW Document]. URL https://curator.jsc.nasa.gov/lunar/lsc/ (accessed 4.26.19).

Millet, M.A., Dauphas, N., Greber, N.D., Burton, K.W., Dale, C.W., Debret, B., Macpherson, C.G., Nowell, G.M., Williams, H.M., 2016. Titanium stable isotope investigation of magmatic processes on the Earth and Moon. Earth Planet. Sci. Lett. 449, 197–205. https://doi.org/10.1016/j.epsl.2016.05.039

Moeller, K., Schoenberg, R., Pedersen, R.B., Weiss, D., Dong, S.F., 2012. Calibration of the New Certified Reference Materials ERM-AE633 and ERM-AE647 for Copper and IRMM-3702 for Zinc Isotope Amount Ratio Determinations. Geostand. Geoanalytical Res. 36, 177–199. https://doi.org/10.1111/j.1751-908X.2011.00153.x

Mougel, B., Moynier, F., Gopel, C., 2018. Chromium isotopic homogeneity between the Moon, the Earth, and enstatite chondrites. Earth Planet Sc Lett 481, 1-8.

Moynier, F., Albarède, F., Herzog, G.F., 2006. Isotopic composition of zinc, copper, and iron in lunar samples. Geochim. Cosmochim. Acta 70, 6103–6117. https://doi.org/10.1016/j.gca.2006.02.030

Moynier, F., Beck, P., Yin, Q.-Z., Ferroir, T., Barrat, J.-A., Paniello, R., Telouk, P., Gillet, P., 2010. Volatilization induced by impacts recorded in Zn isotope composition of ureilites. Chem. Geol. 276, 374–379. https://doi.org/10.1016/J.CHEMGEO.2010.07.005

Moynier, F., Paniello, R.C., Gounelle, M., Albarède, F., Beck, P., Podosek, F., Zanda, B., 2011. Nature of volatile depletion and genetic relationships in enstatite chondrites and aubrites inferred from Zn isotopes. Geochim. Cosmochim. Acta 75, 297–307. https://doi.org/10.1016/j.gca.2010.09.022

Moynier, F., Vance, D., Fujii, T., Savage, P., 2017. The Isotope Geochemistry of Zinc and Copper. Rev. Mineral. Geochemistry. https://doi.org/10.2138/rmg.2017.82.13

Neal, C.R., Taylor, L.A., 1992. Petrogenesis of Mare Basalts - a Record of Lunar Volcanism. Geochim. Cosmochim. Acta 56, 2177–2211. https://doi.org/Doi 10.1016/0016-7037(92)90184-K

Nielsen, S.G., Auro, M., Righter, K., Davis, D., Prytulak, J., Wu, F., Owens, J.D., 2019. Nucleosynthetic vanadium isotope heterogeneity of the early solar system recorded in chondritic meteorites. Earth Planet. Sci. Lett. 505, 131–140. https://doi.org/https://doi.org/10.1016/j.epsl.2018.10.029

Nielsen, S.G., Owens, J.D., Horner, T.J., 2016. Analysis of high-precision vanadium isotope ratios by medium resolution MC-ICP-MS. Journal of Analytical Atomic Spectrometry 31, 531-536.

Nielsen, S.G., Prytulak, J., Halliday, A.N., 2011. Determination of Precise and Accurate V-51/V-50 Isotope Ratios by MC-ICP-MS, Part 1: Chemical Separation of Vanadium and Mass Spectrometric Protocols. Geostand. Geoanalytical Res. 35, 293–306. https://doi.org/10.1111/j.1751-908X.2011.00106.x

Nielsen, S.G., Prytulak, J., Wood, B.J., Halliday, A.N., 2014. Vanadium isotopic difference between the silicate Earth and meteorites. Earth Planet. Sci. Lett. 389, 167–175. https://doi.org/10.1016/j.epsl.2013.12.030

O'Neill, H.S.C., Navrotsky, A., 1984. Cation Distributions and Thermodynamic Properties of Binary Spinel Solid-Solutions. Am Mineral 69, 733-753.

Pahlevan, K., Stevenson, D.J., 2007. Equilibration in the aftermath of the lunar-forming giant impact. Earth Planet Sc Lett 262, 438-449.

Pahlevan, K., Stevenson, D.J., Eiler, J.M., 2011. Chemical fractionation in the silicate vapor atmosphere of the Earth. Earth Planet. Sci. Lett. 301, 433–443. https://doi.org/10.1016/j.epsl.2010.10.036

Paniello, R.C., Day, J.M.D.D., Moynier, F., 2012. Zinc isotopic evidence for the origin of the Moon. Nature 490, 376–+. https://doi.org/10.1038/nature11507

Paniello, R.C., Moynier, F., Beck, P., Barrat, J.-A., Podosek, F.A., Pichat, S., 2012. Zinc isotopes in HEDs: Clues to the formation of 4-Vesta, and the unique composition of Pecora Escarpment 82502. Geochim. Cosmochim. Acta 86, 76–87. https://doi.org/10.1016/J.GCA.2012.01.045

Papike, J.J., Hodges, F.N., Bence, A.E., Cameron, M., Rhodes, J.M., 1976. Mare Basalts - Crystal-Chemistry, Mineralogy, and Petrology. Rev Geophys 14, 475-540.

Papike, J.J., Karner, J.M., Shearer, C.K., 2005. Comparative planetary mineralogy: Valence state partitioning of Cr, Fe, Ti, and V among crystallographic sites in olivine, pyroxene, and

spinel from planetary basalts. Am. Mineral. 90, 277–290. https://doi.org/10.2138/am.2005.1779

PELLY, I.Z., LIPSCHUT.ME, BALSIGER, H., 1970. Vanadium Isotopic Composition and Contents in Chondrites. Geochim Cosmochim Ac 34, 1033-&.

Perron, C. 1976. Cross sections for production of stable and long-lived nuclides by high energy spallation of iron; cosmic ray implications. Physical Review C, 14 (3), 1108-1120.

Poitrasson, F., Halliday, A.N., Lee, D.-C., Levasseur, S., Teutsch, N., 2004. Iron isotope differences between Earth, Moon, Mars and Vesta as possible records of contrasted accretion mechanisms. Earth Planet. Sci. Lett. 223, 253–266. https://doi.org/https://doi.org/10.1016/j.epsl.2004.04.032

Pons, M.-L., Debret, B., Bouilhol, P., Delacour, A., Williams, H., 2016. Zinc isotope evidence for sulfate-rich fluid transfer across subduction zones. Nat. Commun. 7, 13794. https://doi.org/10.1038/ncomms13794

Potts, N.J., Barnes, J.J., Tartèse, R., Franchi, I.A., Anand, M., 2018. Chlorine isotopic compositions of apatite in Apollo 14 rocks: Evidence for widespread vapor-phase metasomatism on the lunar nearside ~4 billion years ago. Geochim. Cosmochim. Acta 230, 46–59. https://doi.org/10.1016/j.gca.2018.03.022

Pringle, E.A., Moynier, F., 2017. Rubidium isotopic composition of the Earth, meteorites, and the Moon: Evidence for the origin of volatile loss during planetary accretion. Earth Planet. Sci. Lett. https://doi.org/10.1016/j.epsl.2017.05.033

Prytulak, J., Nielsen, S.G., Halliday, A.N., 2011. Determination of Precise and Accurate V-51/V-50 Isotope Ratios by Multi-Collector ICP-MS, Part 2: Isotopic Composition of Six Reference Materials plus the Allende Chondrite and Verification Tests. Geostand. Geoanalytical Res. 35, 307–318. https://doi.org/10.1111/j.1751-908X.2011.00105.x

Prytulak, J., Nielsen, S.G., Ionov, D.A., Halliday, A.N., Harvey, J., Kelley, K.A., Niu, Y.L., Peate, D.W., Shimizu, K., Sims, K.W.W., 2013. The stable vanadium isotope composition of the mantle and mafic lavas. Earth Planet. Sci. Lett. 365, 177–189. https://doi.org/10.1016/j.epsl.2013.01.010

Prytulak, J., Sossi, P.A., Halliday, A.N., Plank, T., Savage, P.S., Woodhead, J.D., 2017. Stable vanadium isotopes as a redox proxy in magmatic systems? Geochemical Perspect. Lett. 3, 75–84. https://doi.org/10.7185/geochemlet.1708

Qi, Y., Wu, F., Ionov, D., Puchtel, I., Nicklas, R., Yu, H., Kang, J., L,i C. & Huang, F. 2018. The vanadium isotopic composition of the BSE: constraints from peridotites and komatiites Goldschmidt Abstracts, 2018 2088

Qin, L.P., Alexander, C.M.O., Carlson, R.W., Horan, M.F., Yokohama, T., 2010. Contributors to chromium isotope variation of meteorites. Geochim Cosmochim Ac 74, 1122-1145.

Regnier, S., Hohenberg, C.M., Marti, K., Reedy, R.C. 1979. Predicted versus observed cosmic-ray-produced noble gases in lunar samples: Improved Kr production ratios. Proc. Lunar. Sci. Conf. 10. 1565-1586.

Reufer, A., Meier, M.M.M., Benz, W., Wieler, R., 2012. A hit-and-run giant impact scenario. Icarus 221, 296-299.

Reufer, A., Meier, M.M.M., Benz, W., Wieler, R., 2012. A hit-and-run giant impact scenario. Icarus 221, 296–299. https://doi.org/10.1016/j.icarus.2012.07.021

Ringwood, A.E., 1986. Composition and origin of the moon. Orig. moon; Proc. Conf. Kona, HI, Oct. 13-16, 1984 (A86-46974 22-91). Houston, TX, Lunar Planet. Institute, 1986, p. 673-698. 673–698.

Rizzo, A.L., Caracausi, A., Liotta, M., Paonita, A., Barnes, J.D., Corsaro, R.A., Martelli, M., 2013. Chlorine isotope composition of volcanic gases and rocks at Mount Etna (Italy) and inferences on the local mantle source. Earth Planet. Sci. Lett. 371–372, 134–142. https://doi.org/10.1016/j.epsl.2013.04.004

Rufu, R., Aharonson, O., Perets, H.B., 2017. A multiple-impact origin for the Moon. Nat. Geosci. 10, 89–+. https://doi.org/10.1038/Ngeo2866

Ryder, G., Schuraytz, B.C., 2001. Chemical variation of the large Apollo 15 olivine-normative mare basalt rock samples. J Geophys Res-Planet 106, 1435-1451.

Sarafian, A.R., John, T., Roszjar, J., Whitehouse, M.J., 2017. Chlorine and hydrogen degassing in Vesta's magma ocean. Earth Planet. Sci. Lett. 459, 311–319. https://doi.org/10.1016/j.epsl.2016.10.029

Schauble, 2004. Applying Stable Isotope Fractionation Theory to New Systems. Reviews in Mineralogy and Geochemistry 55, 65-111.

Scherer, P., Herrmann, S., Schultz, L. 1998. Noble gases in twenty-one Saharan LL-chondrites: Exposure ages and possible pairings. Meteoritics & Planetary Science 33, 259-265.

Sedaghatpour, F., Teng, F.Z., Liu, Y., Sears, D.W.G., Taylor, L.A., 2013. Magnesium isotopic composition of the Moon. Geochim Cosmochim Ac 120, 1-16.

Seifert, S., Ringwood, A.E., 1988. The lunar geochemistry of chromium and vanadium. Earth Moon and Planets 40, 45-70.

Selverstone, J., Sharp, Z.D., 2011. Chlorine isotope evidence for multicomponent mantle metasomatism in the Ivrea Zone. Earth Planet. Sci. Lett. 310, 429–440. https://doi.org/10.1016/J.EPSL.2011.08.034

Sharp, Z., Williams, J., Shearer, C., Agee, C., McKeegan, K., 2016. The chlorine isotope composition of Martian meteorites 2. Implications for the early solar system and the formation of Mars. Meteorit. Planet. Sci. 51, 2111–2126. https://doi.org/10.1111/maps.12591

Sharp, Z.D., Barnes, J.D., Brearley, A.J., Chaussidon, M., Fischer, T.P., Kamenetsky, V.S., 2007. Chlorine isotope homogeneity of the mantle, crust and carbonaceous chondrites. Nature 446, 1062–1065. https://doi.org/10.1038/nature05748

Sharp, Z.D., Barnes, J.D., Fischer, T.P., Halick, M., 2010a. An experimental determination of chlorine isotope fractionation in acid systems and applications to volcanic fumaroles. Geochim. Cosmochim. Acta 74, 264–273. https://doi.org/10.1016/J.GCA.2009.09.032

Sharp, Z.D., Mercer, J.A., Jones, R.H., Brearley, A.J., Selverstone, J., Bekker, A., Stachel, T., 2013. The chlorine isotope composition of chondrites and Earth. Geochim. Cosmochim. Acta 107, 189–204. https://doi.org/10.1016/J.GCA.2013.01.003

Sharp, Z.D., Shearer, C.K., McKeegan, K.D., Barnes, J.D., Wang, Y.Q., 2010. The Chlorine Isotope Composition of the Moon and Implications for an Anhydrous Mantle. Science (80-.). 329, 1050–1053. https://doi.org/10.1126/science.1192606

Shearer, C.K., Burger, P. V., Guan, Y., Papike, J.J., Sutton, S.R., Atudorei, N. V., 2012. Origin of sulfide replacement textures in lunar breccias. Implications for vapor element transport in the lunar crust. Geochim. Cosmochim. Acta 83, 138–158. https://doi.org/10.1016/j.gca.2011.11.031

Shearer, C.K., Hess, P.C., Wieczorek, M.A., Pritchard, M.E., Parmentier, E.M., Borg, L.E., Longhi, J., Elkins-Tanton, L.T., Neal, C.R., Antonenko, I., Canup, R.M., Halliday, A.N., Grove, T.L., Hager, B.H., Lee, D.C., Wiechert, U., 2006. Thermal and magmatic evolution of the moon. New Views Moon 60, 365–518. https://doi.org/10.2138/rmg.2006.60.4

Shearer, C.K., Sharp, Z.D., Burger, P. V, McCubbin, F.M., Provencio, P.P., Brearley, A.J., Steele, A., 2014. Chlorine distribution and its isotopic composition in “rusty rock” 66095. Implications for volatile element enrichments of “rusty rock” and lunar soils, origin of “rusty” alteration, and volatile element behavior on the Moon. Geochim. Cosmochim. Acta 139, 411–433. https://doi.org/10.1016/j.gca.2014.04.029

Siebert, C., Nägler, T.F., Kramers, J.D., 2001. Determination of molybdenum isotope fractionation by double-spike multicollector inductively coupled plasma mass spectrometry. Geochemistry, Geophys. Geosystems 2, n/a-n/a. https://doi.org/10.1029/2000GC000124

Simpson, J.J., Moorhouse, P., Jagam, P., 1989. Decay of V-50. Phys Rev C 39, 2367-2369.

Sossi, P.A., Bullet, J.P., O’Neill, H.S.C., 2018. Experimental calibration of vanadium partitioning and stable isotope fractionation between hydrous granitic melt and magnetite at 800 degrees C and 0.5 GPa. Contrib. to Mineral. Petrol. 173. https://doi.org/ARTN 2710.1007/s00410-018-1451-8

Sossi, P.A., Moynier, F., 2017. Chemical and isotopic kinship of iron in the Earth and Moon deduced from the lunar Mg-Suite. Earth Planet. Sci. Lett. 471, 125–135. https://doi.org/10.1016/j.epsl.2017.04.029

Sossi, P.A., Moynier, F., Chaussidon, M., Villeneuve, J., Kato, C., Gounelle, M., 2017. Early Solar System irradiation quantified by linked vanadium and beryllium isotope variations in meteorites. Nat Astron 1.

Sossi, P.A., Nebel, O., O'Neill, H.S.C., Moynier, F., 2018. Zinc isotope composition of the Earth and its behaviour during planetary accretion. Chem. Geol. 477, 73–84. https://doi.org/10.1016/j.chemgeo.2017.12.006

Stauffer, H., Honda, M., 1961. Cosmic-ray-produced V50 and K40 in the iron meteorite Aroos. J. Geophys. Res. 66, 3584–3586. https://doi.org/citeulike-article-id:14501964doi: 10.1029/jz066i010p03584

Stauffer, H., Honda, M., 1962. Cosmic-ray-produced stable isotopes in iron meteorites. J. Geophys. Res. 67, 3503–3512. https://doi.org/10.1029/JZ067i009p03503

Storey, M., Saunders, A.D., Tarney, J., Gibson, I.L., Norry, M.J., Thirlwall, M.F., Leat, P., Thompson, R.N., Menzies, M.A., 1989. Contamination of Indian Ocean asthenosphere by the Kerguelen-Heard mantle plume. Nature 338, 574–576. https://doi.org/10.1038/338574a0

Sutton, S.R., Karner, J., Papike, J., Delaney, J.S., Shearer, C., Newville, M., Eng, P., Rivers, M., Dyar, M.D., 2005. Vanadium K edge XANES of synthetic and natural basaltic glasses and application to microscale oxygen barometry. Geochim. Cosmochim. Acta 69, 2333–2348. https://doi.org/10.1016/j.gca.2004.10.013

Tartèse, R., Anand, M., Joy, K.H., Franchi, I.A., 2014. H and Cl isotope systematics of apatite in brecciated lunar meteorites Northwest Africa 4472, Northwest Africa 773, Sayh al Uhaymir 169, and Kalahari 009. Meteorit. Planet. Sci. 49, 2266–2289. https://doi.org/10.1111/maps.12398

Thode, H.G., Rees, C.E., 1976. Sulphur isotopes in grain size fractions of lunar soils, in: 7th Lunar and Planetary Science Conference Proceedings. pp. 459–468.

Thode, H.G., Rees, C.E., 1979. Sulphur isotopes in lunar and meteorite samples. Lunar Planet. Sci. Conf. Proc. 2, 1629.

Tian Z, Chen H, Fegley, Jr B, Lodders K, Korotev R & Wang K (2018) Goldschmidt Abstracts, 2018 2537

Urey, H.C., 1947, The thermodynamic properties of isotopic substances. J Chem Soc (London), 562-581

Wang, K., Jacobsen, S.B., 2016. Potassium isotopic evidence for a high-energy giant impact origin of the Moon. Nature 538, 487–490. https://doi.org/10.1038/nature19341

Warren, P.H., 1985. The Magma Ocean Concept and Lunar Evolution. Annu. Rev. Earth Planet. Sci. 13, 201–240. https://doi.org/DOI 10.1146/annurev.ea.13.050185.001221

Weyer, S., Anbar, A.D., Brey, G.P., Münker, C., Mezger, K., Woodland, A.B., 2005. Iron isotope fractionation during planetary differentiation. Earth Planet. Sci. Lett. 240, 251–264. https://doi.org/https://doi.org/10.1016/j.epsl.2005.09.023

Wiechert, U., Halliday, A.N., Lee, D.C., Snyder, G.A., Taylor, L.A., Rumble, D., 2001. Oxygen isotopes and the moon-forming giant impact. Science (80-.). 294, 345–348. https://doi.org/DOI 10.1126/science.1063037

Wiesli, R.A., Beard, B.L., Taylor, L.A., Johnson, C.M., 2003. Space weathering processes on airless bodies: Fe isotope fractionation in the lunar regolith. Earth Planet. Sci. Lett. 216, 457–465. https://doi.org/https://doi.org/10.1016/S0012-821X(03)00552-1

Wing, B.A., Farquhar, J., 2015. Sulfur isotope homogeneity of lunar mare basalts. Geochim. Cosmochim. Acta 170, 266–280. https://doi.org/10.1016/j.gca.2015.09.003

Wolf, R., Anders, E., 1980. Moon and Earth : compositional differences inferred from siderophiles, volatiles, and alkalis in basalts. Geochim. Cosmochim. Acta 44, 2111–2124. https://doi.org/10.1016/0016-7037(80)90208-2

Wood, B.J., Wade, J., Kilburn, M.R., 2008. Core formation and the oxidation state of the Earth: Additional constraints from Nb, V and Cr partitioning. Geochim. Cosmochim. Acta 72, 1415–1426. https://doi.org/https://doi.org/10.1016/j.gca.2007.11.036

Wu, F., Qi, Y., Perfit, M.R., Gao, Y., Langmuir, C.H., Wanless, V.D., Yu, H., Huang, F., 2018. Vanadium isotope compositions of mid-ocean ridge lavas and altered oceanic crust. Earth Planet. Sci. Lett. 493, 128–139. https://doi.org/https://doi.org/10.1016/j.epsl.2018.04.009

Wu, F., Qi, Y.H., Yu, H.M., Tian, S.Y., Hou, Z.H., Huang, F., 2016. Vanadium isotope measurement by MC-ICP-MS. Chem. Geol. 421, 17–25. https://doi.org/10.1016/j.chemgeo.2015.11.027

Xue, Y., Li, C.-H., Zhang, C., Miao, B., Huang, F. 2018. The vanadium isotopic composition of L ordinary chondrites. Acta Geochim 37(4):501:508.

Yokoyama, T., Makishima, A., Nakamura, E., 1999. Evaluation of the coprecipitation of incompatible trace elements with fluoride during silicate rock dissolution by acid digestion. Chem Geol 157, 175-187.

Young, E.D., Kohl, I.E., Warren, P.H., Rubie, D.C., Jacobson, S.A., Morbidelli, A., 2016. Oxygen isotopic evidence for vigorous mixing during the Moon-forming giant impact. Science (80-.). 351, 493–496. https://doi.org/10.1126/science.aad0525

Zhang, J.J., Dauphas, N., Davis, A.M., Leya, I., Fedkin, A., 2012. The proto-Earth as a significant source of lunar material. Nat Geosci 5, 251-255.

A1

Appendix 1: Results of Quad ICPMS analysis for lunar basalts and BHVO2

Appendix 1 Results of Quad ICPMS analysis for lunar basalts and BHVO2

Sample		10017	+/-	10017	+/-	10020	+/-	10044	+/-	12018	+/-	12054	+/-	12054	+/-	12063	+/-	14053	+/-	15016	+/-
Sub-sample		400		405		255		655		277		146		150		343		305		240	
TiO2	wt%	11.2	0.2	11.3	0.2	10.7	0.4	9.58	0.23	2.10	0.11	5.28	0.28	4.06	0.12	4.91	0.13	2.71	0.18	2.09	0.08
Al2O3	wt%	7.86	0.14	8.26	0.27	8.67	0.19	8.53	0.43	7.35	0.45	10.6	0.1	11.1	0.3	8.10	0.30	13.2	0.5	8.51	0.40
FeO	wt%	20.3	0.2	19.9	0.3	18.8	0.2	19.0	0.3	20.6	0.3	20.8	0.4	20.4	0.4	21.4	0.5	17.2	0.3	22.3	0.3
MgO	wt%	7.83	0.20	7.93	0.16	7.81	0.13	5.67	0.15	15.1	0.4	6.74	0.20	6.80	0.13	9.82	0.27	8.75	0.25	11.3	0.3
MnO	wt%	0.246	0.004	0.247	0.011	0.262	0.007	0.274	0.007	0.266	0.004	0.280	0.008	0.283	0.012	0.272	0.005	0.256	0.016	0.284	0.011
K2O	wt%	0.324	0.002	0.309	0.002	0.056	0.001	0.098	0.001	0.046	0.001	0.077	0.001	0.074	0.001	0.062	0.001	0.101	0.001	0.041	0.001
Sc	ppm	91.9	3.0	90.5	6.4	94.6	2.0	101	3	46.3	3.9	77.2	4.1	75.5	2.2	62.5	3.1	61.5	5.9	43.0	2.4
V	ppm	67.6	2.2	70.4	2.5	104	2	42.0	2.9	182	5	118	6	143	4	115	4	108	5	234	4
Cr	ppm	2786	40	2638	30	2774	30	1803	30	4371	40	2606	50	2441	20	3693	60	2769	50	5771	30
Co	ppm	26.1	0.7	26.7	0.8	17.1	0.4	9.0	0.2	57.6	1.0	24.4	0.9	33.9	0.6	32.3	1.2	25.1	1.0	51.9	1.2
Ni	ppm	5.3	0.4	5.5	0.1	2.2	0.3	0.50	0.1	75.5	2.8	5.0	0.6	9.6	0.4	23.6	0.9	10.6	0.8	65.1	1.9
Cu	ppm	4.7	0.3	4.7	0.5	5.0	0.5	2.4	0.3	20.3	1.2	5.7	0.4	7.8	0.2	4.2	0.4	19.2	0.7	6.3	0.5
Zn	ppm	8.8	2.9	7.6	2.5	2.9	1.0	2.9	0.9	1.9	0.6	2.0	0.6	3.3	1.1	1.3	0.4	4.1	1.3	1.2	0.4
Sr	ppm	182	6	181	7	132	3	165	4	80	3	161	6	176	6	136	5	105	4	83	4
Y	ppm	182	7	175	3	80	4	116	2	30	2	44	1	55	1	36	0	53	2	24	1
Zr	ppm	516	13	504	9	210	5	222	8	89	3	113	5	127	2	92	2	208	6	90	3
Nb	ppm	22.6	0.6	23.3	0.4	14.4	0.7	9.5	0.4	1.2	1.4	6.8	0.2	4.2	0.2	0.5	0.1	2.9	0.8	5.6	0.3
Ba	ppm	305	10	294	7	64	1	83	1	52	1	51	2	74	2	39	2	151	2	47	1
La	ppm	28.9	0.9	27.8	0.7	7.77	0.11	8.6	0.4	5.28	0.28	5.44	0.30	7.20	0.08	4.09	0.31	12.9	0.3	5.08	0.21
Ce	ppm	82.3	2.8	80.3	2.8	23.7	0.6	30.2	1.1	13.9	0.4	16.3	0.3	20.8	0.6	12.4	0.5	34.7	0.6	14.0	0.6
Pr	ppm	12.5	0.4	11.9	0.5	3.93	0.11	5.25	0.23	2.06	0.14	2.56	0.20	3.36	0.19	2.01	0.06	4.86	0.23	2.03	0.17
Nd	ppm	62.3	1.8	59.6	1.3	21.7	0.9	30.6	1.8	10.3	0.5	13.6	1.1	17.1	1.3	10.5	1.7	20.4	1.8	10.0	1.0
Sm	ppm	22.6	0.4	20.8	0.4	8.23	0.21	12.8	0.4	3.59	0.63	5.03	0.91	6.18	0.24	4.07	0.27	6.19	0.70	3.20	0.46
Eu	ppm	2.46	0.10	2.32	0.04	1.61	0.09	1.88	0.06	0.84	0.03	1.22	0.11	1.64	0.11	0.99	0.11	1.31	0.02	0.87	0.03
Gd	ppm	29.1	0.8	28.2	0.7	12.6	0.9	18.7	0.8	4.97	0.48	7.25	0.70	9.22	0.45	5.87	0.09	7.91	0.38	4.38	0.55
Tb	ppm	5.33	0.24	5.18	0.17	2.32	0.03	3.37	0.19	0.89	0.02	1.29	0.04	1.67	0.06	1.08	0.08	1.55	0.11	0.76	0.02
Dy	ppm	35.8	0.8	34.2	1.7	15.9	0.6	22.6	0.8	6.1	0.3	8.8	0.3	11.6	0.3	7.2	0.3	10.2	1.0	5.10	0.26
Ho	ppm	7.52	0.17	7.40	0.31	3.25	0.08	4.77	0.19	1.19	0.05	1.79	0.06	2.32	0.07	1.46	0.05	2.12	0.15	0.97	0.06
Er	ppm	22.5	0.6	21.3	0.3	10.0	0.2	14.5	0.7	3.6	0.1	5.2	0.2	6.9	0.4	4.5	0.4	6.5	0.4	2.8	0.1
Tm	ppm	3.11	0.09	3.04	0.05	1.41	0.10	2.02	0.12	0.54	0.04	0.75	0.04	1.00	0.03	0.62	0.01	0.98	0.01	0.37	0.02
Yb	ppm	19.2	0.6	18.5	0.8	8.8	0.4	12.7	1.0	2.9	0.2	4.7	0.3	6.0	0.4	3.9	0.6	6.4	0.4	2.3	0.1
Lu	ppm	2.71	0.08	2.63	0.06	1.30	0.05	1.80	0.13	0.44	0.04	0.65	0.06	0.86	0.05	0.53	0.09	0.85	0.07	0.31	0.03
Hf	ppm	17.2	0.6	16.1	0.6	7.34	0.36	8.11	0.38	2.60	0.17	3.86	0.08	4.47	0.29	3.08	0.07	5.23	0.31	2.67	0.06
Pb	ppm	1.21	0.05	1.21	0.09	0.25	0.02	0.25	0.04	0.39	0.05	0.19	0.06	0.29	0.06	0.15	0.05	1.11	0.11	0.15	0.03
Th	ppm	3.73	0.12	3.55	0.09	0.85	0.05	0.82	0.09	1.00	0.07	0.90	0.07	1.10	0.07	0.63	0.09	2.20	0.10	0.79	0.02
U	ppm	0.92	0.06	0.82	0.03	0.13	0.02	0.14	0.04	0.15	0.05	0.13	0.01	0.18	0.01	0.10	0.03	0.46	0.04	0.07	0.03
Li	ppm	19.9	1.1	19.1	2.1	9.0	1.3	10.3	1.7	7.05	1.45	7.15	1.46	11.1	1.4	5.87	1.73	11.9	0.8	6.84	0.87

Error comprises internal measurement RSD and external 2SD (based upon secondary monitor standards throughout the session).

References for BHVO2

Jochum, K.P, Weis, U., Schwager, B., Stoll, B., Wilson, S.A., Haug, G.H., Andreae, M.O., Enzweiler, J. (2016)
Reference Values Following ISO Guidelines for Frequently Requested Rock Reference Materials. Geostandards and Geoanalytical Research. 40, 333-350.

Appendix 1 Results of Quad ICPMS analysis for lunar basalts and BHVO2

Sample		15535	+/-	15556	+/-	70255	+/-	71135	+/-	74275	+/-	75035	+/-	BHVO2	+/-	BHVO2 lit.	+/-	Detection	
Sub-sample		165		258		56		34		355		249				*Jochum et al., 2016*		Limit	
TiO2	wt%	2.06	0.12	2.35	0.12	10.8	0.6	10.3	0.2	12.4	0.6	10.5	0.4	2.74	0.17	2.73	0.02	0.0033	wt%
Al2O3	wt%	7.95	0.37	8.58	0.36	8.86	0.30	9.36	0.52	7.95	0.16	8.84	0.30	9.67	0.49	13.4	0.1	0.0045	wt%
FeO	wt%	23.0	0.4	21.4	0.6	18.5	0.4	18.6	0.3	18.2	0.5	18.5	0.3	11.0	0.2	11.1	0.1	0.0107	wt%
MgO	wt%	11.1	0.3	8.58	0.28	8.37	0.35	7.46	0.28	10.4	0.3	6.15	0.36	5.53	0.18	7.26	0.04	0.0052	wt%
MnO	wt%	0.287	0.012	0.277	0.010	0.264	0.008	0.274	0.012	0.250	0.003	0.271	0.006	0.160	0.013	0.169	0.002	0.0004	wt%
K2O	wt%	0.044	0.001	0.045	0.001	0.066	0.001	0.052	0.001	0.091	0.001	0.081	0.002	0.310	0.028	0.513	0.004	0.0482	wt%
Sc	ppm	44.3	1.8	47.5	3.3	94.7	5.6	96.2	3.6	85.4	2.7	93.1	3.8	33.7	1.2	31.8	0.3	0.16	ppm
V	ppm	217	1	211	6	91.8	1.4	100.5	2.0	118	3	37.0	1.0	300	19	318	2	0.06	ppm
Cr	ppm	4578	80	4369	90	3499	40	2562	50	6315	130	2059	20	288	14	287	3	0.09	ppm
Co	ppm	55.8	1.3	45.5	1.5	19.1	0.7	18.1	0.3	20.2	0.5	14.7	0.3	46	1.4	45	0.3	0.04	ppm
Ni	ppm	67.9	1.7	47.6	1.4	1.5	0.1	1.3	0.1	6.7	0.7	0.7	0.1	127	5	120	1	0.1	ppm
Cu	ppm	7.6	0.6	7.4	0.7	10.7	0.6	4.8	0.5	3.1	0.3	3.6	0.2	126	5	129	1	0.05	ppm
Zn	ppm	3.8	1.2	1.8	0.6	3.7	1.2	2.9	0.9	3.1	1.0	3.7	1.2	103	2	104	1	0.30	ppm
Sr	ppm	89	4	101	4	171	4	137	5	161	3	202	6	369	26	394	2	0.07	ppm
Y	ppm	24	1	24	1	90	3	71	1	73	3	106	3	21	2	25.9	0.3	0.04	ppm
Zr	ppm	87	1	89	3	221	6	192	4	207	4	289	6	165	7	171	1	3.37	ppm
Nb	ppm	0.7	0.4	0.9	0.4	16.3	0.4	15.5	0.3	18.1	1.0	21.8	0.7	18.9	1.0	18.1	0.2	0.1	ppm
Ba	ppm	49	2	50	2	74	3	65	1	60	1	90	2	114	7	131	1	0.02	ppm
La	ppm	5.04	0.19	5.00	0.15	6.00	0.23	5.92	0.27	5.63	0.11	7.29	0.41	15.3	0.7	15.2	0.1	0.01	ppm
Ce	ppm	13.9	0.4	13.8	0.2	20.4	0.6	19.3	0.6	19.2	0.5	25.5	0.4	37.3	1.2	37.5	0.2	0.01	ppm
Pr	ppm	2.08	0.19	2.10	0.17	3.66	0.15	3.46	0.08	3.57	0.12	4.63	0.12	4.92	0.44	5.34	0.03	0.01	ppm
Nd	ppm	10.9	1.0	9.9	0.9	23.0	1.7	19.3	0.8	20.4	0.5	27.0	0.9	23.0	2.1	24.3	0.3	0.08	ppm
Sm	ppm	3.13	0.51	3.54	0.49	9.60	0.45	7.97	0.42	8.49	0.42	11.4	0.3	5.99	0.78	6.02	0.06	0.03	ppm
Eu	ppm	0.91	0.09	0.98	0.04	2.18	0.07	1.69	0.08	1.66	0.09	2.30	0.09	2.08	0.20	2.04	0.01	0.004	ppm
Gd	ppm	4.44	0.30	4.58	0.43	14.2	0.5	11.5	0.3	12.3	0.5	16.6	0.6	5.35	0.65	6.21	0.04	0.007	ppm
Tb	ppm	0.77	0.03	0.77	0.06	2.64	0.15	2.18	0.03	2.20	0.08	3.19	0.07	0.87	0.08	0.94	0.01	0.004	ppm
Dy	ppm	5.21	0.25	5.01	0.40	18.3	0.9	14.3	0.3	14.8	0.3	21.7	0.7	5.05	0.50	5.28	0.03	0.004	ppm
Ho	ppm	0.97	0.08	0.96	0.10	3.77	0.20	3.02	0.06	3.14	0.09	4.49	0.13	1.03	0.09	0.99	0.01	0.006	ppm
Er	ppm	2.8	0.2	2.9	0.3	11.1	0.4	8.7	0.4	9.1	0.3	13.4	0.2	2.7	0.2	2.5	0.0	0.005	ppm
Tm	ppm	0.42	0.03	0.38	0.03	1.56	0.07	1.27	0.04	1.24	0.04	1.91	0.03	0.23	0.03	0.33	0.00	0.004	ppm
Yb	ppm	2.3	0.1	2.1	0.2	9.9	0.4	7.7	0.4	7.9	0.3	11.9	0.3	1.7	0.3	2.0	0.0	0.005	ppm
Lu	ppm	0.29	0.02	0.33	0.03	1.43	0.08	1.13	0.07	1.13	0.05	1.70	0.07	0.18	0.05	0.28	0.00	0.003	ppm
Hf	ppm	2.40	0.27	2.65	0.07	8.50	0.26	6.94	0.58	7.65	0.30	10.11	0.38	4.98	0.32	4.47	0.03	0.05	ppm
Pb	ppm	0.17	0.04	0.15	0.02	0.19	0.01	0.16	0.02	0.17	0.02	0.18	0.07	1.85	0.18	1.65	0.04	0.03	ppm
Th	ppm	0.74	0.05	0.75	0.07	0.57	0.02	0.62	0.04	0.54	0.01	0.66	0.03	1.15	0.12	1.22	0.02	0.40	ppm
U	ppm	0.06	0.02	0.09	0.04	0.07	0.02	0.07	0.02	0.09	0.02	0.07	0.02	0.38	0.04	0.41	0.04	0.04	ppm
Li	ppm	6.29	0.57	6.77	1.08	9.60	1.77	8.16	2.34	6.62	1.21	10.17	1.66	3.31	1.69	4.50	0.09	0.09	ppm

A2

Appendix 2: Literature Data

2a Published trace elements for this suite

2b Published mineralogical values for this suite

2c Gadolinium isotope data

2d Exposure age data

2e Published trace element data for all lunar basalts

2f Chondrite exposure age and V isotope data

2g REE data for this suite

2h References for tables in this appendix

Appendix 2a: Published trace element values for lunar basalts in this study

Sample	References (Table S110	Mission		SiO_2(wt%)	TiO_2(wt%)	Al_2O_3(wt%)	FeO(wt%)	CaO(wt%)	MgO(wt%)	MnO(wt%)	K_2O(wt%)	Na_2O(wt%)	P2O5(wt%)	S(wt%)	Sc(ppm)	V(ppm)	Cr(ppm)	Co(ppm)	Ni(ppm)	Cu(ppm)	Zn(ppm)	Ga(ppm)	Ge(ppb)	As(ppm)	Se(ppm)	Br(ppm)
10017	2,13,34,41,68,74,94,131,150,	A11	AVERAGE	41.42	11.73	8.01	19.78	10.51	7.82	0.24	0.74	0.50	0.15	0.24	77	125	2468	27	6	16	55	13.3	0.0		0.2	0.2
10017	154,165,181,223,230,242,243,		2SD	3.23	1.18	1.45	2.97	2.04	0.74	0.09	2.21	0.09	0.08	0.05	28	462	1550	14	1	27	25	41.8	0.0			
10017	257,262		MIN	39.11	11.00	7.28	17.37	8.13	7.15	0.19	0.17	0.46	0.09	0.22	52	30	1500	10	6	3	47	4.0	0.0		0.2	0.2
10017			MAX	44.50	13.01	10.00	23.29	12.40	8.50	0.35	3.20	0.65	0.18	0.27	96	820	4600	37	6	33	74	56.0	0.0		0.2	0.2
10017			N	10	10	11	13	12	10	10	12	13	5	3	12	11	11	11	2	4	4	6	2		1	1
10020	13,41,46,65,68,80,90,94,102,	A11	AVERAGE	39.84	10.39	10.11	18.91	11.70	7.76	0.27	0.27	0.40	0.09	0.19	88	87	2302	15	26	9	14	4.4	0.0	0.0	0.3	0.1
10020	131,143,165,187,223,230,243,		2SD	2.30	2.14	1.27	1.85	3.97	1.31	0.04	1.36	0.13	0.05	0.08	22	73	892	12	60	15	28	4.2		0.0	0.2	0.1
10020	250,263		MIN	38.00	7.67	9.23	18.00	9.30	6.46	0.24	0.03	0.35	0.07	0.15	72	20	1600	3	4	4	1	1.9	0.0	0.0	0.3	0.0
10020			MAX	41.51	12.00	11.15	21.20	17.08	8.70	0.32	2.20	0.59	0.13	0.24	110	120	3000	21	60	20	26	7.5	0.0	0.1	0.4	0.1
10020			N	8	11	9	11	11	9	10	10	11	7	4	9	7	7	10	3	4	4	5	1	2	2	2
10044	1,9,12,13,23,60,61,74,90,94,1	A11	AVERAGE	42.38	9.09	10.62	18.08	11.67	6.14	0.27	0.10	0.46	0.07	0.20	93	43	1363	13	7	12	34	6.3			0.2	
10044	02,150,154,181,187,223,242,2		2SD	1.17	2.02	2.08	2.02	3.09	0.67	0.04	0.06	0.09	0.07	0.06	17	30	393	4	12	26	86	4.5				
10044	50,257,262		MIN	41.51	6.67	8.69	16.72	7.14	5.80	0.24	0.03	0.37	0.04	0.18	78	27	1168	10	1	4	3	5.0			0.2	
10044			MAX	43.30	10.51	11.90	20.46	12.73	6.80	0.30	0.13	0.50	0.12	0.22	105	66	1700	16	15	38	64	8.9			0.2	
10044			N	9	12	10	11	11	9	10	9	12	5	2	10	7	10	9	4	6	2	3.0			1.0	
12018	20,21,21,25,33,39,73,105,124	A12	AVERAGE	43.42	2.63	8.48	20.95	8.13	14.28	0.31	0.11	0.25	0.05	0.05	45	163	3870	54	82	6	4	4.0	0.3	0.0	0.2	0.1
12018	,185,205		2SD	3.52	0.24	3.12	0.86	2.79	3.45	0.26	0.19	0.22	0.06		24	80	760	18	39	3	4	5.4	0.6	0.1	0.0	
12018			MIN	40.01	2.42	6.92	20.56	6.16	11.28	0.25	0.04	0.19	0.02	0.05	39	96	3540	42	55	4	2	1.5	0.1	0.0	0.2	0.1
12018			MAX	45.15	2.84	12.09	21.73	10.35	15.54	0.61	0.25	0.50	0.07	0.05	70	200	4600	70	100	8	6	9.0	0.5	0.1	0.2	0.1
12018			N	6	8	8	8	6	5	7	7	7	3	1	6	6	6	6	4	6	3	6	2	2	3	1
12054	70,154,157,189	A12	AVERAGE	45.86	4.67	10.29	19.86	10.97	7.23	0.28	0.07	0.30	0.06	0.09	69	168	2430	35	20	27	37	4.1				
12054			2SD		0.10	0.52	0.98	2.73	1.33	0.04	0.01	0.03			17	69	727	8	31							
12054			MIN	45.86	4.63	10.10	19.51	10.00	6.76	0.26	0.06	0.29	0.06	0.09	64	144	2150	31	9	27	37	4.1				
12054			MAX	45.86	4.70	10.47	20.20	11.93	7.70	0.29	0.07	0.31	0.06	0.09	79	193	2841	39	31	27	37	4.1				
12054			N	1	2	2	2	2	2	2	2	2	1	1	3	2	3	3	2	1	1	1				
12063	8,16,21,21,25,32,53,54,56,81,	A12	AVERAGE	43.23	4.74	9.44	20.99	11.19	9.85	2.13	0.07	0.33	0.14	0.09	67	124	2993	41	36	12	11	5.0	0.5	0.1	0.4	0.1
12063	102,124,138,152,154,157,165,		2SD	2.03	0.69	2.57	1.19	2.56	2.46	8.31	0.02	0.26			43	84	791	18	27	14	25	2.6	1.0	0.1		
12063	171,176,216,233,240,255,256,		MIN	41.94	4.17	7.99	20.07	9.93	8.38	0.26	0.06	0.26	0.14	0.09	55	54	2500	23	20	5	2	3.8	0.1	0.1	0.4	0.1
12063	280,282		MAX	44.72	5.00	11.53	21.74	13.01	11.40	9.56	0.08	0.59	0.14	0.09	123	167	3575	54	49	23	32	7.0	0.8	0.1	0.4	0.1
10020			N	8	11	9	11	11	9	10	10	11	7	4	9	7	7	10	3	4	4	5	1	2	2	2
14053	30,31,37,41,52,56,84,86,90,9	A14	AVERAGE	46.67	2.63	13.08	16.86	11.30	8.42	0.26	0.11	0.44	0.12	0.14	55	111	2620	30	15	20	14	12.4	0.4		0.1	0.1
14053	2,142,154,156,177,231,241,24		2SD	1.82	1.04	1.35	1.19	0.96	0.71	0.04	0.03	0.07	0.04	0.01	24	37	1429	14	7	20	25	31.3	0.4			
14053	5,274,282		MIN	45.87	1.50	12.09	16.15	10.61	7.81	0.23	0.10	0.38	0.09	0.13	47	89	2102	22	11	13	2	2.5	0.2		0.1	0.1
14053			MAX	48.35	3.00	13.92	18.60	12.24	8.97	0.28	0.14	0.49	0.14	0.14	90	135	4400	48	21	32	25	42.0	0.6		0.1	0.1
14053			N	7	7	7	14	9	7	5	6	9	5	2	11	4	9	10	5	3	4	6	2		1	1
15016	6,28,29,35,38,53,62,71,83,90,	A15	AVERAGE	44.07	2.27	9.07	21.90	9.37	11.13	0.30	0.04	0.26	0.09	0.09	36	223	5701	58	79	9	6	3.7	0.0		0.1	
15016	92,100,104,106,145,146,154,1		2SD	0.61	0.56	4.37	3.45	0.99	1.27	0.05	0.01	0.09	0.12	0.13	12	112	1491	10	21	10	17	1.3	0.0			
15016	73,188,200,220,238,246,283		MIN	43.56	1.77	8.07	16.53	9.00	9.17	0.26	0.03	0.21	0.06	0.04	25	140	4100	53	66	0	1	2.7	0.0		0.1	
15016			MAX	44.60	3.00	15.97	23.29	10.93	11.76	0.33	0.05	0.32	0.25	0.19	42	304	6400	65	98	14	18	4.6	0.0		0.1	
15016			N	11	12	12	13	13	14	11	10	12	9	4	8	6	7	8	10	5	4	9	3		1	
15535	6,82,83,124,154,184,200	A15	AVERAGE	44.77	2.23	8.54	22.75	9.41	11.11	0.30	0.04	0.25	0.07		45	201	4758	59	70	13	7	3.2	0.0			0.0
15535			2SD	1.04	0.14	0.27	1.30	0.40	0.42	0.06	0.00	0.05	0.04		10	174	413	17	24	10	19	1.0	0.0			0.0
15535			MIN	44.20	2.15	8.37	22.10	9.20	10.80	0.28	0.04	0.22	0.06		41	140	4580	52	46	8	1	2.7	0.0			0.0
15535			MAX	45.30	2.31	8.68	23.80	9.68	11.27	0.33	0.04	0.28	0.09		48	263	5094	69	83	18	18	3.8	0.0			0.0
15535			N	4	4	4	5	4	4	3	4	5	3		2	2	5	3	7	3	3	4	2			2
15556	26,66,71,90,124,136,137,145,	A15	AVERAGE	45.59	2.61	9.46	21.74	10.58	8.10	0.28	0.05	0.27	0.08	0.08	45	261	5163	51	61	10	10	4.2	0.0		0.1	0.0
15556	146,147,154,188,200,220,228,		2SD	1.58	0.37	0.34	0.66	0.47	0.59	0.05	0.04	0.06	0.02		11	124	1390	8	26	10	20	1.1			0.1	
15556	246		MIN	44.70	2.05	9.24	21.30	9.93	7.73	0.23	0.03	0.18	0.07	0.08	35	165	4094	46	40	3	1	3.7	0.0		0.1	0.0
15556			MAX	47.00	2.76	9.85	22.25	10.83	8.67	0.32	0.09	0.30	0.09	0.08	52	358	6177	59	82	17	21	5.0	0.0		0.1	0.0
15556			N	10	12	11	13	15	12	13	12	12	9	2	6	6	9	10	11	8	4	4	1		2	1
70215	27,41,47,50,58,69,71,72,90,1	A17	AVERAGE	37.75	12.86	8.69	19.72	11.16	8.70	0.27	0.04	0.42	0.09	0.16	87	167	2395	22	2	11	13	7.3	0.0	0.0	0.2	0.0
70215	26,134,135,140,147,165,166,1		2SD	1.38	0.70	0.61	2.06	2.25	2.17	0.02	0.04	0.39	0.04	0.10	11	265	819	11	3	19	45	14.4	0.0		0.0	0.0
70215	80,186,190,190,191,194,212,2		MIN	36.44	12.18	7.90	17.96	10.38	7.46	0.25	0.01	0.31	0.05	0.06	77	50	1940	15	1	4	2	3.1	0.0	0.0	0.2	0.0
70215	47,259		MAX	38.71	13.32	9.11	22.50	14.59	11.94	0.29	0.08	1.08	0.11	0.19	92	349	3030	33	4	22	59	20.0	0.0	0.0	0.2	0.0
70215			N	13	15	14	17	16	14	12	9	14	8	6	6	6	6	7	3	3	6	5	3	1	2	2
70255	90,165,190,265	A17	AVERAGE	40.11	11.36	9.06	19.52	10.95	7.82	0.29	0.06	0.39	0.04	0.19	85	76	2860	19								
70255			2SD		0.16	0.11	2.22	0.99	0.52		0.04	0.00			14			3								
70255			MIN	40.11	11.30	9.02	18.73	10.60	7.63	0.29	0.05	0.39	0.04	0.19	80	76	2860	18								
70255			MAX	40.11	11.41	9.10	20.30	11.30	8.00	0.29	0.08	0.39	0.04	0.19	90	76	2860	20								
70255			N	1	2	2	2	2	2	1	2	2	1	1	2	1	1	2								
71135	58,72,166,190,212	A17	AVERAGE	39.71	10.74	10.10	18.57	11.62	7.31	0.28	0.05	0.38	0.06	0.11	82			18								
71135			2SD																							
71135			MIN	39.71	10.74	10.10	18.57	11.62	7.31	0.28	0.05	0.38	0.06	0.11	82			18								
71135			MAX	39.71	10.74	10.10	18.57	11.62	7.31	0.28	0.05	0.38	0.06	0.11	82			18								
71135			N	1	1	1	1	1	1	1	1	1	1	1	1			1								
71546	59,72,165,190,266	A17	AVERAGE	39.14	12.22	9.06	18.41	10.90	7.92	0.26	0.06	0.39	0.05	0.19	79	120	3450	18								
71546			2SD		0.33	0.41	1.99	0.30	1.19	0.06	0.03	0.03			4			1								
71546			MIN	39.14	12.10	8.91	17.70	10.79	7.50	0.24	0.05	0.38	0.05	0.19	77	120	3450	18								
71546			MAX	39.14	12.33	9.20	19.11	11.00	8.34	0.28	0.07	0.40	0.05	0.19	80	120	3450	18								
71546			N	1	2	2	2	2	2	2	2	2	1	1	2	1	1	2								
74275	27,41,47,69,71,72,90,134,149	A17	AVERAGE	38.45	12.34	8.64	18.32	10.59	10.34	0.26	0.08	0.35	0.06	0.14	74	100	3465	23	9	24	24	9.6	0.0	0.0		
74275	,154,163,165,174,180,186,190		2SD	1.38	0.97	0.51	1.56	1.68	0.44	0.02	0.02	0.05	0.02	0.00	12	64	927	7	13	48	63	17.9	0.0			
74275	,195,237,260		MIN	37.24	11.76	8.32	17.59	9.37	10.11	0.25	0.07	0.32	0.06	0.14	66	62	2740	21	5	3	2	3.0	0.0	0.0		
74275			MAX	39.59	13.09	9.07	20.19	12.60	10.78	0.27	0.09	0.39	0.07	0.14	83	146	3900	31	16	49	74	25.0	0.0	0.0		
74275			N	7	9	8	8	11	8	6	4	8	3	2	7	5	5	8	3	4	5	6	2	1		
75035	27,46,69,71,72,107,134,135,1	A17	AVERAGE	41.09	10.51	9.33	18.69	11.66	7.02	0.25	0.07	0.43	0.07	0.22	79	43	2657	16	5	13	3	4.6	0.0	0.0	0.2	0.0
75035	40,149,163,180,183,195,259		2SD	2.98	4.30	1.30	0.80	1.56	2.67	0.02	0.02	0.10	0.03		8	89	2032	6	10	33	2	2.3				
75035			MIN	38.40	8.95	8.42	18.08	10.58	6.12	0.24	0.06	0.39	0.06	0.22	74	16	2060	13	1	3	2	3.6	0.0	0.0	0.2	0.0
75035			MAX	42.61	15.35	10.30	19.24	12.87	10.10	0.27	0.08	0.53	0.08	0.22	84	122	3830	21	11	32	5	6.2	0.0	0.0	0.2	0.0
75035			N	6	9	8	9	9	8	6	4	6	2	1	5	5	3	6	3	3	4	4	1	1	1	1

References

See Appendix 2h

Appendix 2a: Published trace element values for lunar basalts in this study

Sample	Rb(ppm)	Sr(ppm)	Y(ppm)	Zr(ppm)	Nb(ppm)	Mo(ppm)	Ru(ppm)	Rh(ppm)	Pd(ppm)	Ag(ppm)	Cd(ppm)	In(ppm)	Sn(ppm)	Sb(ppb)	Te(ppm)	I(ppm)	Cs(ppm)	Ba(ppm)	La(ppm)	Ce(ppm)	Pr(ppm)	Nd(ppm)	Sm(ppm)	Eu(ppm)	Gd(ppm)	Tb(ppm)	Dy(ppm)	HO(ppm)
10017	5.7	155	194	734	28	1.0			1	16	44	70		0.02			0	277	24.5	73.2	10.8	60.2	21.0	2.2	26.5	4.7	29.4	6.4
10017	1.3	60	121	869	10							137					0	124	4.3	16.4	4.8	13.2	6.2	0.6	7.7	1.0	10.3	3.3
10017	4.2	55	147	410	25	1.0			1	16	44	1		0.02			0	120	21.0	62.0	7.3	50.8	15.0	1.9	19.0	3.9	19.0	3.8
10017	7.4	179	310	1570	32	1.0			1	16	44	138		0.02			0	410	28.0	84.0	12.9	74.0	27.0	2.9	30.0	5.5	36.0	8.3
10017	19	19	6	10	2	1			1	1	1	3		1			7	15	10	10	4	10	13	12	6	9	8	5
10020	1.1	140	123	343	24	0.3			2	45	6	15		0.01			0	77	8.0	28.6	6.4	26.6	9.4	1.6	14.6	2.6	18.4	5.2
10020	1.3	56	78	524	20	0.2				100							0	30	2.5	15.1	6.4	13.3	3.8	0.2	4.6	0.8	10.6	5.1
10020	0.6	85	84	210	18	0.2			2	2	6	15		0.01			0	50	6.6	23.9	4.1	21.8	6.4	1.4	12.4	2.3	14.3	3.4
10020	2.8	189	185	980	36	0.4			2	100	6	15		0.01			0	96	11.0	47.0	8.7	40.0	14.0	1.8	17.0	3.5	30.0	7.0
10020	12	13	5	8	3	2			1	3	1	1		1			3	8	9	9	2	7	10	9	4	7	7	2
10044	2.1	211	170	518	30	0.1				200		3		0.03			0	163	11.1	51.2	7.7	55.4	18.5	2.7	25.7	4.1	29.6	5.6
10044	3.7	99	57	502	20												0	147	3.1	37.8		32.0	10.0	0.8	5.0	0.9	8.6	0.1
10044	0.9	130	147	334	21	0.1				200		3		0.03			0	82	8.7	37.6	7.7	40.3	11.4	2.0	24.0	3.4	24.5	5.6
10044	5.6	301	215	1140	41	0.1				200		3		0.03			0	285	14.0	86.0	7.7	77.7	30.7	3.4	28.6	4.5	36.0	5.6
10044	9.0	9	5	9	3	1.0				1		1		1.00			2	13	9.0	8.0	1.0	5.0	11.0	10.0	3.0	6.0	6.0	2.0
12018	1.4	94	58	135	10	0.7			3	0	1	1		0.13			0	83	9.1	16.1	2.9	13.1	3.7	0.9	4.8	1.0	6.8	1.2
12018	1.4	74	84	210	14							2		0.23			0	90	19.6	12.9	3.2	2.9	0.7	0.3	1.6	0.5	4.7	0.3
12018	0.9	58	30	60	5	0.7			3	0	1	1		0.05			0	55	3.0	6.0	1.8	11.8	3.0	0.8	4.0	0.7	5.3	1.1
12018	3.0	188	106	290	15	0.7			3	0	1	2		0.21			0	200	29.0	26.0	4.0	14.7	3.9	1.2	5.6	1.4	11.0	1.3
12018	8	9	3	4	2	1			1	2	1	2		2			4	9	6	7	2	4	7	6	3	5	5	2
12054	1.1	148	58	175	8												0	71	6.7	19.1	3.3	16.4	5.9	1.3	8.6	1.6	9.8	2.1
12054		65	19	132	3													13	1.2	1.0		1.0	0.7	0.1		0.4	1.2	
12054	1.1	111	51	128	6												0	64	6.3	18.7	3.3	16.0	5.5	1.3	8.6	1.5	9.4	2.1
12054	1.1	171	65	221	9												0	76	7.1	19.7	3.3	16.7	6.1	1.4	8.6	1.9	10.2	2.1
12054	1	3	2	2	2												1	3	2	3	1	2	3	3	1	3	2	1
12063	1.0	149	75	157	7	0.5					1	2	0				0	92	8.6	23.6	4.2	21.5	6.3	1.8	9.5	2.2	11.7	1.9
12063	1.2	19	71	87	7	1.2					0	2					0	83	11.8	18.6	4.3	26.4	2.6	2.1	3.0	2.4	4.8	1.0
12063	0.4	130	55	128	4	0.0					1	1	0				0	60	5.5	17.5	2.9	15.1	3.9	1.2	8.1	1.5	8.9	1.3
12063	3.0	159	128	250	12	0.9					1	3	0				0	146	25.0	45.0	8.0	54.0	9.0	4.4	12.0	5.0	16.0	2.5
10020	12	13	5	8	3	2			1	3	1	1		1			3	8	9	9	2	7	10	9	4	7	7	2
14053	2.2	115	65	239	18	0.2	0			1	20		0	0.02	15		0	171	12.9	37.6	5.1	23.6	6.8	1.2	8.6	1.4	10.3	2.2
14053	0.4	62	31	72	4									0.04			0	41	8.3	13.1	0.8	3.6	0.9	0.2	0.6	0.5	1.5	0.3
14053	2.0	95	50	184	15	0.2	0			1	20		0	0.00	15		0	146	1.5	32.0	4.6	21.9	6.4	1.1	8.3	0.9	9.4	2.0
14053	2.6	180	90	310	19	0.2	0			1	20		0	0.03	15		0	207	17.0	53.0	5.4	27.0	7.5	1.4	9.1	1.7	11.1	2.4
14053	7	9	5	9	5	1	1			1	1		1	2	1		4	8	12	8	3	7	6	11	5	10	5	4
15016	0.9	85	25	94	7	0.1				1	2	0	0	0.00	2		0	51	5.4	14.7	2.1	9.7	3.5	0.9	4.7	0.8	5.0	1.0
15016	0.8	33	7	44	2						1	0					0	27	0.7	1.8	0.3	2.3	0.6	0.1	1.1	0.2	1.1	0.1
15016	0.7	31	21	69	6	0.1				1	2	0	0	0.00	2		0	30	4.8	13.2	2.0	8.0	3.0	0.8	4.2	0.6	4.6	1.0
15016	2.0	100	31	150	9	0.1				1	2	0	0	0.00	2		0	70	5.9	15.6	2.2	11.4	4.1	1.0	5.4	0.9	5.7	1.1
15016	11	14	7	11	5	1				1	3	3	1	1	1		6	9	8	5	3	6	7	6	4	6	4	4
15535	4.4	95	31	85	7	0.2					1	0		0.01	1	2	0	43	4.1	11.3	2.1	8.7	2.8	0.8	3.8	0.6	4.2	0.8
15535	10.1	26	21	11	1						1	0						17	1.6	3.8		5.1	0.6	0.1	0.7	0.1	0.6	0.2
15535	0.9	83	21	79	6	0.2					1	0		0.01	1	2	0	35	3.5	9.7	2.1	6.7	2.6	0.7	3.6	0.6	4.1	0.7
15535	8.0	110	42	90	7	0.2					2	0		0.01	1	2	0	54	5.2	13.2	2.1	12.0	3.1	0.8	4.2	0.7	4.6	0.9
15535	2	5	3	3	2	1					2	2		1	1	1	1	4	4	4	1	4	4	4	3	4	3	3
15556	2.0	103	32	95	8	0.1				1	28	1		0.01	3		0	61	5.4	16.4	2.4	11.2	3.7	1.0	4.7	0.8	5.1	1.1
15556	4.5	22	17	32	2	0.1								0.02			0	28	1.7	3.9	0.3	2.3	0.5	0.1	0.4	0.1	1.0	0.3
15556	0.1	85	24	67	7	0.1				1	28	1		0.00	3		0	44	3.7	14.3	2.3	9.8	3.3	0.9	4.5	0.8	4.4	0.9
15556	6.0	126	50	114	10	0.2				1	28	1		0.01	3		0	90	7.0	20.0	2.6	13.0	4.0	1.1	4.9	0.9	5.4	1.3
15556	11	14	7	9	6	2				1	1	1		2	1		6	11	9	7	3	6	7	6	3	6	4	4
70215	0.5	129	69	187	20					1	2			0.00	2		0	111	5.2	15.8	2.9	18.1	6.7	1.4	9.8	1.8	12.1	2.6
70215	0.5	32	13	38	3												0	295	0.8	5.6	0.2	5.0	0.6	0.1	1.4	0.3	1.0	0.2
70215	0.3	121	58	160	18					1	2			0.00	2		0	47	4.7	11.3	2.8	15.7	6.0	1.3	9.1	1.7	11.5	2.5
70215	1.0	170	75	223	22					1	2			0.00	2		0	475	5.8	19.6	3.0	22.0	7.0	1.5	10.4	2.0	12.7	2.6
70215	9	10	6	7	6					1	1			1	1		4	8	7	7	2	5	7	7	4	5	5	2
70255	0.7	199																85	6.7	24.7		27.3	10.7	2.2	17.6		19.1	
70255	0.0																		0.9				2.0	0.0			3.1	
70255	0.7	199																85	6.4	24.7		27.3	10.0	2.2	17.6		18.0	
70255	0.7	199																85	7.1	24.7		27.3	11.4	2.2	17.6		20.2	
70255	2	2																1	2	1		1	2	2	1		2	
71135	0.4	143		185														61	5.4	17.8		18.6	7.6	1.6	12.0		13.3	
71135																												
71135	0.4	143		185														61	5.4	17.8		18.6	7.6	1.6	12.0		13.3	
71135	0.4	143		185														61	5.4	17.8		18.6	7.6	1.6	12.0		13.3	
71135	2	2		1														1	1	1		1	1	1	1		1	
71546	0.6	191																83	6.6	23.9		25.9	10.1	2.0	16.7	2.3	17.1	
71546	0.0																		0.3	0.3			1.7	0.4			5.8	
71546	0.6	191																83	6.5	23.8		25.9	9.5	1.9	16.7	2.3	15.0	
71546	0.6	191																83	6.7	24.0		25.9	10.7	2.1	16.7	2.3	19.1	
71546	2	2																1	2	2		1	2	2	1	1	2	
74275	1.2	154	92	245	20	0.0											0	90	6.1	20.3	4.3	27.9	9.4	1.8	14.5	2.4	16.8	3.5
74275	0.7	59	32	64	3												0	104	1.0	5.0	0.2	14.2	1.1	0.3	0.6	0.6	1.8	0.2
74275	0.9	115	79	201	19	0.0											0	60	5.5	16.5	4.2	22.5	8.5	1.6	14.2	2.0	15.8	3.5
74275	1.9	225	116	290	22	0.0											0	235	6.8	22.8	4.3	39.0	10.1	1.9	14.8	2.7	17.9	3.6
74275	8	13	5	5	4	1											3	10	7	6	2	5	6	6	3	5	4	2
75035	0.9	191	107	282	26					1	2			0.00	2		0	110	7.5	25.5	5.2	29.2	7.8	2.3	16.7	3.1	20.6	4.2
75035	0.7	48	16	65	6												0	98	2.4	11.8	3.6	11.4	10.4	0.6	6.7	1.1	6.1	1.8
75035	0.6	160	99	255	24					1	2			0.00	2		0	69	6.1	20.4	4.0	22.9	1.8	1.8	13.1	2.5	16.2	3.5
75035	1.5	223	118	319	29					1	2			0.00	2		0	224	9.1	35.0	6.5	36.5	13.6	2.6	19.8	3.8	24.0	4.8
75035	6	6	4	4	3					1	1			1	1		4	8	4	5	2	4	5	5	3	4	5	2

Appendix 2a: Published trace element values for lunar basalts in this study

Sample	Er(ppm)	Tm(ppm)	Yb(ppm)	Lu(ppm)	Hf(ppm)	Ta(ppm)	W(ppm)	Re(ppb)	Os(ppb)	Ir(ppb)	Pt(ppb)	Au(ppb)	Hg(ppm)	Tl(ppm)	Pb(ppm)	Bi(ppb)	Th(ppm)	U(ppm)	Li (ppm)	Be(ppm)	B(ppm)	F (ppm)	Cl (ppm)
10017	17.4	2.5	17.9	2.7	16.7	2.2	0.46			0.02		4.4		6.2	1.5	1.2	3.7	0.8	21.7	2.2	0.7		12.2
10017	7.4	1.0	4.3	1.5	9.0	2.3	0.16					10.4			0.5		2.2	0.2	5.7				
10017	11.5	2.0	15.3	2.1	12.0	1.2	0.40			0.02		0.7		6.2	1.3	1.2	2.6	0.6	18.1	2.2	0.7		12.2
10017	21.0	3.0	23.0	5.0	26.0	5.0	0.51			0.02		8.1		6.2	1.8	1.2	6.4	0.9	25.0	2.2	0.7		12.2
10017	7	3	12	12	10	8	2			1		2		1	3	1	11	5	5	1	1		1
10020	11.9	1.4	8.4	1.3	7.6	1.4	0.13			0.03		1.6		0.3	0.4	0.2	0.8	0.2	10.6	2.0	1.0	85.0	150.0
10020	9.5	0.6	6.3	0.4	3.0	0.8						4.4			0.0		0.7	0.1	8.4				
10020	9.0	1.2	2.5	0.8	6.4	1.1	0.13			0.03		0.1		0.3	0.4	0.2	0.6	0.1	5.0	2.0	1.0	85.0	150.0
10020	19.0	1.6	15.0	1.5	11.0	2.2	0.13			0.03		3.2		0.3	0.4	0.2	1.5	0.2	15.0	2.0	1.0	85.0	150.0
10020	4	2	10	9	8	7	1			1		2		1	2	1	6	5	4	1	1	1	1
10044	17.7	2.2	14.2	2.0	13.3	2.1	0.20					1.4			0.5		0.9	0.3	9.5	2.1	1.2		
10044	4.6		4.7	0.7	4.7	0.9	0.11					1.4					0.6	0.2	12.1				
10044	16.0	2.2	9.5	1.3	9.6	1.5	0.16					0.9			0.5		0.6	0.2	2.6	2.1	1.2		
10044	19.3	2.2	16.6	2.6	18.0	2.7	0.24					1.9			0.5		1.4	0.4	14.0	2.1	1.2		
10044	2.0	1.0	11.0	10.0	11.0	7.0	2.00					2.0			1.0		6.0	5.0	3.0	1.0	1		
12018	4.0		4.3	1.0	2.9	0.5	0.12					1.8			3.0		1.2	0.2	6.8	1.6	1.5	150.0	15.8
12018	1.2		3.3	2.2	0.7	0.4	0.06					0.3					2.4	0.1	3.9		1.6		28.3
12018	3.2		3.4	0.4	2.5	0.4	0.09					1.7			3.0		0.4	0.2	4.5	1.6	0.9	150.0	5.1
12018	4.6		8.0	3.4	3.4	0.9	0.15					1.9			3.0		3.3	0.3	9.0	1.6	2.0	150.0	35.0
12018	4		8	7	5	5	3					2			1		5	4	4	1	2	1	4
12054	6.2	0.9	5.4	0.8	4.9	0.4	0.08								0.2		0.7	0.2		1.3			
12054			0.9	0.0	1.6	0.1											0.2						
12054	6.2	0.9	4.9	0.7	4.1	0.4	0.08								0.2		0.6	0.2		1.3			
12054	6.2	0.9	5.8	0.8	5.7	0.4	0.08								0.2		0.8	0.2		1.3			
12054	1	1	3	3	3	2	1								1		2	1		1			
12063	8.5	1.0	6.6	1.6	5.1	0.6	0.10			0.06		0.1			0.6		0.8	0.2	10.0	1.2	3.6	84.0	32.6
12063	10.2	0.3	6.3	3.7	3.8	0.3	0.10								1.5		0.8	0.2	9.2	0.6	4.5		43.6
12063	5.3	0.9	5.3	0.7	3.6	0.4	0.07			0.06		0.1			0.2		0.6	0.2	5.9	0.9	2.0	84.0	17.2
12063	19.7	1.1	16.0	6.3	10.0	0.8	0.14			0.06		0.1			2.0		1.9	0.5	15.0	1.5	5.2	84.0	48.0
10020	4	2	10	9	8	7	1			1		2		1	2	1	6	5	4	1	1	1	1
14053	6.4	0.7	6.5	0.9	6.0	1.0	0.22	0		0.02		0.1		1.4	1.9	0.3	2.2	0.6	11.9	1.0			
14053	0.8	0.4	2.9	0.2	2.7	0.2									0.9		0.8	0.1	2.5	1.7			
14053	6.0	0.5	5.5	0.8	4.3	0.9	0.22	0		0.02		0.1		1.4	1.1	0.3	1.5	0.5	11.0	0.4			
14053	6.9	0.9	10.0	1.2	9.8	1.1	0.22	0		0.02		0.1		1.4	2.4	0.3	2.8	0.6	12.8	1.6			
14053	4	4	8	10	12	5	1	2		2		1		1	6	1	11	9	2	2			
15016	2.8	0.4	2.8	0.3	2.4	0.4		0		0.09		0.1		0.3	0.3	0.4	0.4	0.1	6.4	0.9			
15016	0.4	0.0	1.8	0.1	0.5	0.1				0.12		0.3			0.6		0.2	0.1	2.8	0.5			
15016	2.6	0.4	2.1	0.3	2.0	0.4		0		0.02		0.0		0.3	0.1	0.4	0.3	0.1	4.6	0.6			
15016	3.1	0.4	4.2	0.4	2.6	0.5		0		0.14		0.3		0.3	0.6	0.4	0.5	0.2	7.5	1.0			
15016	4	2	8	6	9	4		1		3		2		1	2	1	5	7	6	3			
15535	2.5	0.3	1.9	0.3	2.3	0.4				0.06		0.1			0.2		0.4	0.1	7.0	0.4	4.0		1.4
15535			0.4	0.0	0.1	0.1				0.00							0.1	0.1	0.1				2.3
15535	2.5	0.3	1.7	0.2	2.3	0.3				0.06		0.1			0.2		0.4	0.0	7.0	0.4	4.0		0.6
15535	2.5	0.3	2.1	0.3	2.4	0.4				0.06		0.1			0.2		0.5	0.1	7.1	0.4	4.0		2.2
15535	1	1	4	4	2	2				2		1			1		2	3	3	1	1		2
15556	3.0	0.4	2.3	0.3	2.9	0.5	0.18	0		0.04		0.4		0.3	0.2	2.1	0.4	0.2	7.9	0.6	3.0		
15556	0.4	0.1	0.7	0.1	0.3	0.2	0.44					1.2			0.0		0.1	0.1	1.5	0.1			
15556	2.8	0.4	1.6	0.3	2.7	0.4	0.01	0		0.04		0.0		0.3	0.2	2.1	0.4	0.1	7.0	0.6	3.0		
15556	3.3	0.5	2.5	0.4	3.1	0.6	0.43	0		0.04		0.9		0.3	0.2	2.1	0.5	0.2	9.0	0.6	3.0		
15556	4	3	6	6	6	5	3	1		1		2		1	2	1	5	6	5	2	1		
70215	6.1	1.4	6.6	1.1	6.9	1.6	0.08	0		0.00		0.2		0.2		0.1	0.3	0.1	9.3			72.0	4.5
70215	6.2		1.6	0.1	1.7	0.1	0.02					0.4					0.2	0.0	4.0				
70215	0.6	1.4	5.0	1.1	6.2	1.5	0.08	0		0.00		0.0		0.2		0.1	0.2	0.1	7.1			72.0	4.5
70215	7.9	1.4	7.5	1.2	8.3	1.6	0.09	0		0.00		0.3		0.2		0.1	0.4	0.1	11.0			72.0	4.5
70215	5	1	8	6	6	5	2	1		1		2		1		1	5	6	3			1	1
70255	12.1		10.9	1.4	9.7														10.4				
70255			2.5	0.1	0.1																		
70255	12.1		10.0	1.4	9.6														10.4				
70255	12.1		11.8	1.5	9.7														10.4				
70255	1		2	2	2														1				
71135	8.0		7.3														0.6	0.1	8.8				
71135																		0.0					
71135	8.0		7.3														0.6	0.1	8.8				
71135	8.0		7.3														0.6	0.1	8.8				
71135	1		1														1	2	1				
71546	11.2		9.1	1.4	9.2	2.1											0.4	0.2	10.2				
71546			3.5	0.2	0.6																		
71546	11.2		7.8	1.3	9.0	2.1											0.4	0.2	10.2				
71546	11.2		10.3	1.5	9.4	2.1											0.4	0.2	10.2				
71546	1		2	2	2	1											1	1	1				
74275	7.6	0.9	8.8	1.3	8.2	2.3	0.06					0.2			2.2		1.2	0.1	8.8	1.0			
74275	8.8	0.8	2.3	0.2	1.1	3.1	0.06								6.2		3.6	0.0	2.3				
74275	1.0	0.7	7.5	1.2	7.2	1.5	0.03					0.2			0.3		0.4	0.1	8.0	1.0			
74275	10.3	1.4	11.0	1.4	9.0	5.1	0.10					0.2			5.8		4.9	0.2	9.6	1.0			
74275	4	3	7	5	7	5	3					1			3		6	5	2	1			
75035	11.9		10.7	1.6	9.6	1.8	0.10	0		0.00		0.0		0.3	2.8	0.0	0.4	0.1	10.0				
75035	5.5		3.1	0.5	2.5	0.4	0.05					0.0			6.9		0.2	0.0	1.9				
75035	9.7		8.6	1.3	8.5	1.6	0.09	0		0.00		0.0		0.3	0.3	0.0	0.3	0.1	9.1				
75035	15.0		13.2	1.9	11.2	2.0	0.12	0		0.00		0.0		0.3	5.2	0.0	0.5	0.2	11.0				
75035	3		6	5	4	4	2	1		1		2		1	2	1	4	5	3				

Appendix 2b: Published mineralogical contents of lunar basalts in this study

	Parent Sample	Olivine	Pyroxene	Plagioclase	Ilmenite	Spinel	Armalcolite	SiO2 + Cristobalite	Mesostasis
		%	%	%	%	%	%	%	%
Min	10017	0.0	47.0	18.0	10.0	0.0	-	1.0	6.0
Max	10017	0.2	59.4	29.0	15.2	0.0	-	2.2	14.2
Average	10017	0.2	53.2	23.5	13.1	0.0	-	1.6	10.1
Min	10020	2.9	43.3	21.4	12.5	0.1	-	0.9	0.1
Max	10020	6.4	54.8	33.0	14.3	0.6	-	4.9	0.3
Average	10020	4.7	49.1	27.2	13.6	0.3	-	2.9	0.2
Min	10044	0.0	44.8	33.0	6.0	0.0	-	4.0	0.1
Max	10044	0.1	59.0	37.0	12.6	0.4	-	6.7	0.1
Average	10044	0.1	51.9	35.0	10.2	0.4	-	5.4	0.1
Min	12018	11.4	55.7	10.9	0.5	2.0	-	0.2	2.5
Max	12018	22.6	62.3	19.8	0.5	2.0	-	0.4	2.5
Average	12018	17.0	59.0	15.4	0.5	2.0	-	0.3	2.5
Min	12054	0.0	49.2	27.9	5.2	2.4	-	0.1	1.9
Max	12054	10.8	62.0	29.0	11.0	2.4	-	0.1	1.9
Average	12054	10.8	55.6	28.5	7.5	2.4	-	0.1	1.9
Min	12063	2.8	56.0	21.6	4.6	3.4	-	0.1	1.6
Max	12063	9.0	64.6	28.0	6.0	3.4	-	1.6	7.0
Average	12063	5.9	60.3	24.8	5.5	3.4	-	0.9	4.3
Min	14053	0.0	48.0	34.0	2.0	0.2	-	0.9	0.9
Max	14053	3.9	59.0	42.0	4.3	0.8	-	2.6	0.9
Average	14053	3.9	53.5	38.0	2.9	0.5	-	1.8	0.9
Min	15016	6.9	61.0	19.7	1.0	0.5	-	0.2	0.3
Max	15016	12.0	67.0	23.0	6.0	2.8	-	0.2	0.3
Average	15016	9.5	64.0	21.4	3.3	1.7	-	0.2	0.3
Min	15535	10.0	50.8	24.7	3.0	0.8	-	0.5	1.0
Max	15535	20.3	60.0	32.0	4.2	0.8	-	0.5	1.0
Average	15535	15.1	55.4	28.3	3.6	0.8	-	0.5	1.0
Min	15556	0.1	57.0	27.8	2.0	1.0	-	0.8	1.0
Max	15556	2.5	64.1	38.0	5.0	1.7	-	1.0	1.0
Average	15556	1.3	60.5	32.9	3.0	1.4	-	0.9	1.0
Min	70215	6.0	41.0	12.0	13.0	0.1	0.1	0.0	-
Max	70215	9.2	63.0	29.0	37.0	0.1	0.2	4.0	-
Average	70215	7.6	52.0	20.5	17.0	0.1	0.2	2.0	-
Min	70255	5.0	47.7	14.8	13.3	-	-	1.6	-
Max	70255	5.0	47.7	14.8	30.9	-	-	1.6	-
Average	70255	5.0	47.7	14.8	16.1	-	-	1.6	-
Min	71135	0.0	49.7	20.0	11.7	-	-	1.2	4.3
Max	71135	0.2	49.7	20.0	24.8	-	-	1.2	4.3
Average	71135	0.2	49.7	20.0	13.4	-	-	1.2	4.3
Min	71546	2.7	47.8	27.7	17.0	-	-	3.9	0.8
Max	71546	2.7	47.8	27.7	17.0	-	-	3.9	0.8
Average	71546	2.7	47.8	27.7	17.0	-	-	3.9	0.8
Min	74275	9.0	45.7	13.7	15.0	1.9	0.9	-	0.3
Max	74275	10.1	51.0	22.0	15.0	1.9	0.9	-	0.3
Average	74275	9.6	48.4	17.9	15.0	1.9	0.9	-	0.3
Min	75035	-	44.0	31.0	12.0	0.5	-	5.0	0.0
Max	75035	-	45.4	33.0	17.0	0.5	-	6.2	1.9
Average	75035	-	44.7	32.0	13.8	0.5	-	5.6	1.9

"-" denotes a mineral that has not been reported in the literature

Appendix 2b: Published mineralogical contents of lunar basalts in this stu

	Parent Sample	Troilite	Fe-Metal	"Other opaques"	SUM	References
		%	%	%	%	
Min	10017	0.1	0.0	-		
Max	10017	1.1	0.2	-		
Average	10017	0.6	0.2	-	**102.5**	s,f,a,w,k,b
Min	10020	0.5	0.1	-		
Max	10020	1.0	0.1	-		
Average	10020	0.7	0.1	-	**98.7**	k,w,g,j,b
Min	10044	0.0	0.0	-		
Max	10044	0.5	0.0	-		
Average	10044	0.5	0.0	-	**103.6**	e,b,o
Min	12018	0.3	0.7	-		
Max	12018	0.3	0.7	-		
Average	12018	0.3	0.7	-	**97.7**	r,c,s
Min	12054	0.3	0.1	-		
Max	12054	0.3	0.1	-		
Average	12054	0.3	0.1	-	**107.2**	r,u
Min	12063	0.3	0.1	-		
Max	12063	0.3	0.1	-		
Average	12063	0.3	0.1	-	**105.5**	s,r,o
Min	14053	0.1	0.1	-		
Max	14053	0.2	0.3	-		
Average	14053	0.2	0.2	-	**101.8**	v,w,i,o
Min	15016	-	-	-		
Max	15016	-	-	-		
Average	15016	-	-	-	**100.3**	o,w,s,t
Min	15535	-	-	-		
Max	15535	-	-	-		
Average	15535	-	-	-	**104.8**	n,y,z
Min	15556	0.1	-	-		
Max	15556	0.1	-	-		
Average	15556	0.1	-	-	**101.1**	o,n,t
Min	70215	0.0	-	-		
Max	70215	0.0	-	-		
Average	70215	0.0	-	-	**99.4**	d,w,m,o
Min	70255	-	-	14.8		
Max	70255	-	-	14.8		
Average	70255	-	-	14.8	**100.0**	d,x
Min	71135	-	-	11.2		
Max	71135	-	-	11.2		
Average	71135	-	-	11.2	**100.0**	d,x
Min	71546	-	-	-		
Max	71546	-	-	-		
Average	71546	-	-	-	**99.9**	q
Min	74275	0.4	-	5.8		
Max	74275	0.4	-	5.8		
Average	74275	0.4	-	5.8	**100.0**	w,s
Min	75035	1.0	0.5	-		
Max	75035	1.0	0.5	-		
Average	75035	1.0	0.5	-	**100.0**	d,p,w,m

Appendix 2b: Published mineralogical contents of lunar basalts in this study

References

a Adler, I., Walter, L.S., Lowman, P.D., Glass, B.P., French, B.M., Philpotts, J.A. (1970) Electron microprobe analysis of Apollo 11 lunar samples, Proc. Apollo 11 Lunar Sci. Conf. 1, 87-92.
b Beaty, D.W. & Albee, A.L. (1978) Comparative petrology and possible genetic relations among the Apollo 11 basalts, Proc. Lunar Planet. Sci. Conf., 9, 359-463
c Brown, G.M., Emeleus, C.H., Holland, J.G., Peckett, A., Phillips, R. (1971) Picrite basalts, ferrobasalts, feldspathic norites, and rhyolites in a strongly fractionated lunar crust. Proc. Second. Lunar Sci. Conf., 1, 583-600
d Brown, G.M., Peckett, A., Emeleus, C.H., Phillips, R., Pinsent, R.H. (1975) Petrology and mineralogy of Apollo 17 mare basalts. Proc. Lunar Sci. Conf. 6th, 1-13.
e Bailey, J.C., Champness, P.E., Dunham, A.C., Esson, J. Fyfe, W.S., MacKenzie W.S. (1970) Mineralogy and petrology of Apollo 11 lunar samples, Proc. Apollo 11 Lunar Sci. Conf., 1, 169-194.
f Brown, G.M, Emeleu, C.H., Holland, J.G., Phillips, R. (1970) Mineralogical, chemical and petrological features of Apollo 11 rocks and their relationship to igneous processes, Proc. Apollo 11 Lunar Sci. Conf., 1, 195-219
g Chao, E.C.T., James, O.B., Minkin, J.A., Boreman, J.A., Jackson, E.D., Raleigh, C.B. (1970) Petrology of unshocked crystalline rocks and shock effects in Lunar Rocks and Minerals, Science, 167, 644-647.
h Grove, T.L., Walker, D., Longhi, J., Stolper, E., Hays, J.F. (1973) Petrology of rock 12002 and origin of picritic basalts at Oceanus Procellarum. Proc. Fourth Lunar Sci. Conf., 1, 995-1011.
i Gancarz, A.J., Albee, A.L., Chodos, A.A. (1971) Petrologic and mineralogic investigations of some crystalline rocks returned by the Apollo 14 mission, Earth Planet. Sci. Lett., 12, 1-18.
j Haggerty, S.E., Boyd, F.R., Bell, P.M. Finger, L.W., Bryan, W.B. (1970) Opaque minerals and olivine in lavas and breccias from Mare Tranquillitatis. Proc. Apollo 11 Lunar Sci. Conf., 1, 513-538.
k James, O.B., Jackson, E.D. (1970) Petrology of the Apollo 11 Ilmenite Basalts. Journal of Geophysical Research, 75, 5793-5824.
l Kushiro, I., Nakamura, Y. (1970) Petrology of some lunar crystalline rocks, Proc. Apollo 11 Lunar Sci. Conf., 1, 607-626.
m Longhi, J., Walker, D., Grove, T.L., Stolper, E.M., Hays, J.F. (1974) The petrology of the Apollo 17 mare basalts. Proc. Fifth Lunar Conf., 1, 447-469.
n Mason B., Jarosewich E., Melson W.G., and Thompson G. (1972) Mineralogy, petrology, and chemical composition of lunar samples 15085, 15256, 15271, 15471, 15475, 15476, 15535, 15555, and 15556. Proc. Lunar Sci. Conf. 3rd, 785-796.
o McGee, P.E., Warner, J.L., Simonds, C.H. (1977) Introduction to the Apollo Collections: Part I Lunar Igneous Rocks. NASA Lyndon B. Johnson Space Center. Pp1-96.
p Meyer, H.O.A., Boctor, N.Z. (1974) Opaque mineralogy: Apollo 17, rock 75035. Proc. Fifth Lunar Conf., 1, 707-716.
q Warner, R.D., Keil, K., Nehru, C.E., Taylor, G.J. (1978) Catalogue of Apollo 17 rake samples from Stations 1a, 2, 7, and 8. Spec. Publ. #18, UNM Institute of Meteoritics, 88.
r Neal, C.R., Hacker, M.D., Snyder, G.A., Taylor, L.A., Lui, Y.-G., Schmitt, R.A. (1994) Basalt generation at the Apollo 12 site, Part 1: New data, classification, and re-evaluation. Meteoritics, 29, 334-348.
s Papike, J.J., Hodges, F.N., Bence, A.E. (1976) Mare Basalts: Crystal Chemistry, Mineralogy, and Petrology. Reviews of Geophysics and Space Physics. 14, 475-540.
t Rhodes, J.M., Hubbard, N.J. (1973) Chemistry, classification, and petrogenesis of Apollo 15 mare basalts. Proc. Fourth Lunar Sci. Conf., 2, 1127-1148.
u Schaal, R.B., Hörz, F. (1977) Shock metamorphism of lunar and terrestrial basalts. Proc. Lunar Sci. Conf. 8th, 1697-1729.
v Taylor, L.A., Patchen, A. Mayne, R.G., Taylor, D.-H. (2004) The most reduced rock from the moon, Apollo 14 basalt 14053: its unique features and their origin. American Mineralogist, 89, 1617-1624.
w Hallis, L.J., Anand, M., Strekopytov, S. (2014) Trace-element modelling of mare basalt parental melts: Implications for a heterogeneous lunar mantle. Geochimica et Cosmochimica Acta, 134, 289-316.
x Heiken, G.H., Vaniman, D.T. (1990) Characterization of Lunar Ilmenite Resources. Proc. 20th Lunar Plan. Sci. Conf., 239-247.
y LSPET (1972b) Preliminary examination of lunar samples. Apollo 15 Preliminary Science Report. NASA SP-289, 61—6-28.
z Juan V.C., Chen J.C., Huang C.K., Chen P.Y. and Wang Lee C.M. (1972) Petrology and chemistry of some Apollo 15 crystalline rocks. In The Apollo 15 Lunar Samples, 110-115.

Appendix 2c: Published Gd isotope ratios in lunar samples

	Gadolinium Isotopes				Vanadium Isotopes				
Sample	**Specific**	**$^{158}Gd/^{157}Gd$**	**error**	**Reference**	**Specific**	**$\delta^{51}V_{AA}$ (‰)**	**2SD**	**Reference**	**Notes**
10017	*10017-56*	*1.59668*	*0.00035*	*1*	*10017-400 (exterior)*	*-3.47*	*0.19*	*this study*	
10017	*10017-T4,2*	*1.59632*	*0.0003*	*1*	*10017-405 (interior)*	*-3.18*	*0.19*	*this study*	
10017	*10017-32*	*1.59879*		*3*					
average 10017	average 10017	1.59726	0.00046		average 10017	-3.33	0.27	this study	a
10044	10044-30	1.58681	0.0003	3	10044-655	-1.30	0.19	this study	
12018	12018-39	1.58928	0.00038	1	12018-277	-1.42	0.20	this study	
12063	12063-64	1.58768	0.00016	1	12063-343	-1.35	0.21	this study	
74275	74275	1.58524	0.00001	2	74275-355	-1.00	0.19	this study	
Earth	Johnson Matthey oxide standard	1.58509	0.00013	5	Bulk Silicate Earth estimate	-0.70	0.20	4	b

Notes

a The average of several determinations of Gd and V isotope ratios are reported for 10017, since each individual analysis was performed on different sub-sample fragments.

b Terrestrial Gd isotope ratios are reported from measurements of a Johnson Matthey oxide standard with "natural" Gd isotope composition (Ref 5). Terrestrial V isotope ratios are taken from the BSE estimate (Ref 4).

References

1 Lugmair, G.W. & Marti, K. 1971. Neutron capture effects in lunar gadolinium and the irradiation histories of some lunar rocks. Earth and Planet. Sci. Lett. 13. 32-42.

2 Albalat, E., Blichert-Toft, J., Telouk, P., Albarede, F., 2015. The lunar neutron energy spectrum inferred from the isotope compositions of rare-earth elements and hafnium in Apollo samples. Earth and Planet. Sci. Letters 429, 147-156

3 Eugster, O., Tera, F., Burnett, D.S., Wasserburg, G.J. 1970. The isotopic composition of Gd and the Neautron Capture Effects in Samples from Apollo 11. Earth and Planetary Science Letters. 8. 20-30.

4 Prytulak, J., Nielsen, S.G., Ionov, D.A., Halliday, A.N., Harvey, J., Kelley, K.A., Niu, Y.L., Peate, D.W., Shimizu, K., Sims, K.W.W., 2013. The stable vanadium isotope composition of the mantle and mafic lavas. Earth Planet Sc Lett 365, 177-189.

5 Dubois, J.C., Retali, G., Cesario, J. (1992) Isotopic analysis of rare earth elements by total vaporization of samples in thermal ionization mass spectrometry. Int. Journ. Mass Spec. Ion Processes, 120, 163-177.

Appendix 2d: Noble gas exposure ages reported in the literature for this lunar basalt suite

Bold values are those chosen for preferred values. See accompanying text for information on how preferred values are chosen.

Sample	Exp. Age	+/-	Method	Comments	Reference
10017 (400,405)	**480**	**25**	**^{81}Kr-Kr**		**Eberhardt, P., Geiss, J., Graf, H., Grogler, N., Krahenbfihl, U., Schwaller, H., and Stettler, A. : 1974, Geochim. Cosmochim. Acta 38, 97-120.**
	509	**29**	**^{81}Kr-Kr**		**Marti, K., Lugmair, G.W., Urey, H.C. 1970 Solar wind gases, cosmic-ray spallation products and the irradiation history of Apollo 11 samples. Proc. Apollo 11 Lunar Science Conf. 2. 1357-1367.**
	449	**22**	**^{81}Kr-Kr**		**Marti, K., Lugmair, G.W., Urey, H.C. 1970 Solar wind gases, cosmic-ray spallation products and the irradiation history of Apollo 11 samples. Proc. Apollo 11 Lunar Science Conf. 2. 1357-1367.**
	510	*	^{38}Ar		Hintenberger, H., Weber, H. W., and Takaoka, N. : 1971, Proc. SeeondLunar Sci. Conf., 1607-1625.
	340	*	^{21}Ne		Hintenberger, H., Weber, H. W., and Takaoka, N. : 1971, Proc. SeeondLunar Sci. Conf., 1607-1625.
	290	*	^{3}He		Hintenberger, H., Weber, H. W., and Takaoka, N. : 1971, Proc. SeeondLunar Sci. Conf., 1607-1625.
	440	*	^{38}Ar		Turner, G. 1970. Argon-40/argon-39 dating of lunar rock samples. Proc. Of the Apollo 11 Lunar Sci. Conf. 2. 1665-1684.
10017 Preferred Value	479	60	^{81}Kr-Kr	Errors: 2SD of 3 Kr-Kr ages	
10020	**132**	*	**^{39}Ar**		**Guggisberg, S., Eberhardt, P., Geiss, J., Grögler, N., Stettler, A. 1979. Classification of the Apollo-11 mare basalts according to Ar39-Ar40 ages and petrological properties. Proc. Lunar Planet. Sci. Conf. 10. 1-39.**
	122	*	**^{38}Ar**		**Guggisberg, S., Eberhardt, P., Geiss, J., Grögler, N., Stettler, A. 1979. Classification of the Apollo-11 mare basalts according to Ar39-Ar40 ages and petrological properties. Proc. Lunar Planet. Sci. Conf. 10. 1-39.**
	106	*	^{126}Xe		Huneke, J.C., Podosek, F.A., Burnett, D.S., Wasserburg, G.J. 1972. Rare gas studies of the galactic cosmic ray irradiation history of lunar rocks. Geochim. Cosmochim. Acta. 36. 269-301.
	122	*	^{21}Ne		Huneke, J.C., Podosek, F.A., Burnett, D.S., Wasserburg, G.J. 1972. Rare gas studies of the galactic cosmic ray irradiation history of lunar rocks. Geochim. Cosmochim. Acta. 36. 269-301.
10020 Preferred Value	127	*25*	^{39}Ar	No uncertainties reported, error taken to be 20% of value	
10044	**70**	**17**	**^{81}Kr-Kr**		**Hohenberg, C. M., Davis, P. K., Kaiser, W. A., Lewis, R. S., and Reynolds, J. H. : 1970, Proc. Apollo 11 Lunar Sci. Conf., 1283-1309.**
	93	*	^{38}Ar		Hintenberger, H., Weber, H. W., and Takaoka, N. : 1971, Proc. SeeondLunar Sci. Conf., 1607-1625.
	50	*	^{21}Ne		Hintenberger, H., Weber, H. W., and Takaoka, N. : 1971, Proc. SeeondLunar Sci. Conf., 1607-1625.
	64	*	^{3}He		Hintenberger, H., Weber, H. W., and Takaoka, N. : 1971, Proc. SeeondLunar Sci. Conf., 1607-1625.
	70	14	^{38}Ar		Turner, G. 1970. Argon-40/argon-39 dating of lunar rock samples. Proc. Of the Apollo 11 Lunar Sci. Conf. 2. 1665-1684.
	82	16.4	^{38}Ar		Guggisberg, S., Eberhardt, P., Geiss, J., Grögler, N., Stettler, A. 1979. Classification of the Apollo-11 mare basalts according to Ar39-Ar40 ages and petrological properties. Proc. Lunar Planet. Sci. Conf. 10. 1-39.
	90	*	^{126}Xe		Huneke, J.C., Podosek, F.A., Burnett, D.S., Wasserburg, G.J. 1972. Rare gas studies of the galactic cosmic ray irradiation history of lunar rocks. Geochim. Cosmochim. Acta. 36. 269-301.
	61	*	^{21}Ne		Huneke, J.C., Podosek, F.A., Burnett, D.S., Wasserburg, G.J. 1972. Rare gas studies of the galactic cosmic ray irradiation history of lunar rocks. Geochim. Cosmochim. Acta. 36. 269-301.
10044 Preferred Value	70	17	^{81}Kr-Kr		
12018	**195**	**16**	^{81}Kr-Kr		**Marti, K. and Lugmair, G. W. : 1971, Proc. Second Lunar Sci. Conf., 1591-1605**
	200	*	^{38}Ar		Hintenberger, H., Weber, H. W., and Takaoka, N. : 1971, Proc. SeeondLunar Sci. Conf., 1607-1625.
	210	*	^{21}Ne		Hintenberger, H., Weber, H. W., and Takaoka, N. : 1971, Proc. SeeondLunar Sci. Conf., 1607-1625.
	180	*	^{3}He		Hintenberger, H., Weber, H. W., and Takaoka, N. : 1971, Proc. SeeondLunar Sci. Conf., 1607-1625.
	170	34	^{38}Ar		Stettler A., Eberhardt Peter, Geiss J., Grogler N. and Maurer P. (1973) Ar39-Ar40 ages and Ar37-Ar38 exposure ages of lunar rocks. Proc. 4th Lunar Sci. Conf. 1865-1888.
	180	36	^{38}Ar		Stettler A., Eberhardt Peter, Geiss J., Grogler N. and Maurer P. (1973) Ar39-Ar40 ages and Ar37-Ar38 exposure ages of lunar rocks. Proc. 4th Lunar Sci. Conf. 1865-1888.
12018 Preferred Value	195	16	^{81}Kr-Kr		
12054	175	*	^{3}He		**Bogard, D.D., Funkhouser, J.G., Schaeffer, O.A., Zähringer, J. 1971. Noble Gas Abundances in Lunar Material - Cosmic-Ray Spallation Products and Radiation Ages from the Sea of Tranquility and the Ocean of Storms. Journal of Geophysical Research, 76, 2757-2779.**
	260	*	**^{38}Ar**		**Hohenberg, C.M., Marti, K., Podosek, F.A., Reedy, R.A., Shirk, J.R. 1978. Comparisons between observed and predicted cosmogenic noble gases in lunar samples. Proc. Lunar Planet. Sci. Conf. 9. 2311-2344.**
12054 Preferred Value	**260**	*70**	**^{38}Ar**	Ar age based upon reported 38Ar concentrations and refined production rates from Hohenberg et al., 1978. Uncertainty represents the 15% analytical uncertainty, and uncertainties from variations in target element concentrations within the sample.	
12063	**95**	**5**	**^{81}Kr-Kr**		**Marti, K. and Lugmair, G. W. : 1971, Proc. Second Lunar Sci. Conf., 1591-1605**
	72	*	^{38}Ar		Hintenberger, H., Weber, H. W., and Takaoka, N. : 1971, Proc. SeeondLunar Sci. Conf., 1607-1625.
	69	*	^{21}Ne		Hintenberger, H., Weber, H. W., and Takaoka, N. : 1971, Proc. SeeondLunar Sci. Conf., 1607-1625.
	65	*	^{3}He		Hintenberger, H., Weber, H. W., and Takaoka, N. : 1971, Proc. SeeondLunar Sci. Conf., 1607-1625.
12063 Preferred Value	95	5	^{81}Kr-Kr		
14053	**21.2**	**5**	**^{81}Kr-Kr**		**Eugster, O., Eberhardt, P., Geiss, J., Grögler, N., Jungck, M., Meier, F., Mörgell, M., Niederer, F. 1984. Cosmic Ray Exposure Histories of Apollo 14, Apollo 15, and Apollo 16 Rocks. Journal of Geophysical Research, 89 Supplement, B498-B512.**
	25	5	^{38}Ar		Stettler, A., Eberhardt, P., Geiss, J., Grogler, N., and Maurer, P. : 1973, Proc. Fourth Lunar Sci. Conf., 1865-1888.
	23	4.6	^{38}Ar		Stettler, A., Eberhardt, P., Geiss, J., Grogler, N., and Maurer, P. : 1973, Proc. Fourth Lunar Sci. Conf., 1865-1888.
	26	5.2	^{38}Ar		Turner, G., Huneke, J. C., Podosek, F. A., and Wasserburg, G. J. : 1971, Earth Planetary Sei. Letters 12, 19-35.
	21	5	^{38}Ar		Husain, L., Schaeffer, O. A., Funkhouser, J., and Sutter, J. : 1972, Proc. ThirdLunar Sei. Conf., 1557-1567
14053 Preferred Value	21	5	^{81}Kr-Kr		
15016	**367**	**5**	**^{38}Ar**		**Schuster, D.L., Cassata, W.S. 2015. Palaeotemperatures at the lunar surfaces from open system behaior of cosmogenic 38Ar and radiogenic 40Ar. Geochim. Cosmochim. Acta. 155. 154-171.**
	285	**57**	**^{38}Ar**		**Kirsten, T., Horn, P., and Heymann, D. : 1973a, Earth Planetary Sci. Letters 20, 125-130**
	315	**20**	**^{38}Ar**		**Husain, L. 1974. 40Ar-39Ar Chronology and Cosmic Ray Exposure Ages of the Apollo 15 Samples. Journal of Geophysical Research. 79. 2588-2606.**
15016 Preferred Value	322	83	^{38}Ar	Average of ^{38}Ar ages	
15535	**110**	**20**	**^{81}Kr-Kr**		**Alexander, E. C., Jr., Davis, P. K., Reynolds, J. H., and Srinivasan, B. : 1973, Lunar Science IV, 27-29.**
15535 Preferred Value	110	20	^{81}Kr-Kr		
15556	**621**	**7**	**^{38}Ar**		**Schuster, D.L., Cassata, W.S. 2015. Palaeotemperatures at the lunar surfaces from open system behaior of cosmogenic 38Ar and radiogenic 40Ar. Geochim. Cosmochim. Acta. 155. 154-171.**
	490	*	^{3}He		Kirsten, T., Deubner, J., Horn, P., Haneoka, I., Kiko, J., Schaeffer, O. A., and Thio, S. K.: 1972, Proe. Third Lunar Sci. Conf., 1865-1889
	450	*	^{21}Ne		Kirsten, T., Deubner, J., Horn, P., Haneoka, I., Kiko, J., Schaeffer, O. A., and Thio, S. K.: 1972, Proe. Third Lunar Sci. Conf., 1865-1889
	470	*	**^{38}Ar**		**Kirsten, T., Deubner, J., Horn, P., Haneoka, I., Kiko, J., Schaeffer, O. A., and Thio, S. K.: 1972, Proe. Third Lunar Sci. Conf., 1865-1889**
15556 Preferred Value	546	214	^{38}Ar	Average of ^{38}Ar ages	
70215	**126**	**3**	**^{81}Kr-Kr**		**Drozd, R. J., Hohenberg, C. J., Morgan, C. J., Podosek, F. A., Wroge, M. L. (1977) Cosmic-ray exposure history at Taurus-Littrow. Proc. Lunar Sci. Conf. 8th, p3027-3043**
	100	12	^{38}Ar		Kirsten, T. and Horn, P. : 1974, Proe. Fifth Lunar Sci. Conf, 1451-1475
70215 Preferred Value	126	3	^{81}Kr-Kr		
70255	**310**	*	^{38}Ar		Schaeffer G.A. and Schaeffer O.A. (1977a) 39Ar/40Ar ages of lunar rocks. Proc. 8th Lunar Sci. Conf. 2253-2300
	250	*	^{38}Ar		Turner, G. 1977 Potassium-argon chronology of the Moon. Physics and Chemistry of the Earth, vol. 10, no. 3, p. 145-195.
70255 Preferred Value	280	*85*	^{38}Ar	Error: 2SD of 2 Ar ages	
71135	**103**	**3**	^{81}Kr-Kr		**Niemeyer S. (1977) Exposure histories of lunar rocks 71135 and 71569. Proc. 8th Lunar Sci. Conf. 3083-3093**
	58	*	^{3}He		Niemeyer S. (1977) Exposure histories of lunar rocks 71135 and 71569. Proc. 8th Lunar Sci. Conf. 3083-3093
	110	*	^{21}Ne		Niemeyer S. (1977) Exposure histories of lunar rocks 71135 and 71569. Proc. 8th Lunar Sci. Conf. 3083-3093
	111	*	^{38}Ar		Niemeyer S. (1977) Exposure histories of lunar rocks 71135 and 71569. Proc. 8th Lunar Sci. Conf. 3083-3093
	132	*	^{78}Kr, ^{83}Kr		Niemeyer S. (1977) Exposure histories of lunar rocks 71135 and 71569. Proc. 8th Lunar Sci. Conf. 3083-3093
	167	*	^{126}Xe		Niemeyer S. (1977) Exposure histories of lunar rocks 71135 and 71569. Proc. 8th Lunar Sci. Conf. 3083-3093
71135 Preferred Value	103	3	^{81}Kr-Kr		Niemeyer S. (1977) Exposure histories of lunar rocks 71135 and 71569. Proc. 8th Lunar Sci. Conf. 3083-3093
71546	**110**	*	Estimated from other samples in same rake collection.		**Arvidson, R., Drozd, R., Guinness, E., Hohenberg, C., Morgan, C., Morrison, R., Oberbeck, V. 1976. Cosmic ray exposure ages of Apollo 17 samples and the age of Tycho. Proc. Lunar Sci. Conf. 7. 2817-2832.**
71546 Preferred Value	110	55		Value estimated from exposure ages of other samples in rake set.	
74275	**32.2**	**1.4**	**^{81}Kr-Kr**		**Eugster, O., Eberhardt, P., Geiss, J., Grögler, N., Junck, M., Mörgelli, M. 1977 The cosmic-ray exposure history of Shorty Crater samples; The age of Shorty Crater. Proc. Lunar Sci. Conf. 8. 3059-3082.**
	~~28.2~~	~~4~~	^{3}He		Eugster, O., Eberhardt, P., Geiss, J., Grögler, N., Junck, M., Mörgelli, M. 1977 The cosmic-ray exposure history of Shorty Crater samples; The age of Shorty Crater. Proc. Lunar Sci. Conf. 8. 3059-3082.
	35.7	5	^{21}Ne		Eugster, O., Eberhardt, P., Geiss, J., Grögler, N., Junck, M., Mörgelli, M. 1977 The cosmic-ray exposure history of Shorty Crater samples; The age of Shorty Crater. Proc. Lunar Sci. Conf. 8. 3059-3082.
	34.9	6	^{38}Ar		Eugster, O., Eberhardt, P., Geiss, J., Grögler, N., Junck, M., Mörgelli, M. 1977 The cosmic-ray exposure history of Shorty Crater samples; The age of Shorty Crater. Proc. Lunar Sci. Conf. 8. 3059-3082.
	34.8	8.4	^{78}Kr		Eugster, O., Eberhardt, P., Geiss, J., Grögler, N., Junck, M., Mörgelli, M. 1977 The cosmic-ray exposure history of Shorty Crater samples; The age of Shorty Crater. Proc. Lunar Sci. Conf. 8. 3059-3082.
	39.8	10.4	^{83}Kr		Eugster, O., Eberhardt, P., Geiss, J., Grögler, N., Junck, M., Mörgelli, M. 1977 The cosmic-ray exposure history of Shorty Crater samples; The age of Shorty Crater. Proc. Lunar Sci. Conf. 8. 3059-3082.
	38.9	10.4	^{126}Xe		Eugster, O., Eberhardt, P., Geiss, J., Grögler, N., Junck, M., Mörgelli, M. 1977 The cosmic-ray exposure history of Shorty Crater samples; The age of Shorty Crater. Proc. Lunar Sci. Conf. 8. 3059-3082.
	42.9	9.9	^{131}Xe		Eugster, O., Eberhardt, P., Geiss, J., Grögler, N., Junck, M., Mörgelli, M. 1977 The cosmic-ray exposure history of Shorty Crater samples; The age of Shorty Crater. Proc. Lunar Sci. Conf. 8. 3059-3082.
74275 Preferred Value	32	1	^{81}Kr-Kr		
75035	**72**	**2**	**^{81}Kr-Kr**		**Crozaz, G., Drozd, R., Hohenberg, C., Morgan, C., Ralston, C., Walker, R., and Yuhas, D. : 1974, Proc. Fifth Lunar Sd. Conf., 2475-2499**
SS	**71.7**	**1.8**	**^{81}Kr-Kr**		**Arvidson, R., Drozd, R., Guinness, E., Hohenberg, C., Morgan, C., Morrison, R., Oberbeck, V. 1976. Cosmic ray exposure ages of Apollo 17 samples and the age of Tycho. Proc. Lunar Sci. Conf. 7. 2817-2832.**
	88.6	**2.7**	**^{81}Kr-Kr**		**Drozd, R. J., Hohenberg, C. J., Morgan, C. J., Podosek, F. A., Wroge, M. L. (1977) Cosmic-ray exposure history at Taurus-Littrow. Proc. Lunar Sci. Conf. 8th, p3027-3043**
75035 Preferred Value	77	19	^{81}Kr-Kr	Errors: 2SD of 3 Kr-Kr ages	

* No uncertainty reported

Appendix 2d – Accompanying Text

This text is from the supplementary information of Hopkins et al. (2019) and is meant to accompany the Table in this section, **Appendix 2d**.

Exposure Ages

The exposure age of a lunar sample is defined as the period of time over which the sample has been susceptible to high-energy particle reactions resulting from cosmic ray bombardment of samples located at, or near to, the lunar surface. If a sample is buried at a depth of more than a few meters, the effects of primary cosmic rays are negligible, due to the stopping power of overlying rock or regolith. All lunar samples in this suite were collected from the surface of the Moon, and thus have been exposed to cosmic rays for at least one period of time, but the length of time varies from sample to sample and some samples are known to have been exposed to cosmic ray bombardment on more than one occasion (e.g. Drozd et al., 1974). Exposure ages have typically been ascertained by determining the proportion of rare gas isotopes within samples, generated as a product of a number of high-energy particle reactions initiated by cosmic ray bombardment. In general, an exposure age doesn't necessarily represent a "real" age, but instead a time-integrated estimate of the total length of time a sample has spent at shallow depth on the lunar surface to achieve the proportions of rare gas isotopes observed within.

Exposure ages have been calculated by several methods using either radiogenic-stable cosmogenic nuclide pairs (e.g. ^{3}H-^{3}He, ^{39}Ar-^{38}Ar, ^{81}Kr-^{83}Kr), or concentrations of trapped stable cosmogenic noble gas isotopes (e.g. ^{3}He, ^{21}Ne, ^{38}Ar, ^{83}Kr, ^{126}Xe) with an estimated production rate. Multiple factors can systematically affect the accuracy and precision of determined exposure ages including: gas loss, differential sample shielding and orientation, pre-exposure chemical compositions, estimated production rates, and analytical precision (Eugster et al., 2003).

Determining exposure ages of samples in this study

A compilation of all exposure age studies for the samples in this suite is displayed in **Appendix 2d**. In a number of cases there are multiple reported exposure ages for the samples in the suite, and a discussion of the reliability of these studies follows to highlight the method by which a "preferred" exposure age is obtained in this study.

The most reliable method to determine exposure ages is the ^{81}Kr-Kr method, as it excludes the prerequisite knowledge of sample chemical composition and shielding, or estimates of cosmogenic production rates. Furthermore, measurements of isotope ratios often result in higher-precision when compared with concentration measurements of cosmogenic stable isotopes (Marti, 1967). Where ^{81}Kr-Kr data is available, exposure ages derived from this method are preferentially used (**Appendix 2d**). No weighting is given to one ^{81}Kr-Kr study over another where such multiple ^{81}Kr-Kr ages have been reported.

However, ^{81}Kr-Kr measurements have not been made on all of lunar samples in this study. Where exposure age measurements have been made in the lunar sample suite, they have been based upon measurements of cosmogenic isotope concentrations in combination with a production rate. Measurements of $^{38}Ar_{cosm}$ are the most numerous, but concentrations of ^{3}He, ^{21}Ne ^{78}Kr, ^{83}Kr, ^{124}Xe, ^{126}Xe, ^{128}Xe and ^{130}Xe have also been used to differing levels of success. Hohenberg et al. (1978) and Regnier et al. (1979) compared the production rates of cosmogenic isotopes (based upon concentrations of target elements and the cosmic ray spectrum) to those observed within the lunar sample suite and found that ^{38}Ar-derived exposure ages are most accurate. Concentrations of ^{3}He and ^{21}Ne are susceptible to diffusive gas loss, resulting in underestimates of exposure ages compared to "true" values. There are also significant differences (both higher and lower) in the observed and predicted concentrations of cosmogenic Kr and Xe stable isotopes, possibly due to analytical uncertainties (e.g. mass interferences or low concentrations), or a less-complete theoretical understanding of the production pathways, as studies of these noble gas isotopes are less numerous. Thus, for samples lacking ^{81}Kr-Kr ages, ^{38}Ar-derived exposure ages are preferred for this suite of samples, compared to ages derived from other methods.

Estimates of cosmogenic production rates and laboratory precision in the determination of target element concentrations have improved over time since the early 1970s, particularly since production rates have been calibrated to ^{81}Kr-Kr ages (Eugster et al., 2003). Where multiple studies of ^{38}Ar ages exist, the average of these values is taken.

Where no ^{81}Kr-Kr or ^{38}Ar exposure ages exist (samples 12054, 71546) alternative estimates of exposure ages are made. For samples 12054-146 and 12054-150, noble gas isotope data does exist for ^{3}He, ^{21}Ne, ^{38}Ar, ^{126}Xe (Bogard et al., 1971), but only a ^{3}He age (175 ± 26Ma) was determined since the sample chemistry was unknown at the time of this work. Using ^{38}Ar production rates of Hohenberg et al., (1978) and the literature concentrations of target elements (K, Ca, Ti, Fe) gives an estimated exposure age of 260 ± 70 Ma, and this used in this study. Sample 71546 has no reported exposure age, and an estimate of its age is taken from other samples collected as part of the same surface rake (~110 ± 55 Ma, Arvidson et al., 1976). Sample 12054-13 is a glass splash on the surface of the parent sample and no exposure age has been reported for this sub-section of the sample. Sample 71546 and all samples of 12054 are excluded from calculations of regression (**Figure 4.6**) due to their less-reliable or non-existent exposure age data but are presented after regression and are found to lie in agreement with the other data.

Appendix 2e: Published trace element data for lunar basalts

Sample	References (Appendix 2g)	Mission	SiO_2(wt%)	TiO_2(wt%)	Al_2O_3(wt%)	FeO(wt%)	CaO(wt%)	MgO(wt%)	MnO(wt%)	K_2O(wt%)	Na_2O(wt%)	P2O5(wt%)	S(wt%)	Sc(ppm)	V(ppm)	Cr(ppm)	CO(ppm)	Ni(ppm)	Cu(ppm)
10003	3,13,34,53,68,75,80,90,154,165,187,230,251	A11	39.32	10.87	10.33	19.98	11.15	7.38	0.28	0.05	0.39	0.12	0.27	80.38	64.62	1522.80	14.69	5.51	22.14
10017	2,13,34,41,68,74,94,131,150,154,165,181,223,230,242,243,257,262	A11	41.68	11.73	8.08	19.74	10.46	7.89	0.24	0.26	0.51	0.15	0.24	76.27	130.36	2481.93	27.05	6.37	15.87
10020	13,41,46,65,68,80,90,94,102,131,143,165,187,223,230,243,250,263	A11	40.02	10.35	10.22	18.87	11.74	7.74	0.26	0.06	0.40	0.09	0.19	87.81	84.17	2250.43	14.83	37.50	8.69
10022	13,53,74,75,80,90,94,150,165,243	A11	42.16	11.83	8.01	19.24	10.09	7.47	0.24	0.25	0.45	0.10	0.31	82.88	64.00	2375.60	25.80	320.00	5.10
10024	13,34,53,75,90,94,165,176	A11	39.94	12.49	7.76	19.47	10.20	8.10	0.23	0.29	0.48	0.15	0.24	78.45	68.67	2450.00	29.00		16.00
10031	15	A11		11.40	8.00	20.70	10.60	8.00		0.30	0.50			87.00	65.00	2367.33	28.00		
10032	13,15,223	A11	39.49	11.68	7.34	19.24	9.81	8.41	0.27	0.29	0.47	0.11	0.36	77.00	70.00	2209.97	26.00		
10044	1,9,12,13,23,60,61,74,90,94,102,150,154,181,187,223,242,250,257,262	A11	42.38	9.09	10.62	18.08	11.67	6.14	0.27	0.11	0.46	0.07	0.20	92.94	43.03	1362.94	12.75	6.86	12.34
10045	1,9,13,23,34,74,80,90,94,150,165,223,243,257	A11	41.19	10.91	10.28	19.36	10.96	8.36	0.27	0.06	0.39	0.06	0.15	85.54	92.20	2732.50	18.83	4.00	8.88
10047	2,12,13,34,65,75,90,94,165,187,223,257	A11	43.30	9.42	10.19	19.47	12.47	5.88	0.29	0.10	0.45	0.12	0.20	97.74	53.20	1433.05	13.84		14.65
10050	13,46,65,75,94,154,165,187,223,230,242,243,257	A11	40.35	10.92	10.47	18.52	11.55	8.32	0.30	0.06	0.39	0.07	0.13	105.76	98.68	2733.36	15.13	28.58	27.04
10057	2,3,13,41,46,60,61,65,80,94,101,102,143,147,154,165,218,230,243,250,262,263,278	A11	39.55	10.91	9.32	19.05	10.89	7.58	0.25	0.27	0.51	0.14	0.24	83.99	161.39	2772.50	25.61	16.40	15.08
10058	13,41,46,55,68,75,90,94,143,150,154,165,187,223,242,243,278	A11	41.20	9.68	10.85	18.87	12.08	6.21	0.32	0.10	0.44	0.11	0.20	90.04	53.55	1921.57	12.07	40.58	22.36
10062	13,34,68,75,102,165,179,181,187,250,251	A11	39.69	10.22	10.76	18.22	11.92	5.23	0.27	0.07	0.44	0.12	0.17	79.18	75.00	1572.23	13.23	15.00	4.00
10069	3,13,46,55,75,90,94,150,154,165,242	A11	39.54	12.16	7.57	19.32	10.18	7.76	0.26	0.29	0.50	0.15	0.22	79.23	66.45	2320.49	27.47	5.80	18.59
10071	3,13,55,68,74,75,165,187,230,251,263	A11	42.36	10.80	8.71	18.31	10.47	7.16	0.21	0.32	0.55	0.18	0.24	73.35	86.33	2365.78	28.38	7.00	12.50
10072	2,3,13,34,41,46,65,80,94,131,143,165,179,243,251,278	A11	41.25	11.53	8.05	19.36	10.73	7.63	0.24	0.29	0.52	0.14	0.26	72.27	57.86	2980.00	28.30	13.20	12.94
10092	13,90,94,154,187,223	A11	38.45	11.50	9.83	18.68	11.19	8.67	0.26	0.06	0.33	0.05	0.11	82.69	101.01	2693.88	19.72	3.60	43.65
12002	2,8,25,25,32,41,67,73,85,90,138,165,175,176,185,216,237,240,280,282	A12	44.33	2.59	8.21	21.82	9.19	14.82	3.20	0.05	0.21	0.11	0.06	41.96	196.57	5677.27	55.51	106.00	5.47
12004	21,25,33,54,55,56,128,129,144,152,154,165,177,244,255,256,264	A12	43.67	3.07	8.92	21.41	9.58	12.55	0.27	0.06	0.25	0.06	0.07	47.26	165.12	4273.01	53.30	63.21	12.38
12006	70,157,189	A12	44.23	2.90	9.14	20.87	8.97	13.74	0.27	0.08	0.30	0.06	0.06	43.65	172.00	5070.00	52.60	90.00	
12009	8,33,39,41,81,90,102,154,165,176,225,233,237,244,264,275,283	A12	44.53	3.11	9.18	20.66	9.85	11.50	0.26	0.06	0.32	0.07	0.06	45.08	238.17	4164.91	50.90	56.67	12.39
12012	70,157,189,244	A12	39.59	2.81	8.94	21.70	8.59	15.96	0.24	0.05	0.32	0.07	0.07	41.30	125.50	4313.33	53.90	79.33	
12015	10,70,154,157,168,171,189,225,244	A12	44.42	2.97	9.28	19.88	9.54	12.09	0.29	0.06	0.25	0.06	0.09	45.86	146.31	3607.96	50.06	62.39	12.41
12016	70,157,189,251	A12	42.78	3.76	7.72	22.42	8.31	13.88	0.28	0.05	0.24	0.08	0.08	49.20	153.00	3870.00	54.15	51.50	
12017	2,157,168,189	A12	47.27	3.34	9.81	19.91	10.54	8.17	0.28	0.07	0.27	0.03	0.03	53.35	183.00	3530.00	36.70	38.00	
12018	20,21,21,25,33,39,73,105,124,185,205	A12	43.42	2.63	8.48	20.95	8.13	14.28	0.31	0.06	0.25	0.05	0.05	45.37	162.50	3870.00	54.47	82.25	6.33
12019	157	A12		3.00	9.60	20.61	9.10	9.20	0.25	0.05	0.25			53.00	177.00	3670.00	41.50	30.00	
12020	2,25,33,39,81,85,102,103,105,124,154,165,255,256	A12	44.06	2.79	7.82	21.00	8.43	14.89	0.27	0.06	0.21	0.07	0.06	43.49	168.27	4090.95	61.16	72.11	11.36
12021	17,20,25,32,33,39,41,54,56,61,73,81,90,98,102,103,105,144,154,165,185,233,275,283	A12	46.54	3.53	10.90	19.58	11.56	7.23	0.26	0.07	0.33	0.08		52.89	227.16	2560.46	33.40	18.14	11.36
12022	8,33,41,54,56,61,81,85,90,98,99,105,138,154,165,168,185,218,225,233,240,244,264,275,283	A12	41.98	4.97	8.90	22.36	9.95	11.05	0.25	0.07	0.32	0.09		56.24	235.74	3250.64	48.58	41.83	10.26
12035	33,39,54,56,67,85,87	A12	44.80	2.28	8.12	21.39	8.08	16.12	0.29	0.05	0.21	0.06	0.05	37.85	167.00	3933.33	58.73	67.00	4.25
12038	2,8,20,25,33,39,41,81,105,154,171,172,205,216,233,240,244,251,275,282	A12	47.06	3.23	12.66	17.75	11.58	6.77	0.25	0.04	0.64	0.11	0.07	47.85	121.51	2011.26	28.68	5.93	11.46
12040	2,20,24,33,73,90,98,105,157,168,176,207	A12	44.05	2.44	7.23	20.91	7.76	16.53	0.26	0.04	0.19	0.05	0.05	38.80	174.75	4040.00	55.17	63.67	11.50
12046	157,283	A12		4.60	10.50	20.20	10.60	7.30	0.26	0.06	0.29			60.20	138.00	2010.00	31.00	11.30	
12051	2,33,41,53,54,56,67,85,90,128,129,144,154,175,255,256	A12	45.72	4.63	10.16	20.34	12.30	7.01	0.28	0.06	0.30	0.08	0.10	55.38	149.32	2105.35	34.06		14.18
12052	20,25,33,90,98,102,105,124,128,129,138,152,205,216,233,240,244,283	A12	45.85	3.30	10.30	19.96	11.03	8.54	0.27	0.07	0.29	0.07	0.07	52.37	146.80	3418.33	39.73	23.19	16.80
12053	25,67,81,85,87,98,124,144,147,154,165,185,280,282	A12	46.75	3.29	10.55	19.41	10.16	8.12	2.91	0.06	0.27	0.14	0.08	49.69	156.26	3380.62	36.55	27.51	18.35
12054	70,154,157,189	A12	45.86	4.67	10.29	19.86	10.97	7.23	0.28	0.06	0.30	0.06	0.09	68.94	168.27	2430.24	34.52	20.04	26.61
12061	157	A12		4.90	8.80	21.90	9.10	11.60	0.27	0.06	0.28			60.80	158.00	3210.00	45.80	48.00	
12062	157	A12		4.60	10.30	20.70	9.90	8.10	0.27	0.06	0.30			9.10	140.00	2120.00	32.70		
12063	8,16,21,21,25,32,53,54,56,81,102,124,138,152,154,157,165,171,176,216,233,240,255,256,280,282	A12	43.23	4.74	9.44	20.99	11.19	9.85	2.13	0.07	0.33	0.14	0.09	66.71	124.29	2993.19	40.83	35.90	12.28
12064	24,25,33,41,54,81,90,103,105,124,154,165,176,207,233,244,275	A12	45.56	3.57	11.07	19.90	12.40	6.96	0.28	0.08	0.30	0.03	0.07	59.80	119.62	2354.53	31.80	7.30	11.68
12065	2,21,25,33,73,105,124,128,129,138,165,176,218,244,275	A12	45.22	3.42	10.51	20.15	10.79	8.73	0.29	0.07	0.29	0.12		56.74	136.00	3387.50	37.08	19.71	10.76
12072	14,157,225	A12	48.17	2.60	9.55	20.02	9.59	11.72	0.26	0.05	0.28			47.05	165.00	3439.00	49.35	54.75	8.86
12075	39,61,81,85,255,256,275	A12	44.29	2.81	8.09	20.56	8.62	13.86	0.26	0.07	0.23	0.12		40.80	179.33	4350.00	56.40	67.75	7.25
12076	157,189	A12	44.87	2.78	8.30	20.93	9.02	13.43	0.28	0.06	0.22			46.80	167.00	4385.00	54.00	73.00	
12077	157	A12		2.50	7.70	21.20	7.70	15.70	0.27	0.05	0.20			41.40	197.00	5050.00	59.50	125.00	
14053	30,31,37,41,52,56,84,86,90,92,142,154,156,177,231,241,245,274,282	A14	46.80	2.63	12.94	16.86	11.18	8.53	0.26	0.14	0.43	0.11	0.14	55.07	118.69	2684.76	31.10	15.52	20.36
14073	109,133,177,241	A14		1.25	20.40	8.53	12.90		0.11	0.49	0.75			19.85	37.00		18.00		
14168	120,215,268	A14		1.70	12.40	15.50	9.90	11.00	0.22	0.57	0.37			52.00	139.00	3722.05	31.00		
14276	133,193,253,277	A14	47.61	1.18	21.46	7.93	13.20	7.35	0.12	0.48	0.72	0.40		19.10	31.00	1800.00	11.00	113.00	40.00
14310	5,31,37,52,56,57,83,84,86,92,112,125,133,142,151,156,177,182,193,206,231,239,241,245,253,282	A14	47.80	1.23	20.35	8.17	12.24	7.71	0.12	0.50	0.70	0.38	0.04	19.19	36.14	1094.13	19.64	172.56	8.92
15016	6,28,29,35,38,53,62,71,83,90,92,100,104,106,145,146,154,173,188,200,220,238,246,283	A15	44.12	2.28	9.16	21.78	9.37	11.08	0.30	0.05	0.26	0.09	0.09	35.24	218.77	5638.58	57.93	77.41	8.78
15065	6,29,38,64,71,113,137,153,173,228,232,251,259	A15	48.09	1.66	9.20	19.74	9.74	10.13	0.27	0.06	0.29	0.08		50.01	173.67	3643.33	51.71	86.38	36.77
15076	29,30,38,64,71,88,90,136,137,169,170,173,188,232,246,248,251	A15	48.66	1.71	9.02	19.51	10.60	8.89	0.28	0.08	0.32	0.05	0.05	32.33	135.00	3380.00	41.67	25.00	9.10
15085	45,49,64,66,71,82,83,124,232,261	A15	47.25	2.36	9.24	20.98	10.09	8.75	0.30	0.05	0.28	0.09	0.10	45.33	156.80	3717.50	42.84	28.43	17.43
15105	44,117	A15	45.90	2.99	8.35	22.25	9.55	9.15	0.26	0.05	0.34	0.09		42.00	204.00		44.00		
15115	119	A15		1.80	9.60	20.00	10.00	8.00	0.28	0.06	0.31			45.00	187.00	3051.53	41.00		
15117	29,38,64	A15	47.80	2.07	9.52	20.59	10.98	8.02	0.29	0.07	0.33	0.11		44.00	188.00	4450.00	43.00	30.00	12.00
15118	44,90,117,188,219	A15	47.93	2.05	10.34	21.83	10.55	7.06	0.27	0.07	0.35	0.10	0.07	45.00	161.00		44.00	36.00	
15256	30,88,90,124,141,154,169,170,188,200,219,246	A15	44.90	2.50	8.95	22.18	10.08	9.34	0.30	0.12	0.27	0.07	0.08	45.03	196.70	4110.27	50.50	63.66	11.62
15379	29,30,38,106,154,169,170,173,178,200	A15	44.63	2.44	8.68	22.51	9.52	10.29	0.28	0.06	0.25	0.10		40.36	233.30	4741.77	58.34	91.60	9.81
15385	44,90,117,188,219	A15	41.06	2.12	6.80	23.19	6.86	17.59	0.27	0.03	0.23	0.06	0.10	39.00	187.00		64.00	138.00	
15386	51,89,91,155,166,167,188,253,270,271	A15	50.83	2.11	15.58	10.89	10.34	8.16	0.16	0.57	0.77	0.70	0.09	22.33	25.12	2178.50	22.00	11.56	14.60
15388	44,117,281	A15	44.95	4.53	11.60	17.97	10.13	8.60	0.26	0.03	0.38	0.04		45.80	150.00	2323.00	34.45		
15475	28,30,35,88,90,124,165,167,169,170,173,188,219,259	A15	48.46	1.74	9.57	19.86	10.56	8.59	0.30	0.05	0.29	0.06	0.06	47.70	130.00	3975.00	50.30	29.50	6.00
15476	26,45,49,124,173,232	A15	48.05	1.82	9.69	19.94	11.46	8.42	0.27	0.05	0.33	0.07	0.07	40.60	157.50	3600.00	36.85	25.00	5.00
15485	46	A15	47.39	1.77	9.14	19.82	10.21	9.48	0.27	0.03	0.28	0.08	0.06		177.00		42.00	22.00	4.00
15495	#N/A	A15	48.27	1.87	9.13	21.27	10.93	8.51	0.27	0.08	0.30	0.09		44.00	174.50	3716.25	46.10	34.50	19.60
15499	28,35,46,71,100,137,165,173,178,188,220,246,283	A15	47.77	1.79	9.15	20.21	10.36	9.23	0.28	0.03	0.31	0.08	0.07		189.00		44.00	35.00	3.00
15535	6,82,83,124,154,184,200	A15	44.77	2.23	8.54	22.75	9.41	11.11	0.30	0.04	0.25	0.07		44.82	201.49	4758.03	59.05	70.15	13.49
15536	154,200,211,272	A15	44.45	2.32	7.93	23.72	9.79	10.68	0.29	0.05	0.24	0.05		42.81	257.42	4585.82	59.65	79.49	20.27
15545	28,30,35,88,130,154,165,167,169,170,173,188,200,220,283	A15	45.05	2.38	8.65	22.13	9.76	10.20	0.29	0.04	0.28	0.07	0.06	42.78	238.08	4896.99	45.72	63.88	129.43
15555	26,28,29,31,35,38,57,64,66,71,92,100,113,114,122,124,130,141,151,153,154,165,188,200,232,246	A15	44.59	2.19	8.73	22.28	9.48	10.53	0.28	0.05	0.28	0.06	0.05	40.82	235.73	4229.27	63.02	74.56	10.52
15556	26,66,71,90,124,136,137,145,146,147,154,188,200,220,228,246	A15	45.59	2.61	9.46	21.74	10.58	8.10	0.28	0.06	0.27	0.08	0.08	44.70	260.80	5163.27	50.62	60.81	10.11
15557	#N/A	A15	45.18	2.54	8.91	22.42	10.08	9.44	0.29	0.05	0.27	0.07	0.09	43.70	231.48	4269.95	56.33	54.74	14.21
15605	119,211	A15	45.00	2.21	8.46	22.26	9.98	10.64	0.30	0.05	0.25	0.06		43.27	232.00	4328.75	50.73	55.00	
15607	29,38,44,106,117,154,200	A15	45.18	2.48	8.88	22.52	9.72	9.91	0.27	0.05	0.29	0.08		42.27	198.35	4114.98	54.28	56.91	15.69
15614	119	A15		2.00	8.80	21.30	8.90	11.00	0.27	0.03	0.25			38.00	218.00	4679.93	52.00		
15616	119	A15		2.00	8.70	21.80	8.30	12.00	0.26	0.04	0.24			38.00	248.00	6226.22	57.00		
15620	44,117,281	A15	45.35	2.29	9.23	22.30	9.23	11.10	0.30	0.04	0.28	0.13		40.05	225.00	4526.00	50.40	95.00	
15623	44,119,281	A15	45.25	1.91	8.47	22.93	9.43	12.00	0.29	0.04	0.27	0.15		38.50	217.00	5481.00	54.50	45.00	
15630	119,154,200	A15	43.95	2.17	8.88	21.51	9.07	11.17	0.27	0.04	0.26	0.09		39.49	216.63	5774.28	56.45	83.75	9.64

Appendix 2e: Published trace element data for lunar basalts

Sample	References (Appendix 2g)	Mission	SiO_2(wt%)	TiO_2(wt%)	Al_2O_3(wt%)	FeO(wt%)	CaO(wt%)	MgO(wt%)	MnO(wt%)	K_2O(wt%)	Na_2O(wt%)	P2O5(wt%)	S(wt%)	Sc(ppm)	V(ppm)	Cr(ppm)	CO(ppm)	Ni(ppm)	Cu(ppm)
15633	44,83,117,281	A15	45.03	2.31	8.25	23.30	9.02	11.25	0.30	0.03	0.26	0.08		43.03	225.00	3946.50	53.33	101.00	
15634	119	A15		1.50	9.80	19.90	9.10	13.00	0.25	0.02	0.27			38.00	223.00	4358.35	55.00		
15639	119	A15		1.80	9.40	21.90	8.90	12.00	0.26	0.04	0.28			39.00	194.00	4139.41	54.00		
15641	44,119,281	A15	45.45	1.99	9.40	21.47	9.60	11.10	0.30	0.03	0.32	0.08		37.20	212.00	3749.00	52.50	75.00	
15643	29,38,44,106,281	A15	45.20	1.79	8.83	22.31	9.19	12.28	0.29	0.04	0.27	0.09		33.30	154.00	3718.00	64.78	144.00	8.60
15648	119	A15		2.20	9.90	20.10	9.70	11.00	0.26	0.04	0.28			44.00	196.00	3475.74	43.00		
15649	119	A15		2.20	9.10	21.70	9.10	12.00	0.26	0.04	0.26			38.00	174.00	3585.21	46.00		
15659	29,38,106	A15	45.33	2.30	8.11	22.11	9.02	12.51	0.27	0.05	0.26	0.12		37.00	230.00		62.33	87.00	16.16
15661	119	A15		1.90	8.70	21.90	8.60	12.00	0.26	0.04	0.25			35.00	186.00	4467.83	51.00		
15662	119	A15		2.30	9.50	22.50	9.40	10.00	0.27	0.04	0.27			41.00	237.00	4426.77	52.00		
15666	44,117	A15	46.90	2.14	9.75	21.30	9.95	8.35	0.26	0.06	0.37	0.08		42.00	176.00		37.00	49.00	
15669	44,119	A15	44.30	2.75	8.65	23.30	10.35	10.05	0.27	0.04	0.29	0.07		41.00	203.00	3667.31	45.00		
15672	29,38,44,106,117,154,200,281	A15	44.83	2.15	9.11	21.48	9.23	11.57	0.27	0.04	0.27	0.10		37.48	212.32	4623.33	56.10	73.53	7.52
15675	119,154,200	A15	45.00	2.44	9.23	21.90	9.65	9.46	0.27	0.04	0.25	0.07		42.96	218.19	4128.29	49.36	53.87	12.21
15676	29,38,44,106,117,154,200	A15	44.32	2.65	8.95	22.40	9.89	9.39	0.28	0.05	0.28	0.08		41.08	206.28	4037.86	52.60	53.66	14.10
70017	27,41,47,90,114,127,134,153,166,180,183,190,191,194,212,249,251	A17	38.42	13.03	8.82	18.34	10.47	9.44	0.25	0.06	0.39	0.05	0.16	79.40	153.60	3730.00	42.77	24.00	38.27
70075	267	A17		12.10	9.30	19.40	10.30	8.00	0.25	0.07	0.42			86.00	86.00	2798.38	19.00		
70135	41,41,46,58,72,98,107,154,166,190,195,212	A17	38.04	13.58	7.69	19.16	10.62	9.44	0.28	0.07	0.35	0.06	0.17	78.62	205.64	3707.95	20.79	3.35	34.27
70139	160,174	A17		13.10	8.30	17.60	10.00	9.60	0.23	0.04	0.36			80.00	143.00	3810.00	26.20	31.00	
70147	160	A17		13.00	8.40	17.90	9.20	8.80	0.23	0.06	0.39			77.00	131.00	3530.00	22.80	6.00	
70185	58,72,165,190,265	A17	40.18	10.56	9.62	18.27	11.53	8.11	0.26	0.09	0.41	0.02	0.17	84.00	72.00	3580.00	17.80		
70215	27,41,47,50,58,69,71,72,90,126,134,135,140,147,165,166,180,186,190,190,191,194,212,247,259	A17	37.86	12.83	8.72	19.66	11.18	8.71	0.27	0.06	0.42	0.09	0.16	86.38	180.00	2338.00	22.45	2.33	10.86
70255	90,165,190,265	A17	40.11	11.36	9.06	19.52	10.95	7.82	0.29	0.08	0.39	0.04	0.19	85.00	76.00	2860.00	18.50		
70315	59,154,267	A17		13.10	9.30	17.90	10.20	10.00	0.24	0.04	0.39			80.08	146.89	3266.16	22.14	2.22	49.51
71037	267	A17		11.20	8.90	19.40	11.20	7.00	0.25	0.05	0.43			85.00	73.00	2121.02	20.00		
71055	7,22,27,41,50,134,135,183,194,249	A17	37.59	13.44	8.96	19.65	11.31	9.22	0.27	0.05	0.39	0.08	0.20	87.60	193.67	2746.67	27.72	12.93	17.70
71065	267	A17		12.50	8.90	19.80	10.00	8.00	0.26	0.04	0.39			89.00	102.00	2579.43	22.00		
71066	267	A17		14.20	8.90	20.50	9.40	9.00	0.26	0.04	0.41			89.00	133.00	3325.21	24.00		
71069	174,267	A17		12.20	8.60	19.10	9.80	10.00	0.25	0.03	0.31			85.00	140.00	3243.11	21.00		
71136	58,72,165,190,265	A17	40.30	11.11	10.56	18.87	11.57	7.27	0.28	0.05	0.37	0.06	0.17	84.50	89.00	2420.00	15.80		
71155	63,267	A17		10.10	9.20	19.10	10.80	8.00	0.25	0.05	0.35			81.00	118.00	3338.90	23.00		
71175	58,72,165,190,265	A17	37.93	12.89	8.79	19.94	9.50	9.87	0.28	0.06	0.38	0.04	0.16	77.50	122.00	4400.00	19.65		
71505	267	A17		10.50	9.60	19.20	10.30	7.00	0.25	0.05	0.37			86.00	87.00	2093.65	18.00		
71509	265	A17		13.70	7.30	20.60	9.60	10.30		0.05	0.31			95.00	160.00		24.50		
71525	148	A17		12.90	8.80	20.80	11.00	8.20	0.25	0.05	0.39			85.00	106.00	2682.06	20.50		
71536	148	A17		7.80	11.70	16.10	13.60	7.30	0.22	0.07	0.50			73.00	39.00	2312.60	12.70		
71537	148	A17		10.90	9.70	19.30	11.20	8.20	0.26	0.05	0.37			78.00	99.00	2333.12	17.00		
71539	148,174	A17		8.60	9.80	19.10	12.10	5.40	0.26	0.08	0.47			73.00	36.00	1272.61	13.50		
71546	59,72,165,190,266	A17	39.14	12.22	9.06	18.41	10.90	7.92	0.26	0.07	0.39	0.05	0.19	78.50	120.00	3450.00	18.20		
71548	148	A17		12.40	8.70	19.60	9.30	8.50	0.24	0.06	0.41			77.00	110.00	3113.11	17.40		
71549	148	A17		12.20	8.30	20.20	10.00	8.10	0.24	0.06	0.40			81.00	108.00	3236.27	19.20		
71555	148	A17		13.00	8.90	19.60	10.00	9.50	0.24	0.07	0.42			78.00	119.00	3010.48	18.00		
71556	148	A17		11.70	10.00	19.90	10.50	7.50	0.24	0.06	0.45			70.00	74.00	2428.91	17.20		
71557	266	A17		13.00	9.30	19.10	10.50	8.50	0.24	0.06	0.41			80.00	120.00		19.30		
71559	108,266	A17		8.30	10.30	17.80	12.20	6.30	0.23	0.07	0.48			72.00	30.00		14.40		
71565	266	A17		10.80	10.10	17.60	11.70	7.50	0.23	0.07	0.43			76.00	90.00		16.10		
71566	58,72,108,190,266	A17	39.27	11.67	9.34	18.51	10.96	8.27	0.24	0.05	0.43	0.03	0.16	74.67	90.00	3430.00	19.37		
71567	72,108,165,190,266	A17	38.06	11.93	9.06	18.47	10.39	7.94	0.25	0.07	0.39	0.02	0.16	75.00	100.00	3690.00	17.77		
71568	148	A17		9.80	10.10	19.40	13.40	7.90	0.25	0.06	0.46			79.00	27.00	1689.97	14.70		
71569	72,108,163,165,190,259,266	A17	39.47	12.38	8.65	18.64	10.34	8.60	0.24	0.07	0.38	0.06	0.19	77.35	100.00	2301.67	17.90		4.00
71576	148,174	A17		11.80	8.90	20.00	10.60	6.80	0.24	0.05	0.39			80.00	85.00	2292.07	19.20		
71577	72,108,165,190,266	A17	39.18	12.55	8.84	19.97	10.58	8.25	0.26	0.07	0.42	0.05	0.17	79.67	110.00	3610.00	19.87		
71578	108,266	A17		11.70	8.40	18.60	9.50	8.10	0.24	0.07	0.42			74.00	100.00		18.50		
71586	148	A17		10.50	9.20	19.70	9.30	8.30	0.25	0.04	0.33			75.00	131.00	3325.21	22.30		
71587	108,266	A17		12.70	8.70	19.20	10.30	7.60	0.24	0.05	0.39			80.00	100.00		20.80		
71588	108,266	A17		12.00	8.40	19.90	10.10	8.00	0.24	0.04	0.35			79.00	110.00		23.10		
71595	148	A17		10.40	9.30	19.60	10.60	7.40	0.25	0.04	0.39			78.00	100.00	2846.27	18.40		
71596	108,266	A17		11.00	9.20	18.80	10.30	7.80	0.25	0.04	0.38			75.00	120.00		20.20		
72155	22,59,72,107,163,166,190,212,259	A17	38.79	12.24	8.52	19.45	11.08	8.73	0.26	0.07	0.41	0.05	0.15	80.76	100.00	2465.00	19.66	1.45	
74235	72,154,163,166,190,195,212	A17	39.02	12.28	8.91	18.93	10.78	8.51	0.28	0.08	0.39	0.05	0.15	80.98	98.76	2906.42	23.93	2.16	39.30
74245	59,72,90,154,165,190,265	A17	38.59	11.91	8.71	18.23	10.40	10.43	0.27	0.09	0.36	0.04	0.14	75.92	130.83	4014.25	24.68	8.90	51.56
74255	50,72,90,149,154,163,165,166,174,190,195,212	A17	38.36	12.50	8.80	17.88	10.25	10.65	0.26	0.10	0.37	0.05	0.10	70.41	83.83	4147.02	26.99	11.28	36.02
74275	27,41,47,69,71,72,90,134,149,154,163,165,174,180,186,190,195,237,260	A17	38.45	12.34	8.64	18.32	10.59	10.34	0.26	0.08	0.35	0.06	0.14	74.32	99.92	3464.59	23.50	8.59	23.87
75015	72,165,190,265	A17	41.92	9.13	9.98	19.99	11.88	5.80	0.29	0.10	0.48	0.05	0.20	78.00	24.00	1490.00	14.95		
75035	27,46,69,71,72,107,134,135,140,149,163,180,183,195,259	A17	41.63	10.24	9.46	18.71	11.80	6.58	0.25	0.07	0.44	0.07	0.22	78.90	23.75	2070.00	15.04	6.00	13.05
75075	72,114,126,149,166,180,190,191,194,212,251,251	A17	37.93	13.41	8.23	18.80	10.25	9.55	0.27	0.11	0.39	0.07	0.10	80.15	108.00	2880.00	26.25	31.00	34.00
75085	267	A17		13.10	8.70	18.80	9.90	9.00	0.25	0.06	0.42			81.00	133.00	3222.58	19.00		
77516	12,108,174,266	A17		13.70	7.80	20.20	9.40	9.40	0.25	0.04	0.33			80.00	120.00		24.60		
77535	108,165,190,266	A17	38.57	12.20	8.72	19.18	10.09	8.75	0.25	0.07	0.37	0.04	0.16	79.33	120.00	3810.00	20.47		
77536	266	A17		14.50	8.00	18.80	10.20	9.20	0.23	0.07	0.33			78.00	140.00		17.80		
78505	265	A17		12.00	10.60	18.60	9.90	9.50		0.07	0.46			74.00	108.00		18.70		
78575	108,154,266	A17		11.80	9.00	17.00	11.00	7.50	0.22	0.04	0.36			79.04	93.10	3259.84	17.70	3.68	37.30
78578	108,266	A17		11.20	9.00	18.60	10.00	8.20	0.23	0.07	0.40			75.00	90.00		19.40		
78585	154,267	A17		12.20	9.10	19.60	11.00	7.00	0.25	0.04	0.40			97.03	93.95	2537.53	22.73	3.39	44.13
78587	266	A17		12.21	8.80	19.40	10.30	7.00	0.24	0.05	0.37			81.00	90.00		20.30		
78595	265	A17		12.80	9.00	19.90	11.00	9.10		0.06	0.39			86.00	121.00		20.50		
78597	58,72,108,165,190,266	A17	38.54	12.00	8.95	18.56	10.78	7.34	0.26	0.06	0.41	0.11	0.19	78.33	100.00	2800.00	19.23		
78598	108,154,266	A17		8.90	10.00	18.50	11.50	5.20	0.25	0.08	22.22			75.11	50.39	3360.64	16.58	1.86	43.35
78599	72,165,190,266	A17	38.44	12.76	8.94	19.67	10.44	8.14	0.26	0.08	0.40	0.04	0.18	81.50	130.00	3600.00	19.50		
79155	7,22,58,72,147,163,166,190,195,212,259	A17	38.34	12.68	8.74	19.72	10.84	9.21	0.28	0.08	0.38	0.05	0.17	82.78	62.00	2771.25	23.84	3.27	20.83
79515	267	A17		10.20	9.10	18.70	11.00	9.00	0.28	0.05	0.39			82.00	120.00	3003.64	23.00		
79516	267	A17		12.30	8.40	19.90	10.00	8.00	0.25	0.05	0.38			87.00	109.00	2729.96	22.00		

References

See Appendix 2h

Appendix 2e: Published trace element data for lunar basalts

Sample	Zn(ppm)	Ga(ppm)	Ge(ppb)	As(ppm)	Se(ppm)	Br(ppm)	Rb(ppm)	Sr(ppm)	Y(ppm)	Zr(ppm)	Nb(ppm)	MO(ppm)	Ru(ppm)	Rh(ppm)	Pd(ppm)	Ag(ppm)	Cd(ppm)	In(ppm)	Sn(ppm)	Sb(ppb)	Te(ppm)	I(ppm)	Cs(ppm)	Ba(ppm)	La(ppm)	Ce(ppm)	Pr(ppm)	Nd(ppm)	Sm(ppm)	Eu(ppm)	Gd(ppm)
10003	58.44	3.91					0.64	156.50	114.00	381.80	20.65	0.18								0.04			0.03	139.42	15.07	46.59	7.96	39.84	13.84	1.82	19.00
10017	54.64	14.84	0.01		0.22	0.19	5.72	153.90	192.05	754.87	25.09	0.99			1.00	16.00	44.00	69.67		0.02			0.21	276.46	24.30	72.83	10.45	60.44	21.03	2.21	26.51
10020	13.85	4.48	0.00	0.05	0.33	0.06	1.08	142.12	129.75	358.57	26.80	0.32			1.50	44.76	6.37	14.60		0.01			0.12	77.87	8.01	29.15	8.70	27.22	9.45	1.55	15.27
10022	2.90	2.90		0.06	0.70	0.13	6.06	161.00	230.00	586.60						2.30		7.80		0.01			0.20	231.86	25.60	74.78		60.27	20.24	2.12	23.95
10024	14.00	5.00					5.99	181.03	168.00	578.00	25.00													263.67	29.07	86.13	12.00	54.15	19.30	2.08	
10031										370.00														330.00	27.30	78.00			20.70	2.23	
10032							6.09	165.00		370.00														270.00	27.70	73.00		65.00	21.35	2.17	
10044	33.55	6.32			0.23		2.14	211.45	169.71	518.29	30.13	0.12				200.00		3.20		0.03			0.03	162.80	11.10	51.17	7.75	55.43	18.46	2.67	25.74
10045	5.70	3.75		0.07	0.80	0.06	0.91	144.47	112.00	352.17	18.00					4.90		14.00		0.01				136.84	8.14	25.88	6.00	20.96	8.97	1.51	13.20
10047	9.64	5.91			0.25	0.08	1.15	203.60	131.00	401.33	23.00				2.00	17.10	108.80	73.60			13.00		0.05	184.75	12.70	45.95	13.00	40.43	17.45	2.69	
10050	50.38	6.56				0.01	0.74	183.37	125.34	477.15	25.30	0.16			1.40	1.42	2.56	4.40		0.06			0.02	82.93	8.59	32.75	7.19	34.19	13.62	2.13	22.80
10057	17.55	7.93	0.03	0.04	0.15	0.05	5.29	153.89	208.68	587.56	31.61	0.19			8.65	19.88	290.41	14.17	0.60	0.01	8.00		0.21	283.82	24.78	71.13	14.03	58.07	25.96	2.05	27.09
10058	48.68	6.47	0.03	0.07		0.30	1.15	197.80	155.89	291.40	33.38	0.29				70.00	700.00	323.00	1.20	0.01			0.10	109.85	11.50	39.59	10.16	43.83	20.63	2.35	22.98
10062		5.40			0.23		0.90	186.88	105.00	304.50		0.16				62.00							0.03	146.13	13.30	42.47		31.96	11.96	2.03	18.00
10069	66.53	3.92					6.07	166.60	201.46	580.08	29.43	0.26								0.04			0.28	297.88	25.67	75.15	11.57	57.05	20.02	2.14	29.00
10071		6.80					5.73	160.25	164.00	494.75	24.00												0.17	374.25	25.17	79.70		62.99	19.85	2.10	29.30
10072	11.71	5.88	0.03	0.05	0.19	0.09	5.88	146.43	187.60	593.50	30.20	0.40			3.00	211.53	255.91	492.00	0.40	0.01			0.21	285.86	29.07	79.82	18.00	52.76	26.44	2.06	28.50
10092	72.74	3.64					0.75	188.95	92.14	209.95	18.25	0.06								0.02			0.03	76.09	7.41	23.64	4.41	20.99	8.66	1.50	13.40
12002	2.41	6.34	0.03		0.16	0.01	1.04	98.97	36.25	107.33	6.87	0.05				0.42	17.80	9.14	0.23				0.05	61.53	5.64	16.67	2.50	13.12	4.27	0.85	6.27
12004	7.48	2.95	0.30	0.04	0.30	0.06	1.14	98.30	48.84	236.37	8.64	0.34					1.00	4.37		0.01			0.14	76.72	7.79	19.00	3.08	13.38	4.46	1.11	5.60
12006								96.50	31.00	97.00	6.40													86.50	9.00	21.00		19.60	4.74	1.07	
12009	3.33	3.01	0.00		0.11		1.05	100.64	38.11	114.96	6.26	0.15				0.64	5.98	7.57		0.00	4.10		0.05	62.98	6.01	18.39	2.51	12.89	4.96	0.89	5.23
12012							0.64	114.00	36.50	109.50	6.60													66.00	5.30	14.55		10.80	3.81	0.78	
12015	14.56	3.23					1.04	99.28	38.17	124.82	7.17	0.12				0.22				0.02			0.09	60.83	5.98	16.47	2.52	13.54	4.39	0.90	5.83
12016								105.50	45.00	117.00	6.10													59.00	4.30	14.45		10.18	4.83	1.05	
12017	2.16	3.10			0.17	0.03	1.46	113.00								2.13	3.25	3.55					0.07	85.00	7.00	23.40		13.20	4.95	1.00	
12018	3.50	4.02	0.30	0.03	0.19	0.08	1.38	94.20	57.67	134.50	10.00	0.70			3.00	0.01	0.80	1.25		0.13			0.12	82.92	9.08	16.13	2.88	13.13	3.74	0.87	4.75
12019								130.00																71.00	6.70	19.10		12.90	4.60	1.01	
12020	9.12	3.32			0.11	0.02	1.07	90.14	36.46	111.73	8.82	1.12				0.98	1.10	7.35		0.03			0.04	54.91	5.04	19.56	2.36	12.47	3.79	0.79	5.48
12021	4.85	3.69	0.00	0.01	0.21	0.09	1.17	113.87	49.58	122.33	8.58	0.12	25.00			68.85	3.10	7.86		0.03	2.80		0.06	84.38	7.04	23.30	2.82	15.09	5.53	1.11	7.53
12022	4.02	3.58	0.00		0.13		0.72	142.97	60.98	161.68	6.34	0.11	17.00			3.80	2.82	2.07	0.39	0.00	2.20		0.09	57.09	5.94	17.82	3.09	16.75	6.09	1.28	8.66
12035		3.00					0.82	83.50	32.50	84.50	4.00													47.52	3.58	10.13		8.91	3.22	0.73	4.31
12038	8.67	4.95	0.02		0.16	0.01	0.56	192.21	59.06	206.68	9.08	0.04				0.07	3.82	1.15	0.10	0.02				119.50	13.09	29.33	4.97	23.63	7.28	2.07	10.45
12040	4.39	1.75			0.06	0.00	0.66	92.83	26.50	89.00	3.50		15.00			0.41	3.30	0.40					0.01	54.17	3.89	11.90		10.45	3.43	0.81	
12046	0.75		0.00		0.12		0.81	158.00								0.48	2.70	1.11		0.00	4.40		0.04	72.00	6.20	19.30		15.80	5.20	1.32	
12051	9.28	11.67	0.00	0.02	0.20	0.04	1.04	151.37	69.70	151.19	8.86	0.11				0.81	1.15	1.83		0.06			0.06	83.59	6.50	20.04	3.16	15.99	5.83	1.27	7.34
12052	4.95	3.00	0.03	0.01	0.14		1.17	109.05	53.75	144.20	6.50	0.03	9.10			0.85	2.20	4.37	0.16	0.00	3.00		0.04	66.67	6.55	22.54	2.60	17.68	5.04	1.03	7.52
12053	8.83	3.53	0.10	0.02		0.10	1.28	126.20	47.12	128.08	9.14	0.52	1071.00					0.86		0.03			0.08	91.70	6.99	22.08	2.99	15.87	5.21	1.07	6.97
12054	37.27	4.15					1.14	148.11	57.83	174.74	7.50												0.03	71.07	6.72	19.05	3.30	16.35	5.87	1.35	8.65
12061								149.00																	5.20	15.10		13.40	5.20	1.25	
12062								180.00																69.00	6.90	20.20		14.60	5.80	1.36	
12063	11.34	4.96	0.45	0.07	0.40	0.12	0.99	148.83	74.60	157.13	7.44	0.47					1.00	1.78	0.12				0.10	92.31	8.58	23.64	4.24	21.49	6.32	1.83	9.47
12064	11.15	3.75	0.00				0.97	142.36	48.00	146.74	7.57						3.90	1.80		0.21			0.01	59.32	5.94	17.22	2.84	14.26	4.95	1.16	7.18
12065	2.28	3.83	0.20	0.04	0.29	0.07	1.32	108.26	56.50	166.00	16.00	0.60				1.37	1.43	1.90					0.14	97.70	8.84	21.63	5.80	18.57	4.93	1.04	7.20
12072	8.14	2.85					0.88	75.13	30.70	95.90	5.36					0.11							0.05	53.60	6.22	17.35	2.22	11.30	4.11	0.91	3.91
12075	0.98	3.40	0.00				1.26	82.77	39.33	113.50	16.00						1.75	2.80					0.08	59.18	5.83	16.40	2.20	11.63	3.93	0.84	5.67
12076								94.00																64.50	5.90	17.50		11.40	4.02	0.92	
12077																									5.50	15.10		9.00	3.80	0.80	
14053	13.54	14.03	0.40		0.14	0.05	2.20	115.76	64.73	235.85	17.33	0.15	0.11			0.60	20.00		0.08	0.02	15.00		0.11	170.02	12.78	37.52	4.94	23.51	6.68	1.22	8.44
14073							14.20	174.50		735.00														620.00	60.67	160.00			26.80	2.13	
14168							9.76	58.80		80.00														100.00	5.20	14.00		10.62	3.34	0.71	
14276	1.70	4.00		0.16			13.10	194.43	200.00	620.00	33.00		0.30					56.00		0.02			0.57	593.33	48.33				20.00	1.90	
14310	1.75	4.03	0.11	0.03	0.12	0.24	12.83	193.52	178.17	946.55	46.76	0.17	4.31			10780.00	7.24	51.20	0.03	0.01	4.00		0.58	655.00	56.94	145.58	20.43	88.96	24.63	2.20	28.92
15016	5.72	3.79	0.02		0.11		0.93	84.25	24.67	94.93	7.43	0.08				0.84	1.98	0.35	0.19	0.00	2.40		0.03	51.23	5.44	15.02	2.12	9.72	3.53	0.87	4.81
15065	0.92	4.11	0.02	0.00	0.00		2.74	107.14	29.43	83.43	11.00							1.41					0.05	75.00	11.71	22.93	3.43	15.07	4.12	1.04	5.45
15076		4.10					1.01	106.09	27.00	74.40	9.10													60.35	8.02	15.10		11.02	3.56	0.98	4.95
15085	9.60	4.12	0.03	0.00	0.12	0.01	1.30	110.50	36.70	124.17	8.30					1.00	0.68	0.60		0.00	6.20		0.04	79.59	5.34	14.30	2.50	11.17	3.83	0.98	5.07
15105																								80.00	5.00				3.60	0.97	
15115																									6.30				4.10	0.94	
15117		3.80					1.00	150.00	26.00	90.00														100.00	9.83				3.90	1.01	
15118							0.88	98.50																59.00	8.00			11.40	4.31	1.33	
15256	11.11	4.09	0.00		0.12	51.00	0.89	97.99	33.31	95.52	6.06	0.32				0.78	104.00	6.80		0.00	2.00		0.03	54.21	5.37	15.04	2.38	10.77	3.56	0.91	4.72
15379	16.98	4.42					1.18	99.57	26.62	82.78	9.49	0.06								0.01			0.04	59.64	5.07	14.32	2.14	9.73	3.50	0.90	4.55
15385																								60.40	5.48	18.00		9.21	2.94	0.77	6.08
15386	7.63	6.39	0.06		0.07		17.76	187.18	240.90	956.63	72.40	0.21				0.59	9.64	1.99	0.06	0.01			0.77	765.32	73.42	185.82	30.00	109.52	32.50	2.60	44.90
15388																								29.00	1.68	5.00			1.70	0.88	
15475		2.95				0.03	0.65	106.14	29.33	78.25	5.95													50.60	5.08	14.53		9.74	3.16	0.79	
15476		3.00					1.50	110.50	34.93	108.33	5.60												0.31	66.75	5.90				4.30	1.13	
15485								104.00	32.20	113.00	5.50													71.00							
15495	1.85	4.12	0.01	0.01		0.02	1.04	110.25	30.60	109.25	7.53						1.30	1.05					0.03	96.25	9.23	24.50	2.40	22.50	5.55	1.15	5.10
15499	1.07	3.00	0.00		0.12		1.08	106.72	29.55	110.67	6.70					0.99	3.37	0.90		0.00	3.20		0.05	69.00				11.70	3.69		
15535	6.89	3.25	0.02			0.01	4.44	95.34	30.62	84.82	6.74	0.20					1.45	0.34		0.01	1.40	2.00	0.02	42.94	4.13	11.33	2.08	8.65	2.84	0.75	3.79
15536	11.77	3.63	0.02				2.53	104.08	29.27	89.77	8.91	0.61					0.93	0.50					0.03	48.55	4.86	14.09	2.18	9.56	3.31	0.84	4.49
15545	14.58	3.29	0.00		0.12		0.86	98.13	28.76	114.04	7.65	0.04				2.85	1.80	1.45		0.00	2.80		0.05	54.31	4.77	12.81	2.02	9.46	3.31	0.85	4.48
15555	6.98	3.63	0.01		0.13	3.00	0.97	90.61	25.98	90.39	8.63	0.19				67.33	2.10	0.37		0.01	3.40		0.03	41.95	4.70	12.36	2.01	10.47	5.96	0.95	4.09
15556	10.27	4.22	0.01		0.12	0.00	1.96	103.28	32.44	94.87	8.05	0.13				0.85	28.00	0.56		0.01	2.70		0.04	61.18	5.36	16.42	2.42	11.22	3.73	0.98	4.74
15557	8.05	4.29	0.02			0.02	2.03	102.12	29.28	91.93	9.94	0.10				2200.00	1.40	0.50			7.50	1.80	0.02	48.06	12.14	15.33	2.24	11.16	3.90	0.98	5.29
15605								115.00		130.00														50.50	5.60	15.95			3.87	0.91	
15607	20.33	4.48					1.99	107.90	36.24	84.31	8.63	0.17								0.03			0.03	50.13	8.11	14.48	2.24	10.15	3.43	0.88	4.79
15614																									5.20				3.40	0.76	
15616																									5.30				3.50	0.77	
15620																								54.00	5.16	13.20			3.35	0.84	
15623																								55.00	5.22	14.30			3.50	0.84	
15630	15.10	3.34					2.45	89.51	24.53	89.75	7.18	0.09								0.01			0.02	54.09	5.43	15.18	2.29	10.73	3.57	0.83	4.62

Appendix 2e: Published trace element data for lunar basalts

Sample	Zn(ppm)	Ga(ppm)	Ge(ppb)	As(ppm)	Se(ppm)	Br(ppm)	Rb(ppm)	Sr(ppm)	Y(ppm)	Zr(ppm)	Nb(ppm)	MO(ppm)	Ru(ppm)	Rh(ppm)	Pd(ppm)	Ag(ppm)	Cd(ppm)	In(ppm)	Sn(ppm)	Sb(ppb)	Te(ppm)	I(ppm)	Cs(ppm)	Ba(ppm)	La(ppm)	Ce(ppm)	Pr(ppm)	Nd(ppm)	Sm(ppm)	Eu(ppm)	Gd(ppm)
15633		2.90					0.50																0.02	45.00	4.72	13.10		10.80	3.27	0.82	4.60
15634																									2.40				1.80	0.58	
15639																									4.10				2.80	0.76	
15641																									4.22	11.80			2.95	0.77	
15643		4.10						140.00	23.00	59.00														48.67	3.50	9.85			2.36	2.10	
15648																									4.70				3.20	0.82	
15649																									6.10				4.10	0.87	
15659		3.80					1.00	130.00	25.00	111.33														62.00	26.93				3.30	0.79	
15661																									5.10				3.30	0.78	
15662																									5.00				3.40	0.82	
15666																								40.00	6.80				4.30	1.12	
15669																									5.10				3.50	0.87	
15672	17.46	4.07					1.05	103.68	25.02	72.20	5.91	0.04											0.02	45.02	4.49	13.49	2.07	9.60	3.00	0.78	4.10
15675	21.68	3.64					4.03	103.19	30.41	108.00	8.42	0.54								0.06			0.03	57.31	5.40	15.65	2.39	12.71	3.68	0.92	5.18
15676	22.34	3.71					3.01	118.49	27.69	87.03	10.11	0.03											0.12	57.71	7.50	14.50	2.28	9.77	3.65	0.90	4.78
70017	2.00	8.83	0.00				0.58	179.67	88.40	210.00	19.83												0.03	100.35	4.28	13.30		20.37	20.58	1.64	9.05
70075																									6.90	27.00		28.00	10.90	2.21	
70135	39.39	8.77	0.00				0.72	171.18	100.19	258.74	22.81	0.03								0.03				130.01	7.33	27.11	2.87	31.04	11.25	1.99	15.69
70139							0.28	163.00		160.00													0.02	67.00	3.10	13.00		13.65	5.05	1.40	
70147								140.00		210.00													0.04	76.00	4.80	22.00		18.00	7.10	1.70	
70185							0.49	173.00																109.15	8.17	18.50		21.10	12.12	2.31	14.00
70215	12.85	8.24	0.00	0.05	0.17	0.02	0.50	129.89	67.72	186.50	19.96					1.10	1.80			0.00	2.10		0.02	118.27	5.26	15.78	3.00	18.68	6.68	1.39	9.93
70255							0.65	199.00																85.30	6.73	24.70		27.30	10.70	2.22	17.60
70315	119.30	3.75					0.24	162.68	66.32	196.92	20.74													53.84	3.49	14.61	2.74	15.85	6.64	1.50	9.73
71037																									6.10	21.00		23.00	8.10	1.54	
71055	2.30	7.64	0.00				0.72	131.67	69.00	223.00	27.00							4.37					0.07	119.85	4.62	17.40		25.00	6.47	1.49	
71065																									5.10	18.00		19.00	6.90	1.34	
71066																									5.10	18.00		18.00	6.50	1.33	
71069							0.32	146.00																	4.30	17.00		18.65	7.38	1.55	
71136							0.40	147.00																65.90	5.81	19.00		19.80	7.97	1.67	12.30
71155																									5.60	21.00		23.00	8.10	1.49	
71175							0.59	184.00																78.50	5.72	22.30		24.70	9.15	1.99	15.70
71505																									5.90	21.00		22.00	7.80	1.57	
71509																									5.30				8.50	1.62	
71525																									5.80	27.00			7.50	1.43	
71536																									6.20	29.00			9.60	2.17	
71537																									5.80	25.00			7.90	1.47	
71539							0.79	229.00																	8.00	30.00		32.50	12.75	2.44	
71546							0.63	191.00																83.20	6.60	23.90		25.90	10.10	2.02	16.70
71548																									6.50	38.00			9.90	2.01	
71549																									5.50	40.00			8.20	1.95	
71555																									6.60	40.00			9.60	2.06	
71556																									5.80	35.00			8.60	2.11	
71557																									4.80	24.00			7.50	1.72	
71559																									6.60	26.00		24.00	10.40	2.20	
71565																									6.40	26.00			9.20	2.11	
71566																									4.16	19.07		18.00	7.14	1.72	
71567							0.39	161.00																54.40	5.38	20.80		16.30	9.57	1.89	11.40
71568																									5.30	29.00			8.50	1.91	
71569		2.15		0.01	0.11	0.01	0.67	186.67	91.00	258.00	24.00												0.04	86.20	6.44	22.70	4.30	26.15	10.88	2.04	16.10
71576							0.38	127.00																	6.70	31.00		18.20	7.43	1.54	
71577							0.64	191.00																83.90	6.83	26.60		27.50	10.60	2.15	16.80
71578																									6.00	25.00		28.00	9.80	1.96	
71586																									5.70	38.00			7.20	1.47	
71587																									5.70	22.00			7.60	1.40	
71588																									4.90	18.00			6.10	1.30	
71595																									6.40	29.00			6.90	1.43	
71596																									5.50	21.00		20.00	7.20	1.50	
72155	2.20	5.08				0.01	0.61	185.00	93.00	269.00	22.00						1.75	0.79						88.28	6.89	28.86		28.13	10.52	2.06	15.60
74235	55.04	6.11					0.61	191.20	146.82	293.53	26.56	0.15								0.02				190.06	8.95	24.15	4.35	25.62	10.60	2.03	15.23
74245	110.61	3.46					1.14	159.04	83.57	218.50	20.66	0.40											0.04	66.29	6.06	22.73	3.77	23.79	9.55	1.75	13.34
74255	44.85	4.85					1.25	163.07	118.37	274.59	25.31	0.03											0.03	143.73	6.48	23.66	4.08	25.00	10.66	1.88	16.12
74275	24.34	9.61	0.01	0.00			1.21	153.87	91.97	244.52	20.22	0.02											0.04	90.15	6.14	20.29	4.26	27.91	9.41	1.79	14.50
75015							0.65	215.00																109.25	9.47	23.80		26.50	13.95	2.75	17.70
75035	2.75	4.88	0.00	0.00	0.16	0.01	0.87	196.86	109.00	291.33	26.55					0.62	1.70			0.00	1.50		0.03	115.34	7.99	26.50	6.50	31.27	7.38	2.39	18.45
75075	5.00	6.50					0.56	163.32	89.50	246.33	26.00													158.27	5.34	18.55		21.53	18.11	1.89	12.90
75085																									7.50	31.00		32.00	11.60	2.32	
77516							0.34	110.00																	4.70	18.00		17.17	6.13	1.25	
77535							0.55	184.00																70.70	5.55	21.43		21.57	8.77	1.95	13.60
77536																									6.10	20.00		25.00	8.50	1.94	
78505																									5.90				9.40	2.10	
78575	89.39	3.86					0.27	157.36	90.95	256.58	23.32	0.03								0.01				69.46	4.16	17.04	3.38	22.46	7.52	1.57	13.62
78578																									5.40	25.00		22.00	8.60	1.90	
78585	95.17	3.97					0.43	152.45	132.53	271.97	31.99	0.16												62.07	5.63	19.76	3.20	19.74	7.46	1.41	9.76
78587																									5.70	23.00			6.60	1.41	
78595																									7.50				10.50	2.05	
78597							0.37	130.00																60.60	5.42	17.97		18.80	7.26	1.43	11.20
78598	88.03	3.77					0.65	183.01	101.76	230.31	23.33									0.03			0.03	80.67	7.30	27.89	4.06	27.73	11.02	2.25	15.53
78599							0.71	190.00																83.20	6.78	25.35		25.80	10.60	2.16	16.60
79155	2.80	4.59	0.00	0.00	0.21		0.46	163.00	87.00	232.25	17.40						8.00	0.36					0.02	103.43	5.20	21.13	3.50	20.05	8.35	1.90	13.00
79515																									5.30	20.00		21.00	7.70	1.42	
79516																									5.20	20.00		21.00	6.90	1.33	

Appendix 2e: Published trace element data for lunar basalts

Sample	Tb(ppm)	Dy(ppm)	HO(ppm)	Er(ppm)	Tm(ppm)	Yb(ppm)	Lu(ppm)	Hf(ppm)	Ta(ppm)	W(ppm)	Re(ppb)	Os(ppb)	Ir(ppb)	Pt(ppb)	Au(ppb)	Hg(ppm)	Tl(ppm)	Pb(ppm)	Bi(ppb)	Th(ppm)	U(ppm)	Li (ppm)	Be(ppm)	B(ppm)	F (ppm)	Cl (ppm)
10003	3.42	22.17	4.39	13.24	1.85	13.10	1.75	10.42	1.66	0.22								0.50		1.16	0.27	9.00	1.25			
10017	4.66	29.06	6.20	17.06	2.46	17.95	2.73	16.81	2.26	0.46			0.02		4.41		6.16	1.41	1.15	3.76	0.74	22.28	2.24	0.70		12.20
10020	2.65	18.87	7.00	12.67	1.40	8.35	1.30	7.66	1.47	0.13			0.03		1.64		0.33	0.36	0.15	0.83	0.19	10.67	2.00	1.00	85.00	150.00
10022	4.85	30.10	9.00	15.80		16.23	2.49	18.26	1.32						0.10					2.90	0.74	11.50				19.30
10024	5.20	29.30	8.10			17.85	2.73	17.64	2.15											3.46	0.67					
10031	4.30					17.20	2.43	15.40	2.50											2.80						
10032	4.50					16.90	2.40	14.50	2.30											3.30						
10044	4.07	29.59	5.62	17.67	2.20	14.18	2.00	13.34	2.07	0.20					1.40			0.52		0.89	0.28	9.45	2.10	1.20		
10045	2.12	14.65		9.70		7.77	1.30	7.61	1.70											1.18	0.17	15.00				6.80
10047	4.37	32.90	7.90			16.60	2.35	13.22	2.20				0.16		0.23		0.47		1.49	1.22	0.16					
10050	2.99	23.49	4.96	15.20	2.07	10.50	1.72	10.79	1.80	0.13			0.01		0.03		0.33	0.53		1.00	0.20	7.30	1.84			
10057	5.05	31.85	6.67	14.74	1.81	16.37	2.34	14.78	1.73	0.46			0.05		1.24		1.09	2.04	0.27	3.32	0.69	16.00	2.54	2.40	80.00	31.00
10058	4.18	28.98	6.69	17.24	1.65	13.87	2.02	10.77	1.73	0.26					0.73			1.77		12.98	0.20	12.13	1.64	2.00	50.00	50.00
10062	3.05	21.52	4.40	12.33		10.57	1.63	11.06	1.58						5.80					0.85	0.28					
10069	4.96	32.01	6.97	19.42	2.77	19.01	2.45	16.26	2.13	0.53								1.52		3.15	0.83	17.60	2.96			
10071	4.45	32.25	8.60	21.30		17.76	2.62	16.63	2.23									1.69		3.37	0.74	17.00	3.00			
10072	4.88	34.97	10.00	17.31	1.83	16.38	2.86	15.19	2.70	0.42			6.50		0.14		0.92	3.00	0.73	3.77	0.50	14.67	3.35	4.00	100.00	960.00
10092	2.29	14.70	3.34	9.73	1.39	8.28	1.18	6.74	1.22	0.07								0.40		0.58	0.22		1.09			
12002	1.02	7.01	1.30	4.13	1.15	3.73	0.52	3.08	49.76	0.21			0.24		0.02		0.25		1.40	0.76	0.17		0.83			17.00
12004	1.29	6.69	1.35	5.03	0.52	5.09	1.11	6.88	0.45	0.12								1.40		0.87	0.39	8.73	0.73	1.90	113.00	30.25
12006	1.19	8.10				3.70	0.53	3.40	0.56											0.74						
12009	1.11	8.65	1.31	3.70	0.52	3.80	0.57	3.41	0.43	0.17	0.00		0.05		0.04		0.30	0.27	0.27	0.88	0.25	6.45	0.73			
12012	1.02	4.90				3.20	0.47	3.00	0.37											0.67		3.90				
12015	1.08	6.93	1.42	4.04	0.55	3.58	0.51	3.38	0.41	0.16								0.41		0.70	0.29	8.23	0.52			
12016	1.28	5.50				4.30	0.61	4.16	0.26											0.47						
12017	1.24	7.70				4.30	0.62	3.40	0.48				1.42		0.65		0.61		0.42	0.87						
12018	1.01	6.85	1.22	3.95		4.30	0.96	2.94	0.48	0.12					1.80			3.00		1.24	0.22	6.75	1.60	1.45	150.00	15.78
12019	1.20	7.00				4.50	0.54	3.20	0.56											0.79						
12020	1.16	7.57	1.27	3.72	0.53	3.59	1.41	3.23	0.54	0.11			0.03		0.06		0.61	0.29	0.15	0.73	0.24	5.70	1.22			
12021	1.33	9.94	1.88	6.19	0.60	5.52	0.83	3.64	0.50	0.19	0.00	0.95	0.01		1.30		0.50	0.40	0.14	1.09	0.28	7.23	1.34			26.50
12022	1.70	10.96	2.29	6.27	0.83	5.63	0.78	4.37	0.45	0.16	0.01	1.20	0.14		0.05		0.35	0.30	0.24	0.71	0.22	7.37	0.84		40.00	
12035		6.07		3.09	0.42	3.59	0.42															5.80	1.60			
12038	1.60	10.37	1.72	6.02	0.97	5.21	0.69	4.92	0.56	0.10			0.14		2.02		0.76	0.21	0.76	0.53	0.16	8.85	1.06			6.60
12040	0.98	5.20				3.05	0.52	2.31	0.36			0.73	0.17		0.01		0.06		0.45	0.92						
12046	1.70	8.80				4.70	0.70	3.70	0.49		0.00		0.00		0.01		0.80		0.37	0.67	0.21					
12051	1.51	8.74	2.25	5.00	0.97	5.71	0.80	3.94	0.52	0.12			0.32		0.01		0.37	0.38	0.53	0.91	0.27	7.40	1.21	1.20	85.00	32.00
12052	1.67	8.26	1.34	5.88	0.72	4.25	1.20	3.75	0.83	0.15	0.00	0.26	0.00		0.05		0.39	0.62	0.21	1.27	0.34	5.75	0.74	1.10		28.00
12053	1.37	7.71	1.80	4.84	0.61	4.41	1.05	3.56	0.60	0.13		1.69						0.37		0.83	0.25	6.20	1.14	1.40	51.00	28.50
12054	1.62	9.82	2.12	6.15	0.87	5.41	0.75	4.87	0.42	0.08								0.25		0.69	0.23		1.29			
12061	1.35	8.10				4.70	0.69	3.60	0.49											0.56						
12062	1.34	8.80				5.00	0.70	3.90	0.45											0.77						
12063	2.20	11.68	1.95	8.50	0.98	6.58	1.61	5.12	0.56	0.10			0.06		0.05			0.62		0.82	0.22	10.03	1.24	3.60	84.00	32.60
12064	1.29	8.97	1.77	5.46	0.94	4.49	1.09	3.47	0.39	0.06			0.01		0.00			0.55		0.77	0.25	6.45	1.04			
12065	1.64	8.29	1.74	7.80	0.69	5.16	1.04	3.74	0.52				0.07		0.05		0.53	5.00	0.30	1.11	0.47	6.50		3.00	59.00	29.00
12072	0.91	5.56	0.97	2.66	0.37	3.12	0.42	2.93	0.31									0.35		0.74	0.16	6.00	0.32			
12075	0.94	6.39	1.37	4.04		3.80	0.94	2.73	0.33				0.02		0.03					0.72	0.24	5.85				
12076	1.08	7.00				3.35	0.50	3.20	0.53											0.90						
12077	0.93	5.80				3.20	0.46	2.50	0.45											0.65						
14053	1.34	10.20	2.13	6.28	0.71	6.53	0.94	5.94	0.94	0.22	0.01		0.02		0.11		1.40	1.78	0.29	2.17	0.57	11.00	1.01			
14073	4.80					21.67	2.90	17.00	2.40									6.18		10.27	2.91					
14168	0.85	5.40				3.60	0.53	2.40	0.60											0.70						
14276	4.80	23.00	7.30			13.13		16.00	2.10	0.00								9.00		8.00	2.50	21.00	4.00			23.00
14310	4.32	32.65	6.70	19.61	2.98	18.99	2.51	21.21	2.33	1.20	1.02	10.50	8.90		14.00		10.00	7.48	2.50	10.83	3.20	22.70	4.87			22.00
15016	0.77	5.13	1.07	2.91	0.39	2.89	0.33	2.41	0.41		0.00		0.09		0.15		0.32	0.33	0.36	0.42	0.14	6.19	0.87			
15065	0.84	6.73	1.23	3.80	0.47	4.10	0.36	2.63	0.43	0.10			0.05		0.14	0.52		0.24	0.14	0.61	0.17	6.10		32.00		
15076	0.70	5.60		3.40		3.07	0.36	2.59	0.44							0.59		0.27	0.15	0.45	0.14	5.60	1.20			
15085	0.90	5.74	1.19	3.50		2.62	0.42	2.51	0.55	0.06	0.00		0.01		0.23	0.46	0.24	1.10	0.12	0.42	0.13	7.90		5.00	22.40	4.00
15105	0.71	4.90				2.20	0.34	3.10	0.45																	
15115	0.80					2.70	0.37	2.60	0.43																	
15117	0.70					3.73	0.42	2.50	0.44													5.20	1.40			
15118	1.07	5.90				3.00	0.49	3.80	0.62																	
15256	0.84	5.12	1.05	2.82	0.40	2.35	0.32	2.68	0.45	0.03	0.00		0.02		0.02		1.45	0.21	0.41	0.46	0.13	7.61	0.62	3.00		
15379	0.74	4.83	0.98	2.69	0.35	3.08	0.30	2.60	0.38									0.62		0.48	0.14	6.95	0.42			
15385	0.57	4.10		3.19		2.21	0.29	1.85	1.84																	
15386	6.50	42.58	10.30	27.63	3.97	22.28	3.04	25.23	3.30	1.38	0.02		0.05		0.22		5.55	5.85	0.47	11.35	3.23	28.70	6.38			
15388	0.47	3.40				1.79	0.30	1.51	0.32											0.43						
15475	0.79	4.92		2.95		2.47	0.37	2.56	0.34						7.00					0.40	0.12	9.15		4.00	43.00	5.90
15476	0.88	3.50				3.40		3.60	0.40							0.73		0.35	0.19	0.52	0.18	8.00		2.00		
15485																										
15495	1.13	7.03	1.20	3.10		3.73	0.49	3.65	0.51	0.17	2.80	32.00	21.00		55.09					0.74	0.21	6.30				27.00	6.00
15499											0.00		0.00		0.01		0.32		0.16	0.59	0.17					
15535	0.65	4.25	0.79	2.47	0.32	1.87	0.26	2.33	0.37				0.06		0.06			0.23		0.43	0.09	7.04	0.44	4.00		1.40
15536	0.76	4.60	0.95	2.56	0.36	2.10	0.29	2.63	0.37	0.03	360.00	27.00	22.50		36.50			0.60		0.45	0.12	6.70	0.66			
15545	0.71	4.78	0.91	2.60	0.31	1.98	0.30	2.45	0.36	0.01	0.00		0.02		0.01		0.31	0.22	0.21	0.36	0.13	8.30	0.54			
15555	0.73	4.11	0.86	2.55	0.34	2.76	0.30	2.49	0.77		0.00		0.01		0.25	0.44	0.20	0.24	0.28	0.45	0.18	6.14	0.40	3.00		
15556	0.83	5.12	1.08	2.99	0.42	2.27	0.33	2.86	0.45	0.18	0.00		0.04		0.44		0.32	0.19	2.10	0.45	0.15	7.87	0.59	3.00		
15557	0.89	5.81	1.15	3.19	0.38	3.46	0.33	2.55	0.45	0.08		0.81	0.08		0.08	2.59				0.39	0.12	6.50	0.62			4.20
15605	0.84					2.42	0.32	2.83	0.43											0.45	0.18					
15607	0.75	4.72	1.00	2.77	0.37	3.01	0.35	2.83	0.50	0.04								0.24		0.46	0.14	6.60	0.48			
15614	0.60					2.00	0.27	2.40	0.39																	
15616	0.70					2.20	0.34	2.40	0.47																	
15620	0.75	4.40				2.07	0.34	2.41	0.44											0.63						
15623	0.81					2.21	0.34	2.44	0.53											0.67						
15630	0.75	5.00	0.99	2.72	0.36	2.22	0.29	2.53	0.41	0.03								0.23		0.53	0.16	7.16	0.43			

Appendix 2e: Published trace element data for lunar basalts

Sample	Tb(ppm)	Dy(ppm)	HO(ppm)	Er(ppm)	Tm(ppm)	Yb(ppm)	Lu(ppm)	Hf(ppm)	Ta(ppm)	W(ppm)	Re(ppb)	Os(ppb)	Ir(ppb)	Pt(ppb)	Au(ppb)	Hg(ppm)	Tl(ppm)	Pb(ppm)	Bi(ppb)	Th(ppm)	U(ppm)	Li (ppm)	Be(ppm)	B(ppm)	F (ppm)	Cl (ppm)
15633	0.74	4.95	1.04	3.00		2.02	0.34	2.40	0.38											0.45						
15634	0.40					1.20	0.15	1.10	0.15																	
15639	0.50					1.80	0.21	2.10	0.35																	
15641	0.63					1.86	0.26	2.11	0.39											0.47						
15643	0.55	2.30				2.77	0.25	1.60	0.20											0.61		4.70				
15648	0.70					2.20	0.26	2.10	0.39																	
15649	0.80					2.50	0.37	2.80	0.48																	
15659	0.50					3.17	0.30	2.50	0.40													5.40				
15661	0.70					2.00	0.25	2.50	0.41																	
15662	0.70					2.10	0.27	2.50	0.60																	
15666	0.88	5.10				2.50	0.47	3.20	0.41																	
15669	0.80					2.10	0.32	2.60	0.37																	
15672	0.63	4.16	0.90	2.52	0.34	2.53	0.31	2.30	0.38									0.01		0.34		5.84	0.50			
15675	0.78	5.52	1.05	2.92	0.38	2.35	0.31	2.66	0.46	0.06								0.60		0.49	0.13	7.42	0.42			
15676	0.72	4.73	1.02	2.85	0.37	2.86	0.35	2.78	0.47	0.00								0.42		0.43	0.12	7.38	0.51			
70017	2.09	11.57		5.49	0.49	7.09	1.10	7.19	1.62	0.08								0.17		0.97	0.08	8.07				
70075	2.80	18.00				10.40	1.53	9.00	2.10																	
70135	2.89	21.77	2.76	7.21	1.06	10.30	1.46	9.57	1.80	0.09		0.10						3.32		0.60	0.10	11.20	0.77			
70139	1.50	9.70				5.40	0.81	5.70	1.20											0.30	0.10					
70147	2.10	13.20				7.20	1.07	6.90	1.40											0.20	0.10					
70185		22.00		9.52		11.69	1.56	8.20												0.30	0.10	9.60				
70215	1.79	12.23	2.50	5.78	1.40	6.61	1.11	6.97	1.56	0.08	0.00		0.00		0.16		0.16		0.10	0.34	0.11	9.05			72.00	4.50
70255		19.10		12.10		10.90	1.44	9.65														10.40				
70315	1.69	11.90	2.68	7.76	1.05	6.74	0.93	6.05	1.37	0.00								0.15		0.25	0.09		0.60			
71037	1.90	13.00				7.40	1.02	7.00	1.70																	
71055	1.86	13.65		4.31	1.40	6.16	1.07	6.33	1.46	0.09			0.78		0.17			0.19		0.33	0.10	9.46				
71065	1.70	11.00				6.90	1.01	6.80	1.70																	
71066	1.60	11.00				6.70	1.02	6.40	1.80																	
71069	1.90	12.00				7.40	1.07	6.60	1.50																	
71136		14.50		8.34		7.78	1.09	6.80												0.46	0.22	8.40				
71155	1.80	12.00				6.90	0.97	6.30	1.30											0.29	0.13					
71175		16.00		11.00		9.00	1.36	8.90												0.39	0.11	10.00				
71505	1.90	13.00				7.60	1.09	6.90	1.60																	
71509		15.00				9.30	1.20																			
71525	2.10	13.00				7.10	0.98	6.60	1.50																	
71536	2.40	14.00				9.00	1.40	7.20	1.40																	
71537	2.00	13.00				7.40	0.94	6.80	1.40																	
71539	3.30	21.00				11.50	1.52	9.90	1.80																	
71546	2.30	17.05		11.20		9.05	1.39	9.20	2.10											0.40	0.15	10.20				
71548	2.60	17.00				9.40	1.43	9.80	1.00																	
71549	2.20	14.00				8.00	1.23	9.00	0.92																	
71555	2.60	16.00				10.30	1.46	9.40	1.80																	
71556	2.30	15.00				9.40	1.37	8.30	1.70																	
71557	1.80	13.00				7.20	1.10	6.80	1.70																	
71559	2.60	17.00				9.20	1.40	8.80	1.50																	
71565	2.30	15.00				8.30	1.40	8.00	1.90																	
71566	1.80	12.00				6.90	1.37	7.00	1.30											0.31	0.09					
71567	2.60	14.23		8.28		8.72	1.23	8.13	1.70													9.20				
71568	2.40	14.00				8.10	1.36	8.60	1.60																	
71569	2.50	16.53	3.70	11.30		10.05	1.41	8.80	1.72	0.08			4.80		0.25			0.27		0.36	0.13	9.10			78.00	4.90
71576	1.80	12.00				8.00	1.15	7.00	1.50																	
71577	2.60	18.50		11.40		9.67	1.41	9.37	1.70													10.40				
71578	2.50	17.00				8.50	1.30	8.90	1.60																	
71586	1.90	12.00				7.30	1.11	7.00	1.30																	
71587	1.90	12.00				6.90	1.00	6.20	1.60																	
71588	1.70	11.00				6.20	0.91	6.00	1.40																	
71595	1.80	12.00				7.50	1.11	6.50	1.50																	
71596	1.80	11.00				6.50	0.96	6.30	1.30																	
72155	2.65	18.20	4.50	10.80		10.07	1.45	8.78	1.86				0.38		0.04			0.26		0.35	0.12	8.85			49.00	3.50
74235	2.82	18.60	3.95	11.11	1.53	11.33	1.42	8.78	1.79	0.08								2.09		0.38	0.12	12.65	0.53			
74245	2.56	16.17	3.30	9.50	1.28	8.73	1.19	8.32	1.47	0.04								0.25		0.39	0.13	8.50	0.84			
74255	2.80	17.57	3.53	9.77	1.40	9.98	1.31	9.29	1.55	0.15								1.79		0.43	0.14	8.15	1.02			
74275	2.36	16.76	3.55	7.59	0.95	8.84	1.29	8.17	2.30	0.06					0.19			2.25		1.19	0.14	8.80	0.98			
75015		24.55		12.20		13.20	1.91	9.60														10.90				
75035	3.24	21.65	4.80	13.05		11.06	1.73	9.97	1.81	0.10	0.00		0.00		0.02		0.29	2.76	0.04	0.38	0.14	10.50				
75075		15.40		9.19		8.14	1.16	7.48												0.31	0.10	8.70				
75085	3.00	19.00				10.60	1.54	9.70	2.20																	
77516	1.60	10.00				6.00	0.95	6.27	1.40																	
77535	2.40	15.27		9.84		8.37	1.30	8.60	1.60													9.70				
77536	2.00	14.00				8.50	1.30	8.80	2.00																	
78505		15.00				8.90	1.20																			
78575	2.05	13.04	3.54	9.78	1.41	7.65	1.06	6.01	1.28	0.09								0.28		0.30	0.10		0.85			
78578	2.20	14.00				7.80	1.10	7.70	1.50																	
78585	1.88	12.34	2.79	7.52	1.02	7.32	0.98	6.29	1.53	0.06								0.20		0.37	0.21		0.33			
78587	1.60	10.00				6.70	1.00	6.00	1.60																	
78595		16.00				9.90	1.40																			
78597	1.90	12.33		7.94		6.92	1.02	6.40	1.50											0.38	0.11	9.90				
78598	2.89	18.49	3.42	9.84	1.35	10.01	1.46	9.15	1.72	0.09								0.31		0.32	0.11		1.11			
78599	2.50	17.40		11.20		9.80	1.53	9.85	2.10													10.40				
79155	2.13	15.40	3.90	9.76		8.66	1.35	8.42	1.60	0.07			0.09		2.90			1.03		0.35	0.11	8.50				
79515	1.70	12.00				6.70	0.96	6.20	1.40																	
79516	1.70	12.00				6.60	0.94	6.30	1.60																	

Appendix 2f: Compilation of chondrite chemical, V isotope and noble gas data

Sample details		Chemical composition				V isotope data			Neon Concentrations (in 10^{-8} cm^3 STP/g)			
Name	Class	V (ppm)	Reference	Fe (ppm)	Reference	$\delta^{51}V$ (‰)	2sd	Reference	^{20}Ne	^{21}Ne	^{22}Ne	Reference
Alfianello	L6	67	Nielsen et al., 2019	221257	Nielsen et al., 2019	-1.24	0.1	Nielsen et al., 2019	9.60	8.40	9.40	Kirsten et al., 1963
ALH83100	CM	72	Nielsen et al., 2019	216146	Nielsen et al., 2019	-1.05	0.1	Nielsen et al., 2019	12.51	0.09	1.53	Herpers et al., 1989
Borkut	L5	*95*	Nielsen et al., 2019	*225000*	Est. from L-chondrite average (20-25% Fe)	-1.12	0.1	Nielsen et al., 2019	4.40	3.94	4.45	Hintenberger et al., 1965/Schultz & Franke, 2004
EET92002	CK	91	Nielsen et al., 2019	228042	Nielsen et al., 2019	-1.32	0.15	Nielsen et al., 2019	Raw concs not reported, final age taken			Sugira & Zashu, 1995
Lance	CO	76	Nielsen et al., 2019	236606	Nielsen et al., 2019	-1.22	0.26	Nielsen et al., 2019	212.50	1.58	25.20	Alaerts et al., 1979
Mighei	CM2	*59*	Nielsen et al., 2019	*148699*	Vdovykin, 1973	-1.05	0.1	Nielsen et al., 2019	14.20	0.74	2.50	Mazor et al., 1970
NWA753	R3.9	78	Nielsen et al., 2019	242899	Nielsen et al., 2019	-1.13	0.15	Nielsen et al., 2019	4.01	4.32	4.69	Schultz et al., 2004
St. Marks	EH	51	Nielsen et al., 2019	320365	Nielsen et al., 2019	-1.05	0.1	Nielsen et al., 2019	1.34	0.27	0.41	Patzer & Schultz, 2001
Warrenton	CO	66	Nielsen et al., 2019	193920	Nielsen et al., 2019	-1.24	0.11	Nielsen et al., 2019	9.40	7.45	9.04	Mazor et al., 1970
WSG95300	H3.3	66	Nielsen et al., 2019	254226	Nielsen et al., 2019	-1.39	0.1	Nielsen et al., 2019	10.70	8.80	10.23	Wieler et al., 1999

Abrv. Ref. **Full Reference**

Alaerts et al., 1979 Alaerts L., Lewis R.S. and Anders E. (1979) Isotopic Anomalies of Noble Gases in Meteorites and their Origins-IV. C3 (Ornans) Carbonaceous Chondrites.Geochim. Cosmochim. Acta 43,1421-1432

Herpers et al., 198 Herpers U., Vogt,S., Signer P., Wieler R., Beer J., and Woelfli W. (1989) Cosmogenic Radionuclides and Noble Gases in Allan Hills C-Chondrites. IN: Workshop on Differences between Antarctic and Non-Antarctic Meteorites. Wien, 46-48

Hintenberger et al. Hintenberger H., Schultz L. and Waenke H. (1965) Unpublished Data.

Kirsten et al., 1963 Kirsten T., Krankowsky D. and Zaehringer J. (1963) Edelgas- und Kalium-Bestimmungen an einer groesseren Zahl von Steinmeteoriten. Geochim. Cosmochim. Acta 27, 13-42

Mazor et al., 1970 Mazor E., Heymann D. and Anders E. (1970) Noble Gases in Carbonaceous Chondrites. Geochim. Cosmochim. Acta 34, 781-824

Nielsen et al., (201 Nielsen, S.G., Auro, M., Righter, K., Davis, D., Prytulak, J., Wu, F., Owens, J.D. (2019) Nucleosynthetic vanadium isotope heterogeneity of the early solar system recorded in chondritic meteorites. Earth and Planetary Sciences Letters. 505. 131-140

Patzer & Schultz (2 Patzer, A., Schultz, L. (2001) Noble gases in enstatite chondrites I: Exposure ages, pairing, and weathering effects. Meteoritics & Planetary Science 36, 947-961.

Scherer et al., (199 Scherer, P., Herrmann, S., Schultz, L. (1998) Noble gases in twenty-one Saharan LL-chondrites: Exposure ages and possible pairings. Meteoritics & Planetary Science 33, 259-265.

Schultz & Franke (Schultz, L., Franke, L. (2004) Helium, neon, and argon in meteorites: A data collection. Meteoritics & Planetary Science 39, 11, 1889-1890.

Schultz et al., (200 Schultz L., Weber H.W. and Franke L. (2004) Rumuruti(R)-chondrites: Noble gases, exposure ages, pairing, and parent body history.

Sugira & Zashu (19 Sugiura, N., Zashu, S. (1995) Nitrogen isotopic composition of CK chondrites. Meteoritics 30, 430-435.

Vdov Vdovykin, G. P. (1973) The Mighei Meteorite. Space Science Reviews 14, 832-879.

Wieler et al., 1999 Wieler R., Baur H., Busemann H., Heber V.S. and Leya I. (1999) Noble Gases in Desert Meteorites: Howardites, Unequilibrated Chondrites, Regolith Breccias and an LL7. In: Workshop on Extraterrestrial Materials from Cold and Hot Deserts (L. Schultz et al. eds.), LPI Cont. 997, LPI Houston, 90-94.

Appendix 2f: Compilation of chondrite chemical, V isotope and noble gas data

Sample d	Calculations for exposure age (following Scherer et al., 1998)									
Name	$(^{20}Ne/^{22}Ne)_{meas}$	$^{21}Ne_{cosm}$	$(^{21}Ne/^{22}Ne)_{cosm}$	P_{21}	F_{21}	t_e (Myr)	[Fe]/[V]	t_e * [Fe]/[V] (Myr)	t_e * [Fe]/[V] (10^{12} Myr)	Error
Alfianello	1.02	8.40	1.10	0.35	1.00	23.73	3302.34	78374	0.0784	0.0130
ALH83100	8.18	2.88	1.11	0.26	0.79	0.34	3002.03	1029	0.0010	0.0002
Borkut	0.99	3.94	1.11	0.32	0.96	12.39	2368.42	29341	0.0293	0.0049
EET92002	Raw concs not reported, final age taken					*33.10*	2505.96	82947	0.0829	0.0137
Lance	8.43	50.39	1.11	0.32	0.96	4.94	3113.24	15370	0.0154	0.0025
Mighei	5.68	23.68	1.11	0.32	0.96	2.32	2520.33	5846	0.0058	0.0010
NWA753	0.86	4.32	1.09	0.36	0.96	12.06	3114.09	37554	0.0376	0.0062
St. Marks	3.26	8.64	1.11	0.26	0.78	1.04	6281.67	6543	0.0065	0.0011
Warrenton	1.04	7.45	1.19	0.24	0.96	31.30	2938.18	91953	0.0920	0.0152
WSG95300	1.05	8.80	1.14	0.28	0.93	31.77	3851.91	122383	0.1224	0.0202

Appendix 2g: Rare earth element data from literature and this study, with normalisation to CI chondrite

Parent	Reference Code (Appendix 2h)	LA(PPM)	CE(PPM)	PR(PPM)	ND(PPM)	SM(PPM)	EU(PPM)	GD(PPM)	TB(PPM)	DY(PPM)	HO(PPM)	ER(PPM)	TM(PPM)	YB(PPM)	LU(PPM)
10017	41	22.1	62		56	15	1.9		4.7					15.8	2.4
10017	41	23.8	62		54	19	2.1		5			11.5	2	16.4	2.7
10017	68	26.60	77.30		59.50	20.90	2.14	27.40		31.70		20.00		19.20	2.66
10017	74	25.70	79.10			20.00	2.27		3.88	27.20	6.40			18.70	2.70
10017	79	25.8	76.8	11.7	58.2	20.3	2.17	26.5	4.96	32	7.02	19.5		17.5	2.53
10017	94	23.3	69.7		50.8	18.1	2.1		4.8	26.9				15.3	2.12
10017	131					25.00	2.10		4.00					19.00	5.00
10017	154	23.20	81.84	11.16	61.62	21.20	2.03	27.74	4.80	29.81	6.31	17.74	2.39	17.33	2.12
10017	181		75.50		66.10	23.40	2.26	28.40		32.80		19.10		18.10	2.63
10017	223				63.9	21.9									
10017	257	25.00	84.00	12.90	74.00	22.00	2.60	30.00	5.50	36.00	8.30	21.00	3.00	19.00	2.60
10017	257	28.00				27.00	2.90							23.00	3.00
10017	262	21.00	64.00	7.30	58.00	18.90	1.89	19.00	4.60	19.00	3.80	13.00		15.60	2.12
10017,400	*THIS STUDY*	**25.7**	**73.1**	**11.1**	**55.4**	**20.1**	**2.2**	**25.8**	**4.7**	**31.8**	**6.7**	**20.0**	**2.8**	**17.1**	**2.4**
10017,405	*THIS STUDY*	**25.7**	**74.1**	**10.9**	**55.0**	**19.2**	**2.1**	**26.0**	**4.8**	**31.6**	**6.8**	**19.7**	**2.8**	**17.1**	**2.4**
10020	41	7.20	25.00		23.00	8.50	1.50		2.30				1.60	8.20	1.30
10020	68	8.11	25.80		23.90	9.47	1.60	12.80		15.80		10.00		9.87	1.43
10020	79	7.63	24.1	4.14	22.8	9	1.55	12.4	2.36	15.4	3.37	9.48		8.65	1.3
10020	80	8.40	25.60		31.00	9.94	1.75	16.00	2.59	17.80		9.00		9.80	1.41
10020	94	7.20	23.90		21.80	8.50	1.49		2.40	14.30				7.90	1.17
10020	102	6.60	24.90			9.50	1.40		2.60	17.30				6.50	1.45
10020	143	11.00	34.00	8.70	40.00	14.00	1.60	17.00	3.50	30.00	7.00	19.00	1.20	15.00	1.50
10020	187	7.90	27.00			9.60	1.58		2.50					8.80	1.36
10020	223				23.60	9.16									
10020	243													2.50	
10020	250	7.70	47.00			6.40	1.50			18.00				6.60	0.81
10020	*THIS STUDY*	**8.8**	**26.8**	**4.4**	**24.5**	**9.3**	**1.8**	**14.3**	**2.6**	**17.9**	**3.7**	**11.4**	**1.6**	**10.0**	**1.5**
10044	12														2.62
10044	61													16.00	
10044	74	11.20	42.00			16.30	2.64		3.89	24.50	5.60			14.60	1.91
10044	94	11.90	43.10		40.30	17.60	2.71		4.50	28.10				14.40	2.01
10044	102	10.50	37.60			11.40	3.00		3.90	27.60				10.40	2.11
10044	154	11.74	42.06	7.75	43.07	17.10	2.76	24.61	4.23	27.73	5.64	16.04	2.20	14.44	1.90
10044	181		76.60		66.10	23.40	2.21	28.60		33.60		19.30		16.60	
10044	187	9.90	38.00			16.30	2.28		3.40					13.00	1.86
10044	223				77.70	30.70									
10044	250	14.00	86.00			15.00	3.00			36.00				9.50	1.30
10044	257	8.70				17.70	2.00							16.00	2.10
10044	257	10.00				19.70	3.40							16.00	2.20
10044	262	12.00	44.00		50.00	17.90	2.69	24.00	4.50					15.00	1.96
10044	*THIS STUDY*	**11.1**	**38.7**	**6.7**	**39.2**	**16.4**	**2.4**	**24.0**	**4.3**	**29.0**	**6.1**	**18.5**	**2.6**	**16.3**	**2.3**
12018	21	29.00	26.00	4.00	12.00	3.00	1.20	4.00	1.40	11.00		4.60		8.00	0.60
12018	25		12.00			3.90	0.76		0.76	5.60				3.50	0.61
12018	25	5.80	18.00			3.90	0.76		0.74	5.30	1.33	3.20		3.70	0.56
12018	25	5.68	21.00	1.75	14.70	3.80	0.84	4.70	1.00	5.80	1.11	4.20		3.45	0.40
12018	33	3.00	6.00												
12018	39													5.40	
12018	73	5.30	14.00		14.00	3.89	0.80		1.13					3.50	0.60
12018	124	5.68				3.80								3.45	3.40
12018	205		15.90		11.80	3.91	0.83	5.55		6.54		3.80		3.42	0.52
12018	*THIS STUDY*	**5.6**	**14.6**	**2.2**	**10.9**	**3.8**	**0.9**	**5.2**	**0.9**	**6.4**	**1.3**	**3.8**	**0.6**	**3.0**	**0.5**
12054	154	7.13	19.65	3.30	16.71	6.11	1.37	8.65	1.54	10.25	2.12	6.15	0.87	5.54	0.73
12054	157	6.30	18.70		16.00	5.50	1.40		1.48	9.40				4.90	0.75
12054	189		18.80			6.00	1.27		1.85					5.80	0.78
12054,146	*THIS STUDY*	**6.4**	**19.2**	**3.0**	**16.0**	**5.9**	**1.4**	**8.5**	**1.5**	**10.4**	**2.1**	**6.2**	**0.9**	**5.5**	**0.8**
12054,150	*THIS STUDY*	**6.7**	**19.4**	**3.1**	**15.9**	**5.8**	**1.5**	**8.6**	**1.6**	**10.8**	**2.2**	**6.4**	**0.9**	**5.6**	**0.8**
12063	21	25.00	28.00	8.00	54.00	9.00	3.00	9.00	5.00	16.00		19.70		16.00	2.70
12063	25	6.88	19.00	3.10		6.60	1.62	11.00	2.65	10.30	2.46	7.35		5.71	0.84
12063	56						1.31								
12063	81	6.24	17.80		16.00	6.48	4.36	9.40	1.66	11.30	2.00	5.30		5.40	0.79
12063	102	5.50	45.00			3.90	1.20		1.64	14.50				5.30	1.00
12063	124	6.88				6.60								5.71	6.30
12063	154	6.13	17.64	2.98	15.06	5.84	1.29	8.15	1.45	9.88	2.03	5.96	0.86	5.41	0.71
12063	157	7.10	19.20		16.50	5.10	1.17		1.50		1.30		1.10	5.50	0.70
12063	171				16.79	6.25									
12063	171	6.30	18.60		16.50	6.14	1.41	8.55		10.60		6.21		5.38	0.77
12063	240	9.80	30.00	4.20	20.00	7.60	1.60	12.00	2.20	12.00		9.00		6.80	
12063	255	6.00	17.50	2.90	17.10	6.05	1.30	8.20	1.50	8.90		6.00		5.50	0.70
12063	280													5.70	
12063	*THIS STUDY*	**5.9**	**17.8**	**2.9**	**15.1**	**5.8**	**1.4**	**8.4**	**1.5**	**10.3**	**2.1**	**6.4**	**0.9**	**5.6**	**0.8**
14053	41	1.50	32.00		27.00		1.20		1.50				0.52	5.50	1.20
14053	41	12.80	33.00		24.00	6.40	1.10		1.40				0.56	5.70	0.92
14053	52	16.00	53.00				1.30		1.10						0.90
14053	79	14.6	38.3	5.43	24.4	7.47	1.31	9.06	1.71	10.9	2.41	6.92		6.47	0.959
14053	84	12.80	36.40		22.00	6.50	1.23	8.50	1.62	11.10	2.10			6.10	0.89
14053	86	13.00	34.50		21.90	6.56	1.21	8.59		10.50		6.51		6.00	
14053	92	17.00					1.40		1.20						0.90
14053	92	14.00					1.30		0.90						0.90
14053	92	17.00					1.20		1.30						1.00
14053	154	12.41	36.51	4.63	22.54	6.60	1.06	8.33	1.52	9.36	2.05	5.96	0.82	6.19	0.80
14053	156	14.10	37.20	5.25	23.60	7.32	1.20	8.35	1.48	9.86	2.24	6.36	0.92	6.21	0.95
14053	245	10.00												10.00	
14053	*THIS STUDY*	**13.1**	**35.3**	**4.9**	**20.7**	**6.3**	**1.3**	**8.0**	**1.6**	**10.4**	**2.2**	**6.7**	**1.0**	**6.5**	**0.9**
15016	29													4.20	
15016	38													4.20	
15016	79	4.77	13.2	2.01	9.79	3.27	0.796	4.17	0.75	4.6	0.964	2.56		2.13	0.309
15016	83	5.77	15.60		11.40	4.05	0.97	5.40	0.90	5.74	1.10	3.10		2.62	0.32
15016	106	5.50				3.60	0.80		0.59					2.20	0.35
15016	145	5.20													
15016	146	5.20													
15016	154	5.87	14.88	2.24	10.50	3.42	0.87	4.53	0.80	5.10	1.00	2.77	0.38	2.38	0.31
15016	200	5.22	15.20		8.00	3.67	0.82		0.82					2.18	0.31
15016	220				9.09	3.03									
15016	238	5.30	14.40	2.00	9.60	3.42	0.87	4.50	0.73	4.55	1.10	2.86	0.40	2.42	0.38
15016	*THIS STUDY*	**5.0**	**13.8**	**2.0**	**9.8**	**3.1**	**0.9**	**4.3**	**0.7**	**5.0**	**1.0**	**2.8**	**0.4**	**2.2**	**0.3**
15535	82	3.49	9.70		6.70	2.60	0.69	3.60	0.59	4.07	0.73			1.69	0.24
15535	83	3.49	9.70		6.70	2.60	0.69	3.60	0.59	4.07	0.73			1.69	0.24
15535	154	5.20	13.20	2.08	9.21	3.06	0.81	4.18	0.72	4.61	0.90	2.47	0.32	2.11	0.28

CI-normalised

Anders & Grevesse 89:	0.2347	0.6032	0.0891	0.4524	0.1471	0.056	0.1966	0.0363	0.2427	0.0556	0.1589	0.0242	0.1625	0.0243
Chondrite Normalised:	LA(PPM)	CE(PPM)	PR(PPM)	ND(PPM)	SM(PPM)	EU(PPM)	GD(PPM)	TB(PPM)	DY(PPM)	HO(PPM)	ER(PPM)	TM(PPM)	YB(PPM)	LU(PPM)
	94.2	102.8		123.8	102.0	33.9		129.5					97.2	98.8
	101.4	102.8		119.4	129.2	37.5		137.7			72.4	82.6	100.9	111.1
	113.3	128.1		131.5	142.1	38.2	139.4		130.6		125.9		118.2	109.5
	109.5	131.1			136.0	40.5		106.9	112.1	115.1			115.1	111.1
	109.9	127.3	131.3	128.6	138.0	38.8	134.8	136.6	131.9	126.3	122.7		107.7	104.1
	99.3	115.6		112.3	123.0	37.5		132.2	110.8				94.2	87.2
					170.0	37.5		110.2					116.9	205.8
	98.9	135.7	125.3	136.2	144.1	36.3	141.1	132.3	122.8	113.4	111.7	98.9	106.6	87.3
		125.2		146.1	159.1	40.4	144.5		135.1		120.2		111.4	108.2
				141.2	148.9									
	106.5	139.3	144.8	163.6	149.6	46.4	152.6	151.5	148.3	149.3	132.2	124.0	116.9	107.0
	119.3				183.5	51.8							141.5	123.5
	89.5	106.1	81.9	128.2	128.5	33.8	96.6	126.7	78.3	68.3	81.8		96.0	87.2
109.5	**121.3**	**125.0**	**122.4**	**136.4**	**39.1**	**131.5**	**130.5**	**131.2**	**120.2**	**125.8**	**114.2**	**104.9**	**99.3**
109.5	**122.9**	**122.9**	**121.7**	**130.7**	**38.3**	**132.4**	**131.7**	**130.1**	**122.8**	**123.8**	**115.8**	**105.0**	**99.9**
30.7	41.4		50.8	57.8	26.8		63.4				66.1	50.5	53.5
34.6	42.8		52.8	64.4	28.6	65.1		65.1		62.9		60.7	58.8
32.5	40.0	46.5	50.4	61.2	27.7	63.1	65.0	63.5	60.6	59.7		53.2	53.5
35.8	42.4		68.5	67.6	31.3	81.4	71.3	73.3		56.6		60.3	58.0
30.7	39.6		48.2	57.8	26.6		66.1	58.9				48.6	48.1
28.1	41.3			64.6	25.0		71.6	71.3				40.0	59.7
46.9	56.4	97.6	88.4	95.2	28.6	86.5	96.4	123.6	125.9	119.6	49.6	92.3	61.7
33.7	44.8			65.3	28.2		68.9					54.2	56.0
			52.2	62.3									
												15.4	
32.8	77.9			43.5	26.8			74.2				40.6	33.3
37.5	**44.5**	**49.9**	**54.2**	**63.4**	**32.6**	**72.8**	**72.5**	**73.9**	**66.2**	**71.5**	**65.9**	**61.4**	**60.6**
													107.7
												98.5	
47.7	69.6			110.8	47.1		107.2	100.9	100.7			89.8	78.6
50.7	71.5		89.1	119.6	48.4		124.0	115.8				88.6	82.7
44.7	62.3			77.5	53.6		107.4	113.7				64.0	86.8
50.0	69.7	87.0	95.2	116.2	49.3	125.2	116.6	114.3	101.5	100.9	90.9	88.9	78.3
	127.0		146.1	159.1	39.5	145.5		138.4		121.5		102.2	
42.2	63.0			110.8	40.7		93.7					80.0	76.5
			171.8	208.7									
59.7	142.6			102.0	53.6			148.3				58.5	53.5
37.1				120.3	35.7							98.5	86.4
42.6				133.9	60.7							98.5	90.5
51.1	72.9		110.5	121.7	48.0	122.1	124.0					92.3	80.7
47.1	**64.2**	**75.4**	**86.7**	**111.7**	**42.9**	**121.9**	**119.0**	**119.4**	**109.9**	**116.6**	**107.2**	**100.1**	**95.1**
123.6	43.1	44.9	26.5	20.4	21.4	20.3	38.6	45.3		28.9		49.2	24.7
	19.9			26.5	13.6		20.9	23.1				21.5	25.1
24.7	29.8			26.5	13.6		20.4	21.8	23.9	20.1		22.8	23.0
24.2	34.8	19.6	32.5	25.8	15.0	23.9	27.5	23.9	20.0	26.4		21.2	16.5
12.8	9.9												
												33.2	
22.6	23.2		30.9	26.4	14.2		31.1					21.5	24.8
24.2				25.8								21.2	139.9
	26.4		26.1	26.6	14.9	28.2		26.9		23.9		21.0	21.4
23.7	**24.2**	**24.4**	**24.0**	**25.7**	**15.8**	**26.6**	**25.9**	**26.3**	**22.6**	**24.0**	**23.7**	**18.7**	**19.1**
30.4	32.6	37.1	36.9	41.5	24.5	44.0	42.4	42.2	38.1	38.7	35.9	34.1	30.1
26.8	31.0		35.4	37.4	25.0		40.8	38.7				30.2	30.9
	31.2			40.8	22.7		51.0					35.7	32.1
27.3	**31.8**	**33.9**	**35.4**	**40.3**	**25.8**	**43.5**	**42.0**	**42.8**	**37.9**	**38.8**	**36.5**	**34.0**	**31.6**
28.6	**32.2**	**35.2**	**35.1**	**39.1**	**27.3**	**43.7**	**43.0**	**44.5**	**38.8**	**40.3**	**38.4**	**34.4**	**32.8**
106.5	46.4	89.8	119.4	61.2	53.6	45.8	137.7	65.9		124.0		98.5	111.1
29.3	31.5	34.8		44.9	28.9	56.0	73.0	42.4	44.2	46.3		35.1	34.6
					23.4								
26.6	29.5		35.4	44.1	77.9	47.8	45.7	46.6	36.0	33.4		33.2	32.5
23.4	74.6			26.5	21.4		45.2	59.7				32.6	41.2
29.3				44.9								35.1	259.3
26.1	29.2	33.4	33.3	39.7	23.0	41.4	40.0	40.7	36.5	37.5	35.4	33.3	29.2
30.3	31.8		36.5	34.7	20.9		41.3		23.4		45.5	33.8	28.8
			37.1	42.5									
26.8	30.8		36.5	41.7	25.2	43.5		43.7		39.1		33.1	31.8
41.8	49.7	47.1	44.2	51.7	28.6	61.0	60.6	49.4		56.6		41.8	
25.6	29.0	32.5	37.8	41.1	23.2	41.7	41.3	36.7		37.8		33.8	28.8
												35.1	
25.0	**29.6**	**32.4**	**33.3**	**39.6**	**25.4**	**42.8**	**42.6**	**42.3**	**37.6**	**40.4**	**36.9**	**34.4**	**31.3**
6.4	53.1		59.7		21.4		41.3				21.5	33.8	49.4
54.5	54.7		53.1	43.5	19.6		38.6				23.1	35.1	37.9
68.2	87.9				23.2		30.3						37.0
62.2	63.5	60.9	53.9	50.8	23.4	46.1	47.1	44.9	43.3	43.5		39.8	39.5
54.5	60.3		48.6	44.2	22.0	43.2	44.6	45.7	37.8			37.5	36.6
55.4	57.2		48.4	44.6	21.6	43.7		43.3		41.0		36.9	
72.4					25.0		33.1						37.0
59.7					23.2		24.8						37.0
72.4					21.4		35.8						41.2
52.9	60.5	52.0	49.8	44.9	19.0	42.4	41.8	38.6	36.8	37.5	34.0	38.1	32.8
60.1	61.7	58.9	52.2	49.8	21.4	42.5	40.8	40.6	40.3	40.0	38.0	38.2	39.1
42.6												61.5	
55.9	**58.4**	**55.4**	**45.8**	**42.7**	**23.8**	**40.9**	**43.4**	**42.8**	**38.8**	**41.9**	**41.1**	**39.9**	**35.5**
												25.8	
												25.8	
20.3	21.9	22.6	21.6	22.2	14.2	21.2	20.7	19.0	17.3	16.1		13.1	12.7
24.6	25.9		25.2	27.5	17.3	27.5	24.8	23.7	19.8	19.5		16.1	13.2
23.4				24.5	14.3		16.3					13.5	14.4
22.2													
22.2													
25.0	24.7	25.1	23.2	23.3	15.6	23.0	21.9	21.0	18.0	17.4	15.5	14.7	12.6
22.2	25.2		17.7	24.9	14.6		22.6					13.4	12.8
			20.1	20.6									
22.6	23.9	22.4	21.2	23.2	15.5	22.9	20.1	18.7	19.8	18.0	16.5	14.9	15.6
21.2	**22.8**	**22.3**	**21.7**	**21.4**	**15.2**	**21.9**	**20.4**	**20.6**	**17.2**	**17.5**	**15.0**	**13.6**	**12.5**
14.9	16.1		14.8	17.7	12.3	18.3	16.3	16.8	13.1			10.4	9.7
14.9	16.1		14.8	17.7	12.3	18.3	16.3	16.8	13.1			10.4	9.7
22.1	21.9	23.4	20.3	20.8	14.5	21.2	19.9	19.0	16.1	15.5	13.3	13.0	11.6

Appendix 2g: Rare earth element data from literature and this study, with normalisation to CI chondrite

Parent	Reference Code (Appendix 2h)	LA(PPM)	CE(PPM)	PR(PPM)	ND(PPM)	SM(PPM)	EU(PPM)	GD(PPM)	TB(PPM)	DY(PPM)	HO(PPM)	ER(PPM)	TM(PPM)	YB(PPM)	LU(PPM)
15535	200	4.33	12.70		12.00	3.11	0.81		0.68					1.99	0.27
15535	*THIS STUDY*	**4.8**	**13.1**	**2.0**	**10.3**	**3.0**	**0.9**	**4.2**	**0.7**	**4.9**	**0.9**	**2.7**	**0.4**	**2.2**	**0.3**
15556	26	4.80	18.00			4.00	1.00		0.77	4.40	0.91	3.30		1.59	0.39
15556	145	5.50													
15556	146	5.50													
15556	154	5.79	15.39	2.33	10.66	3.60	0.92	4.81	0.85	5.44	1.09	2.98	0.39	2.51	0.31
15556	154	5.46	15.44	2.35	11.12	3.73	0.95	4.92	0.82	5.34	1.04	2.83	0.39	2.39	0.33
15556	200	5.20	15.80		13.00	3.65	0.96		0.87					2.27	0.31
15556	200	5.32	14.30		12.00	3.85	0.95		0.83					2.34	0.33
15556	220				9.77	3.31									
15556	228	7.00	20.00												
15556	228	3.70	16.00	2.60	10.80	3.95	1.10	4.50	0.85	5.30	1.30	2.85	0.48	2.50	0.33
15556	*THIS STUDY*	**5.4**	**15.0**	**2.3**	**10.7**	**3.8**	**1.1**	**5.0**	**0.8**	**5.4**	**1.0**	**3.1**	**0.4**	**2.3**	**0.4**
70255	190	7.05	24.70		27.30	11.40	2.23	17.60		20.20		12.10		11.80	1.48
70255	265	6.40				10.00	2.20			18.00				10.00	1.40
70255	*THIS STUDY*	**6.1**	**20.6**	**3.7**	**23.3**	**9.7**	**2.2**	**14.3**	**2.7**	**18.5**	**3.8**	**11.2**	**1.6**	**10.0**	**1.4**
71135	212	5.43	17.80		18.60	7.55	1.56	12.00		13.30		7.95		7.28	
71135	*THIS STUDY*	**5.6**	**18.1**	**3.2**	**18.1**	**7.5**	**1.6**	**10.7**	**2.0**	**13.4**	**2.8**	**8.2**	**1.2**	**7.2**	**1.1**
74275	27	5.98	16.50			9.70	1.93		2.05	17.90				7.50	1.34
74275	41	5.90	21.00		31.00		1.70		2.70			1.02	0.70	8.90	1.40
74275	41	5.50	18.00		39.00	8.50	1.60		2.00				0.75	7.60	1.20
74275	79	6.1	21.3	3.97	22.9	9.59	1.78	13.1	2.52	16.2	3.5	9.67		8.6	1.27
74275	154	5.78	22.76	4.32	24.27	10.08	1.81	14.50	2.57	17.04	3.49	10.27	1.39	9.17	1.20
74275	174				22.50	9.27									
74275	190	6.33	21.40		22.80	9.19	1.80	14.80		16.30		9.66		8.70	
74275	195													11.00	
74275	237	6.80													
74275	260	6.70	22.10	4.20		9.73	1.91	14.20	2.50	15.80	3.60	9.40		9.02	1.30
74275	*THIS STUDY*	**5.9**	**20.1**	**3.7**	**21.3**	**8.9**	**1.7**	**12.9**	**2.3**	**15.4**	**3.3**	**9.5**	**1.3**	**8.2**	**1.2**
75035	27	7.60	20.40			2.90	2.25		2.81	22.90				10.70	1.82
75035	107	7.30	27.00		30.00	1.80	2.20		3.10	20.00				10.00	1.50
75035	183		23.60		27.30	11.20	2.52	17.10		19.70		11.10		11.40	1.70
75035	195													10.00	
75035	259	9.07	35.00	6.50	36.50	13.60	2.60	19.80	3.80	24.00	4.80	15.00		13.20	1.88
75035	*THIS STUDY*	**6.9**	**24.2**	**4.4**	**25.6**	**10.9**	**2.2**	**15.8**	**3.0**	**20.5**	**4.3**	**12.7**	**1.8**	**11.3**	**1.6**

References
See 2g

CI-normalised

Anders & Grevesse 89:	0.2347	0.6032	0.0891	0.4524	0.1471	0.056	0.1966	0.0363	0.2427	0.0556	0.1589	0.0242	0.1625	0.0243
Chondrite Normalised:	**LA(PPM)**	**CE(PPM)**	**PR(PPM)**	**ND(PPM)**	**SM(PPM)**	**EU(PPM)**	**GD(PPM)**	**TB(PPM)**	**DY(PPM)**	**HO(PPM)**	**ER(PPM)**	**TM(PPM)**	**YB(PPM)**	**LU(PPM)**
	18.4	21.1		26.5	21.1	14.5		18.7					12.2	11.1
	20.3	**21.8**	**22.1**	**22.7**	**20.1**	**15.3**	**21.3**	**20.0**	**20.3**	**16.6**	**16.8**	**16.4**	**13.5**	**11.3**
	20.5	29.8			27.2	17.9		21.2	18.1	16.4	20.8		9.8	16.0
	23.4													
	23.4													
	24.7	25.5	26.1	23.6	24.5	16.5	24.5	23.5	22.4	19.6	18.7	16.3	15.5	12.8
	23.2	25.6	26.3	24.6	25.3	16.9	25.0	22.7	22.0	18.7	17.8	16.0	14.7	13.4
	22.2	26.2		28.7	24.8	17.1		24.0					14.0	12.8
	22.7	23.7		26.5	26.2	17.0		22.9					14.4	13.6
				21.6	22.5									
	29.8	33.2												
	15.8	26.5	29.2	23.9	26.9	19.6	22.9	23.4	21.8	23.4	17.9	19.8	15.4	13.6
	23.1	**24.8**	**25.5**	**23.7**	**26.1**	**19.0**	**25.3**	**23.0**	**22.4**	**18.7**	**19.8**	**17.1**	**14.3**	**14.6**
	30.0	40.9		60.3	77.5	39.8	89.5		83.2		76.1		72.6	60.9
	27.3				68.0	39.3			74.2				61.5	57.6
	25.8	**34.1**	**41.4**	**51.4**	**65.8**	**39.4**	**72.7**	**73.3**	**76.1**	**68.4**	**70.6**	**64.9**	**61.6**	**59.5**
	23.1	29.5		41.1	51.3	27.9	61.0		54.8		50.0		44.8	
	23.7	**30.0**	**36.4**	**40.0**	**50.9**	**28.4**	**54.7**	**56.3**	**55.3**	**51.0**	**51.6**	**49.2**	**44.3**	**43.6**
	25.5	27.4			65.9	34.5		56.5	73.8				46.2	55.1
	25.1	34.8		68.5		30.4		74.4			6.4	28.9	54.8	57.6
	23.4	29.8		86.2	57.8	28.6		55.1				31.0	46.8	49.4
	26.0	35.3	44.6	50.6	65.2	31.8	66.6	69.4	66.7	62.9	60.9		52.9	52.3
	24.6	37.7	48.5	53.7	68.6	32.4	73.7	70.8	70.2	62.8	64.6	57.5	56.5	49.4
				49.7	63.0									
	27.0	35.5		50.4	62.5	32.1	75.3		67.2		60.8		53.5	
													67.7	
	29.0													
	28.5	36.6	47.1		66.1	34.1	72.2	68.9	65.1	64.7	59.2		55.5	53.5
	25.0	**33.2**	**41.8**	**47.2**	**60.3**	**31.0**	**65.5**	**63.3**	**63.6**	**59.1**	**60.0**	**53.6**	**50.5**	**48.7**
	32.4	33.8			19.7	40.2		77.4	94.4				65.8	74.9
	31.1	44.8		66.3	12.2	39.3		85.4	82.4				61.5	61.7
		39.1		60.3	76.1	45.0	87.0		81.2		69.9		70.2	70.0
													61.5	
	38.6	58.0	73.0	80.7	92.5	46.4	100.7	104.7	98.9	86.3	94.4		81.2	77.4
	29.4	**40.1**	**49.3**	**56.6**	**73.8**	**39.0**	**80.2**	**83.3**	**84.6**	**76.6**	**80.0**	**74.7**	**69.7**	**66.2**

Appendix 2h: Supplementary References for Published Data

Code	Extended Reference
1	Agrell S.O., Scoon J.H., Muir I.D., Long J.V.P., McConnell J.D.C., and Peckett A. (1970) Observations on the chemistry, mineralogy and ptrology of some Apollo 11 lunar samples. Proc. Apollo 11 Lunar Sci. Conf., 93-128.
2	Anders E., Ganapathy R., Keays R.R., Laul J.C., and Morgan J.W. (1971) Volatile and siderophile elements in lunar rocks: Comparsion with terrestrial and meteoritic basalts. Proc. Lunar Sci. Conf. 2nd, 1021-1036.
3	Annell C.S. and Helz A.W. (1970) Emission spectrographic determination of trace elements in lunar samples from Apollo 11. Proc. Apollo 11 Lunar Sci. Conf., 991-994
4	Arai T. and Warren P.H. (1997) "large" (1.7g) compositionally pristine diabase 14434: A lithology transitional between magnesium-gabbronorite and high-aluminum mare basalt. Meteor. Planet. Sci. 32, A7-A8.
5	Badaecker P.A., Chou C.-L., and Wasson J.T. (1972) The extralunar component in lunar soils and breccias. Proc. Lunar Sci. Conf. 3rd, 1343-1359.
6	Badaecker P.A., Chou C.-L., Grudewicz E.B., and Wasson J.T. (1973) Volatile and siderophilic trace elements I Apollo 15 samples: Geochemical implcations and characterization of the long-lived and short-lived extralunar materials. Proc. Lunar Sci. Conf. 4th, 1177-1195
7	Badaecker P.A., Chou C.-L., Sundberg L.L., and Wasson J.T. (1974) Volatile and siderophile trace elements in the soils and rocks of Taurus-Littrow. Proc. Lunar Sci. Conf. 5th, 1625-1643.
8	Baedecker P.A., Schaudy R., Elzie J.L., Kimberlin J., and Wasson J.T. (1971) Trace element studies of rocks and soils from Oceanus Procellarum and Mare Tranquilitatis. Proc. Lunar Sci. Conf. 2nd, 1037-1061.
9	Bailey J.C., Champness P.E., Dunham A.C., Esson J., Fyfe W.S., MacKenzie W.S., Stumpfl E.F., and Zussman J. (1970) Mineralogy and petrology of Apollo 11 lunar samples. Proc. Apollo 11 Lunar Sci. Conf., 169-194.
10	Baldridge W.S., Beaty D.W., Hill S.M.R., and Albee A.L. (1979) The petrology of the Apollo 12 pigeonite basalt suite. Proc. Lunar Planet. Sci. Conf. 10th, 141-179.
11	Basu A. and Bower J.F. (1976) Petrography of KREEP basalt fragments from Apollo 15 soils. Proc. Lunar Sci. Conf. 7th, 659-678.
12	Beard B.L., Taylor L.A., Scherer E.E., Johnson C.M., and Snyder G.A. (1998) The source region and melting mineralogy of high-titanium and low-titanium lunar basalts deduced from Lu-Hf isotope data.Geochim. Cosmochim. Acta 62, 525-544.
13	Beaty D.W. and Albee A.L. (1978) Comparative petrology and possible genetic relations among the Apollo 11 basalts. Proc. Lunar Planet. Sci. Conf. 9th, 359-463.
14	Beaty D.W., Hill S.M.R., Albee A.L., and Baldridge W.S. (1979) Apollo 12 feldspathic basalts 12031, 12038, and 12072: Petrology, comparison and interpretations. Proc. Lunar Sci. Conf. 10th, 115-139.
15	Beaty D.W., Hill S.M.R., Albee A.L., Ma M.-S., and Schmitt R.A. (1979) The petrology and chemistry of basaltic fragments from the Apollo 11 soil, part 1. Proc. Lunar Sci. Conf. 10th, 41-75.
16	Becker R.H. and Clayton R.N. (1975) Nitrogen abundances and isotopic composition in lunar samples. Proc. Lunar Sci. Conf. 6th, 2131-2149.
17	Becker R.H., Clayton R.N., and Mayeda T.K. (1976) Characterization of lunar nitrogen abundances. Proc. Lunar Sci. Conf. 7th, 441-458.
18	Blanchard D.P. and Budahn J.R. (1979) Remnants from the ancient lunar crust: Clasts from consortium breccia 73255. Proc. Lunar Planet. Sci. Conf. 10th, 803-816.
19	Blanchard D.P., Haskin L.A., Jacobs J.W., Brannon J.C., and Korotev R.L. (1975) Major and trace element chemistry of Boulder 1 at Station 2, Apollo 17. The Moon 14, 359-371.
20	Bottino M.L., Fullagar P.D., Schnetzler C.C., and Phillpotts J.A. (1971) Sr isotopic measurements in Apollo 12 samples. Proc. Lunar Sci. Conf. 2nd, 1487-1491.
21	Bouchet M., Kaplan G., Voudon A., and Bertoletti M.-J. (1971) Spark source spectrometric analysis of major and minor elements in six lunar samples. Proc. Lunar Sci. Conf. 2nd, 1247-1252.
22	Boynton W.V., Baedecker P.A., Chou C.-L., Robinson K.L., and Wasson J.T. (1975) Mixing and transport of lunar surface materials: Evidence obtained by the determination of lithophile, siderophile, and volatile elements. Proc. Lunar Sci. Conf. 6th, 2241-2259.
23	Brown G.M., Emeleus C.H., Holland J.G., and Phillips R. (1970) Mineralogical, chemical, and etrological features of Apollo 11 rocks and their relationship to igneous processes. Proc. Apollo 11 Lunar Sci. Conf., 195-219.
24	Brown G.M., Emeleus C.H., Holland J.G., Peckett A., and Phillips R. (1971) Picrite basalts, ferrobasalts, feldspathic norites, and rhyolites in a strongly fractionated lunar crust. Proc. Lunar Planet. Sci. Conf. 2nd, 583-600.
25	Brunfelt A.O., Heier K.S., and Steiennes E. (1971) Determination of 40 elements in Apollo 12 materials be neutron activation analysis. Proc. Lunar Sci. Conf. 2nd, 1281-1290.
26	Brunfelt A.O., Heier K.S., Nilssen B., Steiennes E., and Sundvoll B. (1972) Elemental composition of Apollo 15 samples. In The Apollo 15 Lunar Samples (Chamberlain J.W. and Watkins C., eds.), 195-197. The Lunar Science Institute, Houston, TX.
27	Brunfelt A.O., Heier K.S., Nilssen B., Steiennes E., and Sundvoll B. (1974) Elemental composition of Apollo 17 fines and rocks. Proc. Lunar Sci. Conf. 5th, 981-990.
28	Chappell B.W. and Green D.H. (1973) Chemical compositions and petrogenetic relationships in Apollo 15 mare basalts. Earth Planet. Sci. Lett., 18, 237-246.
29	Christian R.P., Annell C.S., Carron M.K., Cuttitta F., Dwornik E.J., Ligon D.T., Jr., and Rose H.J., Jr. (1972) Chemical composition of some Apollo 15 igneous rocks. In The Apollo 15 Lunar Samples (Chamberlain J.W. and Watkins C., eds.), 1206-209. The Lunar Science Institute, Houston, TX.
30	Church S.E., Bansal B.M., and Wiesmann H. (1972) The distribution of K, Ti, Zr, U, and Hf in Apollo 14 and 15 materials. In The Apollo 15 Lunar Samples (Chamberlain J.W. and Watkins C., eds.), 210-213. The Lunar Science Institute, Houston, TX.
31	Chyi L.L. and Ehmann W.D. (1973) Zirconium and hafnium abundances in some lunar materials and implications of their ratios. Proc. Lunar Sci. Conf. 4th, 1219-1226.
32	Cliff R.A., Lee-Hu C., and Wetherill G.W. (1971) Rb_Sr and U, Th-Pb measurements on Apollo 12 material. Proc. Lunar Sci. Conf. 2nd, 1493-1502.
33	Compston W., Berry H., Vernon M.J., Chappell B.W., and Kaye M.J. (1971) Rubidium-strontium chronology and chemistry of lunar material from the Ocean of Storms. Proc. Lunar Sci. Conf. 2nd, 1471-1485.
34	Compston W., Chappell B.W., Arriens P.A., and Vernon M.J. (1970) The chemistry and age of Apollo 11 lunar material. Proc. Apollo 11 Lunar Sci. Conf., 1007-1027.
35	Compston W., de Laeter J.R., and Vernon M.J. (1972) Strontium isotope geochemistry of Apollo 15 basalts. In The Apollo 15 Lunar Samples (Chamberlain J.W. and Watkins C., eds.), 347-351. The Lunar Science Institute, Houston, TX.
36	Compston W., Foster J.J., and Gray C.M. (1975) Rb-Sr ages of clasts from within Boulder 1, Station 2, Apollo 17. The Moon 14, 445-462.
37	Compston W., Vernon M.J., Berry H., Rudowski R., Gray C.M., and Ware N. (1972) Age and petrogenesis of Apollo 14 basalts. Lunar Planet. Sci. III, 151-153.
38	Cuttita R., Rose H.J., Annell C.S., Carron M.K., Christian R.P., Ligon D.T., Dwornik E.J., Wright T.L., and Greenland L.P. (1973) Chemistry of twenty-one igneous rocks and soils returned by the Apollo 15 mission. Proc. Lunar Sci. Conf. 3rd, 1081-1096.
39	Cuttitta F., Rose H.J.Jr., Annell C.S., Carron M.K., Christian R.P., Dwornik E.J., Greenland L.P., Helz A.P., and Ligon D.T. Jr. (1971) Elemental composition of some Apollo 12 lunar rocks and soils. Proc. Lunar Sci. Conf. 2nd, 1217-1229.
40	Dasch E.J., Shih C.-Y., Bansal B.M., Wiesmann H., and Nyquist L.E. (1987) Isotopic analysis of basaltic fragments from lunar breccia 14321: Chronology and petrogenesis of pre-Imbrium mare volcanism. Geochim. Cosmochim. Acta 51, 3241-3254.
41	Dickinson T., Taylor G.J., Keil K., and Bild R.W. (1989) Germanium abundances in lunar basalts: Evidence of mantle metasmatism. Proc. Lunar Planet. Sci. Conf. 19th, 189-198.
42	Dickinson T., Taylor G.J., Keil K., Schmitt R.A., Hughes S.S., and Smith M.R. (1985) Apollo 14 aluminous mare basalts and their possible relationship to KREEP. Proc. Lunar Planet. Sci. Conf. 15th, in J. Geophys. Res. 90, C365-C374.
43	Dowty E., Keil K., Prinz M., Gros J., and Takahashi H. (1976) Meteorite-free Apollo 15 crystalline KREEP. Proc. Lunar Sci. Conf. 7th, 1833-1844.
44	Dowty E., Prinz M., and Keil K. (1973) Composition, mineralogy, and petrology of 28 mare basalts from Apollo 15 rake samples. Proc. Lunar Sci. Conf. 4th, 423-444.
45	Duncan A.R., Sher M.K., Abraham Y.C., Erlank A.J., Willis J.P., and Ahrens L.H. (1975) Interpretation of the compositional variability of Apollo 15 soils. Proc. Lunar Sci. Conf. 6th, 2309-2320.
46	Duncan A.R., Erlank A.J., Sher M.K., Abraham Y.C., Willis J.P., and Ahrens L.H. (1976) Some trace element constraints on lunar basalt petrogenesis. Proc. Lunar Sci. Conf. 7th, 1659-1671.
47	Duncan A.R., Erlank A.J., Willis J.P., Sher M.K., and Ahrens L.H. (1974) Trace element evidence for a two-stage origin of some titaniferous mare basalts. Proc. Lunar Sci. Conf. 5th, 1147-1157.
48	Duncan A.R., McKay S.M., Stoeser J.W., Lindstrom M.M., Lindstrom D.J., Fruchter J.S., and Goles G.G. (1975) Lunar polymict breccia 14321: A compositional study of its principal components. Geochim. Cosmochim. Acta 39, 247-260.
49	Duncan A.R., Sher M.K., Abraham Y.C., Erlank A.J., Willis J.P., and Ahrens L.H. (1975) Interpretation of the compositional variability of Apollo 15 soils. Proc. Lunar Sci. Conf. 6th, 2309-2320.
50	Dymek R.F., Albee A.L., and Chodos A.A. (1975) Comparative mineralogy and petrology of Apollo 17 mare basalts: Samples 70215, 71055, 74255, and 75055. Proc. Lunar Sci. Conf. 6th, 49-77.
51	Ebihara E., Wolf R., Warren P.H., and Anders E. (1992) Trace elements in 59 mostly highland Moon rocks. Proc. Lunar Planet. Sci. 22nd, 417-426
52	Ehmann W.D. (1972) Elemental abundance studies of Apollo 15 and some Fra Mauro formation lunar samples. In The Apollo 15 Lunar Samples (Chamberlain J.W. and Watkins C., eds.), 214-216. The Lunar Science Institute, Houston, TX.
53	Ehmann W.D. and Chyi L.L. (1974) Abundances of the group IVB elements Ti, Zr, and Hf and implications of their ratios in lunar materials. Proc. Lunar Sci. Conf. 5th, 1015-1024.
54	Ehmann W.D. and Morgan J.W. (1971) Major element abundances in Apollo 12 rocks and fines by 14 MeV neutron activation. Proc. Lunar Sci. Conf. 2nd, 1237-1245.
55	Ehmann W.D., Chyi L.L., Garg A.N., Hawke B.R., Ma M.-S., Miller M.D., James W.D., and Pacer R.A. (1975) Chemical studies of the lunar regolith with emphasis on zirconium and hafnium. Proc. Lunar Sci. Conf. 6th, 1351-1361.
56	Ehmann W.D., Gillum D.E., and Morgan J.W. (1972) Oxygen and bulk element composition studies of Apollo 14 and other lunar rocks and sopil. Proc. Lunar Sci. Conf. 3rd, 1149-1160.
57	Eisentraut K.J., Black M.S., Hileman F.D., Sievers R.E., and Ross W.D. (1972) Beryllium and chromium abundances in Fra Mauro and Hadley-Apennine lunar samples. Proc. Lunar Sci. Conf. 3rd, 1327-1333.
58	Eldridge J.S., O'Kelley G.D., and Northcutt K.J. (1974) Primordial radioelement concentrations in rocks and soils from Taurus-Littrow. Proc. Lunar Sci. Conf. 5th, 1025-1033.
59	Eldridge J.S., O'Kelley G.D., and Northcutt K.J. (1975) Primordial and cosmogenic radionuclides in Descartes and Taurus-Littrow materials: Extension of studies by nondestructive gamma-ray spectrometry. Proc. Lunar Sci. Conf. 6th, 1407-1418.
60	Engel A.E.J. and Engel C.G. (1970) Lunar rock compositions and some interpretations. Proc. Apollo 11 Lunar Sci. Conf., 1081-1084.
61	Engel A.E.J., Engel C.G., Sutton A.L., and Myers A.T. (1971) Composition of five Apollo 11 and Apollo 12 rocks and one Apollo 11 soil and some petrogenetic considerations. Proc. Lunar Sci. Conf. 2nd, 439-448.
62	Evensen N.M., Murthy V.R., and Coscio M.R. (1973) Rb-Sr ages of some mare basalts and the isotopic and trace element systematics in lunar fines. Proc. Lunar Sci. Conf. 4th, 1707-1724.
63	Fruchter J.S., Rancitelli L.A., and Perkins R.W. (1975) Primordial radionuclide variations in the Apollo 15 and 17 deep core samples and in Apollo 17 igneous rocks and breccias. Proc. Lunar Sci. Conf. 6th, 1399-1406.
64	Fruchter J.S., Stoeser J.W., Lindstrom M.M., and Goles G.G. (1973) Apollo 15 clastic materials and their relationship to local geologic features. Proc. Lunar Sci. Conf. 4th, 1227-1237.
65	Ganapathy R., Keays R.R., Laul J.C., and Anders E. (1970) Trace elements in Apollo 11 lunar rocks: Implications for meteorite influx and origin of moon. Proc. Apollo 11 Lunar Sci. Conf., 1117-1142.
66	Ganapathy R., Morgan J.W., Krahenbuhl U., and Anders E. (1973) Ancient meteoritic components in lunar highland rocks: Clues from trace elements in Apollo 15 and 16 samples. Proc. Lunar Sci. Conf. 4th, 1239-1261.
67	Gast P.W. and Hubbard N.J. (1970) Rare earth abundances in soil and rocks from the Ocean of Storms. Earth Planet. Sci. Lett., 10, 94-101.
68	Gast P.W., Hubbard N.J., and Wiesmann H. (1970) Chemical composition and petrogenesis of basalts from Tranquility Base. Proc. Apollo 11 Lunar Sci. Conf., 1143-1163.
69	Gibson E.K., Jr. and Moore G.W. (1974) Sulfur abundances in the valley of Tauru-Littrow. Proc. Lunar Sci. Conf. 5th, 1823-1837.
70	Gibson E.K., Jr., Brett R., and Andrawes F. (1977) Sulfur in lunar mare basalts as a function of bulk composition. Proc. Lunar Sci. Conf. 8th, 1417-1428.
71	Gibson E.K., Jr., Chang S., Lennon K., Moore G.W., and Pearce G.W. (1975) Sulfur abundances and distributions in mare basalts and their source magmas. Proc. Lunar Sci. Conf. 6th, 1287-1301.
72	Gibson E.K., Jr., Usselman T.M., and Morris R.V. (1976) Sulfur in Apollo 17 basalts and their source regions. Proc. Lunar. Sci. Conf. 7th, 1491-1505.
73	Goles G.G., Duncan A.R., Lindstrom D.J.,Martin M.R., Beyer R.L., Osawa M., Randle K., Meek L.T., Steinborn T.L., and McKay S.M. (1971) Analyses of Apollo 12 specimens: Compositional variations, differentiation processes, and lunar soil mixing models. Proc. Lunar Sci. Conf. 2nd, 1063-1081.
74	Goles G.G., Randle K., Osawa M., Lindstrom D.J., Jerome D.Y., Steinborn T.L., Beyer R.L., Martin M.R., and McKay S.M. (1970) Interpretations and speculations on elemental abundances in lunar samples. Proc. Apollo 11 Lunar Sci. Conf., 1177-1194.
75	Goles G.G., Randle K., Osawa M., Schmitt R.A., Wakita H., Ehmann W.D., and Morgan J.W. (1970) Elemental abundances by instrumental activation analyses in chips from 27 lunar rocks. Proc. Apollo 11 Lunar Sci. Conf., 1165-1176.
76	Goodrich C.A., Taylor G.J., Keil K., Kallemeyn G.W., and Warren P.H. (1986) Alkali norite, troctolites, and VHK mare basalts from breccia 14304. Proc. Lunar Planet. Sci. Conf. 16th, in J. Geophys. Res. 91, D305-D318.
77	Grieve R.A., McKay G.A., and Weill D.F. (1975) Lunar polymict breccia 14321: A petrographic study. Geochim. Cosmochim. Acta. 39, 229-245.
78	Gros J., Takahashi H., Hertogen J., Morgan J.W., and Anders E. (1976) Composition of the projectiles that bombarded the lunar highlands. Proc. Lunar Sci. Conf 7th, 2403-2425.
79	Hallis, L.J., Anand, M., Strekopytov, S. (2014) Trace-element modelling of mare basalt parental melts: Implications for a heterogeneous lunar mantle. Geochim. Cosmochim. Acta. 134, 289-316.
80	Haskin L.A., Allen R.O., Helmke P.A., Paster T.P., Anderson M.R., Korotev R.L., and Zweifel K.A. (1970) Rare earths and other trace elements in Apollo 11 lunar samples. Proc. Apollo 11 Lunar Sci. Conf., 1213-1231.
81	Haskin L.A., Helmke P.A., Allen R.O., Anderson M.R., Korotev R.L., and Zweifel K.A. (1971) Rare-earth elements in Apollo 12 lunar materials. Proc. Lunar Sci. Conf. 2nd, 1307-1317.
82	Helmke P.A. and Haskin L.A. (1972) Rare earths and other trace elements in Apollo 15 samples. In The Apollo 15 Lunar Samples (Chamberlain J.W. and Watkins C., eds.), 217-220. The Lunar Science Institute, Houston, TX.
83	Helmke P.A., Blanchard D.P., Haskin L.A., Telander K., Weiss C., and Jacobs J.W. (1973) Major and trace elements in igneous rocks from Apollo 1. The Moon 8, 129-148.
84	Helmke P.A., Haskin L.A., Korotev R.L., and Ziege K. (1972) Rare earths and other trace elements in Apollo 14 samples. Proc. Lunar Sci. Conf. 3rd, 1275-1292.
85	Hubbard N.J. and Gast P.W. (1971) Chemical composition and origin of nonmare lunar basalts. Proc. Lunar Sci. Conf. 2nd, 999-1020.
86	Hubbard N.J., Gast P.W., Rhodes J.W., Bansal B.M., Wiesmann H., and Church S.E. (1972) Nonmare basalts: Part II. Proc. Lunar Sci. Conf. 3rd, 1161-1179.

Appendix 2h: Supplementary References for Published Data

Code	Extended Reference
87	Hubbard N.J., Meyer C. Jr., Gast P.W., and Wiesmann H. (1970) The composition and derivation of Apollo 12 soils. Earth Planet. Sci. Lett. 10, 341-350.
88	Hubbard N.J., Rhodes J.M., Gast P.W., Bansal B.M., Shih C.-Y., Wiesmann H., and Nyquist L.E. (1973) Lunar rock types: The role of plagioclase in non-mare and highland rock types. Proc. Lunar Sci. Conf. 4th, 1297-1312.
89	Hubbard N.J., Rhodes J.M., Wiesmann H., Shih C.-Y., and Bansal B.M. (1974) The chemical definition and interpretation of rock types returned from the non-mare regions of the Moon. Proc. Lunar Sci. Conf. 5th, 1227-1246.
90	Hughes S.S. and Schmitt R.A. (1985) Zr-Hf-Ta fractionation during lunar evolution. Proc. Lunar Planet. Sci. Conf. 16th, in J. Geophys. Res. 90, D31-D45.
91	Irving A.J. (1977) Chemical variation and fractionation of KREEP basalt magmas. Proc. Lunar Sci. Conf. 8th, 2433-2448.
92	Janghorbani M., Miller M.D., Ma M.-S., Chyi L.L., and Ehmann W.D. (1973) Oxygen and other elemental abundance data for Apollo 14, 15, 16, and 17 samples. Proc. Lunar Sci. Conf. 4th, 1115-1126.
93	Janssens M.-J., Palme H., Hertogen J., Anderson A.T., and Anders E. (1978) Meteoritic material in lunar highland samples from the Apollo 11 and 12 sites. Proc. Lunar Planet. Sci. Conf. 9th, 1537-1550.
94	Jerde E.A., Snyder G.A., Taylor L.A., Liu Y.-G., and Schmitt R.A. (1994) The origin and evolution of lunar high-Ti basalts: Periodic melting of a single source at Mare Tranquilitatis. Geochim. Cosmochim. Acta 58, 515-527.
95	Jolliff B.L. (1991) Fragments of Quartz Monzodiorite and felsite in Apollo 14 soil particles. Proc. Lunar Planet. Sci. Conf. 21st, 101-118.
96	Jolliff B.L., Korotev R.L., and Haskin L.A. (1991) Geochemistry of 2-4 mm particles from Apollo 14 soil (14161) and implications regarding igneous components and soil-forming processes. Proc. Lunar Planet. Sci. Conf. 21st, 193-219.
97	Jolliff B.L., Rockow K.M., Korotev R.L., and Haskin L.A. (1996) Lithologic distribution and geologic history of the Apollo 17 site: The record in soils and small rock particles from the highland massiffs. Meteor. Planet. Sci. 31, 116-145.
98	Jovanovic S. and Reed G.W., Jr. (1976) Chemical fractionation of Ru and Os in the Moon. Proc. Lunar Sci. Conf. 7th, 3437-3446.
99	Kaplan I.R. and Petrowski C. (1971) Carbon and sulfur isotope studies on Apollo 12 lunar samples. Proc. Lunar Sci. Conf. 2nd, 1397-1406.
100	Kaplan I.R., Kerridge J.F., and Petrowski C. (1976) Light element geochemistry of the Apollo 15 site. Proc. Lunar Sci. Conf. 7th, 481-492.
101	Kaplan I.R., Smith J.W., and Ruth E. (1970) Carbonb and sulfur concentration and isotopic composition in Apollo 11 lunar samples. Proc. Apollo 11 Lunar Sci. Conf., 1317-1329.
102	Kharkar D.P. and Turekian K.K. (1971) Analyses of Apollo 11 and Apollo 12 rocks and soils by neutron activation. Proc. Lunar Sci. Conf. 2nd, 1301-1305.
103	Klein C. Jr., Drake J.C., and Frondel C. (1971) Mineralogical. Petrological, and chemical features of four Apollo 12 lunar microgabbros. Proc. Lunar Sci. Conf. 2nd, 265-284.
104	Kushiro I. (1972) Petrology of some Apollo 15 basalts. In The Apollo 15 Lunar Samples (Chamberlain J.W. and Watkins C., eds.), 128-130. The Lunar Science Institute, Houston, TX.
105	Kushiro I. And Haramura H. (1971) Major element variation and possible source material of Apollo 12 crystalline rocks. Science 171, 1235-1237.
106	Laul J.C. and Schmitt R.A. (1973) Chemical composition of Apollo 15, 16, and 17 samples. Proc. Lunar Sci. Conf. 4th, 1349-1367.
107	Laul J.C., Hill D.W., and Schmitt R.A. (1974) Chemical studies of Apollo 16 and 17 samples. Proc. Lunar Sci, Conf. 5th, 1047-1066.
108	Laul J.C., Schmitt R.A., Robyn M., and Goles G.G. (1975) Chemical composition of 18 Apollo 17 rake basalts and one basalt-breccia. Lunar Planet. Sci. VI, 492-494.
109	Laul J.C., Wakita H., Showalter D.L., Boynton W.V., and Schmitt R.A. (1972) Bulk, rare earth, and other trace elements in Apollo 14 and 15 and Luna 16 samples. Proc. Lunar Sci. Conf. 3rd, 1181-1200/
110	Lindstrom M.M., Duncan A.R., Fruchter J.S., McKay S.M., Stoeser J.W., Goles G.G., and Lindstrom D.J. (1972) Compositional characteristics of some Apollo 14 clastic materials. Proc. Lunar Sci. Conf. 3rd, 1201-1214.
111	Lindstrom M.M., Nielsen R.L., and Drake M.J. (1977) Petrology and geochemistry of lithic fragments separated from the Apollo 15 deep-drill core. Proc. Lunar Sci. Conf. 8th, 2869-2888.
112	Longhi J., Walker D., and Hays J.F. (1972) Petrography and crystallization history of basalts 14310 and 14072. Proc. Lunar Sci. Conf. 3rd, 131-139.
113	Longhi J., Walker D., Stolper E.N., Grove T.L., and Hays J.F. (1972) Petrology of mare/rille basalts 15555 and 15065. In The Apollo 15 Lunar Samples, 131-134.
114	Lugmair G.W. (1975) Sm-Nd systematics of some Apollo 17 basalts. Conference on Origins of Mare Basalts and their Implications for Lunar Evolution, 107-109. Lunar Science Institute.
115	Lugmair G.W. and Carlson R.W. (1978) The Sm-Nd history of KREEP. Proc Lunar Planet Sci. Conf. 9th, 689-704.
116	Ma M.-S. (1980) VLT mare basalt and aluminous mare basalt from Apollo 17 drill core. Lunar Planet. Sci. XI, 655-657
117	Ma M.-S., Murali A.V., and Schmitt R.A. (1976) Chemical constraints for mare basalt genesis. Proc. Lunar Sci. Conf. 7th, 1673-1695.
118	Ma M.-S., Schmitt R.A., Beaty D.W., and Albee A.L. (1980) The petrology and chemistry of basaltic fragments from the Apollo 11 soil: Drive tubes 10004 and 10005. Proc. Lunar Planet. Sci. Conf. 11th, 37-47.
119	Ma M.-S., Schmitt R.A., Warner R.D., Taylor G.J., and Keil K. (1978) Genesis of Apollo 15 olivine normative mare basalts: Trace element correlations. Proc. Lunar Sci. Conf. 9th, 523-533.
120	Ma M.-S., Schmitt R.A., Warner R.D., Taylor G.J., Barker S., and Keil K. (1980) Aluminous mare basalts and basaltic-textured KREEPy rocks from Apollo 14 coarse fines. Lunar Planet. Sci. XI, 652-654.
121	Mark R.K., Cliff R.A., and Wetherill G.W. (1975) More on Rb-Sr in lunar breccia 14321. Proc. Lunar Sci. Conf. 6th 1501-1507.
122	Mark R.K., Cliff R.A., Lee-Hu C., and Wetherill G.W. (1973) Rb-Sr studies of lunar breccias and soils. Proc. Lunar Sci. Conf. 4th 1785-1795.
123	Mark R.K., Lee-Hu C.-N., and Wetherill G.W. (1974) Equilibration and ages: Rb-Sr syidues of breccias 14321 and 15265. Proc. Lunar Sci. Conf. 5th, 1477-1485.
124	Mason B., Jarosewich E., Melson W.G., and Thompson G. (1972) Mineralogy, petrology, and chemical composition of lunar samples 15085, 15256, 15271, 15471, 15475, 15476, 15535, 15555, and 15556. Proc. Lunar Sci. Conf. 3rd, 785-796.
125	Masuda A., Nakamura N., Kurasawa H., and Tanaka T. (1972) Precise determination of rare-earth elements in the Apollo 14 and 15 samples. Proc. Lunar Sci. Conf. 3rd, 1307-1313.
126	Masuda A., Tanaka T., Nakamura N., and Kurasawa H. (1974) Possible REE anomalies of Apollo 17 REE patterns. Proc. Lunar Sci. Conf. 5th, 1247-1253.
127	Mattinson J.M., Tilton G.R., Todt W., and Chen J.H. (1977) Lead isotope studies of mare basalt 70017. Proc. Lunar Sci. Conf. 8th, 1473-1487.
128	Maxwell J.A. and Wiik H.B. (1970) Chemical composition of Apollo 12 lunar samples 12004, 12033, 12051, 12052, and 12065. Earth Planet. Sci. Lett. 10, 285-288.
129	Maxwell J.A. and Wiik H.B. (1971) Chemical compositions of Apollo 12 lunar samples 12004, 12033, 12051, 12052, and 12065. Earth Planet. Sci. Lett. 10, 285-288.
130	Maxwell J.A., Bouvier J.-L., and Wiik H.B. (1972) Chemical composition of some Apollo 15 lunar samples. In The Apollo 15 Lunar Samples (Chamberlain J.W. and Watkins C., eds.), 233-238. The Lunar Science Institute, Houston, TX.
131	Maxwell J.A., Peck L.C., and Wiik H.B. (1970) Chemical composition of Apollo 11 lunar samples 10017, 10020, 10072, and 10084. Proc. Apollo 11 Lunar Sci. Conf., 1369-1374
132	McKay G.A., Wiesmann H., Bansal B.M., and Shih C.-Y. (1979) Petrology, chemistry, and chronology of Apollo 14 KREEP basalts. Proc. Lunar Planet. Sci. Conf. 10th, 181-205
133	McKay G.A., Wiesmann H., Nyquist L.E., Wooden J.L., and Bansal B.M. (1978) Petrology, chemistry, and chronology of 14078: Chemical constraints on the origin of KREEP. Proc. Lunar Planet. Sci. Conf. 9th, 661-687.
134	Miller M.D., Pacer R.A., Ma M.-S., Hawke B.R., Lookhart G.L., and Ehmann W.D. (1974) Compositional studies of the lunar regolith at the Apollo 17 site. Proc. Lunar Sci. Conf. 5th, 1079-1086.
135	Moore C.B., Lewis C.F., and Cripe J.D. (1974) Total carbon and sulfur contents of Apollo 17 lunar samples. Proc. Lunar Sci. Conf. 5th, 1897-1906. 5th, 1897-1906
136	Moore C.B., Lewis C.F., and Gibson E.K. (1972) Carbon and nitrogen in Apollo0 15 lunar samples. In The Apollo 15 Lunar Samples (Chamberlain J.W. and Watkins C., eds.), 316-318. The Lunar Science Institute, Houston, TX.
137	Moore C.B., Lewis C.F., and Gibson E.K., Jr. (1973) Total carbon contents of Apollo 15 and 16 lunar samples. Proc. Lunar Sci. Conf. 4th, 1613-1623.
138	Moore C.B., Lewis C.F., Larimer J.W., Delles F.M., Gooley R.C., Nichiporuk W., and Gibson E.R. (1971) Total carbon and nitrogen abundances in Apollo 12 lunar samples. Proc. Lunar Sci. Conf. 2nd, 1343-1350.
139	Morgan J.W., Ganapathy R., and Krahenbuhl U. (1975) Meteoritic trace elements in lunar rock 14321, 184. Geochim. Comsochim. Acta 39, 261-264.
140	Morgan J.W., Ganapathy R., Higuchi H., Krahenbuhl U., and Anders E. (1974) Lunar basins: Tentative characterization of projectiles from meteoritic elements in Apollo 17 boulders. Proc. Lunar Sci. Conf. 5th, 1703-1736.
141	Morgan J.W., Krahenbuhl U., Ganapathy R., and Anders E. (1972) Trace elements in Apollo 15 samples: Implications for meteorite influx and volatile depletion on the moon. Proc. Lunar Sci. Conf. 3rd, 1361-1376.
142	Morgan J.W., Laul J.C., Krahenbuhl U., Ganapathy R., and Anders E. (1972) Major impacts on the Moon: Characterization from trace elements in Apollo 12 and 14 samples. Proc. Lunar Sci. Conf. 3rd, 1377-1395.
143	Morrison G.H., Gerard J.T., Kashuba A.T., Gangadharam E.V., Rothenberg A.M., Potter N.M., and Miller G.B. (1970) Elemental abundances of lunar soil and rocks. Proc. Apollo 11 Lunar Sci. Conf., 1383-1392.
144	Morrisson G.H., Gerard J.T., Potter N.M., Gangadharam E.V., Rothenberg A.M., and Burdo R.A. (1971) Elemental abundances of lunar soil and rocks from Apollo 12. Proc. Lunar Sci. Conf. 2nd, 1169-1185.
145	Müller O. (1972) Alkali and alkaline earth elements, La, and U in Apollo 14 and Apollo 15 samples. In The Apollo 15 Lunar Samples (Chamberlain J.W. and Watkins C., eds.), 240-243. The Lunar Science Institute, Houston, TX.
146	Muller O. (1975) Lithophile trace and major elements in Apollo 16 and 17 lunar samples. Proc. Lunar Sci. Conf. 6th, 1303-1311.
147	Muller O., Grallath E., and Tolg G. (1976) Nitrogen in lunar igneous rocks. Proc. Lunar Sci. Conf. 7th, 1615-1622.
148	Murali A.V., Ma M.-S., Schmitt R.A., Warner R.D., Keil K., and Taylor G.J. (1977) Chemistry of 30 Apollo 17 rake samples; 71597 a product of partial olivine accumulation. Lunar Planet. Sci. VIII, 703-705.
149	Murthy V.R. and Coscio M.R. (1976) Rb-Sr ages and isotopic systematics of some Serenitatis mare basalts. Proc. Lunar Sci. Conf. 7th, 1529-1544.
150	Murthy V.R., Evensen N.M., and Coscio M.R. Jr. (1970) Distribution of K, Rb, Sr, and Ba and Rb-Sr isotopic relations in Apollo 11 lunar samples. Proc. Apollo 11 Lunar Sci. Conf., 1393-1406.
151	Murthy V.R., Evensen N.M., Jahn B.-M., and Coscio M.R., Jr. (1972) Apollo 14 and 15 samples: Rb-Sr ages, trace elements, and lunar evolution. Proc. Lunar Sci. Conf. 3rd, 1503-1514.
152	Murthy V.R., Evensen N.M., Jahn B-M., and Coscio M.R. (1971) Rb-Sr ages and elemental abundances of K, Rb, Sr, and Ba samples from the Ocean of Storms. Geochim. Cosmochim. Acta 35, 1139-1153.
153	Nava D.F. (1974) Chemical compositions of some soils and rock types from the Apollo 15, 16, and 17 lunar sites. Proc. Lunar Sci. Conf. 5th, 1087-1096.
154	Neal C.R. (2001) Interior of the Moon: The presence of garnet in the primitive deep lunar mantle. J. Geophys. Res. 106, 27865-27885.
155	Neal C.R. and Kramer G.Y. (2003) The composition of KREEP: A detailed study of KREEP basalt 15386. Lunar Planet. Sci. XXXIV (abstract # 2023 [CD-ROM]).
156	Neal C.R. and Kramer G.Y. (2005) The petrogenesis of the high-Al mare basalts. Am. Mineral. (submitted 2005).
157	Neal C.R., Hacker M.D., Snyder G.A., Taylor L.A., Liu Y-G., and Schmitt R.A. (1994) Basalt generation at the Apollo 12 site, Part 1: New data, classification, and re-evaluation. Meteoritics 29, 334-348.
158	Neal C.R., Taylor L.A., and Lindstrom M.M. (1988) Apollo 14 mare basalt petrogenesis: Assimilation of KREEP-like components by a fractionating magma. Proc. Lunar Planet. Sci. Conf. 18, 139-153.
159	Neal C.R., Taylor L.A., and Lindstrom M.M. (1988) The importance of Lunar Granite and KREEP in Very High Potassium (VHK) basalt petrogenesis. Proc. Lunar Planet. Sci. Conf. 18th, 121-137.
160	Neal C.R., Taylor L.A., Hughes S.S., and Schmitt R.A. (1990) The significance of fractional crystallization in the petrogenesis of Apollo 17 Type A and Type B high-Ti basalts. Geochim. Cosmochim. Acta 54, 1817-1833.
161	Neal C.R., Taylor L.A., Patchen A.D., Schmitt R.A., Hughes, S.S., and Lindstrom, M.M. (1989) High alumina (HA) and very high potassium (VHK) basalt clasts from Apollo 14 breccias, part 2 - whole-rock geochemistry; Further evidence for combined assimilation and fractional crystallization within the Lunar crust. Proc. Lunar Planet. Sci. Conf. 19th, 147-162.
162	Nunes P.D. and Tatsumoto M. (1975) U-Th-Pb systematics of selected samples from Apollo 17, Boulder 1, Station 2. The Moon 14, 463-471.
163	Nunes P.D., Tatsumoto M., and Unruh D.M. (1974) U-Th-Pb systematics of some Apollo 17 lunar samples and implications for a lunar basin excavation chronology. Proc. Lunar Sci. Conf. 5th, 1487-1514.
164	Nyquist L., Lindstrom M., Bansal B., Mittlefehldt D., Shih C.-Y., and Wiesmann H. (1989) Chemical and isotopic constraints on the petrogenesis of the large mare basalt clast in breccia 15459. Proc. Lunar Planet. Sci. Conf. 19th, 163-174.
165	Nyquist L.E. (1977) Lunar Rb-Sr Chronology. Phys. Chem Earth 10, 103-142.
166	Nyquist L.E., Bansal B.M., and Wiesmann H. (1975) Rb-Sr ages and initial 87Sr/86Sr for Apollo 17 basalts and KREEP basalt 15386. Proc. Lunar Sci. Conf. 6th, 1445-1465.
167	Nyquist L.E., Bansal B.M., Wiesmann H., and Jahn B.-M. (1974) Taurus-Littrow chronology: Some constraints on early lunar crustal development. Proc. Lunar Sci. Conf. 5th, 1515-1539.
168	Nyquist L.E., Bansal B.M., Wooden J.L., and Wiesmann H. (1977) Sr-isotopic constraints on the petrogensis of Apollo 12 mare basalts. Proc. Lunar Sci. Conf. 8th, 1383-1415.
169	Nyquist L.E., Gast P.W., Church S.E., Wiesmann H., and Bansal B.M. (1972) Rb-Sr systematics for chemically defined Apollo 15 materials. In The Apollo 15 Lunar Samples (Chamberlain J.W. and Watkins C., eds.), 380-384. The Lunar Science Institute, Houston, TX.
170	Nyquist L.E., Hubbard N.J., Gast P.W., Bansal B.M., Wiesmann H., and Jahn B. (1973) Rb-Sr systematics for chemically defined Apollo 15 and 16 materials. Proc. Lunar Sci. Conf. 4th, 1823-1846.
171	Nyquist L.E., Shih C.-Y., Wooden J.L., Bansal B.M., and Wiesmann H. (1979) The Sr and Nd isotopic record of Apollo 12 basalts: Implications for lunar geochemical evolution. Poroc. Lunar Planet. Sci. Conf. 10th, 77-114.
172	Nyquist L.E., Wooden J.L., Shih C.-Y., Wiesmann H., and Bansal B.M. (1981) Isotopic and REE studies of lunar basalt 12038: implications for petrogenesis of aluminous mare basalts. Earth Planet. Sci. Lett. 55, 335-355.

Appendix 2h: Supplementary References for Published Data

Code	Extended Reference
173	O'Kelley G.D., Eldridge J.S., and Northcutt K.J. (1972) Abundances of primordial radioelements K, Th, and U in Apollo 15 samples, as determined by non-destructive gamma-ray spectrometry. In The Apollo 15 Lunar Samples (Chamberlain J.W. and Watkins C., eds.), 244-246. The Lunar Science Institute, Houston, TX.
174	Paces J.B., Nakai S., Neal C.R., Taylor L.A., Halliday A.N., and Lee D.-C. (1991) A strontium and neodymium isotopic study of Apollo 17 high-Ti mare basalts: Resolution of ages, evolution of magmas, and origins of source heterogeneities. Geochim. Cosmochim. Acta 55, 2025-2043.
175	Papanastassiou D.A and Wasserburg G.J. (1970) Rb-Sr ages from the Ocean of Storms. Earth Planet. Sci. Lett. 8, 269-278.
176	Papanastassiou D.A. and Wasserburg G.J. (1971) Lunar chronology and evolution from Rb-Sr studies of Apollo 11 and 12 samples. Earth Planet. Sci. Lett. 11, 37-62.
177	Papanastassiou D.A. and Wasserburg G.J. (1971) Rb-Sr ages of igneous rocks from the Apollo 14 mission and the age of the Fra Mauro formation. Earth Planet. Sci. Lett. 12, 36-48.
178	Papanastassiou D.A. and Wasserburg G.J. (1973) Rb-Sr ages and initial strontium in basalts from Apollo 15. Earth Planet.Sci. Lett. 17, 324-337.
179	Papanastassiou D.A., DePaolo D.J., and Wasserburg G.J. (1977) Rb-Sr and Sm-Nd chronology and genealogy of mare basalts from the Sea of Tranquility. Proc. Lunar Sci. Conf. 8th, 1639-1672.
180	Petrowski C., Kerridge J.F., and Kaplan I.R. (1974) Light element geochemistry of the Apollo 17 site. Proc. Lunar Sci. Conf. 5th, 1939-1948.
181	Philpotts J.A. and Schnetzler C.C. (1970) Apollo 11 lunar samples: K, Rb, Sr, Ba, and rare-earth concentrations in some rocks and separated phases. Proc. Apollo 11 Lunar Sci. Conf., 1471-1486.
182	Philpotts J.A., Schnetzler C.C., Nava D.F., Bottino M.L., Fullagar P.D., Thomas H.H., Schuhmann S., and Kouns C.W. (1972) Apollo 14: Some geochemical aspects. Proc. Lunar Sci. Conf. 3rd, 1293-1305.
183	Philpotts J.A., Schuhmann S., Kouns C.W., Lum R.K.L., and Winzer S. (1974) Origin of Apollo 17 rocks and soils. Proc. Lunar Sci. Conf. 5th, 1255-1267.
184	Reed G.W. and Jovanovic S. (1972) Trace element comparisons between mare and Apennine-Front nonmare samples. In The Apollo 15 Lunar Samples (Chamberlain J.W. and Watkins C., eds.), 247-249. The Lunar Science Institute, Houston, TX.
185	Rees C.E. and Thode H.G. (1972) Sulphur concentrations and isotope ratios in lunar samples. Proc. Lunar Sci. Conf. 3rd, 1479-1485.
186	Rees C.E. and Thode H.G. (1974) Sulfur concentrations and isotope ratios in Apollo 16 and 17 samples. Proc. Lunar Sci. Conf. 5th, 1963-1973.
187	Rhodes J.M. and Blanchard D.P. (1980) Chemistry of Apollo 11 low-K mare basalts. Proc. Lunar. Planet. Sci. Conf. 11th, 49-66.
188	Rhodes J.M. and Hubbard N.J. (1973) Chemistry. Classification, and petrogenesis of Apollo 15 mare basalts. Proc. Lunar Sci. Conf. 4th, 1127-1148.
189	Rhodes J.M., Blanchard D.P., Dungan M.A., Brannon J.C., and Rodgers K.V. (1977) Chemistry of Apollo 12 mare basalts: Magma types and fractionation processes. Proc. Lunar Sci. Conf. 8th, 1305-1338.
190	Rhodes J.M., Hubbard N.J., Wiesmann H., Rodgers K.V., Brannon J.C., and Bansal B.M. (1976) Chemistry, classification, and petrogenesis of Apollo 17 mare basalts. Proc. Lunar Sci. Conf. 7th, 1467-1489.
191	Rhodes J.M., Rodgers K.V., Shih C., Bansal B.M., Nyquist L.E., Wiesmann H., and Hubbard N.J. (1974) The relationships between geology and soil chemistry at the Apollo 17 landing site. Proc. Lunar Sci. 5th, 1097-1117.
192	Ridley W.I. (1975) On high-alumina mare basalts. Proc. Lunar Sci. Conf. 6th, 131-145.
193	Rose H.J., Cuttitta F., Annell C.S., Carron M.K., Christian R.P., Dwornik E.J., Greenland L.P., and Ligon D.T. Jr. (1972) Compositional data for twebty-one Fra Mauro lunar materials. Proc. Lunar Sci. Conf. 3rd, 1215-1229.
194	Rose H.J., Cuttitta F., Berman S., Brown F.W., Carron M.K., Christian R.P., Dwornik E.J., and Greenland L.P. (1974) Chemical composition of rocks and soils at Taurus-Littrow. Proc. Lunar Sci. Conf. 5th, 1119-1133.
195	Rose H.J., Jr., Baedecker P.A., Berman S., Christian R.P., Dwornik E.J., Finkelman R.B., and Schnepfe M.M. (1975) Chemical composition of rcks and soils returned by the Apollo 15, 16, and 17 missions. Proc. Lunar Sci. Conf. 6th, 1363-1373.
196	Ryder G. (1990) A distinct variant of high-titanium mare basalt from the Van Serg core, Apollo 17 landing site. Meteoritics 25, 249-258.
197	Ryder G. and Burling T.C. (1996) An Apollo 15 mare basalt fragment and lunar mare provinces. Meteor. Planet. Sci. 31, 50-59.
198	Ryder G. and Martinez R.R. (1991) Evolved hyperbyssal rocks from Station 7, Apennine Front, Apollo 15. Proc. Lunar Planet Sci. Conf. 21st, 137-150.
199	Ryder G. and Martinez R.R. (1991) Evolvede hypabyssal rocks from Station 7, Apennine Front, Apollo 15. Proc. Lunar Planet. Sci. Conf. 21, 137-150.
200	Ryder G. and Schuraytz B.C. (2001) Chemical variation of the large Apollo 15 olivine-normative mare basalt rock samples. J. Geophys. Res. 106, 1435-1451.
201	Ryder G., Lindstrom M.M., and Willis K. (1988) The reliability of macroscopic identification of lunar coarse fines particles and the petrogenesis of 2-4 mm particles in Apenine Front sample 15243. Proc. Lunar Planet. Sci. Conf. 18th, 219-232.
202	Ryder G., Stoeser D.B., and Wood J.A. (1977) Apollo 17 KREEPy basalt: A rock type intermediate between mare and KREEP basalts. Earth Planet. Sci. Lett. 35, 1-13.
203	Salpas P.A., Taylor L.A., and Lindstrom M.M. (1987) Apollo 17 KREEPy basalts: Evidence for nonuniformity of KREEP. Proc. Lunar Planet. Sci. Conf. 17th, in J. Geophys. Res. 92, E340-E348.
204	Schaal, R.B., Hörz, F. (1977) Shock metamorphism of lunar and terrestrial basalts. Proc. Lunar Sci. Conf. 8th, 1697-1729
205	Schnetzler C.C. and Philpotts J.A. (1971) Alkali, alkaline earth, and rare earth element concentrations in some Apollo 12 soils, rocks, and separated phases. Proc. Lunar Sci. Conf. 2nd, 1101-1122.
206	Schonfeld E., O'Kelley G.D., Eldridge J.S., and Northcutt K.J. (1972) K, U, and Th concentrations in rake sample 15382 by non-destructive gamma-ray spectroscopy. In The Apollo 15 Lunar Samples (Chamberlain J.W. and Watkins C., eds.), 253-254. The Lunar Science Institute, Houston, TX.
207	Scoon J.H. (1971) Chemical analyses of lunar samples 12040 and 12064. Proc. Lunar Sci. Conf. 2nd, 1259-1260.
208	Shervais J.W., Taylor L.A., and Laul J.C. (1983) Ancient crustal components in the Fra Mauro breccias. Proc. Lunar Planet Sci. Conf. 14th, in J. Geophys. Res. 88, B177-B192.
209	Shervais J.W., Taylor L.A., and Lindstrom M.M. (1985) Apollo 14 mare basalts: Petrology and geochemistry of clasts from consortium breccia 14321. Proc. Lunar Planet. Sci. Conf. 15, in J. Geophys. Res. 90, C375-C395.
210	Shervais J.W., Taylor L.A., Laul J.C., Shih C.-Y., and Nyquist L.E. (1985) Very high potassium (VHK) basalt: Complications in mare basalt petrogenesis. Proc. Lunar Planet. Sci. Conf. 16th, in J. Geophys. Res. 90, D3-D18.
211	Shervais J.W., Vetter S.K., and Lindstrom M.M. (1990) Chemical differences between small subsamples of Apollo 15 olivine-normative basalts. Proc. Lunar Planet. Sci. Conf. 20th, 109-126.
212	Shih C.-Y., Haskin L.A., Wiesmann H., Bansal B.M., and Brannon J.C. (1975) On the origin of high-Ti mare basalts. Proc. Lunar Sci. Conf. 6th, 1255-1285.
213	Shih C.-Y., Nyquist L.E., Bansal B.M., and Wiesmann H. (1992) Rb-Sr and Sm-Nd chronology of an Apollo 17 KREEP basalt. Earth Planet. Sci. Lett. 108, 203-215.
214	Shih C.-Y., Nyquist L.E., Bogard D.D., Bansal B.M., and Wiesmann H. (1987) Geochronology of high-K aluminous mare basalt clasts from Apollo 14 breccia 14304. Geochim. Cosmochim. Acta 51, 3255-3271.
215	Shih C.-Y., Nyquist L.E., Bogard D.D., Bansal B.M., Wiesmann H., Johnson P., Shervais J.W., and Taylor L.A. (1986) Geochronology and petrogenesis of Apollo 14 very high potassium mare basalts. Proc. Lunar Planet. Sci. Conf. 16th in J. Geophys. Res. 91, D214-D228.
216	Sievers R.E., Eisentraut K.J., Griest D.J., Richardson M.F., Wolf W.R., Ross W.D., Frew N.M., and Isenhour T.L. (1971) Variations in beryllium and chromium contents in lunar fines compared with crystalline rocks. Proc. Lunar Sci. Conf. 2nd, 1451-1459.
217	Simon S.B., Papike J.J., and Laul J.C. (1988) Chemistry and petrology of the Apennine Front, Apollo 15, Part I: KREEP basalts and plutonic rocks. Proc. Lunar Planet. Sci. Conf. 18th, 187-201.
218	Smales A.A., Mapper D., Webb M.S.W., Webster R.K., Wilson J.D., and Hislop J.S. (1971) Elemental composition of lunar surface material (part 2). Proc. Lunar Sci. Conf. 2nd, 1253-1258.
219	Snyder G.A., Borg L.E., Lee D.-C., Taylor L.A., Nyquist L.E., and Halliday A.N. (1997) Nd-Sr-Hf isotopic and geochronologic studies of Apollo 15 basalts. Lunar Planet. Sci. Conf. XXVIII, abstract# 1505. CD Rom.
220	Snyder G.A., Borg L.E., Taylor L.A., Nyquist L.E., and Halliday A.N. (1998) Volcanism in the Hadley-Apennine region of the Moon: Geochronology, Nd-Sr isotopic systematics and depths of melting. Lunar Planet Sci. Conf. XXIX, abstract# 1141.CD Rom.
221	Snyder G.A., Hall C.M., Lee C.-C., Taylor L.A., and Halliday A.N. (1996) Meteor. Planet. Sci. 31, 328-334.
222	Snyder G.A., Jerde E.A., Taylor L.A., Lee D.-C., and Halliday A.N. (1994) A sortie for pristine rocks at Mare Tranquillitatis: A ferroan anorthosite, a new Group D basalt, and the isotopic composition of Group D high-Ti basalts. Lunar Planet. Sci. XXV, 1299-130
223	Snyder G.A., Lee D.-C., Taylor L.A., Halliday A.N., and Jerde E.A. (1994) Evolution of the upper mantle of the Earth's Moon: Neodymium and strontium isotopic constraints from high-Ti mare basalts. Geochim. Cosmochim. Acta 58, 4795-4808.
224	Snyder G.A., Neal C.R., Jain J., and Taylor L.A. (1997) A "stormy" sortie for pristine rocks in lunar soils: 1. Trace-element compositions of basalts and impact melts from Apollo 12. Lunar Planet. Sci. XXVIII, abstract# 1502 [CD-ROM].
225	Snyder G.A., Neal C.R., Taylor L.A., and Halliday A.N. (1997) Anatexis of lunar cumulate mantle in time and space: Clues from trace-element, strontium, and neodymium isotopic chemistry of parental Apollo 12 basalts. Geochim. Cosmochim. Acta 61, 2731-2747.
226	Snyder G.A., Taylor L.A., and Jerde E.A. (1997) "New" basalts at Mare Tranquilitatis: A sortie for pristine rocks in soil 10085. Lunar Planet. Sci. XXVIII, abstract# 1498 [CR-ROM].
227	Snyder G.A., Taylor L.A., Liu Y.-G., and Schmit R.A. (1992) Petrogenesis of the Western Highlands of the Moon: Evidence from a diverse group of whitlockite-rich rocksfrom the Fra Mauro formation. Proc. Lunar Planet. Sci. 22nd, 399-416.
228	Strasheim A., Coetzee J.H.J., Jackson P.F.S., Strelow F.W.E., Wybenga F.T., Gricius A.J., and Kokot M.L. (1972) Analysis of lunar samples 15065, 15301, and 15556, with isotopic data for 7Li/6Li. In The Apollo 15 Lunar Samples (Chamberlain J.W. and Watkins C., eds.), 257-259. The Lunar Science Institute, Houston, TX.
229	Takeda H., Miyamoto M., and Ishii T. (1980) Comparison of basaltic clasts in lunar and eucritic polymict breccias. Proc. Lunar Planet. Sci. Conf. 11th, 135-147.
230	Tatsumoto M. (1970) Age of the Moon: An isotopic study of U-Th-Pb systematics of Apollo 11 lunar samples - II. Proc. Apollo 11 Lunar Sci. Conf., 1595-1612.
231	Tatsumoto M., Hedge C.E., Doe B.R., and Unruh D.M. (1972) U-Th-Pb and Rb-Sr measurements on some Apollo 14 samples. Proc. Lunar Sci. Conf. 3rd, 1531-1555.
232	Tatsumoto M., Hedge C.E., Knight R.J., Unruh D.M., and Doe B.R. (1972) U-Th-Pb, Rb-Sr, and K measurements on some Apollo 15 and Apollo 16 samples. In The Apollo 15 Lunar Samples (Chamberlain J.W. and Watkins C., eds.), 391-395. The Lunar Science Institute, Houston, TX.
233	Tatsumoto M., Knight R.J., and Doe B.R. (1971) U-Th-Pb systematics of Apollo 12 lunar samples. Proc. Lunar Sci. Conf. 2nd, 1521-1546.
234	Taylor G.J., Warner R.D., and Keil K. (1977) Chemical distinctions among very low-Ti mare basalts. In Papers Presented to the Conference on Luna 24, 183-185. Lunar Science Institue, Houston.
235	Taylor G.J., Warner R.D., and Keil K. (1978) VLT mare basalts: Impact mixing, parent magma types, and petrogenesis. In Mare Crisium: The View from Luna 24 (Merrill R.B. and Papike J.J., eds.) 357-370. Pergamon.
236	Taylor L.A., Shervais J.W., Hunter R.H., Shih C.-Y., Bansal B.M., Wooden J., Nyquist L.E., and Laul J.C. (1983) Pre-4.2 AE mare-basalt volcanism in the lunar highlands. Earth Planet. Sci. Letters 66, 33-47.
237	Taylor S.R. and Bence A.E. (1975) Trace element characteristics of the mare basalt source region: Implications for the cumulate versus primitive source model. In Papers Presented to the Conference of the Origins of Mare Basalts and Their Implications for Lunar Evolution, p. 159-163. The Lunar Science Institute, Houston.
238	Taylor S.R., Gorton M.P., Muir P., Nance W., Rudowski R., and Ware N. (1973) Lunar highlands composition: Apennine front. Proc. Lunar Sci. Conf. 4th, 1445-1459
239	Taylor S.R., Kaye M., Muir P., Nance W., Rudowski R, and Ware N. (1972) Composition of the lunar uplands: Chemistry of Apollo 14 samples from Fra Mauro. Proc. Lunar Sci. Conf. 3rd, 1231-1249.
240	Taylor S.R., Rudowski R., Muir P., Graham A., and Kaye M. (1971) Trace element chemistry of lunar samples from the Ocean of Storms. Proc. Lunar Sci. Conf. 2nd, 1083-1099.
241	Tera F and Wasserburg G.J. (1972) U-Th-Pb systematics in three Apollo 14 basalts and the problem of initial Pb in lunar rocks. Earth Planet. Sci. Lett. 14, 281-304.
242	Tera F., Eugster O., Burnett D.S., and Wasserburg G.J. (1970) Comparative study of Li, Na, K, Rb, Cs, Ca, Sr, and Ba abundances in achondrites and in Apollo 11 lunar samples. Proc. Apollo 11 Lunar Sci. Conf., 1637-1657.
243	The Lunar Sample Preliminary Examination Team (1969) Preliminary examination of the Lunar samples from Apollo 11. Science 165, 1211-1227.
244	The Lunar Sample Preliminary Examination Team (1970) Preliminary examination of Lunar samples from Apollo 12. Science 167, 1325-1339.
245	The Lunar Sample Preliminary Examination Team (1971) Preliminary examination of Lunar samples from Apollo 14. Science 173, 681-693.
246	The Lunar Sample Preliminary Examination Team (1972) Prelinary examination of Lunar samples from Apollo 15. Science 175, 363-375.
247	The Lunar Sample Preliminary Examination Team (1973) Preliminary examination of Lunar samples from Apollo 17. Science 182, 659-672.
248	Thode H.G. and Rees C.E. (1972) Sulphur concentrations and isotope ratios in Apollo 14 and 15 samples. In The Apollo 15 Lunar Samples (Chamberlain J.W. and Watkins C., eds.), 402-403. The Lunar Science Institute, Houston, TX.
249	Tilton G.R. and Chen J.H. (1979) Lead isotope systematics of three Apollo 17 mare basalts. Proc. Lunar Planet. Sci. Conf. 10th, 259-274.
250	Turekian K.K. and Kharkar D.P. (1970) Neutron activation analysis of milligram quantities of Apollo 11 lunar rocks and soil. Proc. Apollo 11 Lunar Sci. Conf., 1659-1664.
251	Unruh D.M., Stille P., Patchett P.J., and Tatsumoto M. (1984) Lu-Hf and Sm-Nd evolution in lunar mare basalts. Proc. Lunar Planet. Sci. Conf. 14th, in J. Geophys. Res. 89, B459-B477.
252	Vaniman D.T. and Papike J.J. (1977) Very low Ti (VLT) basalts: A new mare rock type from the Apollo 17 drill core. Proc. Lunar Sci. Conf. 8th, 1443-1471.
253	Vaniman D.T. and Papike J.J. (1980) Lunar highland melt rocks: Chemistry, petrology and silicate mineralogy. Proc. Conf. Lunar Highlands Crust (Papike J.J. and Merrill R.B., eds.) 271-337. Pergamon.
254	Vetter S.K., Shervais J.W., and Lindstrom M.M. (1989) Petrology and geochemistry of olivine-normative and quartz-normative basalts from regolith breccia 15498: New diversity in Apollo 15 mare basalts. Proc. Lunar Planet. Sci. Conf. 18th, 255-271.
255	Wakita H. and Schmitt R.A. (1971) Bulk elemental composition of Apollo 12 samples: Five igneous and one breccia rocks and four soils. Proc. Lunar Sci. Conf. 2nd, 1231-1236.
256	Wakita H., Rey P., and Schmitt R.A. (1971) Abundances of the 14 rare earth elements and 12 other trace elements in Apollo 12 samples: Five igneous and one breccia rocks and four soils. Proic. Lunar Sci. Conf. 2nd, 1319-1329.
257	Wakita H., Schmitt R.A., and Rey P. (1970) Elemental abundances of major, minor, and trace elements in Apollo 11 lunar rocks, soil, and core samples. Proc. Apollo 11 Lunar Sci. Conf., 1685-1717.
258	Wanke H., BaddenhausenH., Balacescu A., Teschke F., Spettel B., Dreibus G., Palme H., Quijano-Rico M., Kruse H., Wlotzka F., and Begemann F. (1972) Multielement analyses of lunar samples and some implications of the results. Proc. Lunar Sci. Conf. 3rd, 1251-1268.

Appendix 2h: Supplementary References for Published Data

Code	Extended Reference
259	Wanke H., Palme H., Baddenhausen H., Dreibus G., Jagoutz E., Kruse H., Palme C., Spettel B., Teshke F., and Thacker R. (1975) New data on the chemistry of lunar samples: Primary matter in the lunar highlands and the bulk composition of the Moon. Proc. Lunar Sci. Conf. 6th, 1313-1340.
260	Wanke H., Palme H., Baddenhausen H., Dreibus G., Jagoutz E., Kruse H., Spettel B., Teshke F., and Thacker R. (1974) Chemistry of Apollo 16 and 17 samples: Bulk composition, late stage accumulation and early differentiation of the Moon. Proc. Lunar Sci. Conf. 5th, 1307-1335.
261	Wanke H., Palme H., Kruse H., Baddenhausen H., Cendales M., Dreibus G., Hofmeister H., Jagoutz E., Palme C., Spettel B., and Thacker R. (1976) Chemistry of lunar highland rocks: A refined evaluation of the composition of the primary matter. Proc. Lunar Sci. Conf. 7th, 3479-3499.
262	Wanke H., Rieder R., Baddenhausen H., Spettel B., Teschke F., Quijano-Rico M., and Balacesu A. (1970) Major and trace elements in lunar material. Proc. Apollo 11 Lunar Sci. Conf., 1719-1727.
263	Wanless R.K., Loveridge W.D., and Stevens R.D. (1970) Age determinations and isotopic abundance measurements on lunar samples (Apollo 11). Proc. Lunar Sci. Conf. 1st, 1729-1739.
264	Warner J.L. (1971) Continuing compilation of Apollo chemical, age, and modal information. MSC Curator's Office (unpublished), published in Brett R., Butler P., Meyer C., Reid A.M., Takeda H., and Williams R. (1971) Apollo 12 igneous rocks 12004, 12008, 12009, and 12022: A mineralogical and petrological study. Proc. Lunar Sci. Conf. 2nd, 301-317.
265	Warner R.D., Keil K., Muralli A.V., and Schmitt R.A. (1975) Petrogenetic relationships among Apollo-17 mare basalts. In Papers Presented to the Conference of the Origins of Mare Basalts and Their Implications for Lunar Evolution, p. 179-183. The Lunar Science Institute, Houston.
266	Warner R.D., Keil. K., Prinz M., Laul J.C., Murali A.V., and Schmitt R.A. (1975) Mineralogy, petrology, and chemistry of mare basalts from Apollo 17 rake samples. Proc. Lunar Sci. Conf. 6th, 193-220.
267	Warner R.D., Taylor G.J., Conrad G.H., Northrop H.R., Barker S., Keil K., Ma M.-S., and Schmitt R.A. (1979) Apollo 17 high-Ti mare basalts: New bulk compositional data, magma types, and petrogenesis. Proc. Lunar Planet. Sci. Conf. 10th, 225-247.
268	Warner R.D., Taylor G.J., Keil K., Ma M.-S., and Schmitt R.A. (1980) Aluminous mare basalts: New data from Apollo 14 coarse fines. Proc. Lunar Planet. Sci. Conf. 11th, 87-104.
269	Warren P.H. and Jerde E.A. (1990) Olivine-porphyritic vitrophyre 12024,15: A sample of the margin of a lunar lava flow. Lunar Planet. Sci. XXI, 1293-1294.
270	Warren P.H. and Wasson J.T. (1978) Compositional-petrographic investigation of pristine non-mare rocks. Proc. Lunar Planet. Sci. Conf. 9th, 185-217.
271	Warren P.H., Afiattalab F., and Wasson J.T. (1978) Investigation of unusual KREEPy samples: Pristine rock 15386, Conce Crater soil fragments 14143, and 12023, a typical Apollo 12 soil. Proc. Lunar Planet. Sci. Conf. 9th, 653-660.
272	Warren P.H., Jerde E.A., and Kallemeyn G.W. (1987) Pristine Moon rocks" A "large" felsite and a metal-rich ferroan anorthosite. Proc. Lunar Planet. Sci. Conf. 17th in J. Geophys. Res. 92, E303-E313.
273	Warren P.H., Jerde E.A., and Kallemeyn G.W. (1990) Pristine Moon rocks: An Alkali anorthosite with coarse augite exsolution from plagioclase, a magnesian harzburgite, and other oddities. Proc. Lunar Planet. Sci. Conf. 20th, 31-59.
274	Warren P.H., Kallemeyn G.W., and Kyte F.T. (1997) Siderophile element evidence indicates that Apollo 14 high-Al mare basalts are not impact melts. Lunar Planet. Sci. XXVIII, 1501-1502.
275	Warren P.H., Shirley D.N., and Kallemeyn G.W. (1986) A potpourri of pristine Moon rocks, inclusing a VHK mare basalt and a unique, augite-rich Apollo 17 anorthosite. Proc. Lunar Planet. Sci. Conf. 16th in J. Geophys. Res. 91, D319-D330.
276	Warren P.H., Taylor G.J., Keil K., Kallemeyn G.W., Shirley D.N., and Wasson J.T. (1983) Seventh foray: Whitlockite-rich lithologies, a diopside-bearing troctolitic anorthosite, ferroan anorthosites, and KREEP. Proc. Lunar Planet. Sci. Conf. 14th, in J. Geophys. Res. 88, B151-B164.
277	Wasserburg G.J. and Papanastassiou D.A. (1971) Age of an Apollo 15 mare basalt: Lunar crust and mantle evolution. Earth Planet. Sci. Lett. 13, 97-104.
278	Wasson J.T. and Baedecker P.A. (1970) Ga, Ge, In, Ir, and Au in lunar terrestrial and meteoritic basalts. Proc. Lunar Sci. Conf. 1st, 1741-1750.
279	Wentworth S., Taylor G.J., Warner R.D., Keil K., Ma M.-S., and Schmitt R.A. (1979) The unique nature of Apollo 17 VLT mare basalts. Proc. Lunar Planet. Sci. Conf. 10th, 207-223.
280	Willis J.P., Ahrens L.H., Danchin R.V., Erlank A.J., Gurney J.J., Hofmeyr P.K., McCarthy T.S., and Orren M.J. (1971) Some inter-element relationships between lunar rocks and fines, and stony meteorites. Proc. Lunar Sci. Conf. 2nd, 1123-1138.
281	Willis J.P., Erlank A.J., Gurney J.J., and Ahrens L.H. (1972) Geochemical features of Apollo 15 materials. In The Apollo 15 Lunar Samples (Chamberlain J.W. and Watkins C., eds.), 268-271. The Lunar Science Institute, Houston, TX.
282	Willis J.P., Erlank A.J., Gurney J.J., Theil R.H., and Ahrens L.H. (1972) Major, minor, and trace element data for some Apollo 11, 12, 14, and 15 samples. Proc. Lunar Sci. Conf. 3rd, 1269-1273.
283	Wolf R., Woodrow A., and Anders E. (1979) Lunar basalts and pristine highland rocks: Comparison of siderophile and volatile elements. Proc. Lunar Planet. Sci. Conf. 10th, 2107-2130.

A3

Appendix 3: Results of Zn isotope analysis by MC-ICPMS

3a Results of Zinc Isotope Analyses (Lunar Samples and USGS reference materials)

3b Compilation of all lunar zinc isotope data (this study and published)

Appendix 3
Zinc Isotope Measurements

		Run 1	Run 2	Run 3	Run 4	Average			Relative to JMC-Lyon	
Generic	Specific	δ^{66}Zn (‰)	δ^{66}Zn (‰)	δ^{66}Zn (‰)	δ^{66}Zn (‰)	δ^{66}Zn (‰)	2SD	n	δ^{66}Zn (‰)	2SD
10017	400	-6.54	-6.60	-6.49		-6.54	0.11	3	-6.42	0.15
10017	405	-9.83	-9.60	-9.72	-9.67	-9.71	0.19	4	-9.59	0.23
10020	255	1.42	1.43	1.44		1.43	0.02	3	1.55	0.06
10044	655	1.15	1.01	1.04		1.07	0.14	3	1.19	0.18
12018	277	-0.89	-0.89	-0.87		-0.88	0.02	3	-0.76	0.06
12054	13	0.92	0.99	1.02		0.98	0.10	3	1.10	0.14
12054	146	1.80	1.85	1.76		1.80	0.09	3	1.92	0.13
12054	150	1.73	1.63			1.68	0.14	2	1.80	0.18
12063	343	1.68				1.68	0.09*	1	1.80	0.13*
14053	305	-1.10	-1.13			-1.12	0.04	2	-1.00	0.08
15016	240	-1.57	-1.63	-1.64		-1.61	0.08	3	-1.49	0.12
15535	165	1.31	1.48	1.43		1.41	0.17	3	1.53	0.21
15556	258	1.43	1.41			1.42	0.03	2	1.54	0.07
70215	389	1.37	1.34	1.32		1.34	0.05	3	1.46	0.09
70255	56	1.17	1.10	1.04		1.10	0.13	3	1.22	0.17
71135	34	1.53	1.57	1.52	1.49	1.53	0.07	4	1.65	0.11
71546	22	1.49	1.49	1.29		1.42	0.23	3	1.54	0.27
74275	355	1.45	1.54	1.58		1.52	0.13	3	1.64	0.17
75035	249	0.50	1.00			0.75	0.71	2	0.87	0.75
BCR2	1	0.21	0.18			0.20	0.04	2	0.32	0.08
BCR2	2	0.17	0.18			0.18	0.01	2	0.30	0.05
BHVO2	1	0.24	0.23			0.24	0.01	2	0.36	0.05
BHVO2	2	0.2	0.21			0.21	0.01	2	0.33	0.05
BIR1a	1	0.15	0.09			0.12	0.08	2	0.24	0.12
BIR1a	2	0.08	0.14			0.11	0.08	2	0.23	0.12
					Average BCR2	0.19	0.03	4	0.31	0.07
					Average BHVO2	0.22	0.04	4	0.34	0.08
					Average BIR1a	0.12	0.07	4	0.24	0.11

*Error is the 2SD of the London-Zn bracketing standards in this measurement session.

Note that run data is reported to London-Zn. Data is converted to JMC-Lyon at e

Literature values for USGS reference materials (reported relative to JMC-Lyon a

	Bridgestock et al. (2014) - Double Spiked			*Moynier et al. (2017) - Recommended Values*	
	δ^{66}Zn (‰)	2SD	n	δ^{66}Zn (‰)	2SE
BCR2	0.28	0.09	5	0.25	0.03
BHVO2	0.31	0.23	5	0.28	0.04
BIR1a	0.27		2	0.26	0.06

Appendix 3b: Compilation of all Zn isotope data for lunar samples

Sample	Sub	Mission	Sub-type	Ref.	[Zn] (ppm)	±	$\delta^{66}Zn_{JMC\text{-}LYON}$ (‰)	±
Lunar Basalts								
10017	52	A11	HK	Herzog 09	12.1	1.2	-5.42	0.06
10017	400	A11	HK	this study	6.7	0.1	-6.42	0.15
10017	405	A11	HK	this study	5.5	0.1	-9.59	0.23
10022	47	A11	HK	Herzog 09	2.2	0.2	1.24	0.08
10024	108	A11	HK	Herzog 09	2.8	0.3	1.40	0.10
10049		A11	HK	Hopkins 14	9.6	1.0	2.34	0.15
10057		A11	HK	Kato 15	5.4	0.5	1.80	0.08
10003		A11	LK	Kato 15	1.4	0.1	1.47	0.10
10020	255	A11	LK	this study	1.3	0.0	1.55	0.06
10044	655	A11	LK	this study	2.1	0.0	1.19	0.18
12054	13	A12	Glass//Ilmenite Basalt		1.5	0.0	1.10	0.14
12005		A12	Ilmenite basalt	Kato 15	0.8	0.1	-0.22	0.10
12016		A12	Ilmenite basalt	Paniello 12	0.9	0.1	1.56	0.10
12054	146	A12	Ilmenite basalt	this study	0.8	0.0	1.92	0.13
12054	150	A12	Ilmenite basalt	this study	0.8	0.0	1.80	0.18
12063	343	A12	Ilmenite basalt	this study	0.8	0.0	1.80	0.13
12063		A12	Ilmenite basalt	Paniello 12	1.0	0.1	1.18	0.10
12002		A12	Olivine basalt	Paniello 12	1.5	0.2	0.84	0.10
12018	277	A12	Olivine basalt	this study	1.5	0.0	-0.76	0.06
12018		A12	Olivine basalt	Paniello 12	1.3	0.1	-3.10	0.08
12012		A12	Olivine Basalt	Kato 15	1.0	0.1	1.62	0.10
12040		A12	Olivine Basalt	Kato 15	0.8	0.1	1.58	0.10
12011		A12	Pigeonite Basalt	Hopkins 14	0.8	0.1	1.93	0.15
12021		A12	Pigeonite basalt	Paniello 12	1.4	0.1	1.15	0.10
12052		A12	Pigeonite basalt	Paniello 12	1.1	0.1	1.34	0.10
12065		A12	Pigeonite basalt	Paniello 12	1.1	0.1	1.52	0.10
14053	305	A14	Mare Basalt (Al-rich)	this study	1.6	0.0	-1.00	0.08
14053		A14	Mare Basalt (Al-rich)	Kato 15	2.7	0.3	-0.97	0.10
15016	240	A15	Ol-norm Basalt	this study	1.0	0.0	-1.49	0.12
15016		A15	Ol-norm Basalt	Kato 15	2.1	0.2	-1.47	0.10
15016		A15	Ol-norm Basalt	Hopkins 14	1.0	0.1	-0.43	0.15
15535	165	A15	Ol-norm Basalt	this study	1.0	0.0	1.53	0.21
15555		A15	Ol-norm Basalt	Paniello 12	1.1	0.1	1.56	0.10
15556	258	A15	Ol-norm Basalt	this study	0.9	0.0	1.54	0.07
15557		A15	Ol-norm Basalt	Paniello 12	0.6	0.1	1.34	0.10
15499		A15	Pigeonite Basalt	Kato 15	0.9	0.1	1.23	0.10
15058		A15	Qtz-norm basalt	Paniello 12	1.7	0.2	1.41	0.10
15065		A15	Qtz-norm basalt	Paniello 12	1.1	0.1	1.33	0.10
70035		A17	Type A	Hopkins 14	1.7	0.2	1.03	0.15
70255	56	A17	Type A	this study	1.6	0.0	1.22	0.17
75035	249	A17	Type A	this study	1.0	0.0	0.87	0.75
75055	118	A17	Type A	Herzog 09	1.3	0.1	1.53	0.10
70135		A17	Type B/Type A	Kato 15	1.8	0.2	1.13	0.10
70135		A17	Type B/Type A	Hopkins 14	1.7	0.2	1.54	0.15
71546	22	A17	Type B/Type A	this study	1.8	0.0	1.54	0.27
70017		A17	Type B	Kato 15	2.7	0.3	1.20	0.10
70215	323	A17	Type B	Herzog 09	0.8	0.1	1.44	0.10
70215	389	A17	Type B	this study	2.1	0.0	1.46	0.09
71055	234	A17	Type B	Herzog 09	2.1	0.2	1.35	0.10
71135	34	A17	Type B	this study	1.5	0.0	1.65	0.11
75075	193	A17	Type B?	Herzog 09	2.0	0.2	1.90	0.10
75075	193	A17	Type B?	Hopkins 14	1.4	0.1	1.51	0.15
74255	191	A17	Type C	Herzog 09	1.2	0.1	1.77	0.10
74275	318	A17	Type C	Moynier 06			0.46	0.82
74275	355	A17	Type C	this study	1.2	0.0	1.64	0.17
LAP 02205			Meteorite-Olivine basalt	Paniello 12		0.0	1.20	0.20

Appendix 3b: Compilation of all Zn isotope data for lunar samples

Sample	Sub	Mission	Sub-type	Ref.	[Zn] (ppm)	±	$\delta^{66}Zn_{JMC\text{-}LYON}$ (‰)	±
Breccias								
Rusty Rock								
66095	Average		Average bulk	Day17	236	24	-13.63	0.53
Ferroan anorthosite								
62255			Anorthosite (w/melt)	Kato 15	1.2	0.12	0.00	0.10
60015			Cataclastic Anorthosite	Kato 15	1.4	0.14	-0.24	0.10
65315			Cataclastic Anorthosite	Kato 15	75.0	7.5	-11.37	0.10
15415			Ferroan Anorthosite	Kato 15	0.6	0.06	4.24	0.10
67955			Nortic Anorthosite	Kato 15	5.9	0.59	-6.98	0.10
Mg suite								
72415			Cataclastic Dunite	Kato 15	2.6	0.26	6.27	0.10
Alkali suite								
77215			Cataclastic Norite	Kato 15	3.6	0.36	3.04	0.10
Lunar PGB								
15426		15	Green Glass	Kato 15	53	5	-0.98	0.10
74001	2207	17	Total	H09	129	13	-4.05	0.20
74220	average	17		M06, H09	177	18	-3.53	0.48
Lunar Soils								
14163	868		Soil	Moynier 06	33	3	2.59	0.20
15021	169		Bulk soil	Herzog 09	21	2.1	4.88	0.20
15231	200		Soil	Moynier 06			6.39	0.20
15231	90		Bulk soil	Herzog 09	12	1.2	5.32	0.20
64501	226		Soil	Moynier 06	24	2	4.41	0.20
66041	131		Soil	Moynier 06			4.17	0.20
68841	47		Soil	Moynier 06			2.18	0.20
69941	53		Soil	Moynier 06			3.40	0.20
70011	209		Soil	Moynier 06	28	3	3.44	0.20
70181	170		Bulk soil	Herzog 09	32.9	3.29	3.14	0.20
72501	226		Soil	Moynier 06	31	3	4.45	0.20
75081	688		Soil	Moynier 06	25	3	4.07	0.20
76501	184		Soil	Moynier 06			3.79	0.20
65701			Soil	Kato 15	25	2	4.26	0.20
78221			Soil	Kato 15	32	3	5.42	0.20
79221	143		Bulk soil	Herzog 09	31.8	3.18	5.08	0.20
15041			Trench Soil	Kato 15	17	2	6.35	0.20

References

Day, J.M.D., Moynier, F., Shearer, C.K., 2017. Late-stage magmatic outgassing from a volatile-depleted Moon 114, 9547–9551. https://doi.org/10.1073/pnas.1708236114

Hopkins, S.S., Larner, F., Barling, J., Halliday, A. N. 2014. Copper and zinc stable isotopes and the formation of the Moon. *Unpublished Masters Thesis. University of Oxford.*

Herzog, G.F., Moynier, F., Albarède, F., Berezhnoy, A.A., 2009. Isotopic and elemental abundances of copper and zinc in lunar samples, Zagami, Pele's hairs, and a terrestrial basalt. Geochim. Cosmochim. Acta 73, 5884–5904. https://doi.org/10.1016/j.gca.2009.05.067

Kato, C., Moynier, F., Valdes, M.C., Dhaliwal, J.K., Day, J.M.D.D., Kato, C., Moynier, F., 2015. Extensive volatile loss during formation and differentiation of the Moon. Nat. Commun. 6, 1–4. https://doi.org/ARTN 7617 10.1038/ncomms8617

Moynier, F., Albarède, F., Herzog, G.F., 2006. Isotopic composition of zinc, copper, and iron in lunar samples. Geochim. Cosmochim. Acta 70, 6103–6117. https://doi.org/10.1016/j.gca.2006.02.030

Paniello, R.C., Day, J.M.D.D., Moynier, F., 2012. Zinc isotopic evidence for the origin of the Moon. Nature 490, 376–+. https://doi.org/10.1038/nature11507

A4

Appendix 4: Supplementary Figures

Contents:

Supplementary Figures for Chapter 4

Figure S1 – REE plots for lunar sample suite

Figure S2 – Bivariate plots of V and major elements for lunar mare basalts

Figure S3 **–** [V] and $\delta^{51}V$ in primary hosts of V in lunar samples

Figure S4 **–** $\delta^{51}V$ versus stable Cr and Fe isotope data from literature.

Figure S5 **–** $\delta^{51}V$ versus neutron-sensitive $\varepsilon^{50}Ti$

Figure S6 – $\delta^{51}V$ versus exposure age multiplied by [target]/[V]

Figure S7 – The sum of cross-sections for each reaction pathway for ^{50}V and ^{51}V

High Quality Figures from Chapter 4

Figure 4.1

Figure 4.2

Figure 4.3

Figure 4.4

Figure 4.5

Figure 4.6

Figure 4.7

Figure 4.8

Figure 4.9

Figure 4.10

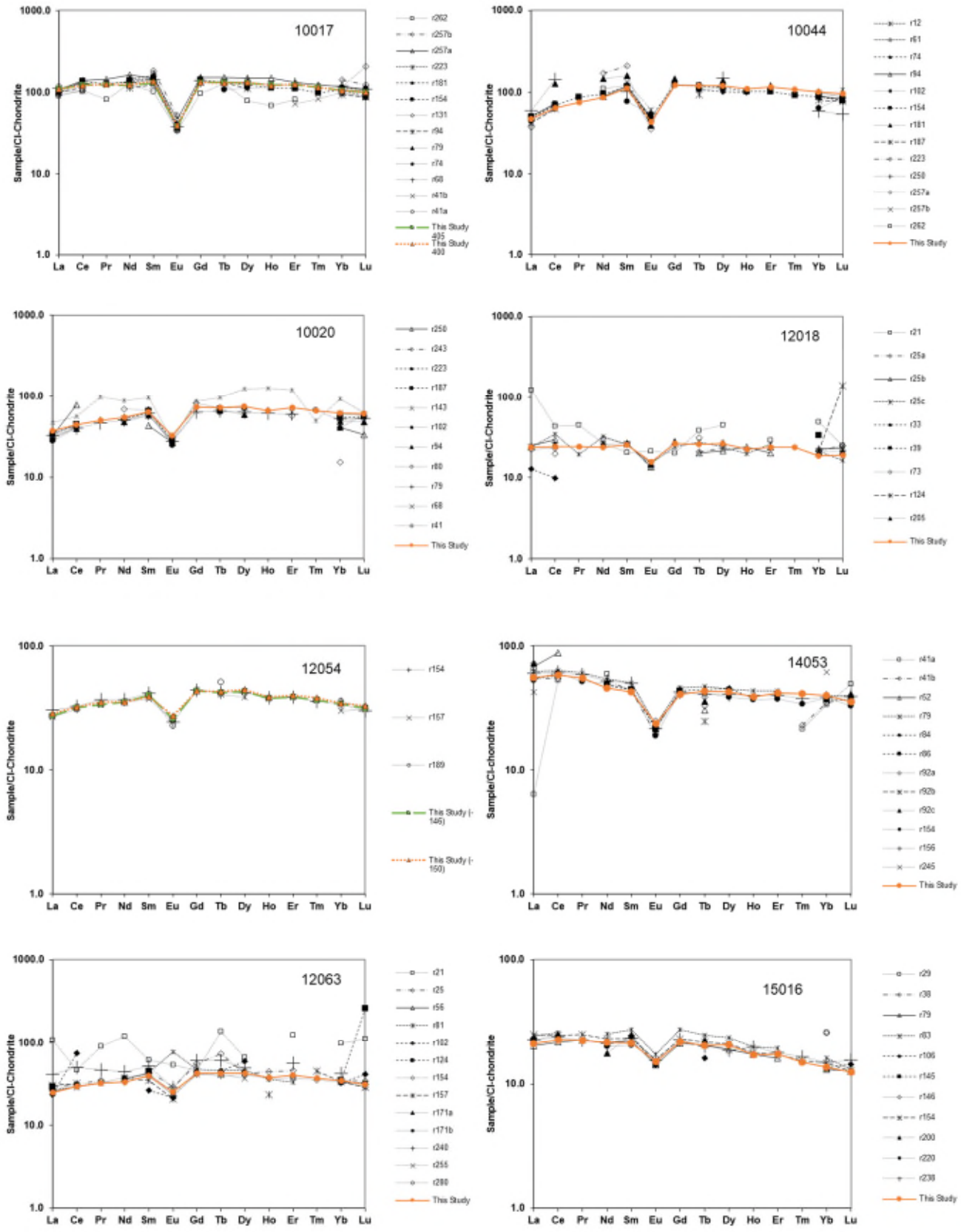


Figure S1 – REE plots for lunar sample suite *(continued onto next page).*

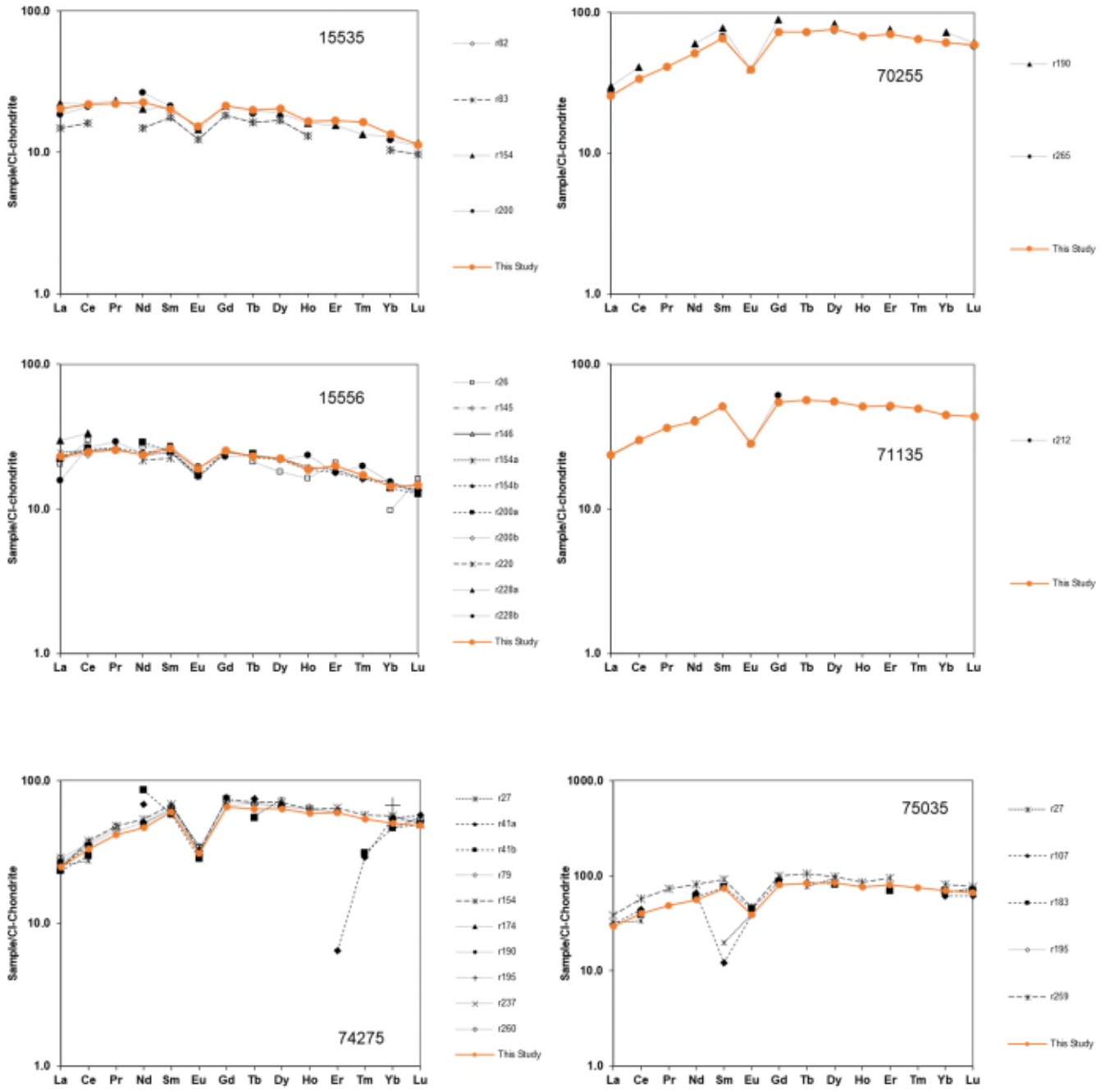


Figure S1 – CI-normalised REE plots for lunar sample suite verus previous studies

*Comparison of measured REE concentrations (normalised to CI, Anders & Grevesse, 1989) showing the similarity in REE patterns obtained for samples in this study to those made by previous researchers (see **Appendix 2g** for data and full references). Orange lines denotes results of ICPMS analyses in this study, black dashed lines represent previous work. References in legend and in **Appendix 2h.***

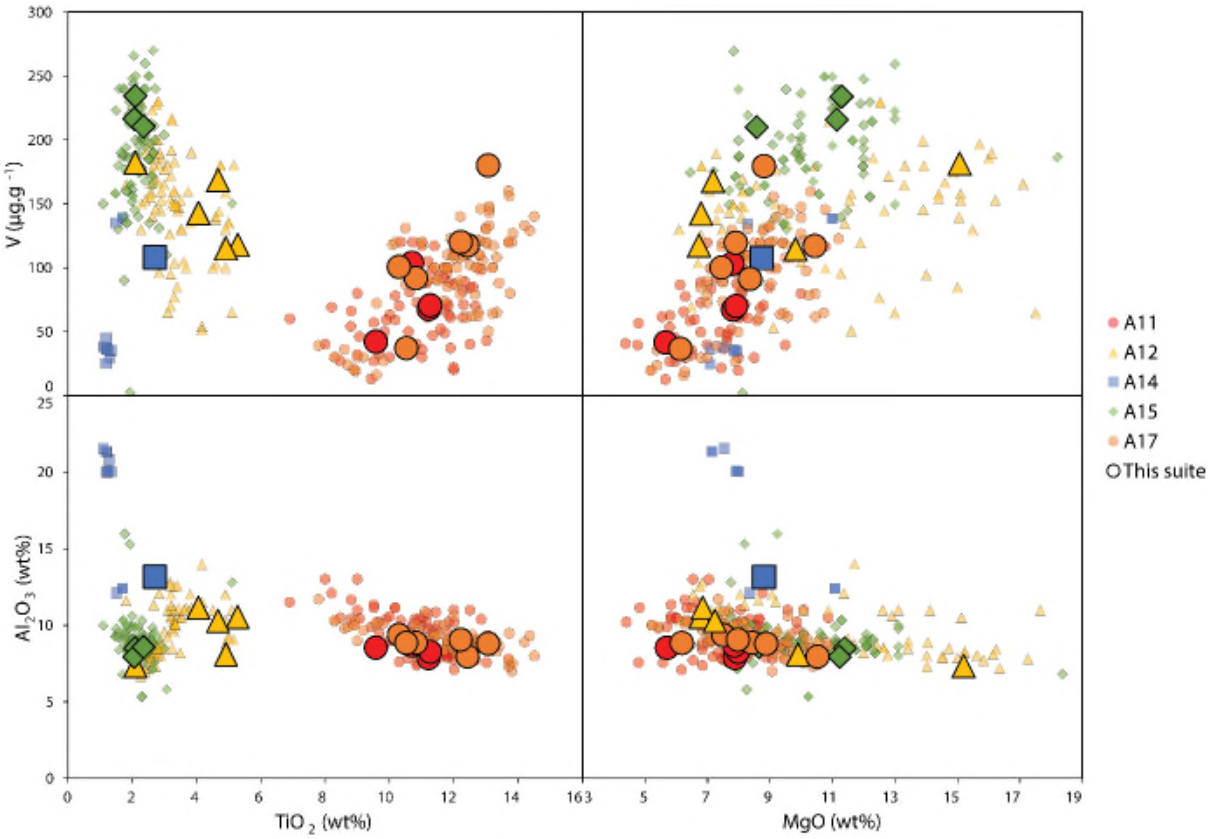


Figure S2 – Bivariate plots of V and major elements for lunar mare basalts

*Bi-variate plots summarising the differences in geochemical compositions between the lunar mare basalt suites. Individual datapoints from previous studies of Apollo lunar mare basalts from Apollo 11, 12, 14, 15, 17 (to reflect the suite in this study) are shown. Of significance, V appears to follow TiO_2 concentrations in the high-Ti basalt suite. In low-Ti basalt crystallisation sequences, ilmenite is a late-forming mineral and Ti behaves relatively incompatibly throughout the early crystallisation sequences. In contrast, V can partition strongly into early-crystallising pyroxene and Cr-spinel (as V^{3+}) and partially into olivine (as V^{2+}). In high-Ti basalt melts, Ti contents are so high that significant proportions of armalcolite and ilmenite are present throughout the whole crystallisation sequence. Titanium behaves much more compatibly in these melts, and V partitions into these minerals strongly. Smaller symbols in semi-transparent represent previously-published data (**Appendix 2e**). Larger solid symbols represent the samples analysed in this study. Colours represent the different missions as follows: red (Apollo 11), yellow (Apollo 12), blue (Apollo 14), green (Apollo 15), orange (Apollo 17).*

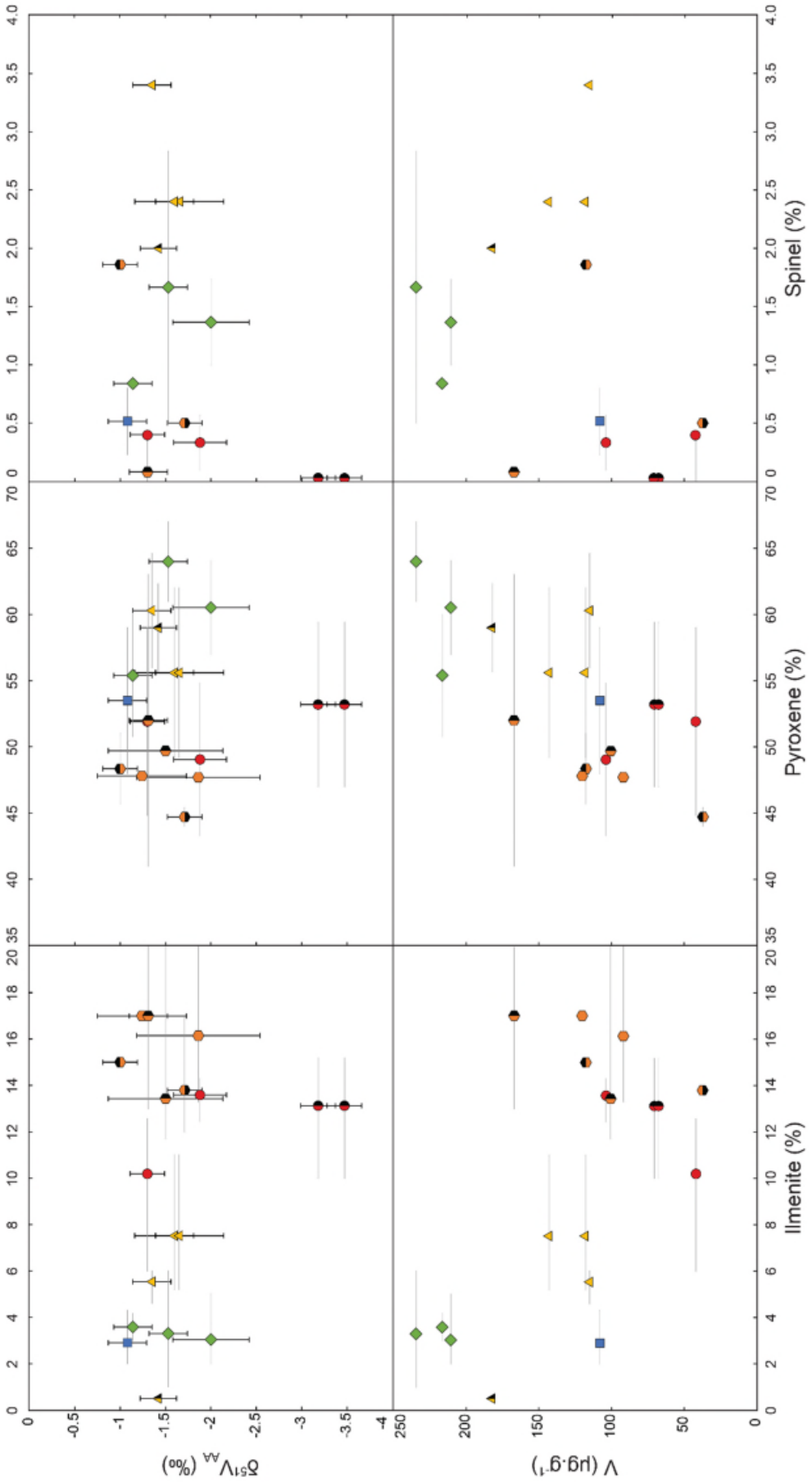


Figure S3 – [V] and $\delta^{51}V$ in primary hosts of V in lunar samples (caption overleaf)

Figure S3 – [V] and $\delta^{51}V$ in primary hosts of V in lunar samples

*Literature-reported average modal contents of the major V-hosting minerals against sample $\delta^{51}V$ and V concentrations. $\delta^{51}V$ does not correlate with the modal mineral contents. Ilmenite concentrations correlate with V concentrations in high-Ti basalts, although low-Ti basalts generally have higher V concentrations than high-Ti basalts. Vanadium concentrations show a similar pattern with ilmenite contents as with TiO_2 concentration (**Figure 4.3c**). Samples with higher pyroxene contents generally have higher V concentrations. Despite the high concentrations of V in spinel, there is a lack of systematic correlation between the proportion of this mineral and V concentration or $\delta^{51}V$. This is probably due to the relatively low spinel abundance in samples compared to V-hosting ilmenite and pyroxene. Symbols as in **Figure 4.2**. The range of reported mineral contents (where more than one previous study exists) is displayed with grey bars. See **Appendix 2b** for full literature values of sample modal mineralogy.*

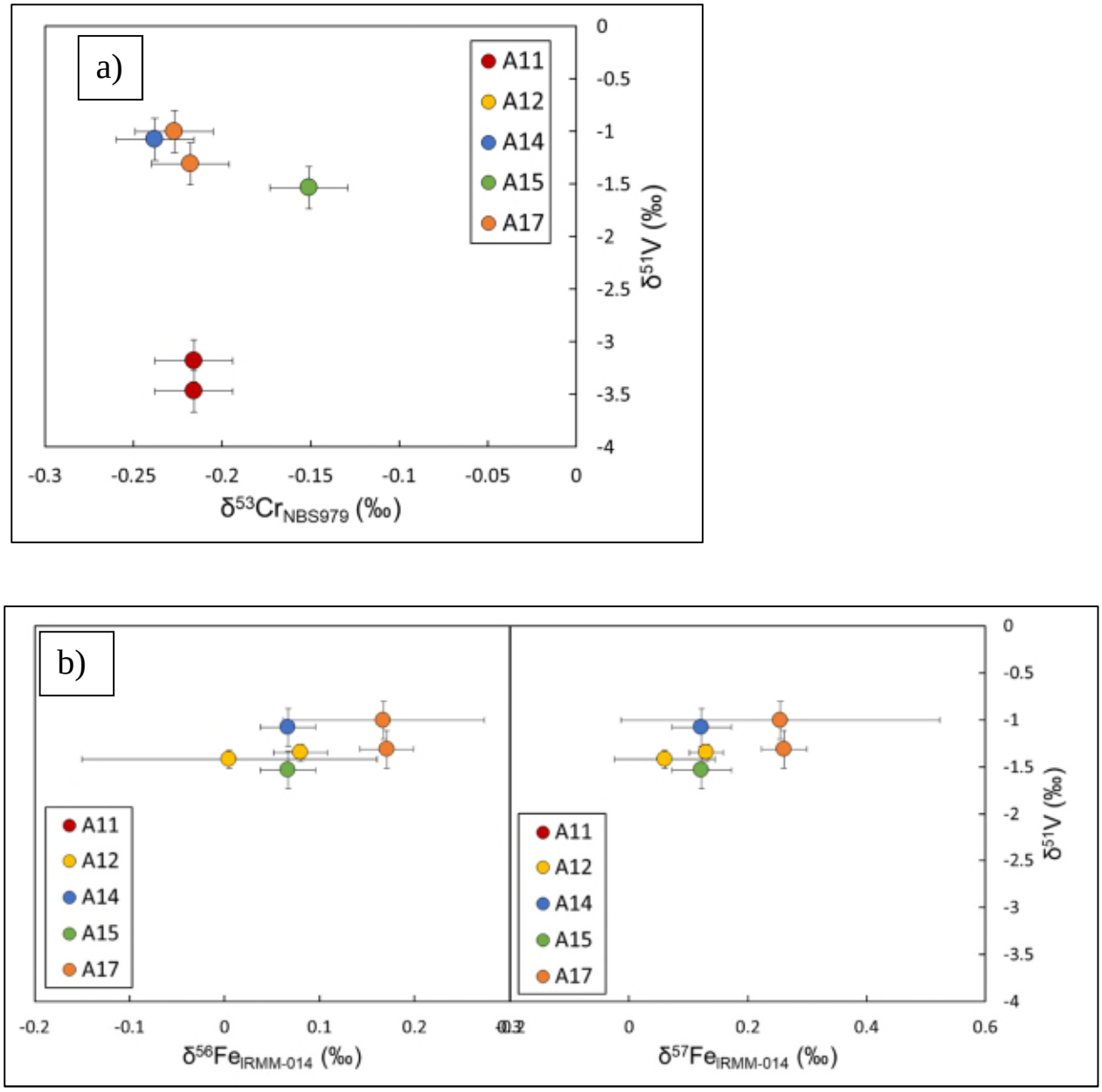


Figure S4 – $\delta^{51}V$ versus stable Cr and Fe isotope data from literature.

*Some samples have been previously measured for $\delta^{53}Cr$ (Fig S5a) and $\delta^{56,57}Fe$ (Fig S5b). Where data overlaps with samples from this set, the relationships with $\delta^{51}V$ are plotted above. Error bars on $\delta^{51}V$ (2SD) from **Table 4.1**. Chromium isotope data from Bonnand et al., (2016). Errors on $\delta^{53}Cr$ represent 2SD. Iron isotope data is compiled from Wiesli et al., (2003), Liu et al., (2010) and Sossi and Moynier, (2017). Errors represent 2SD of measurements (where only one measurement exists) or the 2SD for repeats measurements.*

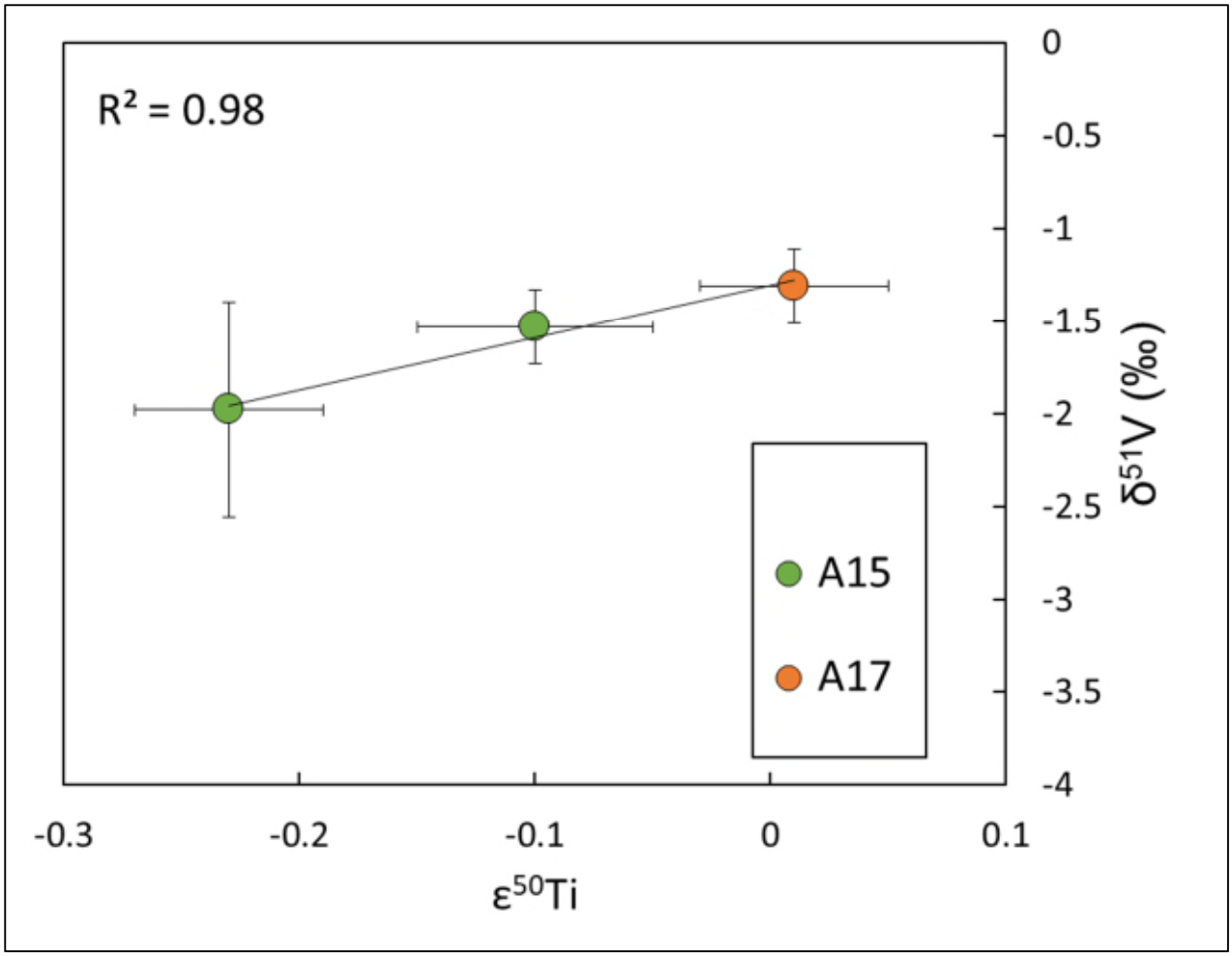


Figure S5 – $\delta^{51}V$ versus neutron-sensitive $\varepsilon^{50}Ti$

*Zhang et al., (2012) reported slight depletions (after internal normalisation to $^{49}Ti/^{47}Ti$ = 0.749766) in ^{50}Ti in lunar samples which result from neutron capture processes on target Ti. Three samples measured in that study were measured for $\delta^{51}V$ here and show a strong linear correlation. This operates in the same fashion to the correlations seen between $\delta^{51}V$ and $^{158}Gd/^{157}Gd$ and exposure age (**Figs 4.4, 4.5**) – i.e. the most exposed sample have the lighted $\delta^{51}V$ – providing further evidence for significant cosmogenic isotopic effects in V isotopes. Errors on Ti represent 95% confidence intervals on the measurements (Zhang et al., 2012).*

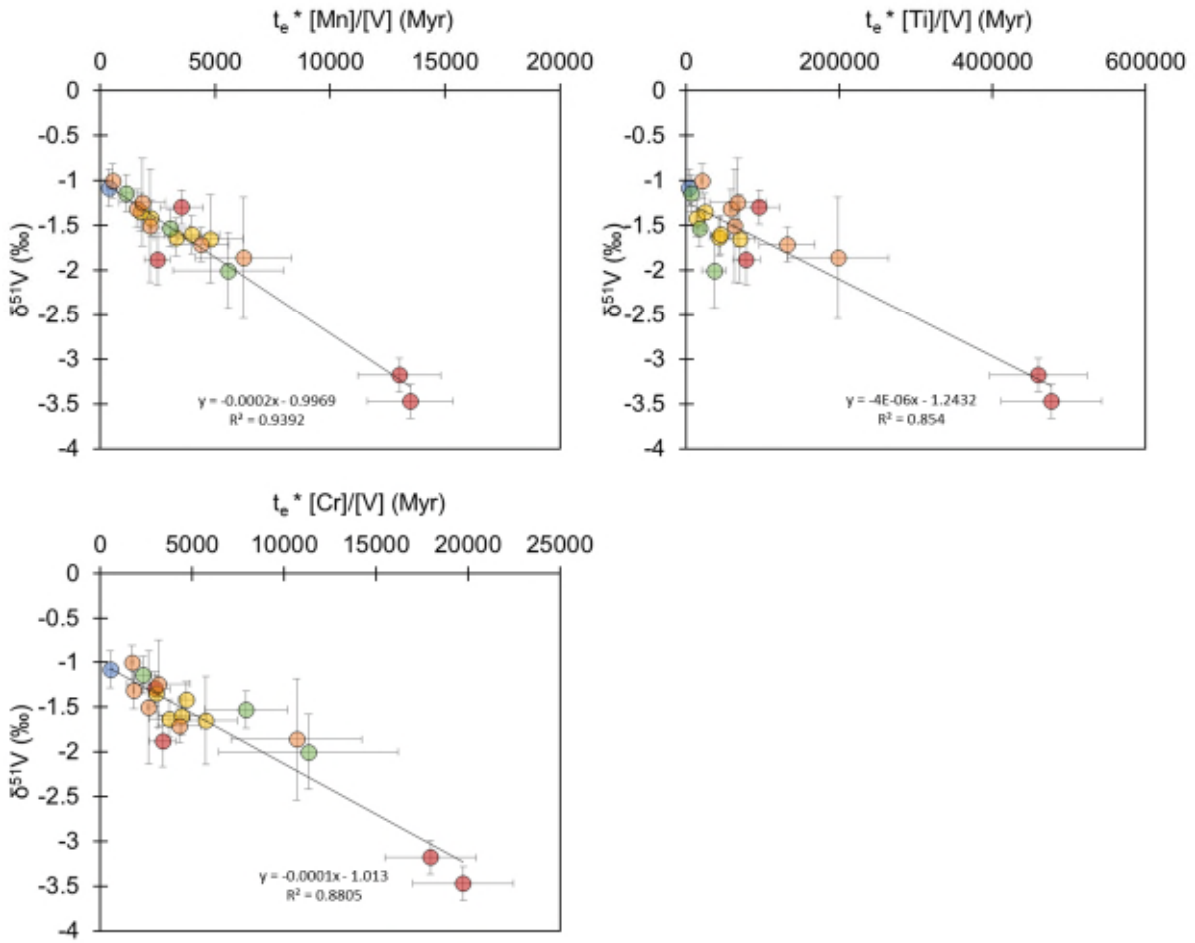


Figure S6 – δ^{51}V versus exposure age multiplied by [target]/[V]

*The linear regression between $\delta^{51}V$ and t_e * [Mn]/[V] shows a strong correlation (R^2 = 0.94). However, Mn is not likely to be the primary target element, due to its lower abundance and much lower effective cross section (**Figs 4.6, 4.7**) than iron. Despite the potential for Ti to be a target for cosmogenic isotopic effects in protons, alpha particles and neutrons (**Figs 4.6,4.7**) the correlation between $\delta^{51}V$ and t_e * [Ti]/[V] is not as strong as perhaps anticipated, suggest that either particle fluxes are not as strong in the energy ranges where Ti shows strong $\varepsilon^{51}\sigma$ deviations (~5-50MeV for protons and alpha particles), or thermal neutrons (where Ti may contribute to positive $\varepsilon^{51}\sigma$ deviations) counterbalance charged particle reactions at higher energies.*

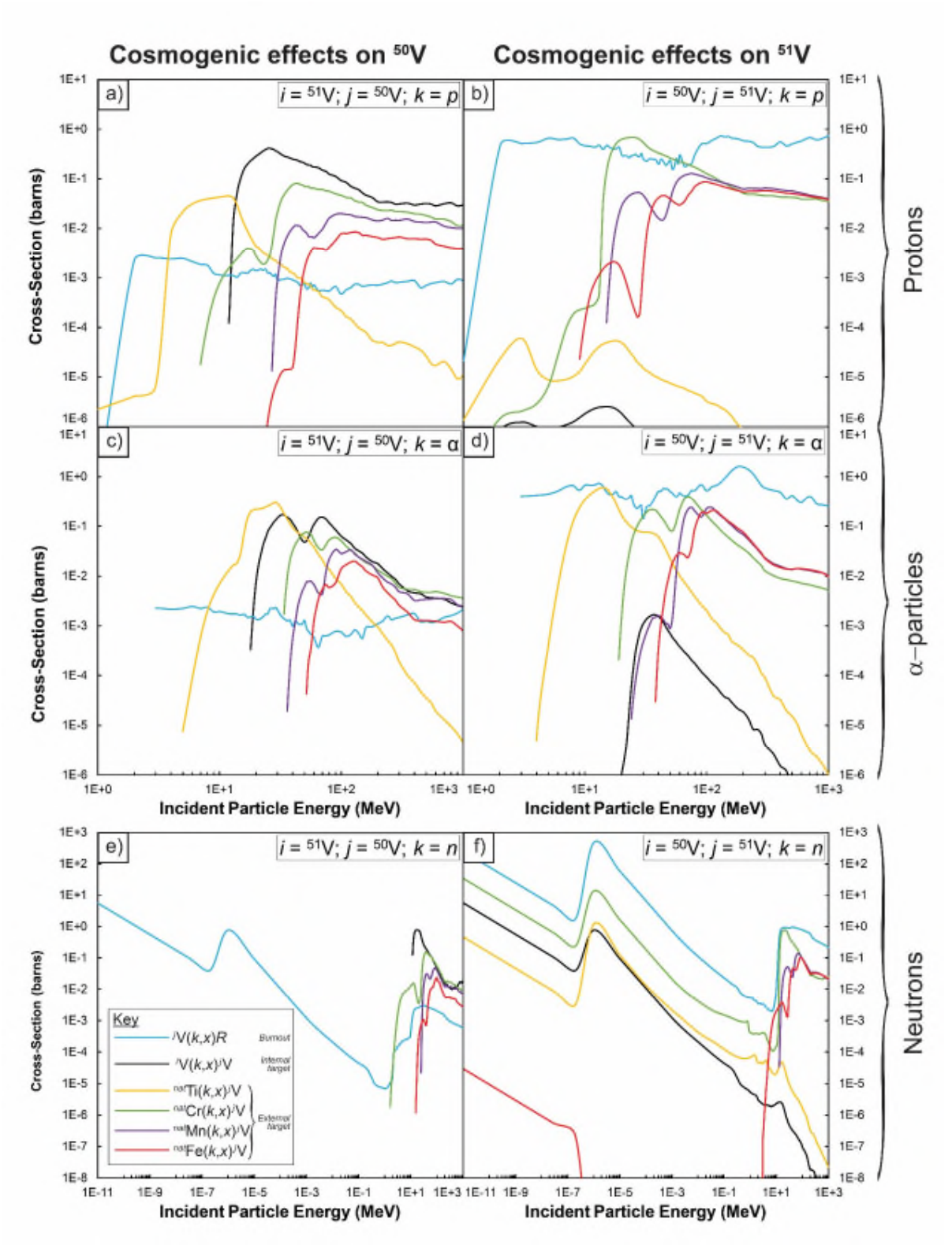


Figure S7 – *The sum of cross-sections for each reaction pathway for ^{50}V and ^{51}V prior to adjustment for sample elemental concentrations (see* ***Section 4.4.6****)*

Figure 4.1 (High-Quality)

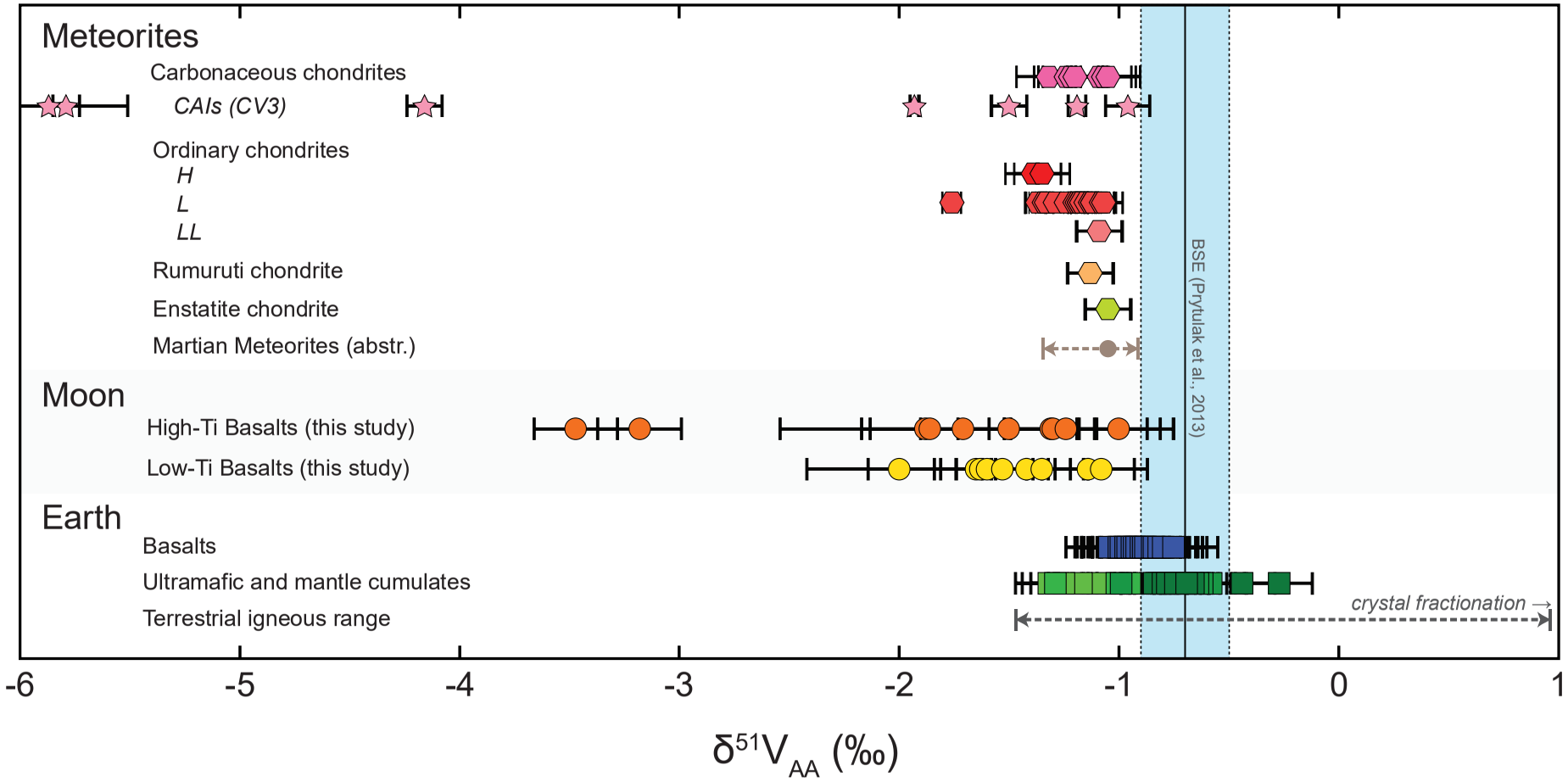
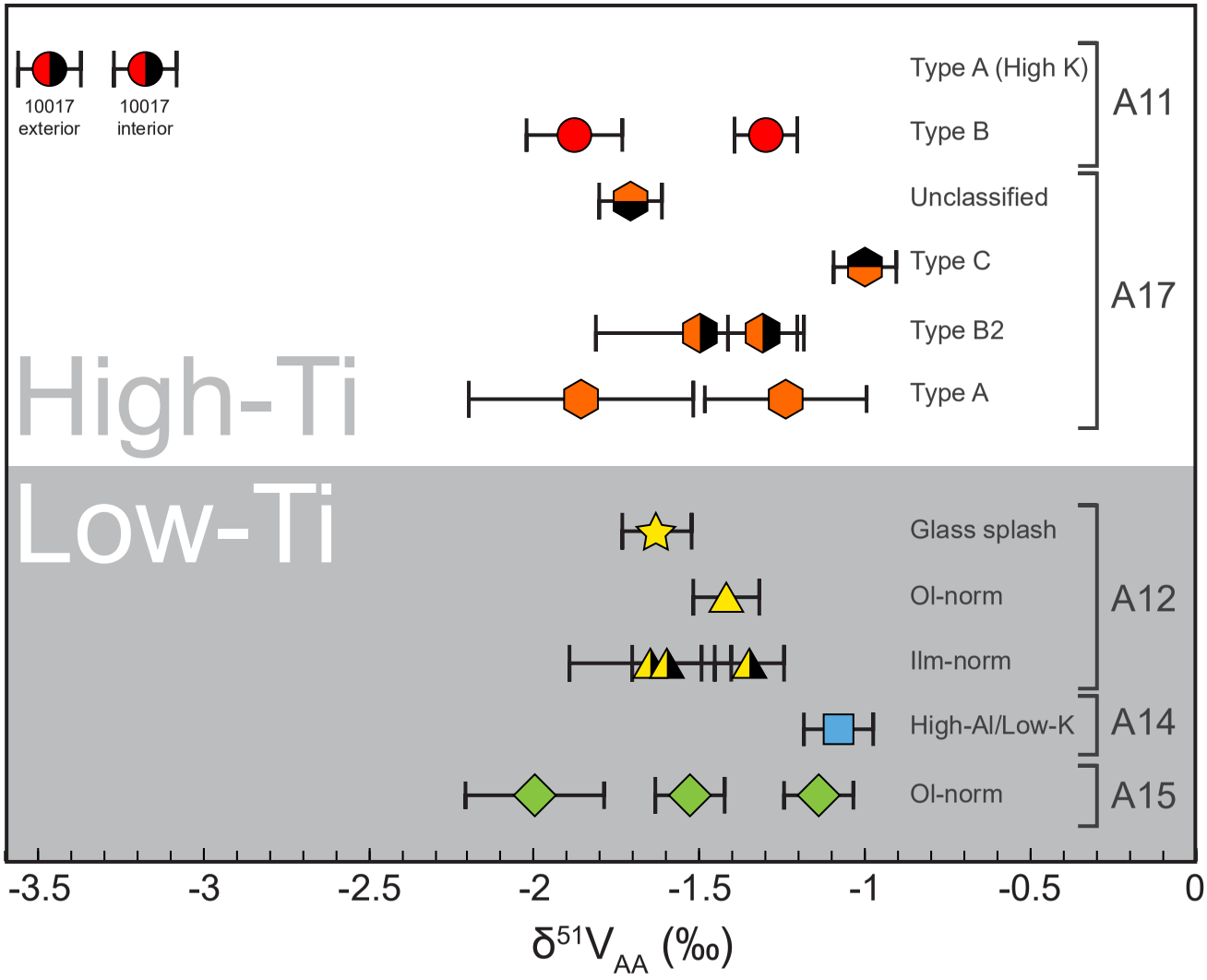


Figure 4.2 (High-Quality)



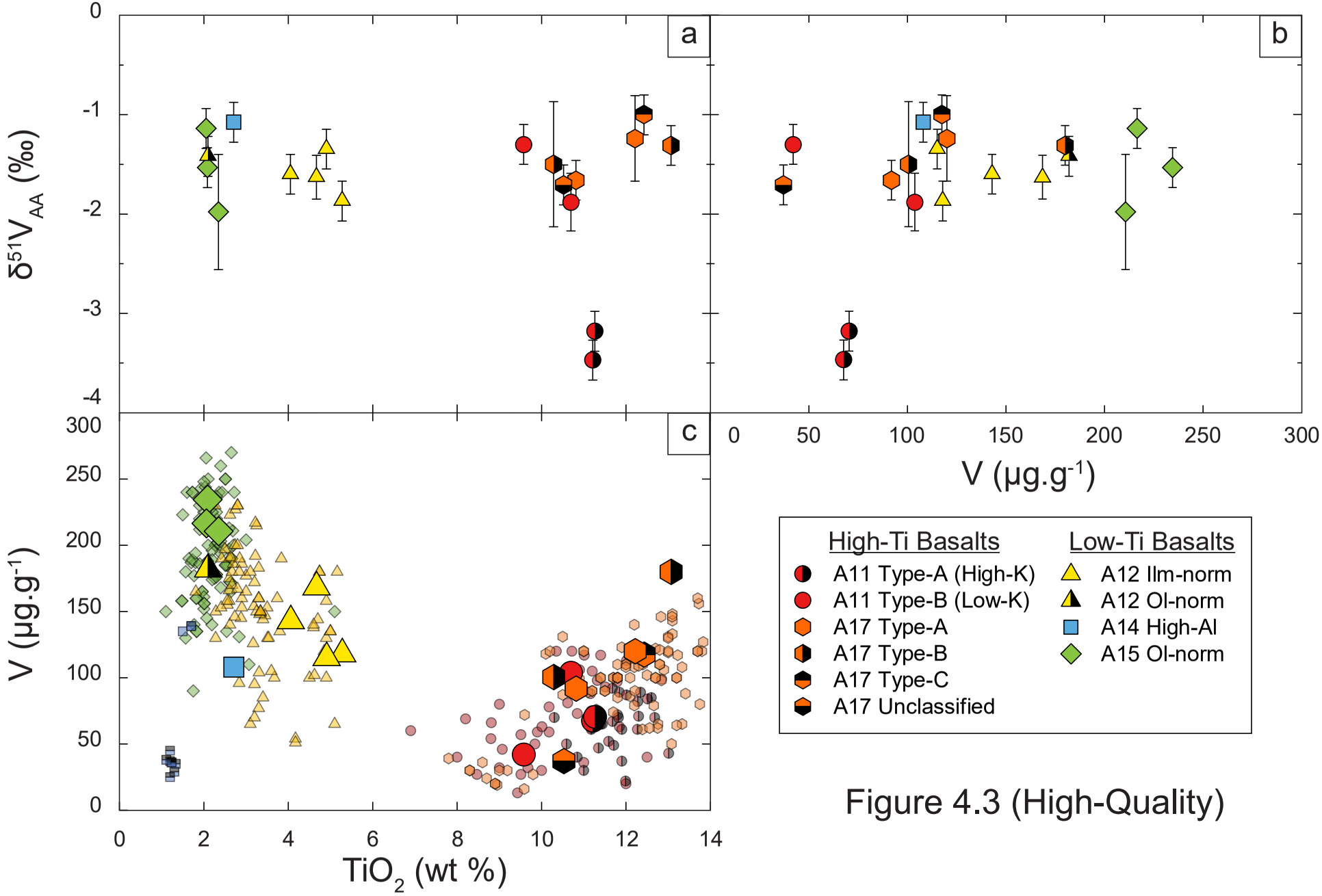


Figure 4.3 (High-Quality)

Figure 4.4 (High-Quality)

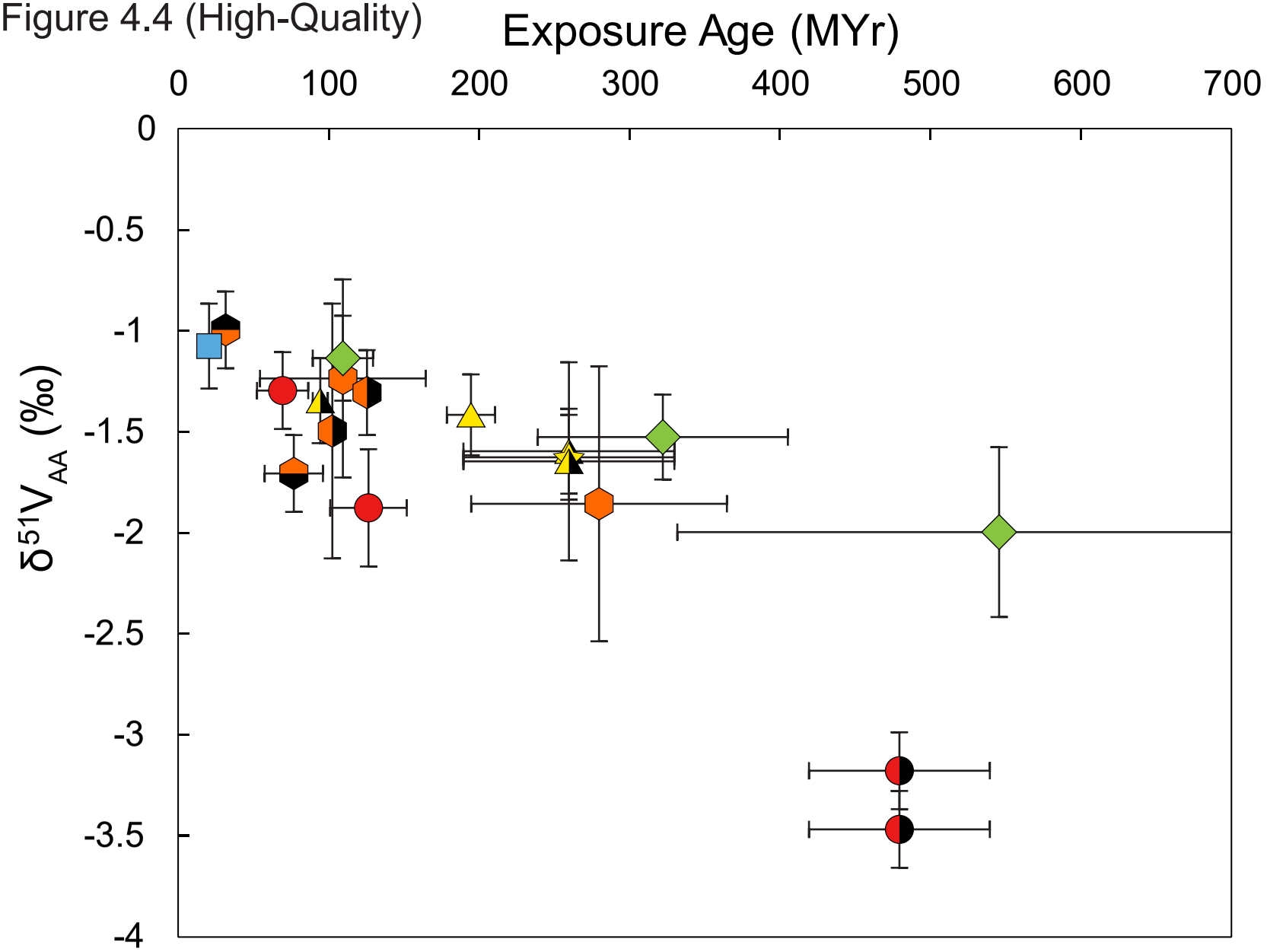


Figure 4.5 (High-Quality)

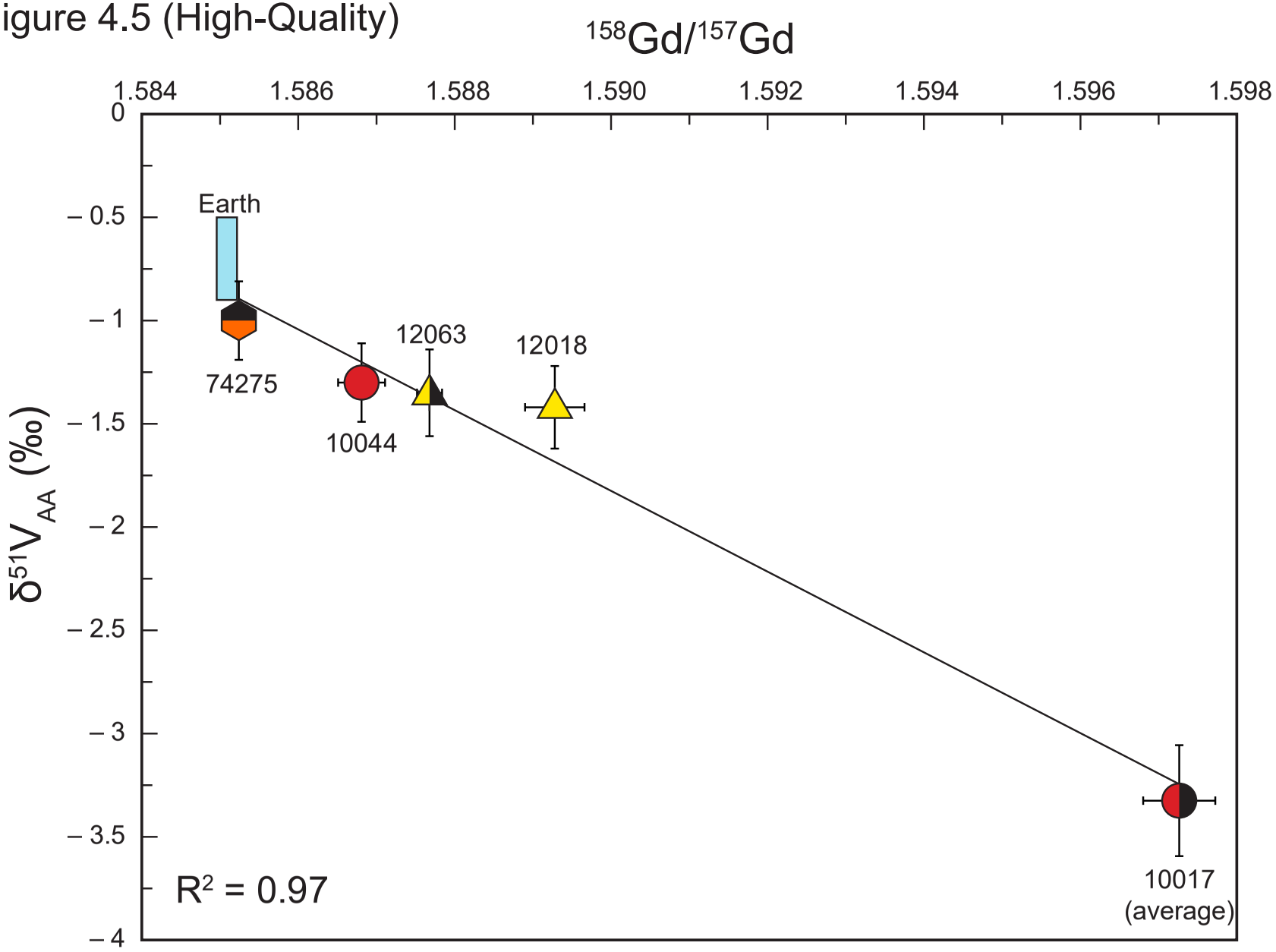


Figure 4.6 (High-Quality)

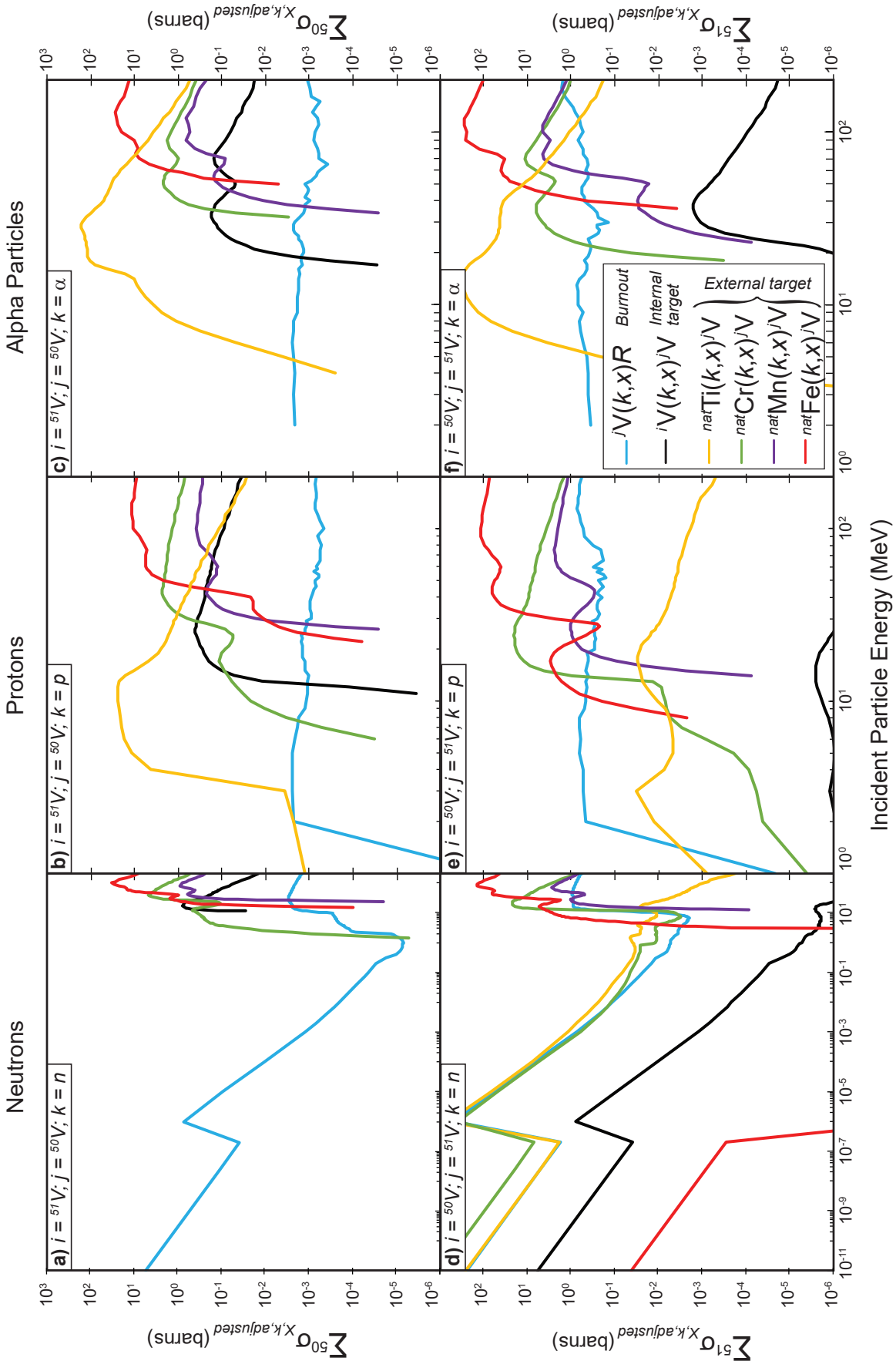


Figure 4.7 (High-Quality)

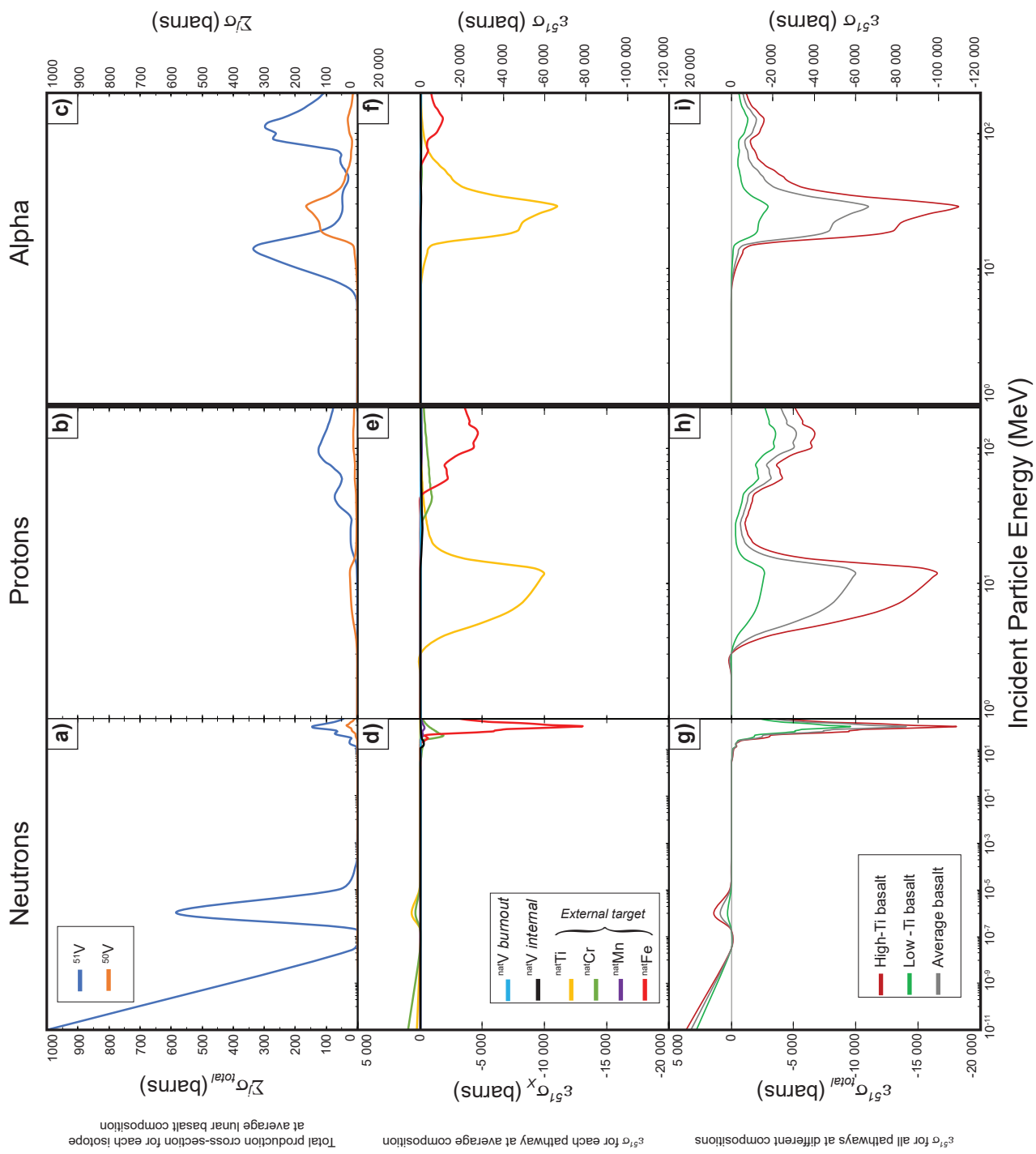


Figure 4.8 (High-Quality)

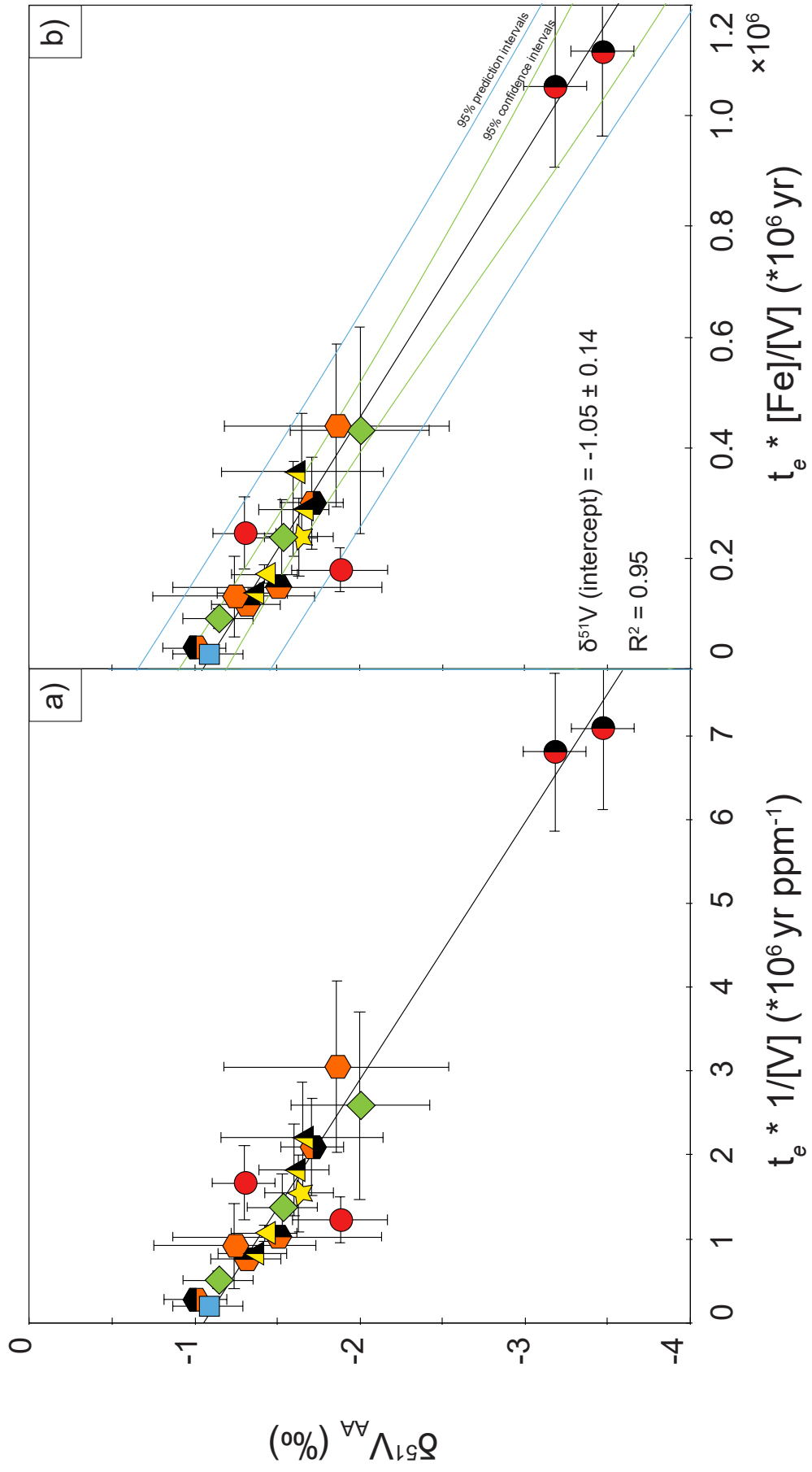
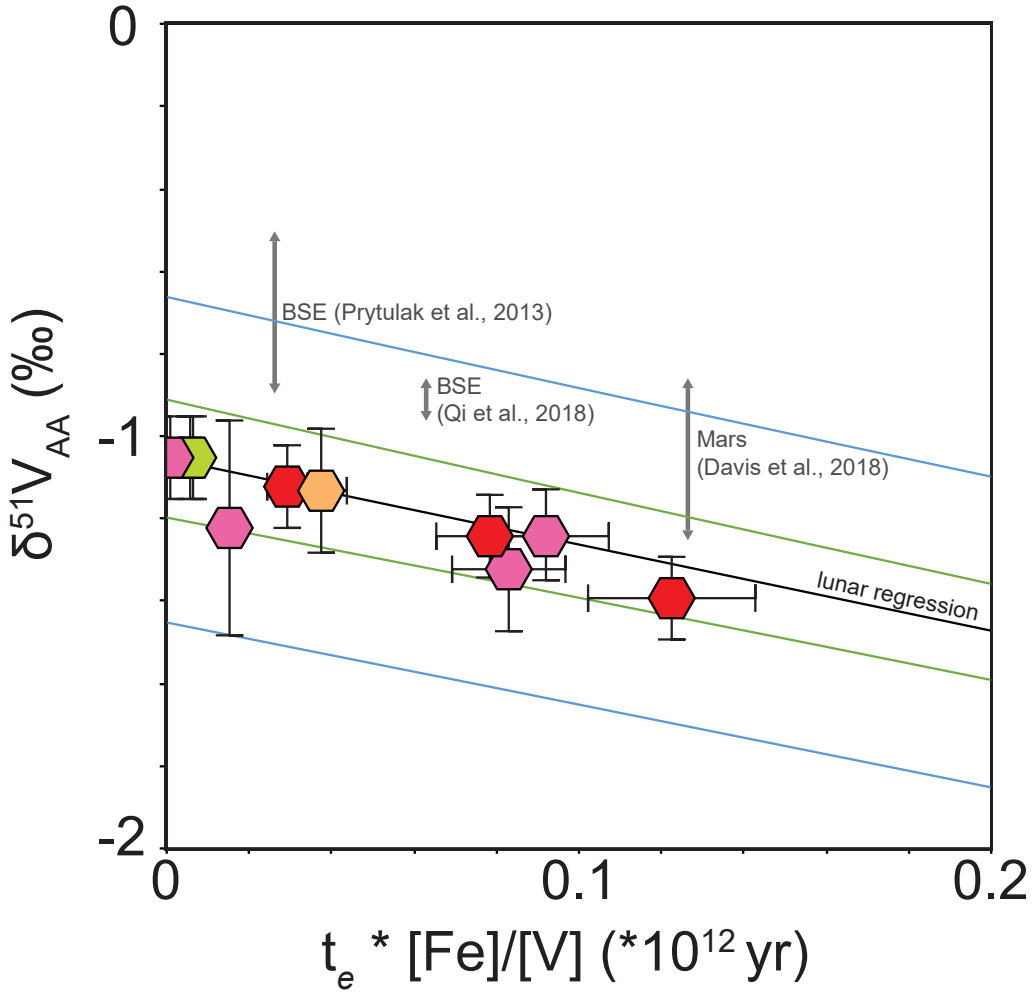


Figure 4.9 (High-Quality)



A5

Appendix 5: Manuscript for Hopkins et al. (2019)

Full Reference:

Hopkins, S.S., Prytulak, J., Barling, J., Russell, S.S., Coles, B.J., Halliday, A.N., 2019. The vanadium isotopic composition of lunar basalts. Earth Planet. Sci. Lett. 511, 12–24. https://doi.org/10.1016/j.epsl.2019.01.008

Earth and Planetary Science Letters 511 (2019) 12–24

Contents lists available at ScienceDirect

Earth and Planetary Science Letters

www.elsevier.com/locate/epsl

The vanadium isotopic composition of lunar basalts

S.S. Hopkins [a,*], J. Prytulak [b,c], J. Barling [a], S.S. Russell [d], B.J. Coles [b], A.N. Halliday [a,e]

[a] Department of Earth Sciences, University of Oxford, OX1 3AN, United Kingdom
[b] Department of Earth Sciences and Engineering, Imperial College, London, SW7 2AZ, United Kingdom
[c] Department of Earth Sciences, Durham University, DH1 3LE, United Kingdom
[d] Natural History Museum, London, SW7 5BD, United Kingdom
[e] The Earth Institute, Columbia University, Hogan Hall, 2910 Broadway, New York, NY 10025, USA

ARTICLE INFO

Article history:
Received 11 May 2018
Received in revised form 14 December 2018
Accepted 3 January 2019
Available online 1 February 2019
Editor: M. Bickle

Keywords:
vanadium isotopes
moon formation
exposure age
cosmogenic effects
lunar basalt
irradiation

ABSTRACT

We present the first high-precision vanadium (V) isotope data for lunar basalts. Terrestrial magmatic rock measurements can display significant V isotopic fractionation (particularly during (Fe,Ti)oxide crystallisation), but the Earth displays heavy V (i.e. higher $^{51}V/^{50}V$) isotopic compositions compared to meteorites. This has been attributed to early irradiation of meteorite components or nucleosynthetic heterogeneity. The Moon is isotopically-indistinguishable from the silicate Earth for many refractory elements and is expected to be similar in its V isotopic composition.

Vanadium isotope ratios and trace element concentrations were measured for 19 lunar basalt samples. Isotopic compositions are more variable (~2.5‰) than has been found thus far for terrestrial igneous rocks and extend to lighter values. Magmatic processes do not appear to control the V isotopic composition, despite the large range in oxide proportions in the suite. Instead, the V isotopic compositions of the lunar samples are lighter with increasing exposure age (t_e). Modelling nuclear cross-sections for V production and burnout demonstrates that cosmogenic production may affect V isotope ratios via a number of channels but strong correlations between V isotope ratios and t_e*[Fe]/[V] implicate Fe as the primary target element of importance. Similar correlations are found in the latest data for chondrites, providing evidence that most V isotope variation in chondrites is due to recent cosmogenic production via Fe spallation. Contrary to previous suggestions, there is no evidence for resolvable differences between the primary V isotopic compositions of the Earth, Moon, chondrites and Mars.

© 2019 The Author(s). Published by Elsevier B.V. This is an open access article under the CC BY license (http://creativecommons.org/licenses/by/4.0/).

1. Introduction

1.1. Lunar origin

The most widely-accepted theory of lunar origin is the so-called "giant impact" model whereby a smaller planetary object struck the proto-Earth in its final stages of accretion leading to an impact-generated disk from which the Moon formed (Cameron and Ward, 1976; Hartmann and Davis, 1975). The model satisfies constraints on the geodynamical properties, planetary densities, and broad chemical features of the Earth-Moon system. In early numerical simulations of the giant impact most of the Moon-forming material derives from the impactor, with only a small contribution from Earth (e.g. Canup, 2004). Extra-terrestrial bodies typically have distinct isotopic compositions (Goderis et al., 2016), thus it was assumed that the Moon should also be isotopically distinct. The Earth and the Moon are remarkably similar in mass-independent isotope variations such as ^{54}Cr (Lugmair and Shukolyukov, 1998; Mougel et al., 2018), ^{50}Ti (Zhang et al., 2012), ^{17}O (Young et al., 2016) and ^{96}Zr (Akram and Schonbachler, 2016), mass-dependent isotope variations of moderately refractory element such as Si (Armytage et al., 2012), Cr (Bonnand et al., 2016), Ti (Millet et al., 2016), Fe (Sossi and Moynier, 2017; Liu et al., 2010; Wiesli et al., 2003), and in radiogenic ^{182}W (Kruijer et al., 2015).

Several explanations have been advanced for the unexpected isotopic similarity between the Earth and the Moon. In the aftermath of a giant impact, a re-equilibration of isotopes between the Earth and newly-forming Moon might have taken place (Pahlevan and Stevenson, 2007). However, the timescales and temperatures of re-equilibration do not favour isotopic homogenisation of refractory elements – e.g. Cr and Ti. Predicted isotopic offsets in silicon based upon this model (Pahlevan et al., 2011) were not found (Armytage et al., 2012). Alternative impact scenarios have been proposed to reconcile the isotopic similarity of the Earth

* Corresponding author.
E-mail address: sean.hopkins@stx.ox.ac.uk (S.S. Hopkins).

https://doi.org/10.1016/j.epsl.2019.01.008
0012-821X/© 2019 The Author(s). Published by Elsevier B.V. This is an open access article under the CC BY license (http://creativecommons.org/licenses/by/4.0/).

and the Moon. These include high-energy impacts (Canup, 2012; Cuk and Stewart, 2012), a hit-and-run model (Reufer et al., 2012), and a multiple-impact scenario (Rufu et al., 2017). Compared to the canonical model, each of these scenarios invokes restricted dynamic conditions prior, or subsequent, to impact.

Models of an impactor with Earth-like isotopic composition (Dauphas et al., 2014), and models of inner Solar System homogeneity have also been proposed (Mastrobuono-Battisti et al., 2015). These studies argue against the assumption of an isotopically-distinct impactor. However, a consensus on the best model of lunar formation has yet to be reached.

1.2. Chemical and isotopic variations in lunar basalts

Lunar basalts are primarily divided by TiO_2 contents into very-low-Ti basalts (VLT) (<1.5 wt% TiO_2), low-Ti basalts (1.5–6 wt% TiO_2) and high-Ti basalts (>6 wt% TiO_2). Chemically-distinct regions of the lunar mantle must exist to explain the compositional diversity of mare basalts (Papike et al., 1976), with high-Ti basalts requiring significant amounts of ilmenite in their sources. Lunar mantle heterogeneities arise from the differentiation of the lunar magma ocean (LMO), a global melting of the lunar mantle as a result of accretion, during which differentially-dense regions of the mantle inefficiently mixed as crystallisation proceeded (Elkins-Tanton et al., 2011). Stable isotope studies of lunar basalts have not only provided evidence of the isotopic kinship between the Moon and the Earth, but also the extent of lunar mantle heterogeneity, the provenance of lunar sample subsets and the nature of lunar differentiation processes. For example, high-Ti basalts show light Mg (Sedaghatpour et al., 2013), and heavy Fe and Ti isotope ratios (Liu et al., 2010; Sossi and Moynier, 2017; Wiesli et al., 2003). These isotopic differences are thought to relate to crystallisation of ilmenite during LMO differentiation, or partial melting during formation of high-Ti and low-Ti parental melts. In contrast, Cr isotope ratios show mass-dependent fractionations correlating with indices of magmatic differentiation, but no difference between high-Ti and low-Ti basalts (Bonnand et al., 2016). Fractionations in Cr isotopes result from crystallisation of Cr-spinel and Cr-bearing ülvospinel. Post-crystallisation processes can modify isotopic compositions further (in a mass-independent fashion), and lead to difficulty in identifying the original isotopic signatures of the samples. For example, small excesses in ^{53}Cr and ^{54}Cr (Mougel et al., 2018) and depletions in $\varepsilon^{50}Ti$ (Zhang et al., 2012) have been found in mare basalts, reflecting cosmogenic processes at the lunar surface.

1.3. Vanadium

Vanadium occurs in multiple oxidation states (V^{2+}, V^{3+}, V^{4+}, V^{5+}) and behaves as a moderately incompatible element in terrestrial igneous systems. Previous studies have taken advantage of the strongly redox-dependent behaviour of V to investigate oxidation states of mantle and melts throughout Earth's history (e.g. Canil, 1997; Lee et al., 2003; Lee et al., 2005, 2004; Mallmann and O'Neill, 2009; Wood et al., 2008). Vanadium is depleted in the Earth's mantle compared to CI chondrites (McDonough and Sun, 1995), and its abundance relative to siderophile elements has been used to argue for changes in mantle oxidation during Earth's accretion and core formation (Wood et al., 2008). The lunar and terrestrial upper mantles are estimated to have similar V contents (79 ppm and 81 ppm, respectively; Seifert and Ringwood, 1988). Vanadium is incompatible in plagioclase, and so is unaffected by anorthite crystallisation during LMO differentiation. Differing oxygen fugacity (fO_2) of planetary mantles can affect the partitioning behaviour of V. For example, at low lunar fO_2, 1 to 2 log units below the Iron–Wüstite buffer (IW-1 to IW-2) most V is present in lunar magmas as V^{3+}. Vanadium is more compatible in lunar olivine, pyroxene, and spinel than for terrestrial analogues, where V^{4+} is the major species (Papike et al., 2005). The multiple valence states of V over a wide range of fO_2 makes it attractive as a potential tracer of planetary magmatic processes.

1.4. Vanadium isotopes

Vanadium has two stable isotopes: ^{50}V (0.25%) and ^{51}V (99.75%) and has been of cosmochemical interest for decades, due to the hypothesis that ^{50}V could be generated by cosmic ray irradiation processes (Stauffer and Honda, 1961). Advances in high precision multiple collector inductively-coupled-plasma mass spectrometry (MC-ICPMS) and the development of more effective separation procedures (e.g. Nielsen et al., 2011; Wu et al., 2016) now allow V isotope determination to precisions useful for geological applications (~0.2‰). Vanadium isotopes are reported in per mil (‰) deviation relative to an Alfa Aesar (AA) V solution standard introduced by Nielsen et al. (2011):

$$\delta^{51}V_{AA} = \left\{ \frac{(^{51}V/^{50}V)_{sample}}{(^{51}V/^{50}V)_{AA}} - 1 \right\} \times 1000$$

Terrestrial magmatic samples show a range of ~2.3‰ in $\delta^{51}V$. This variability has been interpreted in terms of equilibrium fractionation (Prytulak et al., 2011; Prytulak et al., 2013; Prytulak et al., 2017; Wu et al., 2018, Fig. 1). The bulk silicate Earth (BSE) is estimated at $\delta^{51}V_{AA} = -0.7 \pm 0.2$‰ based on analyses of bulk peridotites (Prytulak et al., 2013), although more recent work suggests a lighter BSE ($\delta^{51}V = -0.91 \pm 0.05$, 2SD; Qi et al., 2018). Metal–silicate experiments suggest terrestrial core formation does not significantly fractionate V isotopes (Nielsen et al., 2014). Much of the variation in magmatic samples has been proposed to result from crystallisation of (Fe,Ti) oxides during magmatic differentiation (Prytulak et al., 2017; Sossi et al., 2018; Wu et al., 2018). The similarity in whole rock $\delta^{51}V$ variation with respect to indicators of magmatic evolution in two cogenetic lava suites with disparate redox conditions (Hekla, Iceland and Anatahan, Mariana arc) suggests crystallisation of (Fe,Ti) oxides and the coordination difference between melt and mineral are dominant in driving isotope fractionation rather than $\delta^{51}V$ variation directly reflecting changes in oxidation state (Prytulak et al., 2017). Recent experimental work directly determining V magnetite–melt isotope fractionation factors ($\Delta^{51}V_{magnetite-melt}$) at variable, controlled redox conditions yields $\Delta^{51}V_{magnetite-melt}$ consistent with those needed to explain the variation seen in ~ closed system crystallisation and resulting Rayleigh isotope fractionation (Sossi et al., 2018). Interestingly, Sossi et al. (2018) also observed a strong positive relationship between the magnitude of $\Delta^{51}V_{\ magnetite-melt}$ and fO_2.

Initial analyses of chondrites, achondrites and martian meteorites returned a restricted range of $\delta^{51}V$ compositions ($\delta^{51}V_{AA} = -1.7 \pm 0.2$) uniformly-lighter than BSE (Nielsen et al., 2014). This was suggested to be due to incorporation of irradiated components in meteorites. However, more recent analyses of chondrites with medium-resolution mass spectrometry ($M/\Delta M > 4000$) suggests a revised isotopically-heavier composition for chondrites ($\delta^{51}V_{AA}$ between −1.35 to −1.05‰ for all chondrites except Xinglongquan, $\delta^{51}V = -1.76 \pm 0.05$‰; Xue et al., 2018; Nielsen et al., 2019) and martian meteorites ($\delta^{51}V_{AA} = -1.3$ to −0.7‰; Davis et al., 2018) (Fig. 1). Nielsen et al. (2019) suggest that incomplete resolution of mass interferences (e.g. polyatomic S interferences) during analyses of extra-terrestrial samples resulted in inaccurate and light $\delta^{51}V$ values for initial studies of meteorites, which were performed at lower-resolution (Nielsen et al., 2014; Prytulak et al., 2011). At medium-resolution (e.g. Wu et al., 2016; Nielsen et al., 2016) these

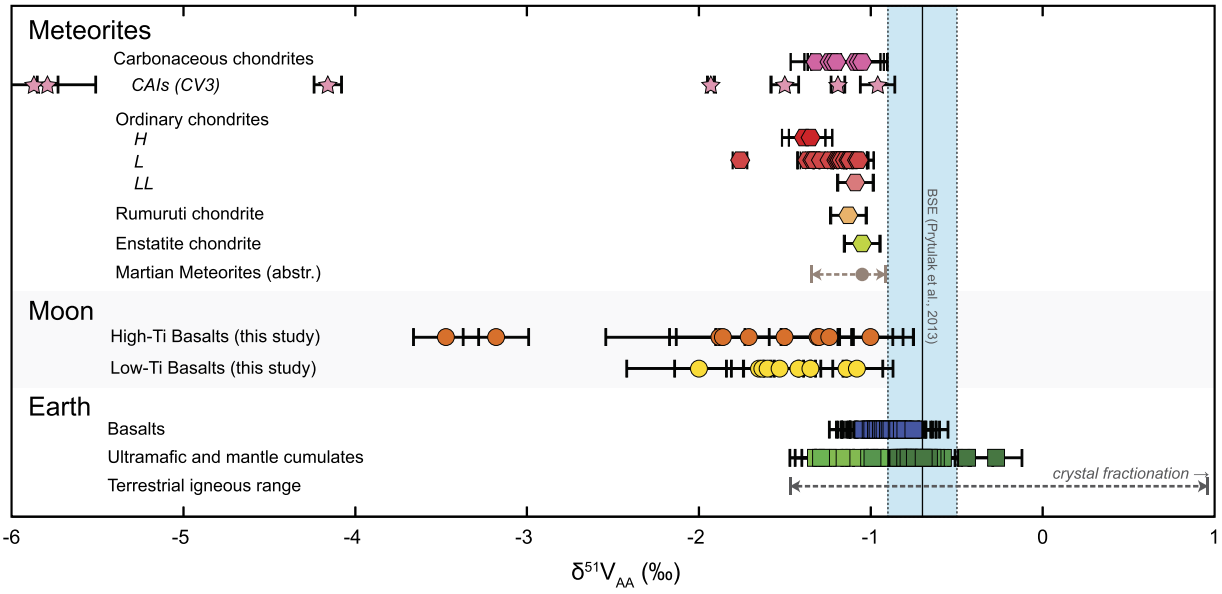


Fig. 1. Compilation of published V isotope data for Solar System materials including the lunar basalts measured in this study. Lunar basalts vary more widely in composition than all other samples, except CAIs (Sossi et al., 2017). Some CAIs show the isotopically-lightest values measured in the Solar System. Published data for chondrites is from Xue et al. (2018) and Nielsen et al. (2019) Recent data for Martian meteorites (presented only in abstract form) is included (Davis et al., 2018). The BSE estimate is indicated by the blue bar (Prytulak et al., 2013). Terrestrial basalts from multiple settings shows a much more restricted range than lunar basalts (Prytulak et al., 2011, 2013, 2017; Wu et al., 2018). The measured V isotope range (~2.3‰) of terrestrial magmatic rocks is displayed by the grey dashed line, with the heaviest V isotope samples thought to result from oxide fractionation (Prytulak et al., 2017). (For interpretation of the colours in the figure(s), the reader is referred to the web version of this article.)

interferences are resolved. Inter-laboratory comparison shows no resolvable differences in δ^{51}V for silicate rock reference materials (which generally have low S contents) at low- or medium-resolution MC-ICPMS (Nielsen et al., 2019). Despite the heavier, revised δ^{51}V, chondrites are isotopically-lighter than BSE (Nielsen et al., 2019; Xue et al., 2018, Fig. 1). Nielsen et al. (2019) attributed this to nucleosynthetic-heterogeneity in the Solar System (demonstrated by correlations between chondrite class average δ^{51}V and ε^{54}Cr). Measurements of calcium–aluminium inclusions (CAIs) in CV chondrites show one subset (fine-grained CV3 CAIs) to have the lightest δ^{51}V measured thus far in the solar system ($\delta^{51}V_{AA} < -5.87‰$, Sossi et al., 2017, Fig. 1). These light δ^{51}V values have been attributed to ^{50}V production during intense early solar cosmic ray (SCR) irradiation, in agreement with mathematical predications for CAI formation close to an early, active Sun (Gounelle et al., 2001; Lee et al., 1998). This suggests cosmogenic reactions are viable mechanisms for production of light δ^{51}V.

One body for which δ^{51}V data is lacking is the Moon. As a refractory element, V is expected to be isotopically-similar in the Moon and the Earth. Data from the Moon may also provide constraints on the origin of the difference in δ^{51}V observed between chondrites and the Earth.

2. Sampling approach

Nineteen unbrecciated lunar basalts from Apollo missions 11, 12, 14, 15, and 17 were selected based on geochemical and mineralogical variability (Table 1). Samples were processed in sufficient quantities for both V isotope and trace element measurements. The samples include both low-Ti and high-Ti basalts, with reported TiO_2 contents ranging from 2.2 wt% (15535) to 12.9 wt% (70215) (Table S7) and have reported modal ilmenite contents from 0.5% (12018) to 17% (70215, Table S5). An Apollo 11 Type A (high-K) basalt (10017), enriched in K, REEs and other incompatible trace elements (Tables S7, S9, Neal and Taylor, 1992), and a high-Al/low-K Apollo 14 basalt (14053) were included. Samples were extracted from the interior of their parents, with three exceptions. The exteriors of the parent samples 10017 and 12054 were sampled and a fragment of a glass-splash coating from sample 12054 was also analysed. The glass was emplaced after a nearby impact or an eruptive event and has an Apollo 12 ilmenite basalt composition (similar to its host rock, Hartung et al., 1978). Interior aliquots of samples were obtained from a maximum depth of 2.5 cm within their parent samples (except 12063-343 which was located between 0.5–5 cm).

3. Methods

3.1. Sample preparation

Details of procedures for sample preparation, dissolution, ion-exchange chromatography and elemental and isotopic analyses can be found in the Supplementary Text. Briefly, sample chips were washed in ~18.2 MΩ·cm ultra-pure water (MQ H_2O), centrifuged and dried at low temperature. Samples were crushed to homogenise any intra-sample geochemical variation using an agate pestle and mortar. Separate fractions of these powders were weighed for trace element determinations (~10 mg) and vanadium isotope analyses (20–100 mg). Samples were digested in a multi-stage hotplate dissolution procedure.

3.2. Trace element analysis by ICPMS

Trace element analyses were performed using a *PerkinElmer® NexION®* 350D quadrupole ICPMS (at the Department of Earth Sciences, University of Oxford) on ×10000 dilutions of digested sample solutions. A Re-Rh-In internal standard addition (for monitoring instrumental drift) was performed using an in-line *ESI prepFAST* auto-dilution system. The relative standard deviation was <5%, except for Li (7.9%). United States Geological Survey (USGS) reference material, BHVO-2, was measured alongside the lunar sample suite to assess accuracy.

3.3. Vanadium isotope analysis by MC-ICPMS

Chemical isolation of V was performed using methods outlined in Wu et al. (2016). Sample aliquots containing 5–10 μg of V

Table 1
$\delta^{51}V_{AA}$, selected element concentrations from ICPMS data, literature values for $^{158}Gd/^{157}Gd$, and sample exposure age.

Mission	Sample	Type	Sub-type	Location	$\delta^{51}V_{AA}$ (‰)	2s.d. (‰)	*n*	[V] ($\mu g\,g^{-1}$)	TiO_2 (wt%)	$^{158}Gd/^{157}Gd$[a]	+/−	Exposure age (Ma)[b]
A11	10017-400	High-Ti/High-K	11A	*exterior*	−3.47	0.19	1	55	11.2	1.59726	0.00046	479 ± 60
	10017-405	High-Ti/High-K	11A	*interior*	−3.18	0.19	1	61	11.3			479 ± 60
	10020-255	High-Ti/Low-K	11B3	*interior*	−1.88	0.29	2	113	10.7			127 ± 25
	10044-655	High-Ti/Low-K	11B1	*interior*	−1.30	0.19	3	56	9.6	1.58681	0.00030	70 ± 17
A12	12018-598	Low-Ti Olivine		*interior*	−1.42	0.20	3	185	2.1	1.58924	0.00040	195 ± 16
	12054-13	Glass Splash			−1.63	0.21	4	168*	4.7*			–
	12054-146	Low-Ti Ilmenite Basalt		*interior*	−1.65	0.49	3	152	5.3			260 ± 70*
	12054-150	Low-Ti Ilmenite Basalt		*exterior*	−1.60	0.21	4	126	4.1			260 ± 70*
	12063-343	Low-Ti Ilmenite Basalt		*interior*	−1.35	0.21	3	188	4.9	1.58768	0.00016	95 ± 5
A14	14053-305	Low-Ti/High-Al/Low-K Basalt	HA	*interior*	−1.08	0.21	3	106	2.7			21 ± 5
A15	15016-240	Low-Ti Olivine-normative		*interior*	−1.53	0.21	2	224	2.1			322 ± 83
	15535-165	Low-Ti Olivine-normative		*interior*	−1.14	0.21	2	197	2.1			110 ± 20
	15556-258	Low-Ti Olivine-normative		*interior*	−2.00	0.42	2	227	2.4			546 ± 214
A17	70215-389	High Ti	17B2	*interior*	−1.31	0.21	2	167*	12.9*			126 ± 3
	70255-56	High Ti	17A	*interior*	−1.86	0.68	3	83	10.8			280 ± 85
	71135-34	High Ti	*17B2*	*interior*	−1.50	0.63	3	90	10.3			103 ± 3
	71546-22	High Ti	17A	*interior*	−1.24	0.49	2	120*	12.2*			110 ± 55*
	74275-355	High Ti	17C	*interior*	−1.00	0.19	3	131	12.4	1.58524	0.00001	32 ± 1
	75035-249	High Ti	*Unclassified*	*interior*	−1.71	0.19	2	31	10.5			77 ± 19
	Average High-Ti				*−1.85*	*1.66*						
	– excluding 10017				*−1.48*	*0.64*						
	Average Low-Ti				*−1.49*	*0.56*						

* Samples 12054-13, 70215-389, 71546-22 were not analysed for element concentrations by ICPMS in this study. An average of previously-reported elemental concentrations is used hereon (see Table S7). [a,b] Gd isotopes and exposure ages compiled from published values (Supplementary Text, Tables S3, S6). Exposure ages for 12054 (independently-calculated) and 71546 (estimated from other samples in the same rake) are less reliable than for the other samples in the suite (Section 4.5, Supplementary Text, Table S6).

were passed twice through cation-exchange columns (using *Bio-Rad®* AG50W-X12 200–400 mesh resin) to remove the majority of matrix elements (Fe, Ti, Al, Ca). An anion-exchange column (using *Bio-Rad®* AG1-X8 200–400 mesh resin) was then used to separate V from Cr, and repeated in scaled-down form to remove any remaining Cr.

Quantitative yield of V must be obtained to exclude possible isotopic fractionation during incomplete elution in ion-exchange chromatography. The yield was found to be 100 ± 15% at the end of the procedure (by comparing MC-ICPMS beam intensities to Quad ICP-MS measurements). Cuts were collected before and after the vanadium elution steps in the cation-exchange columns to ensure the calibration of V elution (Wu et al., 2016). Total V blanks were <0.3 ng, which is insignificant compared to the amount of V processed. Samples returned $^{49}Ti/^{51}V$ and $^{53}Cr/^{51}V$ ratios <0.00001 (Nielsen et al., 2011), confirming negligible contributions of ^{50}Cr and ^{50}Ti to the ^{50}V signal.

Vanadium isotopes were analysed on a *Plasma II* (*Nu Instruments*) MC-ICPMS in the MAGIC laboratories at the Department of Earth Sciences and Engineering, Imperial College London. Measurements were performed at solution concentrations of 600–800 $ng\,g^{-1}$. Samples were aspirated into a *Nu Instruments* DSN-100 to desolvate before injection into the plasma. Masses 49, 50, 51, 52 and 53 were monitored to measure V isotopes and to correct for Ti and Cr interferences on mass 50 (Table S1). Pseudo-high-resolution mode ($M/\Delta M > 5000$) was used to resolve polyatomic interferences (particularly $^{40}Ar^{12}C^{+}$ from $^{52}Cr^{+}$) from the isotopes of interest. Faraday cups were equipped with 10^{11} Ω resistors, except for cups with low-intensity signals (m/z: 49, 50, 53), which were equipped with 10^{12} Ω resistors. This amplifies the resultant signal by a factor of 10 and improves signal/noise ratios. Each sample analysis was bracketed by two measurements of an Alfa Aesar (AA) V solution, and a well-characterised secondary standard from BDH chemicals (BDH, Nielsen et al., 2011). The AA standard defines zero (Section 1.4). BDH has been measured ($n = 1329$) to have a composition of $\delta^{51}V_{AA} = -1.17 \pm 0.17$‰ (Prytulak et al., 2017). Measurements of BDH in this study gave an average $\delta^{51}V_{AA} = -1.21 \pm 0.22$‰ ($n = 121$). United States Geological Survey (USGS) reference materials BCR-2, BHVO-2, and BIR-1a were processed through the same ion-exchange procedures and $\delta^{51}V$ values were found to be in agreement with literature values (Table S2).

4. Results & discussion

4.1. Major and trace elements

Comparison of ICPMS elemental concentrations to previous analyses of lunar basalts shows that samples lie within expected ranges for their mare basalt subtype (Table 1, Figs. 3c, S2, S3). Sample sizes in this study are small (up to 125 mg) compared to the majority of literature chemical analyses (Table S7), which were typically performed on much larger aliquots (>1 g) and would be expected to be more representative of the geochemistry of parent samples (e.g. Ryder and Schuraytz, 2001). However, obtaining major and trace element concentrations and V isotope ratios on the same aliquots allows internally-consistent interpretation of isotopic variations. Major element concentrations of samples lie within 5% of published values, with minor exceptions. Samples 12018 (−9%), 12054-150 (+6.3%), and 70255 (−9.8%) show TiO_2 contents that differ by more than 5% from published values. Sample 12054-146 differs in K_2O by +8%, and sample 70255 differs in MnO by −6.3%. Chondrite-normalised REE patterns of the lunar samples match those of previous analyses and show the characteristic patterns expected for their sub-groups (Fig. S2). A detailed discussion of the trace element behaviour of the sample suite is beyond the scope of this study, however, elemental concentrations from this study and previously-reported values can be found in Tables S4, S7 & S9 and Supplementary Figs. S2 & S3.

4.2. Vanadium isotopes

Lunar basalts span a $\delta^{51}V$ range of ~2.5‰, varying from $\delta^{51}V_{AA} = -3.47$‰ (10017-400) to −1.00‰ (74275-355) (Table 1, Fig. 2). There is no systematic difference between $\delta^{51}V$ in high-Ti and low-Ti basalts (High-Ti: $\delta^{51}V_{AA} = -1.85 \pm 1.66$‰; Low-Ti: $\delta^{51}V_{AA} =$

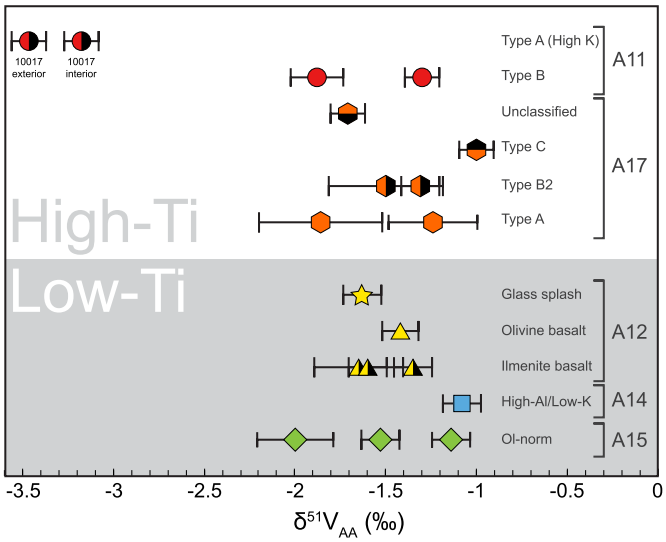


Fig. 2. δ^{51}V of the samples measured in this study. Samples are divided by high-Ti vs low-Ti type, mission, and sub-classification (Neal and Taylor, 1992). Aside from the two samples of 10017 (Apollo 11 Type A basalt), all chemical groups show an overlap in δ^{51}V between ~−2‰ to ~−1‰. Note in particular the range displayed by Apollo 15 olivine-normative basalts, despite their similarity in major and trace element compositions.

−1.49 ± 0.56‰, 2SD, Table 1, Figs. 2, 3a, b). Interior and exterior aliquots of Apollo 11 Type-A (high-K) basalt 10017 have the lightest isotopic compositions ($\delta^{51}V_{AA}$ = −3.18 ± 0.19‰ and −3.47 ± 0.19‰, Fig. 2). Excluding these two samples reduces the lunar δ^{51}V range to ~1‰ and populations of high-Ti and low-Ti basalts are essentially indistinguishable (high-Ti basalt excl. 10017: $\delta^{51}V_{AA}$ = −1.48 ± 0.64‰). The total lunar δ^{51}V range is larger than the total range of magmatic samples yet measured on the Earth (~2.3‰, Fig. 1). Thirteen of the nineteen lunar basalts show δ^{51}V lighter than any terrestrial samples ($\delta^{51}V_{AA}$ < −1.32‰). Only three samples, 74275-355, 14053-305, and 15535-165 have isotopic compositions within the published range for terrestrial basalts ($\delta^{51}V_{AA}$ = −0.95 ± 0.25‰ 2SD, Prytulak et al., 2013; Wu et al., 2018, Fig. 1).

4.3. Magmatic effects on V and δ^{51}V

Under terrestrial magmatic conditions V behaves relatively incompatibly through magmatic evolution except during crystallisation of (Fe,Ti) oxides into which V^{3+} partitions readily (O'Neill and Navrotsky, 1984). On Earth, the most extreme δ^{51}V arises from ~ closed system crystallisation of isotopically light (Fe, Ti) oxides, which drives residual melts to heavier compositions (up to $\delta^{51}V_{AA}$ ~+1‰; Prytulak et al., 2017). Given the high modal proportions of (Fe,Ti) oxides (particularly ilmenite) in lunar basalts, it is tempting to assume that the large variability recorded in the lunar sample suite is a result of ilmenite–melt fractionation. However, oxygen fugacity is much lower on the Moon (IW-1 to IW-2) than in terrestrial melts, which not only affects the speciation and partitioning behaviour of V ($V^{3+} > V^{4+}$, on Earth $V^{4+} > V^{3+}$), but also the crystallising mineral phases (e.g. from lack of available Fe^{3+}). Analyses of minerals in lunar basalts show V present in spinel (<8000 ppm, Papike et al., 2005), armalcolite (<3000 ppm) and ilmenite (<2500 ppm, El Goresy et al., 1974), pyroxene (<500 ppm), and olivine (<80 ppm – Papike et al., 2005). Likewise, partition coefficients for V at low fO_2, show V to be compatible in spinel, armalcolite, ilmenite and pyroxene (in decreasing order of compatibility, Karner et al., 2006; Klemme et al., 2006; Papike et al., 2005). Under lunar conditions, V appears more compatible than in terrestrial settings. The abundances of minerals in samples is highly-variable (Table S5) and crystal fractionation may control the observed range of δ^{51}V.

Although V varies within the suite with varying major element compositions (Fig. 3c, Fig. S3) and mineralogy (e.g. ilmenite, pyroxene Fig. S4) there is no systematic relationship between δ^{51}V and TiO_2 or V (Fig. 3a, b) or between δ^{51}V and modal proportions of the major hosts for V (spinel, ilmenite, pyroxene, Fig. S4). Likewise, samples previously studied for mass-dependent isotopes (e.g. Cr, Fe, Fig. S5) do not show correlations with δ^{51}V (Bonnand et al., 2016; Liu et al., 2010; Sossi and Moynier, 2017; Wiesli et al., 2003). Apollo 11 Type-A basalt 10017 is >1‰ lighter than the other basalts (Table 1, Fig. 2). Although the origin of the Apollo 11 Type-A basalts remains contested, the high-abundances of K, REEs, and other incompatible trace elements suggest involvement of a KREEP-like component (Neal and Taylor, 1992). The light δ^{51}V in this sample may reflect the extreme composition of this KREEP-y reservoir. However, KREEP is thought to represent the last vestiges of LMO prior to crystallisation. Prior removal of oxides from the LMO should leave this reservoir enriched in heavy δ^{51}V (i.e. opposite to the direction of δ^{51}V offset observed, assuming similar mineral–melt fractionations to terrestrial settings). The lack of evidence for systematic magmatic-driven δ^{51}V variability in this suite is further highlighted by the 0.84‰ isotopic difference between samples 15535 and 15556 (Fig. 2). These samples are genetically-related by olivine fractionation (Mason et al., 1972), which is unlikely to account for the large δ^{51}V difference observed.

4.4. Reduced magmatic δ^{51}V fractionation at lower fO_2

Considering the magnitude of isotopic fractionation associated with (Fe,Ti)oxide crystallisation on Earth (e.g. $\Delta^{51}V_{magnetite-melt}$ = −0.4 to −0.5‰ in Hekla and Anatahan lavas, Prytulak et al., 2017), the lack of correlation of δ^{51}V with TiO_2 or ilmenite or oxide content is notable, particularly since the range in abundances of (Fe,Ti) oxides in lunar basalts is much larger than in terrestrial samples. Wu et al. (2018) recently proposed a smaller terrestrial $\Delta^{51}V_{mineral-melt}$ of −0.15‰. However, this factor was derived from a MORB-suite that is not cogenetic and has documented evidence of magma-mixing (indeed, their isotope-mixing calculations fit the δ^{51}V variation observed just as well as their reduced mineral–melt V isotope fractionation factor). A recent experimental study of V isotope fractionation between magnetite and hydrous granitic melt at 800 °C and controlled fO_2 conditions (from FMQ-1 to FMQ+5) suggests $\Delta^{51}V_{magnetite-melt}$ reduces with decreasing fO_2 (Sossi et al., 2018). Extrapolating these results to lunar fO_2 and temperatures ($1/T^2$ dependence; Schauble, 2004) yields a $\Delta^{51}V_{oxide-melt}$ ~−0.2‰ (assuming lunar oxides fractionate δ^{51}V similarly to magnetite, which is not present at lunar fO_2). For lunar basalts, a reduced fractionation factor at lower fO_2 may explain a lack of variation between δ^{51}V and other geochemical parameters but cannot explain the wide range and light δ^{51}V of the suite.

4.5. Cosmogenic irradiation

Exposure ages have been previously-determined for most of the samples in this suite (Table 1, Table S6). To allow the most consistent cross-sample comparisons, exposure ages calculated using ^{81}Kr–Kr and ^{38}Ar (where ^{81}Kr–Kr data are absent) were chosen over other techniques due to their widespread adoption and intercalibration (e.g. Hohenberg et al., 1978; see Supplementary Text, Table S6). The range of sample δ^{51}V is lighter and more variable at longer exposure ages (t_e, Fig. 4), implicating modification of primitive isotopic compositions by exposure-related processes.

Samples exposed at the lunar surface may be affected by meteorite sputtering, surficial contamination, solar wind implantation, or irradiation from high-energy particles derived from solar

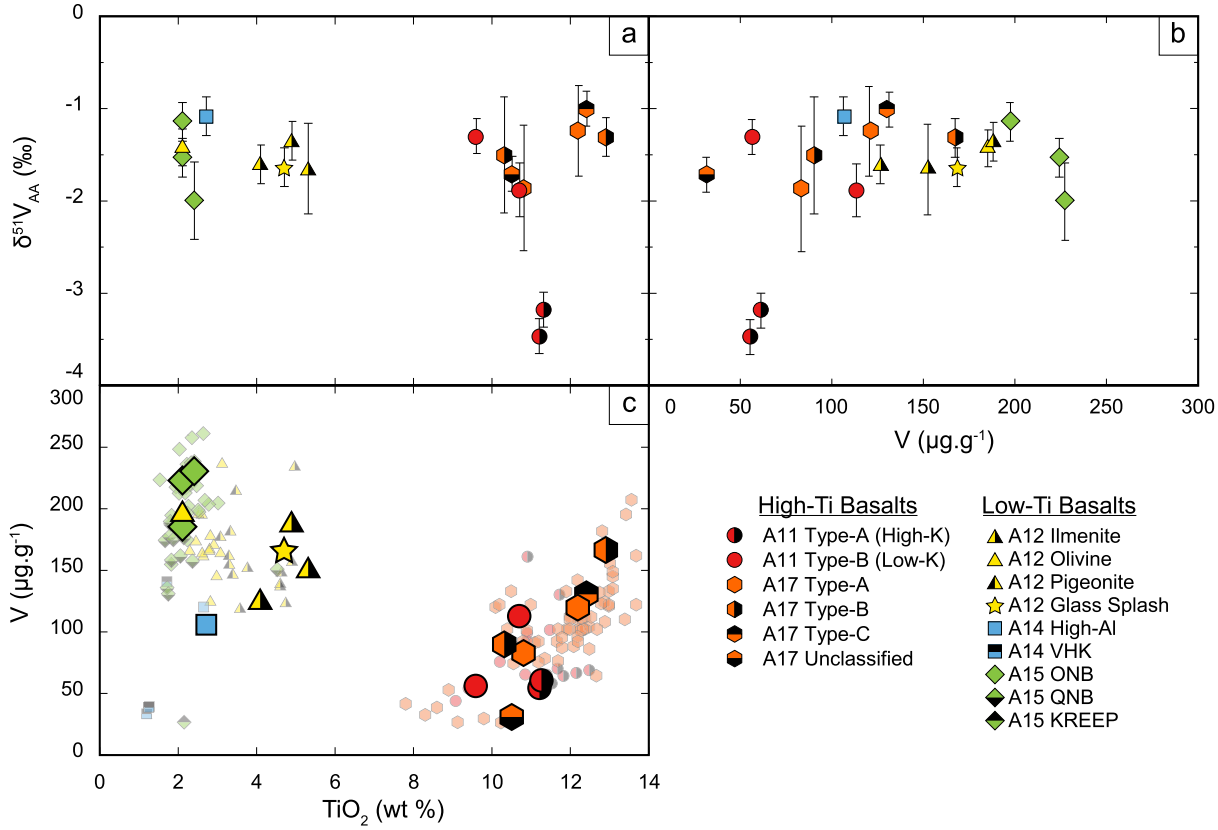


Fig. 3. Comparison of δ^{51}V, V and TiO_2 concentrations: a) δ^{51}V versus TiO_2 (wt%) contents; b) δ^{51}V versus V concentration; c) V concentration against TiO_2 concentration. Samples analysed in this study lie in the regions expected for their mare basalt subtype (c). A strong correlation exists between V and TiO_2 in the high-Ti basalts. Larger, solid symbols represent data from the samples in this study. Semi-transparent symbols are a compilation of literature-reported values for V and TiO_2 in lunar basalts (Table S8). There is no similar correlation between TiO_2 and δ^{51}V (a) or between V and δ^{51}V (b). Sample 10017 (two Apollo 11 high-K basalts) has δ^{51}V values which lie outside of the range of the other mare basalts.

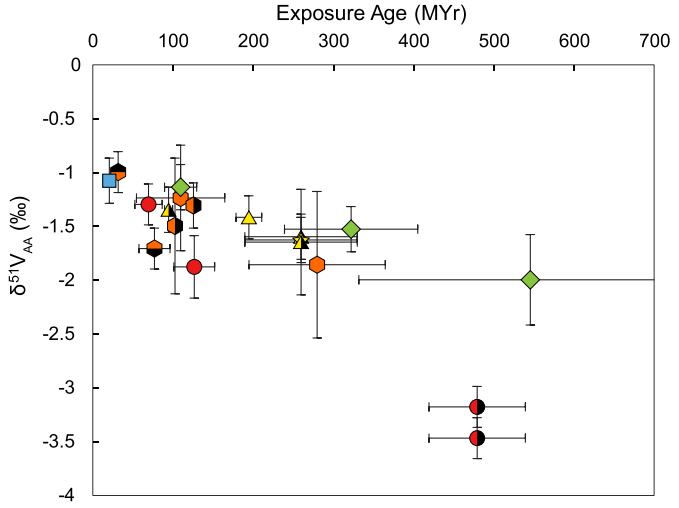


Fig. 4. Exposure age versus δ^{51}V. Samples with longer exposure ages have lighter V isotopic compositions. Details of sample exposure ages are outlined in the Supplementary Text and Table S6. Symbols as in Fig. 2.

and galactic cosmic rays (SCRs and GCRs). If exposure-related isotopic variability is achieved after crystallisation (as indicated by Fig. 4), sputtering, surficial contamination and solar wind implantation processes are unlikely to explain the observed δ^{51}V variability. All but three samples are picked from the interiors of their parents and would be shielded from these weakly-penetrating processes. Thus, cosmogenic irradiation from SCRs and GCRs is most likely. Cosmogenic effects have been observed in lunar samples for neighbouring Ti and Cr isotope systems, with negative anomalies in ε^{50}Ti (Zhang et al., 2012) and positive anomalies in ε^{54}Cr and ε^{53}Cr (Mougel et al., 2018) attributed to neutron-capture processes. It is possible that similar processes operate on V isotopes.

The flux of energetic particles in SCRs and GCRs consists mainly of protons and alpha-particles (with minor fluxes of heavier nuclei). These primary particles can react with sample material to produce a cascade of secondary energetic particles (e.g. protons, neutrons, alpha-particles, ^{3}He, deuterium, muons, kaons, and pions) which can then further interact with sample material. Secondary neutrons are of particular interest for a number of elements, particularly those having isotopes with large neutron-capture cross-sections (e.g. gadolinium, Gd, where neutron-capture cross-sections for ^{157}Gd $\gg$ ^{156}Gd; Eugster et al., 1970). The ^{158}Gd/^{157}Gd ratio is sensitive to the flux of thermal neutrons generated during cosmic-ray reactions. Sample δ^{51}V shows a negative correlation with ^{158}Gd/^{157}Gd for five samples with published Gd isotope data (Fig. 5, Table S3), although the strength of this relationship may be enhanced by the position of sample 10017, which lies far outside the range of δ^{51}V and ^{158}Gd/^{157}Gd for the other samples. This correlation operates in a similar sense to that between δ^{51}V and exposure age (i.e. the most-exposed samples have the lightest δ^{51}V). However, three different samples (15016, 15556, 70215) have been measured for ε^{50}Ti (another neutron-capture-sensitive proxy, Zhang et al., 2012) and show similar trends (Fig. S6).

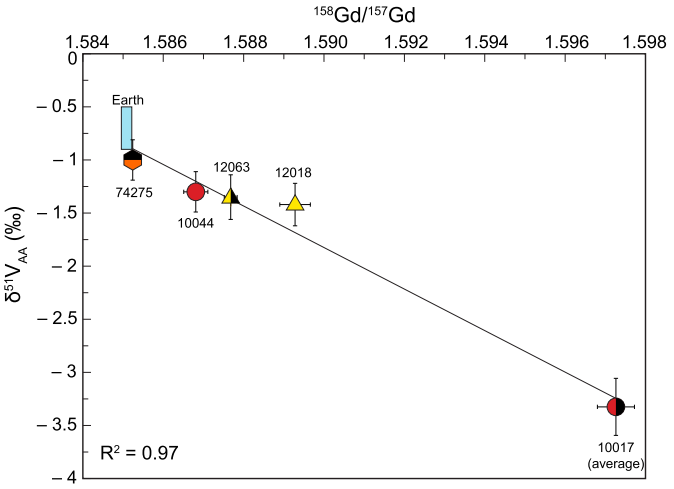


Fig. 5. Neutron-sensitive gadolinium isotope ratios versus δ^{51}V. The ratio of ^{158}Gd/^{157}Gd is a sensitive monitor of secondary neutrons produced during cosmic-ray bombardment of lunar material. Published ^{158}Gd/^{157}Gd for samples in this study linearly correlate with δ^{51}V. The internal and external aliquots of 10017 are averaged (for both δ^{51}V and ^{158}Gd/^{157}Gd) and plotted here as analyses were performed on different aliquots of this sample. The blue box represents the BSE estimate for δ^{51}V (Prytulak et al., 2013) and the terrestrial Gd isotope value from Dubois et al. (1992). A linear regression is calculated on the lunar samples. References for the Gd isotope data can be found in Table S3. Symbols as in Fig. 2.

4.6. Cross-sections

Earlier modelling of cosmogenic V isotope effects focused on production of ^{50}V from solar proton and He-nuclei interactions with CAI-precursor target materials (Gounelle et al., 2001; Lee et al., 1998). However, only a select handful of reaction pathways and target elements (Ti, Cr, and ^{51}V) were considered. Under lunar conditions, other target elements (e.g. Fe, Mn) may be important. Secondary particle fluxes (e.g. neutrons, Fig. 5, Fig. S6) are clearly present in these samples and should be considered. Cosmogenic reactions affecting ^{51}V must also be considered to ascertain the resultant effects on δ^{51}V.

Cross-sections for reactions involving the production or burnout of both ^{50}V and ^{51}V via proton-, alpha particle- and neutron-interactions with lunar sample compositions were calculated using TALYS-1.9 (Koning et al., 2008). This is the most recent iteration of the TALYS nuclear-modelling code and one of the most accurate codes for energies <200 MeV, being regularly evaluated and updated against experimental data. Although the energies of incident SCR and GCR particles regularly exceed this upper energy limit, this energy range should provide insights into both spallation- and capture-processes, and the relative importance of different target elements.

Cross-sections were calculated for nuclear reactions between target elements Ti, V, Cr, Mn and Fe (assumed to be present in natural isotope proportions) and incident neutrons (at energies 10^{-11} MeV–200 MeV), protons, and alpha-particles (energies 0.1 MeV–200 MeV). To allow comparison between the reactions ($n > 1000$), cross-section data was sub-divided into three categories: *burnout* of V isotopes (where target V isotope, j, forms another resulting element, R), *internal production* (target V isotope, i, produces the other V isotope, j – i.e. $^{50}\text{V} \rightarrow {}^{51}\text{V}$ or vice versa), and *external production* (where ^{nat}Ti, ^{nat}Cr, ^{nat}Mn, or ^{nat}Fe produces V isotope, j). All other factors being constant, *burnout* and *internal* production are controlled by the abundance of target V, and *external* production is controlled by the abundance of the non-V target element. The sums of the cross-sections, $\sum^{j}\sigma_{X,k}$, for *burnout*, *internal* and *external* production were calculated for each target, X, at different energies of incident particle, k (where k = proton, neutron, or alpha-particle; Fig. S10).

Reactions producing radioactive isotopes ^{51}Sc, ^{51}Ti, ^{51}Cr, ^{51}Mn, ^{51}Fe included in the sum of cross-sections for ^{51}V production (these isotopes are assumed to decay to before further interaction with energetic particles). Cross-sections for reaction pathways where the product nucleus is the same as the target nucleus (e.g. ^{50}V(n,n)^{50}V, or ^{51}V(p,n)^{51}Cr which decays to ^{51}V) were excluded.

The compiled cross-sections for each target ($\sum^{j}\sigma_{X,k}$) were adjusted to reflect atomic abundances of target elements relative to V in samples via:

$$\sum^{j}\sigma_{X,k,adjusted} = \sum^{j}\sigma_{X,k} \times [X]/[\text{V}] \quad (1)$$

where [X]/[V] is the ratio of target isotope or element relative to V. Total concentration-adjusted cross-sections ($\sum^{j}\sigma_{X,k,adjusted}$) of different particle pathways are compared for their effects on ^{50}V and ^{51}V (Fig. 6, where the "average" lunar sample composition is used).

Internal production displays lower cross-sections than external production in all scenarios, indicating that non-V target elements likely dominate cosmogenic production. Above ~50 MeV, Fe displays the largest cross-sections for production of both V isotopes in proton and alpha-particle reactions (Fig. 6b, c, e, f). Between 5–50 MeV, cross-sections for production of ^{50}V from protons with ^{nat}Ti (Fig. 6b) is higher than for production of ^{51}V (Fig. 6e). Burnout of either V isotope becomes increasingly-important at lower proton and alpha-particle energies (<5 MeV). At neutron energies >1 MeV, Cr and Fe appear to be most important for production of ^{51}V and ^{50}V (Fig. 6a, d). At neutron energies >50 MeV, Fe is the most important target element for production of either V isotope. Below 1 MeV, there are numerous pathways towards production of ^{51}V (via neutron interaction with Ti, Cr, ^{50}V), but no pathways for ^{50}V production. This has important implications: if thermal neutron capture is most significant amongst the array of possible reaction pathways, it is impossible to reconcile with the direction of cosmogenic isotope shift. Thus, charged-particle reactions or high-energy neutrons must contribute a significant amount to the total cosmogenic V production. In general, production cross-sections for ^{51}V appear larger than for ^{50}V (Fig. 7a, b, c) – however, a direct comparison must be carried out to ascertain the resulting effect on sample δ^{51}V.

4.7. Contribution to sample $\delta^{51}V$

The total ^{51}V/^{50}V in irradiated samples can be displayed as follows:

$$\left(\frac{n(^{51}\text{V})}{n(^{50}\text{V})}\right)_{final} = \frac{[n(^{51}\text{V})_0 + n(^{51}\text{V})_{cosm}]}{[n(^{50}\text{V})_0 + n(^{50}\text{V})_{cosm}]} \quad (2)$$

where $n(^{j}\text{V})_0$ is the initial number of atoms of isotope, j, and $n(^{j}\text{V})_{cosm}$ is the number of atoms of isotope, j (i.e. ^{51}V, ^{50}V), produced through cosmogenic reactions:

$$n(^{j}\text{V})_{cosm} = n(^{j}\text{V})_{external} + n(^{j}\text{V})_{internal} - n(^{j}\text{V})_{burnout} \quad (3)$$

The resulting isotopic effect is:

$$\Delta^{51}\text{V}_{cosm} = \left[\frac{\frac{n(^{51}\text{V}_{final})}{n(^{50}\text{V}_{final})}}{\frac{n(^{51}\text{V}_0)}{n(^{50}\text{V}_0)}} - 1\right] \times 1000 \quad (4)$$

Assuming a natural isotopic ratio ($\frac{n(^{51}\text{V}_0)}{n(^{50}\text{V}_0)} = 400$) substituting for the terms in Equation (2) gives:

$$\Delta^{51}\text{V}_{cosm} = \left[\frac{n(^{51}\text{V}_{cosm}) - n(^{50}\text{V}_{cosm}) \times 400}{n(^{50}\text{V}_{cosm}) + n(^{51}\text{V}_0)}\right] \times 1000 \quad (5)$$

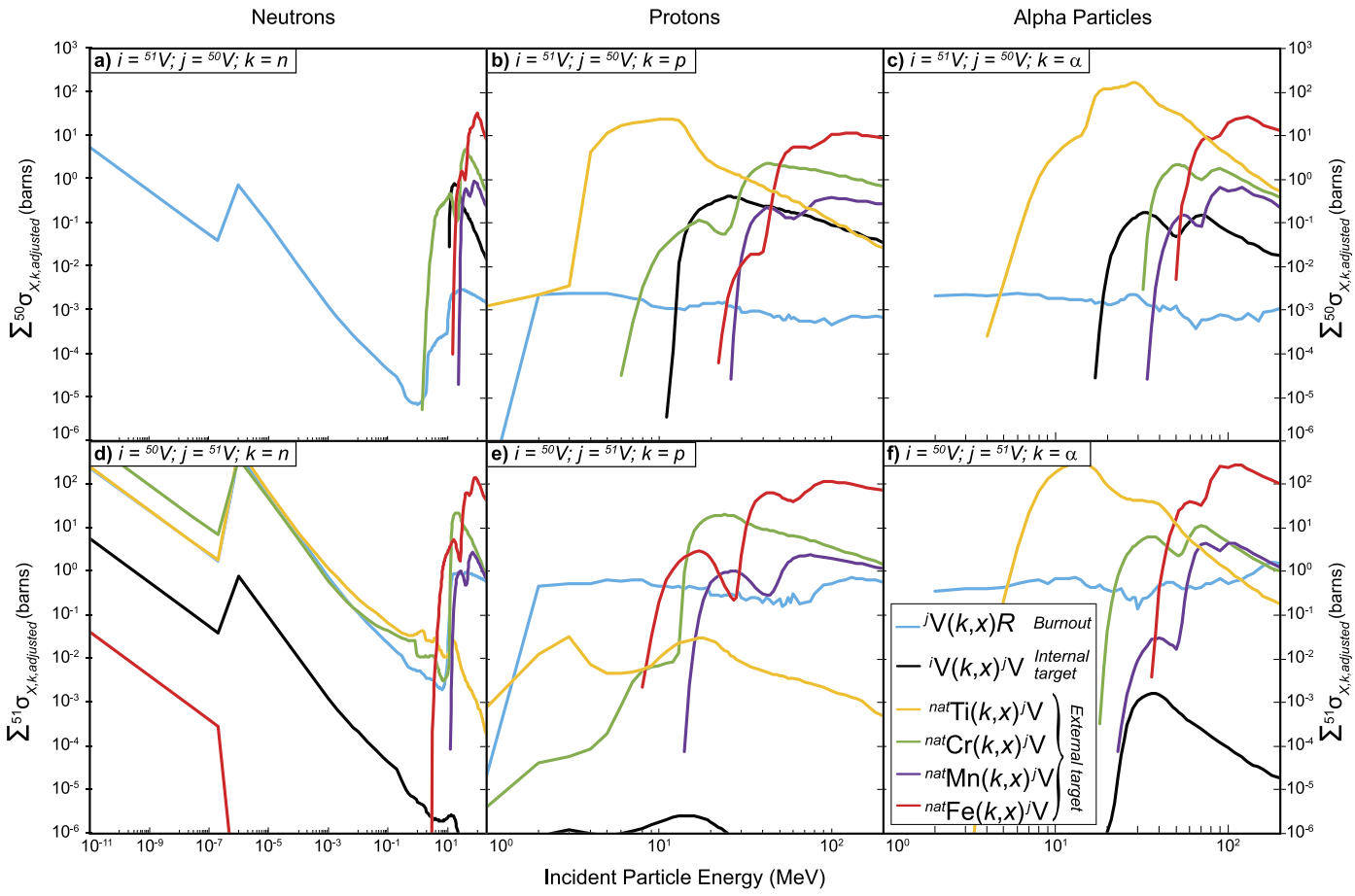


Fig. 6. The sum of adjusted cross-sections ($\sum {}^{j}\sigma_{X,k}$, y-axes) for reactions between an incident particle, k, (k = neutron, proton or alpha particle) and nuclei (X) to either produce or burn out ^{j}V (where j is the V-isotope of interest – i.e. ^{50}V, ^{51}V) at different particle energies (x-axis). Reactions are broken down into three categories: burnout (light blue) of ^{j}V to another isotope, R; internal production (black) of ^{j}V from ^{i}V ($j = 50, 51$; $i = 51, 50$); external production of ^{j}V from target elements ^{nat}Ti (gold); ^{nat}Cr (green); ^{nat}Mn (purple); ^{nat}Fe (red). Cross-sections are adjusted to the average composition of the suite via [X]/[V] (where [X] is the atomic abundance of the target element or isotope, [V] is the atomic abundance of V). Targets are assumed to have natural isotopic abundances. Cross-section curves are displayed for each incident particle (neutrons a, d; protons b, e; alpha-particles c, f) and its effect on each isotope of V (^{50}V: a, b, c; ^{51}V: d, e, f). Within each panel, the curves represent reactions which add to the abundance of isotope ^{j}V, except the burnout curves (light blue) which will decrease the abundance of ^{j}V. Note the different energy scales for neutrons and protons/alpha-particles.

Thus, for a resulting cosmogenic isotopic shift ($\Delta^{51}V_{cosm}$) of 0‰:

$$n\left({}^{51}V_{cosm}\right) = n\left({}^{50}V_{cosm}\right) \times 400 \tag{6}$$

The production of cosmogenic ^{51}V and ^{50}V is proportional to the sum (i.e. *internal* + *external* − *burnout*) of their concentration-adjusted cross-sections ($\sum {}^{j}\sigma_{total\text{-}adjusted}$). Assuming $[V]_0 \gg [V]_{cosm}$, if $\sum {}^{51}\sigma_{total\text{-}adjusted} > (\sum {}^{50}\sigma_{total\text{-}adjusted} \times 400)$ the resulting isotope ratio will increase and if $\sum {}^{51}\sigma_{total\text{-}adjusted} < (\sum {}^{50}\sigma_{total\text{-}adjusted} \times 400)$ the resulting isotope ratio will decrease. For ease of comparison between the total adjusted cross-sections a new variable, the "excess total ^{51}V cross-section" is defined:

$$\varepsilon^{51}\sigma_{total} = \left(\sum {}^{51}\sigma_{total\text{-}adjusted} - \sum {}^{50}\sigma_{total\text{-}adjusted} \times 400\right)/\left[{}^{51}V\right] \tag{7}$$

This is more useful than a direct cross-section ratio ($\sum {}^{51}\sigma_{total\text{-}adjusted} / \sum {}^{50}\sigma_{total\text{-}adjusted}$) since it allows direct inspection of the isotopic effects of particular pathways at different energies and can account for instances where the sum of concentration-adjusted cross-sections for an isotope is ≤0 (e.g. where burnout is more significant than production).

For all the particle reactions considered, it appears that only neutron capture ($<1 \times 10^{-3}$ MeV) can produce excesses in $\varepsilon^{51}\sigma_{total}$ (Fig. 7d, g). There are negative excursions in $\varepsilon^{51}\sigma_X$ for proton and alpha-particle reactions with Ti between 20–100 MeV (Fig. 7e, f), and smaller negative excursions in $\varepsilon^{51}\sigma_{total}$ for Fe reactions with protons >50 MeV. Similarly, high-energy neutrons display negative $\varepsilon^{51}\sigma_X$ for Fe (>10 MeV, Fig. 7d). The magnitude of the cosmogenic isotope effect is expected to vary with sample compositions (i.e. changing [X]/[V] ratio, Fig. 7g, h, i). High-Ti samples are expected to show a stronger $\varepsilon^{51}\sigma$ response to interactions with protons and alpha-particles when compared to average sample or low-Ti sample compositions. However, at lower neutron energies ($<10^{-3}$ MeV), high-Ti samples would be expected to display isotopically-heavier cosmogenic signatures when compared to low-Ti samples (Fig. 7g). It appears that for protons and alpha-particles, Fe and Ti are the primary contributors to V isotope anomalies for the energy ranges investigated. Burnout of V and internal production are relatively unimportant in affecting the final isotopic ratio.

4.8. Reconciling with chemical compositions

Plotting sample δ^{51}V against exposure age over V concentration (t_e/[V]) yields a strong linear correlation (Fig. 8a). This correlation is stronger than the relationship between δ^{51}V and t_e*[Ti]/[V] (and t_e*[Cr]/[V], Fig. S7), and similar to the correlation between δ^{51}V and t_e*[Fe]/[V] (Fig. 8b) and t_e*[Mn]/[V] (Fig. S7). The strong correlation between δ^{51}V and t_e/[V] suggests the concentration of [V] (assuming $[V]_0 \gg [V]_{cosm}$) in samples is more

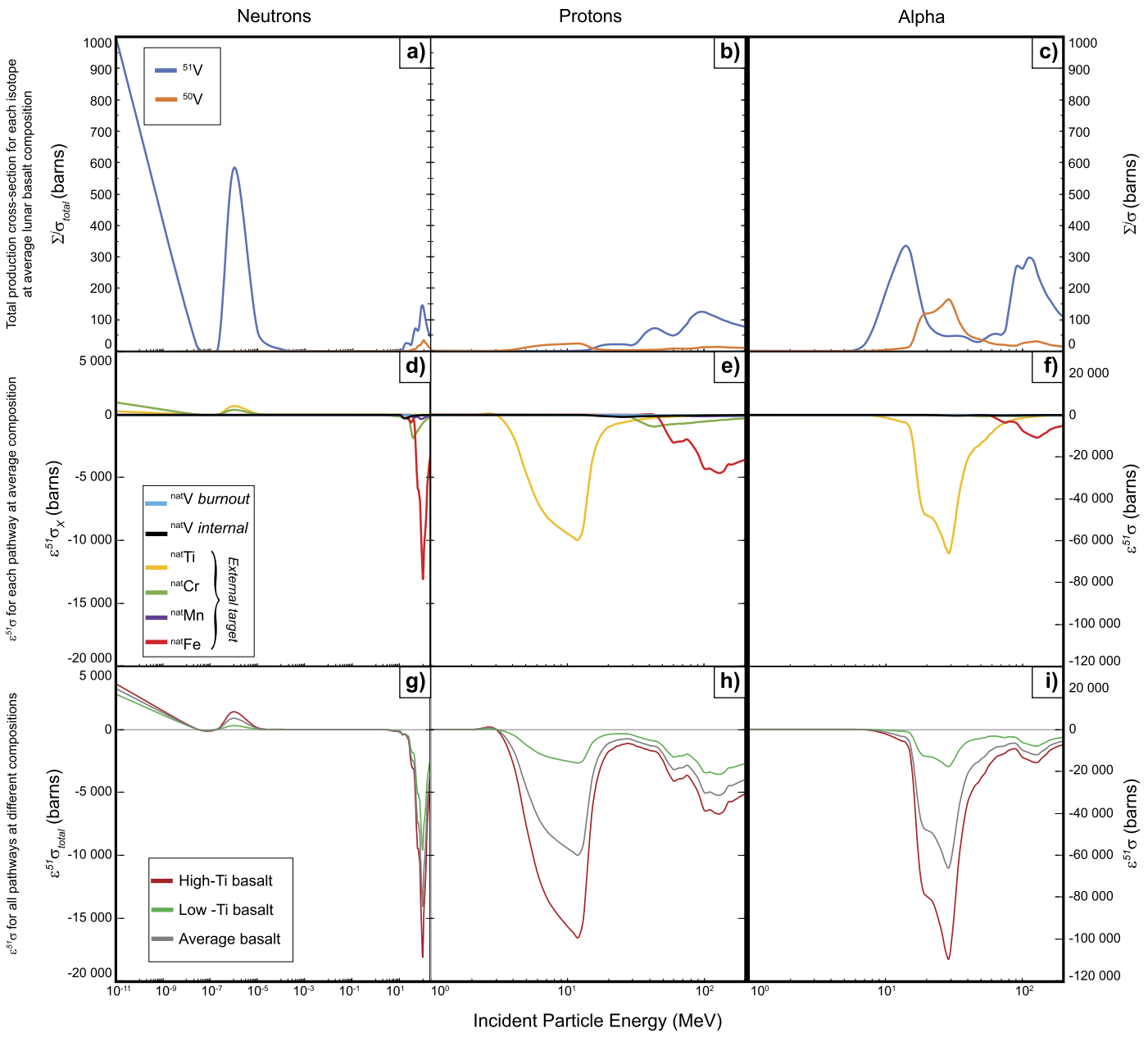


Fig. 7. The resulting isotopic effects of cosmogenic reactions between neutrons, protons, and alpha-particles and lunar basalt compositions at different energies. The total concentration-adjusted cross-sections affecting ^{50}V and ^{51}V from interactions between neutrons (a), protons (b), and alpha-particles (c) and targets of average lunar basalt composition at different energies are displayed. Cross-sections for production of ^{51}V is higher than ^{50}V, except for alpha-particle reactions between 20–50 MeV. The excess ^{51}V production cross-section for different target elements ($\varepsilon^{51}\sigma_X$, see Section 4.7) varies across the range of incident particle energies and particle compositions (d, e, f). The total excess ^{51}V production cross-section ($\varepsilon^{51}\sigma_{\text{total}}$) changes in intensity with changing target chemical compositions (g, h, i). For all particles (except neutrons below 10^{-5} MeV) there are significant negative $\varepsilon^{51}\sigma$ deviations. Thermal neutrons ($\leq 2.5 \times 10^{-8}$ MeV) show positive $\varepsilon^{51}\sigma$ deviations (**g**), as only ^{51}V production is viable the target elements investigated (Fig. 6a, 6d). Average and low-Ti basalts show reduced $\varepsilon^{51}\sigma_{\text{total}}$ deviations compared to high-Ti basalts reflecting variation in [X]/[V] between samples. At high-energies (>50 MeV) negative deviations in $\varepsilon^{51}\sigma$ are seen from the effect of Fe as a target. Key displayed in a), d), g).

important in controlling the resultant δ^{51}V after cosmogenic exposure than the concentration of the target element – i.e. the target element concentration doesn't vary much compared to [V]. Both Mn and Fe are relatively restricted in variability compared to V, Cr, and Ti (Table S4, S7). However, the concentration-adjusted cross-sections for Mn are orders of magnitude lower than for Fe (Fig. 6), and Fe is therefore more likely to be the primary target element. Iron is relatively invariable within this suite (RSD ~8%). A lone high-energy (600 MeV and 21 GeV) experimental-study of V-production from proton-induced Fe-spallation (Perron, 1976) indicates that production cross-sections are still significant at high-energies, and the ratio of ^{51}V/^{50}V produced is low (<1, and this ratio is lower at higher proton energies). Thus, Fe appears to remain an important target for production of light δ^{51}V for higher-energies particle fluxes (e.g. as seen in GCRs) than directly calculated here.

The weaker correlation with $t_e \times$ [Ti]/[V] (despite strong $\varepsilon^{51}\sigma$ depletion at certain energy intervals, Fig. 7e, f) could be due to a number of reasons: 1) the real energetic particle flux is stronger for parts of the energy spectrum where cross-sections with Fe are strongest (typically energies >50 MeV), or 2) thermal neutron capture on Ti at low energies is quantitatively-important – the production of ^{51}V here would counteract production of lower ^{51}V/^{50}V from Ti reactions and protons/alpha-particles.

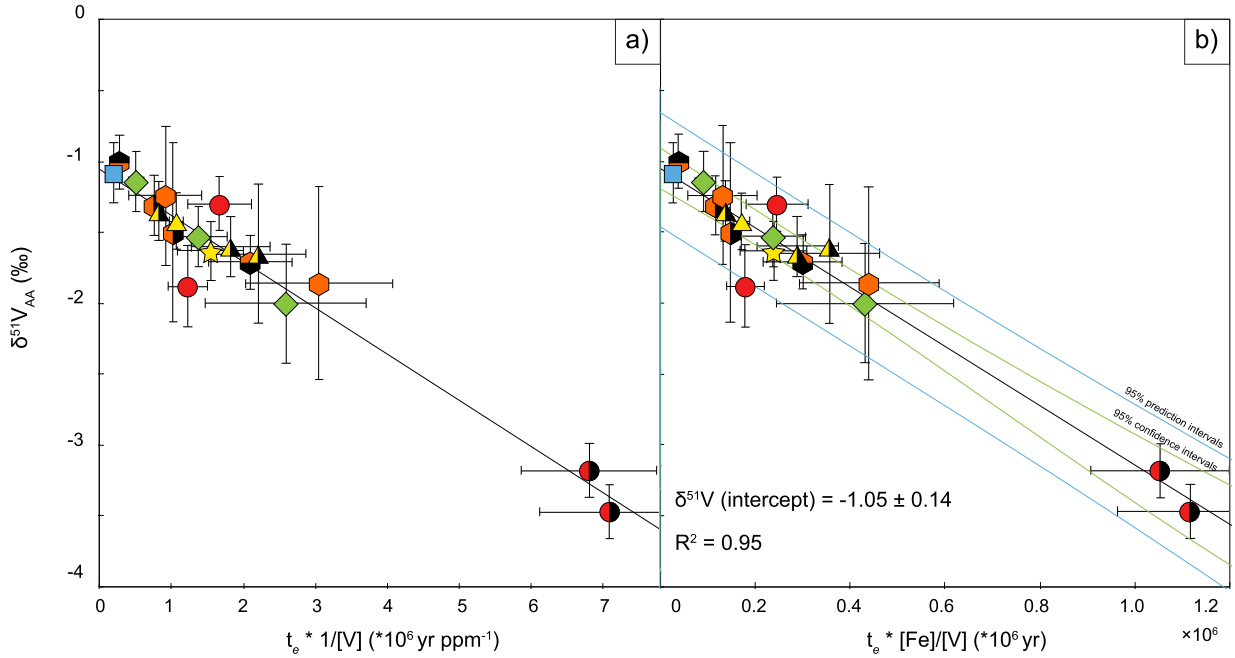


Fig. 8. Sample δ^{51}V versus $t_e \times 1/[V]$ and $t_e \times [Fe]/[V]$. Strong correlations between δ^{51}V and $t_e \times 1/[V]$ (a) indicate that the important targets for isotopic effects are relatively invariant in abundance in the samples. The most likely target element of importance is Fe (b) due to its high-concentration within the samples, relative invariance in concentration, high cross-sections (especially >50 MeV) and negative $\varepsilon^{51}\sigma$ deviations (where cosmogenic reactions will shift δ^{51}V to lighter values). Correlations between δ^{51}V and $t_e \times 1/[V]$ and $t_e \times [Fe]/[V]$ are stronger than those for Ti, Cr and Mn (Fig. S7). The fact that most samples fall on the same trendline indicates that pre-irradiation δ^{51}V variation is restricted, despite highly-variable magmatic histories. A linear regression ($R^2 = 0.95$) is calculated to intercept at $\delta^{51}V = -1.05 \pm 0.14$ (95% confidence intervals). Samples with only literature chemical compositions available (Table 1) or estimated exposure ages (12054-13, 12054-146, 12054-150, 70215-389, 71546-22) were excluded from regression calculations, but included in the calculation of R^2 (excluding literature samples: slope $= -2.0911$, intercept $= -1.054$, $R^2 = 0.9500$; including all samples: slope $= -2.0915$, intercept $= -1.043$, $R^2 = 0.9477$). Symbols same as Figs. 2, 3, 4, 5.

In summary, thermal neutrons – although clearly present in sufficient fluxes to impart significant ^{158}Gd/^{157}Gd excesses (Fig. 5) and ε^{50}Ti depletions (Fig. S6) – cannot be the sole cause of δ^{51}V alteration due the lack of viable pathways for neutron capture production of ^{50}V (Fig. 6). Significant fluxes of higher-energy neutrons (>1 MeV, Fig. 7d, f), protons, or alpha-particles (>5 MeV) must have been present in the samples during their periods of exposure at the lunar surface. The most plausible target element is Fe (Fig. 8a, b). Although SCRs have significantly weaker penetrative-ability than GCRs, both processes may be important for these samples obtained from shallow depths (Section 2).

4.9. Pre-irradiation compositions and implications for the solar system

A linear regression is calculated on the data in Fig. 8b yielding a slope of -2.091×10^{-6}, and a y-intercept of -1.05 ($R^2 = 0.95$). Samples with less-reliable exposure ages (12054, 71546, Supplementary Text, Table S6) or where only literature chemical data exists (12054-13, 70215, 71546) were excluded from this calculation, but their inclusion only slightly affects the resulting regression (slope $= -2.092 \times 10^{-6}$, $R^2 = 0.95$). The coincidence of high-Ti and low-Ti basalts upon the same regression line indicates that, despite different mantle sources and magmatic histories, high-Ti and low-Ti basalts have similar pre-exposure δ^{51}V. The two samples with the shortest exposure age (14053-305, 74275-355) have similar δ^{51}V values despite their significant geochemical differences. Exclusion of the unusually-light sample, 10017, (Section 4.3) results in a similar regression with slope -1.989×10^{-6} and intercept -1.06. Thus, the δ^{51}V range across all samples can largely be attributed to cosmogenic processes post-crystallisation. The intercept of Fig. 8b defines the pre-irradiation average δ^{51}V for the suite. Pre-irradiation lunar basalt composition is estimated to be $\delta^{51}V_{AA} = -1.05 \pm 0.14$‰ (95% CI). Although fractionation during partial melting cannot be excluded, and so an estimate of the bulk lunar mantle δ^{51}V cannot be confidently made, the convergence of high-Ti and low-Ti suites suggests δ^{51}V may be relatively uniform in the basalt source regions.

Recent work by Nielsen et al. (2019) and Xue et al. (2018) using higher-resolution MC-ICPMS shows chondrites to have a restricted range in isotopic compositions (Section 1.4). For chondrites with published noble gas data, cosmogenic exposure ages (using Ne isotopes following Scherer et al., 1998, Table S10) vary between 0.3 and 33.1 Ma. This is shorter than most of the lunar basalts in this study. Plotting meteorite sample δ^{51}V against t_e*[Fe]/[V] shows meteorites to lie on the same trend as lunar samples (within analytical error, Fig. 9). Linear regression shows meteorites to intercept at $\delta^{51}V_{AA} = -1.06 \pm 0.06$‰ (95% CI). Thus, it appears that recent cosmogenic exposure can explain δ^{51}V variations in chondrites in Nielsen et al. (2019). This is not related to differential incorporation of irradiated components (e.g. CAIs), but to irradiation processes operating after the breakup of meteorite parent bodies. The δ^{51}V variability seen in chondrites is unlikely to be related to nucleosynthetic heterogeneities: ordinary chondrites show ε^{54}Cr deficits relative to carbonaceous chondrites (Qin et al., 2010), but variable δ^{51}V (Nielsen et al., 2019; Xue et al., 2018). In summary, not only do lunar samples and chondrites show small pre-irradiation δ^{51}V variability within their own suites, but the Moon and chondrites have similar pre-irradiation values.

Early studies of V isotope ratios in geological materials (prior to the development of MC-ICPMS) were hindered by relatively poor analytical precision, but studies of iron meteorites (e.g. Stauffer and Honda, 1961) reported samples with remarkable ^{51}V/^{50}V ratios (ranging from ~ 5 to 150). In light of the relationship between δ^{51}V and t_e*[Fe]/[V] seen in lunar samples and chondrites, and the apparent importance of Fe as a target element, these extreme ratios appear to be in accordance with the chemical compositions of iron meteorites where [V] typically is <1 ppm.

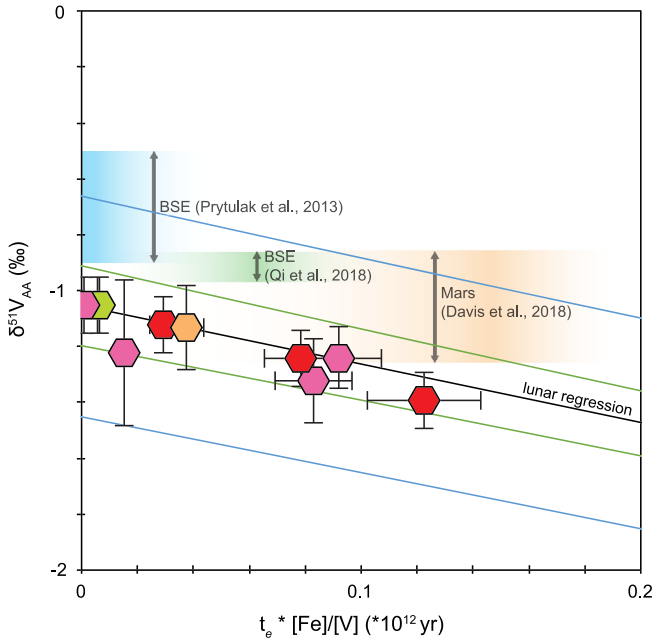


Fig. 9. Chondrite δ^{51}V versus t_e × [Fe]/[V]. Samples with available exposure age, chemical and δ^{51}V data (from Nielsen et al., 2019) fall on the linear regression calculated for lunar samples (within analytical error, Fig. 8b), strongly suggesting the variation observed in recent chondrite data (Nielsen et al., 2019; Xue et al., 2018) is also due to irradiation of samples. Pre-irradiation values overlap with estimates for the BSE (Prytulak et al., 2013; Qi et al., 2018) and Mars (Davis et al., 2018) suggesting that δ^{51}V is relatively uniform between planetary and chondrite parent bodies measured thus far. Symbols as in Fig. 1 (carbonaceous chondrites: pink; ordinary chondrites: red; enstatite chondrite: green; Rumuruti-chondrite: yellow). Data displayed in Table S10.

The pre-irradiation δ^{51}V calculated for the Moon ($\delta^{51}V_{AA} = -1.05 \pm 0.14$‰, 95% CI) is in accordance with the value obtained for chondrites ($\delta^{51}V_{AA} = -1.06 \pm 0.06$‰, 95% CI) and Mars ($\delta^{51}V_{AA} = -1.05 \pm 0.20$‰, 2SD, Davis et al., 2018). These values are similar to the composition of BSE ($\delta^{51}V_{AA} = -0.7 \pm 0.2$‰) from Prytulak et al. (2013) and largely overlap with a more recent estimate from Qi et al. (2018) ($\delta^{51}V_{AA} = -0.91 \pm 0.05$, 2SD, Fig. 9). In contrast to initial studies (Nielsen et al., 2014) it appears that the δ^{51}V of planetary bodies (Earth, Moon, Mars) and chondrites are remarkably similar.

5. Conclusions

1. Vanadium is more compatible during melting, and has higher partition coefficients in crystallising mineral phases, on the Moon compared to the Earth. Therefore, multiple phases can host V in significant quantities during lunar fractional crystallisation.
2. There is no correlation between sample δ^{51}V and mineralogy or chemical composition. High-Ti (excluding 10017) and low-Ti basalts span a similar range in δ^{51}V. Lunar basalts are mostly isotopically lighter than terrestrial basalts, but also show a high degree of variability, spanning a range equal to the most extreme products of magmatic differentiation processes on Earth (Prytulak et al., 2017).
3. Terrestrial crystallisation of (Fe,Ti) oxides strongly fractionates V isotopes, but despite large variations in oxide content in the lunar suite, there is little evidence for oxide crystallisation controlling δ^{51}V. Recent experiments demonstrate $\Delta^{51}V_{magnetite-melt}$ decreases with progressively reducing conditions (Sossi et al., 2018). Thus, it is possible that reduced lunar fO_2 could render $\Delta^{51}V_{oxide-melt}$ analytically-insignificant.
4. Vanadium isotopes correlate with exposure age and neutron-sensitive Gd isotopes, with longer-exposed samples having lighter δ^{51}V (Fig. 4). Calculations of reaction cross-sections protons, alpha-particles and neutrons indicate that Ti and Fe are most important potential targets for cosmogenic alteration of δ^{51}V. However, neutron-capture alone cannot drive the isotopic variability observed.
5. The correlation observed between δ^{51}V and t_e* [Fe]/[V] suggests Fe is the primary target element of importance for cosmogenic V isotope effects, and similar pre-exposure δ^{51}V for high-Ti and low-Ti basalts ($\delta^{51}V_{AA} = -1.05 \pm 0.14$‰, 95% CI, Fig. 8b). The similarity in V isotope ratios between lunar basalts and the BSE adds further weight to the growing body of evidence that the Moon is the Earth's isotopic twin.
6. The co-linearity of the lunar and meteorite correlations for V isotopes versus t_e* [Fe]/[V] implicates cosmogenic effects as the dominant cause of solar system V isotope variability. There is no longer evidence for a significant difference between the BSE and other reservoirs.
7. The magnitude of cosmogenic isotope effects seen in vanadium isotope ratios is much larger than those seen in Cr and Ti isotopes. Vanadium isotopes therefore have the potential to be a useful proxy for recording exposure histories in extra-terrestrial materials.

Acknowledgements

Research funding for this work was provided by the Science and Technology Facilities Council (STFC) to A.N.H. (STFC Planetary Origins and Developments: ST/M001318/1) and by the Natural Environment Research Council (NERC; NE/N009568/1) to J.P. Thanks to NASA-JPL and CAPTEM for provision of lunar samples. Thanks to Jeremy Kent at NASA-JPL for additional communication regarding samples. Thanks to Sune Nielsen for discussion of V isotope data and its implications. Thanks to Matthew Jerram and Naomi Saunders for assistance and coordination in lunar sample preparation, Phil Holdship and Nick Belshaw for providing instrumental support, and Fiona Larner for advice and support throughout this project. Thanks also to Mike Bickle and two anonymous reviewers whose comments greatly improved the manuscript. The research materials supporting this publication can be accessed by contacting SH.

Appendix A. Supplementary material

Supplementary material related to this article can be found online at https://doi.org/10.1016/j.epsl.2019.01.008.

References

Akram, W., Schonbachler, M., 2016. Zirconium isotope constraints on the composition of Theia and current Moon-forming theories. Earth Planet. Sci. Lett. 449, 302–310.

Armytage, R.M.G., Georg, R.B., Williams, H.M., Halliday, A.N., 2012. Silicon isotopes in lunar rocks: implications for the Moon's formation and the early history of the Earth. Geochim. Cosmochim. Acta 77, 504–514.

Bonnand, P., Parkinson, I.J., Anand, M., 2016. Mass dependent fractionation of stable chromium isotopes in mare basalts: implications for the formation and the differentiation of the Moon. Geochim. Cosmochim. Acta 175, 208–221.

Cameron, A.G.W., Ward, W.R., 1976. The origin of the Moon. In: Abstracts of the Lunar and Planetary Science Conference 7, p. 120.

Canil, D., 1997. Vanadium partitioning and the oxidation state of Archaean komatiite magmas. Nature 389, 842–845.

Canup, R.M., 2004. Simulations of a late lunar-forming impact. Icarus 168, 433–456.

Canup, R.M., 2012. Forming a Moon with an Earth-like composition via a Giant Impact. Science 338, 1052–1055.

Cuk, M., Stewart, S.T., 2012. Making the Moon from a fast-spinning Earth: a giant impact followed by resonant despinning. Science 338, 1047–1052.
Dauphas, N., Burkhardt, C., Warren, P.H., Fang-Zhen, T., 2014. Geochemical arguments for an Earth-like Moon-forming impactor. Philos. Trans. R. Soc. A, Math. Phys. Eng. Sci. 372, 20130244.
Davis, D.M., Nielsen, S.G., Magna, T., Mezger, K., 2018. Constraints on the vanadium isotope composition of Mars. In: LPSC 49th Abstr., p. 1696.
Dubois, J.C., Retali, G., Cesario, J., 1992. Isotopic analysis of rare earth elements by total vaporization of samples in thermal ionization mass spectrometry. Int. J. Mass Spectrom. Ion Process. 120, 163–177.
El Goresy, A., Ramdohr, P., Medenbach, O., Bernhardt, H.J., 1974. Taurus–Littrow TiO_2-rich basalts: opaque mineralogy and geochemistry. In: Proceedings of the 5th Lunar Science Conference, vol. 1. Houston, Tex., March 18–22, 1974. Pergamon Press, Inc., New York, pp. 627–652.
Elkins-Tanton, L.T., Burgess, S., Yin, Q.Z., 2011. The lunar magma ocean: reconciling the solidification process with lunar petrology and geochronology. Earth Planet. Sci. Lett. 304, 326–336.
Eugster, O., Tera, F., Burnett, D.S., Wasserburg, G.J., 1970. Isotopic composition of Gd and neutron capture effects in samples from Apollo-11. Earth Planet. Sci. Lett. 8, 20.
Goderis, S., Chakrabarti, R., Debaille, V., Kodolanyi, J., 2016. Isotopes in cosmochemistry: recipe for a Solar System. J. Anal. At. Spectrom. 31, 841–862.
Gounelle, M., Shu, F.H., Shang, H., Glassgold, A.E., Rehm, K.E., Lee, T., 2001. Extinct radioactivities and protosolar cosmic rays: self-shielding and light elements. Astrophys. J. 548, 1051–1070.
Hartmann, W.K., Davis, D.R., 1975. Satellite-sized planetesimals and lunar origin. Icarus 24, 504–515.
Hartung, J.B., Hauser, E.E., Horz, F., Morrison, D.A., Schonfeld, E., Zook, H.A., Mandeville, J.-C., McDonnell, J.A.M., Schaal, R.B., Zinner, E., 1978. Lunar surface processes – report of the 12054 consortium. In: Lunar and Planetary Science Conference Proceedings, pp. 2507–2537.
Hohenberg, C.M., Marti, K., Podosek, F.A., Reedy, R.A., Shirk, J.R., 1978. Comparisons between observed and predicted cosmogenic noble gases in lunar samples. In: Proc. Lunar Planet. Sci. Conf., vol. 9, pp. 2311–2344.
Karner, J., Papike, J.J., Shearer, C.K., 2006. Comparative planetary mineralogy: pyroxene major- and minor-element chemistry and partitioning of vanadium between pyroxene and melt in planetary basalts. Am. Mineral. 91, 1574–1582.S.
Klemme, S., Gunther, D., Hametner, K., Prowatke, S., Zack, T., 2006. The partitioning of trace elements between ilmenite, ulvospinel, annalcolite and silicate melts with implications for the early differentiation of the moon. Chem. Geol. 234, 251–263.
Koning, A.J., Hilaire, S., Duijvestijn, M.C., 2008. TALYS-1.0. In: Bersillon, O., Gunsing, F., Bauge, E., Jacqmin, R., Leray, S. (Eds.), Proceedings of the International Conference on Nuclear Data for Science and Technology. April 22–27, 2007, Nice, France. EDP Sciences, pp. 211–214.
Kruijer, T.S., Kleine, T., Fischer-Gödde, M., Sprung, P., 2015. Lunar tungsten isotopic evidence for the late veneer. Nature 520, 534.
Lee, C.-T.A., Brandon, A.D., Norman, M., 2003. Vanadium in peridotites as a proxy for paleo-fO_2 during partial melting: prospects, limitations, and implications. Geochim. Cosmochim. Acta 67, 3045–3064.
Lee, C.-T.A., Leeman, W.P., Canil, D., Li, Z.-X.A., 2005. Similar V/Sc systematics in MORB and arc basalts: implications for the oxygen fugacities of their mantle source regions. J. Petrol. 46, 2313–2336.
Lee, T., Shu, F.H., Shang, H., Glassgold, A.E., Rehm, K.E., 1998. Protostellar cosmic rays and extinct radioactivities in meteorites. Astrophys. J. 506, 898–912.
Li, Z.-X.A., Lee, C.-T.A., 2004. The constancy of upper mantle fO_2 through time inferred from V/Sc ratios in basalts. Earth Planet. Sci. Lett. 228, 483–493.
Liu, Y., Spicuzza, M.J., Craddock, P.R., Day, J.M.D., Valley, J.W., Dauphas, N., Taylor, L.A., 2010. Oxygen and iron isotope constraints on near-surface fractionation effects and the composition of lunar mare basalt source regions. Geochim. Cosmochim. Acta 74, 6249–6262.
Lugmair, G.W., Shukolyukov, A., 1998. Early solar system timescales according to Mn-53–Cr-53 systematics. Geochim. Cosmochim. Acta 62, 2863–2886.
Mallmann, G., O'Neill, H.S.C., 2009. The crystal/melt partitioning of V during mantle melting as a function of oxygen fugacity compared with some other elements (Al, P, Ca, Sc, Ti, Cr, Fe, Ga, Y, Zr and Nb). J. Petrol. 50, 1765–1794.
Mason, B., Jarosewich, E., Melson, W.G., 1972. Mineralogy, petrology, and chemical composition of lunar samples 15085, 15256, 15271, 15471, 15475, 15476, 15535, 15555, and 15556. In: Proceedings of the Lunar Science Conference, vol. 3, pp. 785–796.
Mastrobuono-Battisti, A., Perets, H.B., Raymond, S.N., 2015. A primordial origin for the compositional similarity between the Earth and the Moon. Nature 520, 212.
McDonough, W.F., Sun, S.S., 1995. The composition of the Earth. Chem. Geol. 120, 223–253.
Millet, M.A., Dauphas, N., Greber, N.D., Burton, K.W., Dale, C.W., Debret, B., Macpherson, C.G., Nowell, G.M., Williams, H.M., 2016. Titanium stable isotope investigation of magmatic processes on the Earth and Moon. Earth Planet. Sci. Lett. 449, 197–205.
Mougel, B., Moynier, F., Gopel, C., 2018. Chromium isotopic homogeneity between the Moon, the Earth, and enstatite chondrites. Earth Planet. Sci. Lett. 481, 1–8.
Neal, C.R., Taylor, L.A., 1992. Petrogenesis of mare basalts – a record of lunar volcanism. Geochim. Cosmochim. Acta 56, 2177–2211.
Nielsen, S.G., Prytulak, J., Halliday, A.N., 2011. Determination of precise and accurate V-51/V-50 isotope ratios by MC-ICP-MS, part 1: chemical separation of vanadium and mass spectrometric protocols. Geostand. Geoanal. Res. 35, 293–306.
Nielsen, S.G., Prytulak, J., Wood, B.J., Halliday, A.N., 2014. Vanadium isotopic difference between the silicate Earth and meteorites. Earth Planet. Sci. Lett. 389, 167–175.
Nielsen, S.G., Owens, J.D., Horner, T.J., 2016. Analysis of high-precision vanadium isotope ratios by medium resolution MC-ICP-MS. J. Anal. At. Spectrom. 31, 531–536.
Nielsen, S.G., Auro, M., Righter, K., Davis, D., Prytulak, J., Wu, F., Owens, J.D., 2019. Nucleosynthetic vanadium isotope heterogeneity of the early solar system recorded in chondritic meteorites. Earth Planet. Sci. Lett. 505, 131–140.
O'Neill, H.S.C., Navrotsky, A., 1984. Cation distributions and thermodynamic properties of binary spinel solid-solutions. Am. Mineral. 69, 733–753.
Pahlevan, K., Stevenson, D.J., 2007. Equilibration in the aftermath of the lunar-forming giant impact. Earth Planet. Sci. Lett. 262, 438–449.
Pahlevan, K., Stevenson, D.J., Eiler, J.M., 2011. Chemical fractionation in the silicate vapor atmosphere of the Earth. Earth Planet. Sci. Lett. 301, 433–443.
Papike, J.J., Hodges, F.N., Bence, A.E., Cameron, M., Rhodes, J.M., 1976. Mare basalts – crystal-chemistry, mineralogy, and petrology. Rev. Geophys. 14, 475–540.
Papike, J.J., Karner, J.M., Shearer, C.K., 2005. Comparative planetary mineralogy: valence state partitioning of Cr, Fe, Ti, and V among crystallographic sites in olivine, pyroxene, and spinel from planetary basalts. Am. Mineral. 90, 277–290.
Perron, C., 1976. Cross sections for production of stable and long-lived nuclides by high energy spallation of iron; cosmic ray implications. Phys. Rev. C 14 (3), 1108–1120.
Prytulak, J., Nielsen, S.G., Halliday, A.N., 2011. Determination of precise and accurate V-51/V-50 isotope ratios by multi-collector ICP-MS, part 2: isotopic composition of six reference materials plus the Allende chondrite and verification tests. Geostand. Geoanal. Res. 35, 307–318.
Prytulak, J., Nielsen, S.G., Ionov, D.A., Halliday, A.N., Harvey, J., Kelley, K.A., Niu, Y.L., Peate, D.W., Shimizu, K., Sims, K.W.W., 2013. The stable vanadium isotope composition of the mantle and mafic lavas. Earth Planet. Sci. Lett. 365, 177–189.
Prytulak, J., Sossi, P.A., Halliday, A.N., Plank, T., Savage, P.S., Woodhead, J.D., 2017. Stable vanadium isotopes as a redox proxy in magmatic systems? Geochem. Perspect. Lett. 3, 75–84.
Qi, Y., Wu, F., Ionov, D., Puchtel, I., Nicklas, R., Yu, H., Kang, J., Li, C., Huang, F., 2018. The vanadium isotopic composition of the BSE: constraints from peridotites and komatiites. In: Goldschmidt Abstracts, 2088.
Qin, L.P., Alexander, C.M.O., Carlson, R.W., Horan, M.F., Yokoyama, T., 2010. Contributors to chromium isotope variation of meteorites. Geochim. Cosmochim. Acta 74, 1122–1145.
Reufer, A., Meier, M.M.M., Benz, W., Wieler, R., 2012. A hit-and-run giant impact scenario. Icarus 221, 296–299.
Rufu, R., Aharonson, O., Perets, H.B., 2017. A multiple-impact origin for the Moon. Nat. Geosci. 10, 89–94.
Ryder, G., Schuraytz, B.C., 2001. Chemical variation of the large Apollo 15 olivine–normative mare basalt rock samples. J. Geophys. Res., Planets 106, 1435–1451.
Schauble, 2004. Applying stable isotope fractionation theory to new systems. Rev. Mineral. Geochem. 55, 65–111.
Scherer, P., Herrmann, S., Schultz, L., 1998. Noble gases in twenty-one Saharan LL-chondrites: exposure ages and possible pairings. Meteorit. Planet. Sci. 33, 259–265.
Sedaghatpour, F., Teng, F.Z., Liu, Y., Sears, D.W.G., Taylor, L.A., 2013. Magnesium isotopic composition of the Moon. Geochim. Cosmochim. Acta 120, 1–16.
Seifert, S., Ringwood, A.E., 1988. The lunar geochemistry of chromium and vanadium. Earth Moon Planets 40, 45–70.
Sossi, P.A., Bullet, J.P., O'Neill, H.S.C., 2018. Experimental calibration of vanadium partitioning and stable isotope fractionation between hydrous granitic melt and magnetite at 800 degrees C and 0.5 GPa. Contrib. Mineral. Petrol. 173, 27.
Sossi, P.A., Moynier, F., 2017. Chemical and isotopic kinship of iron in the Earth and Moon deduced from the lunar Mg-Suite. Earth Planet. Sci. Lett. 471, 125–135.
Sossi, P.A., Moynier, F., Chaussidon, M., Villeneuve, J., Kato, C., Gounelle, M., 2017. Early Solar System irradiation quantified by linked vanadium and beryllium isotope variations in meteorites. Nat. Astron. 1, 0055.
Stauffer, H., Honda, M., 1961. Cosmic-ray-produced V50 and K40 in the iron meteorite Aroos. J. Geophys. Res. 66, 3584–3586.
Wiesli, R.A., Beard, B.L., Taylor, L.A., Johnson, C.M., 2003. Space weathering processes on airless bodies: Fe isotope fractionation in the lunar regolith. Earth Planet. Sci. Lett. 216, 457–465.
Wood, B.J., Wade, J., Kilburn, M.R., 2008. Core formation and the oxidation state of the Earth: additional constraints from Nb, V and Cr partitioning. Geochim. Cosmochim. Acta 72, 1415–1426.
Wu, F., Qi, Y., Perfit, M.R., Gao, Y., Langmuir, C.H., Wanless, V.D., Yu, H., Huang, F., 2018. Vanadium isotope compositions of mid-ocean ridge lavas and altered oceanic crust. Earth Planet. Sci. Lett. 493, 128–139.

Wu, F., Qi, Y.H., Yu, H.M., Tian, S.Y., Hou, Z.H., Huang, F., 2016. Vanadium isotope measurement by MC-ICP-MS. Chem. Geol. 421, 17–25.
Xue, Y., Li, C.-H., Zhang, C., Miao, B., Huang, F., 2018. The vanadium isotopic composition of L ordinary chondrites. Acta Geochim. 501, 508.
Young, E.D., Kohl, I.E., Warren, P.H., Rubie, D.C., Jacobson, S.A., Morbidelli, A., 2016. Oxygen isotopic evidence for vigorous mixing during the Moon-forming giant impact. Science 351, 493–496.
Zhang, J.J., Dauphas, N., Davis, A.M., Leya, I., Fedkin, A., 2012. The proto-Earth as a significant source of lunar material. Nat. Geosci. 5, 251–255.